Ultracold scattering of alkali-metal atoms in magnetic fields

BLACKLEY, CAROLINE,LAURA-ANNE

BLACKLEY, CAROLINE,LAURA-ANNE (2015) *Ultracold scattering of alkali-metal atoms in magnetic fields*, Durham theses, Durham University. Available at Durham E-Theses Online: http://etheses.dur.ac.uk/11202/

Ultracold scattering of alkali-metal atoms in magnetic fields

Caroline Laura-Anne Blackley

Submitted for the degree of Doctor of Philosophy
June 30, 2015

Abstract

This thesis reports on calculations of the scattering properties of a variety of ultracold alkali-metal mixtures. In particular, we have calculated the scattering properties of homonuclear mixtures of ^{85}Rb, in a variety of incoming channels, and we have calculated the properties of heteronuclear mixtures of the isotopologues of Rb and Cs, and K and Cs. In general, we are interested in the location and character of Feshbach resonances in these mixtures with a view towards ultracold molecule formation. In ^{85}Rb there is a rich Feshbach structure and potential uses for the resonances that we find, in the scattering lengths of the various incoming channels, are discussed. In ^{85}RbCs there is a rich Feshbach structure and the prospects for ultracold molecule formation using this system are detailed. Similarly, we detail the Feshbach resonances of ^{87}RbCs and discuss our results in the context of the successful formation of ultracold ground-state molecules. In the isotopologues of KCs each system has a rich Feshbach structure and we detail the location and width of the resonances, as well as the potential for ultracold molecule formation using each of the isotopes of potassium. In addition to scattering calculations, we have also calculated the location and character of the highest-lying bound states of each system. We have investigated the energy dependence of the scattering length using accurate coupled-channel calculations on ^{6}Li, ^{39}K and ^{133}Cs to explore the behaviour of the effective range in the vicinity of both broad and narrow Feshbach resonances. We present an alternative parametrization of the effective range and further demonstrate that an analytical form of an energy and magnetic field-dependent phase shift, based on multichannel quantum defect theory, gives accurate results for the energy-dependent scattering length. Lastly, we examine the effect of additional external fields on alkali-metal collisions and discuss how external fields can be used to manipulate the interaction properties of a system.

Ultracold scattering of alkali-metal atoms in magnetic fields

Caroline Laura-Anne Blackley

A Thesis presented for the degree of
Doctor of Philosophy

Department of Chemistry
University of Durham

June 30, 2015

Contents

Abstract **i**

Declaration **xii**

Acknowledgements **xiii**

1 Introduction **1**

1.1 Ultracold atoms and molecules 1

1.2 Outline of Thesis 7

1.3 List of Publications 9

2 Scattering Theory **11**

2.1 Wavefunction Scattering 11

2.1.1 The partial-wave expansion 12

2.1.2 Scattering S-matrix 14

2.2 Low-energy scattering 15

2.3 Scattering resonances 17

2.3.1 Inelastic scattering 18

2.4 Zero-energy Feshbach resonances 19

2.5 Coupled-Channel methods 21

2.5.1 Propagators 23

2.5.1.1 Renormalised Numerov propagator 23

2.5.1.2 Log-Derivative propagators 24

2.5.2 MOSLCAT, FIELD, BOUND 25

3 Alkali-Alkali Scattering **27**

3.1 Collision Hamiltonian in a static magnetic field 27

3.1.1 Monomer Hamiltonian 28

3.1.2 Interaction Potentials 28

3.2 Matrix elements of the Hamiltonian 30

4 Homonuclear Scattering 35

4.1 85-Rubidium 35

4.1.1 Scattering in the $(f, m_f) = (2, -2) + (2, -2)$ channel 37

4.1.2 Scattering in the ground state 41

4.1.3 Scattering in mixed states 45

4.1.4 Potential application of a spin mixture 47

4.2 87-Rubidium 50

4.3 133-Cesium 53

5 Heteronuclear Molecule Formation 56

5.1 RbCs 57

5.1.1 ^{85}RbCs 58

5.1.1.1 Resonances and bound states in the s-wave incoming channel 58

5.1.1.2 Resonances and bound states in the p-wave incoming channel 62

5.1.1.3 Dipole-trap induced features 64

5.1.1.4 Outlook for molecule formation 64

5.1.2 ^{87}RbCs 69

5.1.2.1 Feshbach resonances and bound states 69

5.1.2.2 Magnetic moments of bound states 70

5.1.2.3 Molecule formation 70

5.2 KCs 76

5.2.1 ^{39}KCs 76

5.2.2 ^{40}KCs 78

5.2.3 ^{41}KCs 80

5.3 Prospects for alkali-alkali ultracold molecule formation 87

6 Analysis of singlet and triplet character 95

6.1 A molecular basis 95

6.1.1 The isotropic potential operator 96

6.1.2 The spin-spin interactions 96

6.1.3 The hyperfine interactions 98

6.1.4 The Zeeman interactions 99
6.1.5 Bound states of ^{85}RbCs 99
6.1.6 Bound states of ^{6}Li$_2$ 103
6.2 Transformation of the product states of the field-dressed Hamiltonian to the $|SM_Sm_{i,a}m_{i,b}\rangle$ basis set 104

7 Effective Range Theory 107
7.1 Introduction to Effective Range Theory 107
7.2 Behaviour of the effective range near a Feshbach resonance 109
7.3 Limitations of the effective-range expansion 116
7.4 MQDT approach to an energy-dependent phase shift 118
7.5 Effectiveness of the MQDT formula 123
7.6 Conclusions 126

8 Radio-Frequency dressing of Feshbach resonances 128
8.1 Collision Hamiltonian in a static magnetic field and rf field 129
8.2 A spin-1/2 system 130
8.3 Building an rf-dressed basis set 132
8.4 RF-induced resonances in RbCs 134

9 Conclusions 142

Appendix 148

A Angular Momentum coupling and matrix elements 148
A.1 Notes on angular momentum coupling 148
A.2 Matrix elements in the $|(s_a, i_a)f_a\rangle\,|(s_b, i_b)f_b\rangle\,|F, M_F\rangle\,|L, M_L\rangle$ basis set . . . 152

B Complete list of p-wave resonances in ^{85}RbCs 155

C Complete list of Feshbach resonances in KCs 158

D Consideration of the intra- and inter-species scattering-length combinations in mixtures ^{85}RbCs 162

E Mixed-state scattering lengths in ^{85}Rb 165

F Triplet fraction in products of field-dressed eigenfunctions of ^{85}RbCs 168

List of Figures

2.1 Diagram of wavefunction scattering 12

2.2 Spherical Bessel functions of the first kind (left) and second kind (right) . . 13

2.3 Diagram showing the asymptotic behaviour of a wavefunction at zero energy 16

2.4 Diagrams relating to Feshbach resonance discussion 19

3.1 Breit-Rabi diagram of ^{85}Rb 29

3.2 Potential energy curves for RbCs 31

3.3 Potential energy curves for KCs 32

4.1 ^{85}Rb$_2$: s-wave scattering length in the $(f, m_f) = (2, -2) + (2, -2)$ channel and bound states 39

4.2 Experimental features observed in the $(f, m_f) = (2, -2) + (2, -2)$ channel of ^{85}Rb$_2$. 40

4.3 Experimental loss behaviour of the two inelastically dominated features observed in the $(2, -2)$ state in ^{85}Rb$_2$. 41

4.4 The rate coefficient for 2-body loss K_{loss} and the corresponding real part of the scattering length (dashed lines) for the $(f, m_f) = (2, -2) + (2, -2)$ channel of ^{85}Rb 42

4.5 ^{85}Rb$_2$: s-wave scattering length in the $(f, m_f) = (2, +2) + (2, +2)$ channel and bound states 44

4.6 Breit-Rabi diagram of ^{85}Rb$_2$ 45

4.7 Scattering length of the $(f, m_f) = (2, +2) + (3, +3)$ channel of ^{85}Rb. 46

4.8 A resonance measured between the $(2, +2)$ and $(3, +3)$ spin states in ^{85}Rb at 817.45(5) G. 46

4.9 The s-wave scattering length for the $(f, m_f) = (2, 2) + (3, 2)$, $(2, 2) + (2, 2)$ and $(3, 2) + (3, 2)$ channels of ^{85}Rb 49

4.10 Breit-Rabi diagram of ^{87}Rb 50

4.11 $^{87}\mathrm{Rb}_2$: s-wave scattering length in the $(f, m_f) = (1, +1) + (1, +1)$ channel and bound states 52

4.12 Breit-Rabi diagram of $^{133}\mathrm{Cs}$ 54

4.13 $^{133}\mathrm{Cs}_2$: s-wave scattering length in the $(f, m_f) = (3, 3) + (3, 3)$ channel and bound states 55

5.1 Bound states of ^{85}RbCs calculated using restricted sets of the $|(f_a, f_b)F, M_F\rangle$ basis 61

5.2 Temperature data for a mixture of ^{85}Rb and ^{133}Cs in the (2,+2) and (3,+3) state, respectively, evaporated at different magnetic bias fields from 0 to 700 G 62

5.3 An intraspecies ^{85}Rb resonance at 368.78(3) G neighboring an interspecies resonance at 370.39(1) G in $^{85}\mathrm{Rb}^{133}\mathrm{Cs}$ 63

5.4 ^{85}RbCs: s-wave scattering length and bound states 66

5.5 ^{85}RbCs: s-wave scattering length and highest-lying bound state 67

5.6 ^{85}RbCs: p-wave scattering length and bound states 68

5.7 Magnetic moments of the bound states of ^{87}RbCs 72

5.8 Experimental magnetoassociation sequence for ^{87}RbCs 73

5.9 ^{87}RbCs: s-wave scattering length and bound states 74

5.10 ^{87}RbCs: s-wave scattering length and highest-lying bound state 75

5.11 ^{39}KCs: Effect of spin-orbit coupling on Feshbach resonances 79

5.12 ^{39}KCs: s-wave scattering length and bound states 82

5.13 ^{40}KCs: s-wave scattering length and bound states 83

5.14 ^{40}KCs: s-wave scattering length and the highest-lying bound state 84

5.15 ^{41}KCs: s-wave scattering length and bound states 85

5.16 ^{41}KCs: s-wave scattering length and the highest-lying bound state 86

5.17 Scattering length of Cs in the s-wave incoming $(f, m_f) = (3, -3) + (3, -3)$ channel 89

5.18 Scattering lengths for isotopologues of RbCs, together with those of the corresponding isotopes of Rb and Cs. The coloured bars facilitate the identification of regions where the combination is conducive to molecule formation. 91

5.19 Scattering lengths for isotopologues of KCs, together with those of the corresponding isotopes of K and Cs. The coloured bars facilitate the identification of regions where the combination is conducive to molecule formation. 93

6.1 Bound states of ^{85}RbCs in an $|SIFM_F\rangle$ basis 100

6.2 Bound states of ^{85}RbCs between 300 and 400 G in an $|SIFM_F\rangle$ basis . . . 101

6.3 ^{85}RbCs bound-state wavefunction for the state which causes the resonance around 187 G 102

6.4 ^{85}RbCs bound-state wavefunction for the state which causes the resonance around 370 G 102

6.5 Bound states of ^{6}Li$_2$ in an $|SIFM_F\rangle$ basis 103

6.6 ^{6}Li$_2$ bound-state wavefunction for the state which causes the resonance around 543 G 104

6.7 Triplet fraction of the products of the field-dressed atomic eigenfunctions of ^{85}RbCs 106

7.1 The field-dependent effective range for the $(f, m_f) = (3, +3) + (3, +3)$ channel of ^{133}Cs 111

7.2 The field-dependent effective range for the $(f, mf) = (1/2, 1/2)+(1/2, -1/2)$ channel of ^{6}Li from coupled-channel calculations and as calculated from Eq. (7.2.1); the quantity $r_{\rm eff}a_0^2$ for both the wide and narrow resonances; the function $f(r_{\rm eff})$ of Eq. (7.2.4) with parameters appropriate for each resonance112

7.3 Energy dependence of the phase shift $\eta(E)$ at magnetic fields around narrow resonances in ^{6}Li, ^{39}K and ^{133}Cs 117

7.4 Energy dependence of the phase shift $\eta(E)$ at magnetic fields around the broad resonance in ^{6}Li 119

7.5 The two-channel model of the resonance at 226.73 G in the $(f, m_f) = (3, +3) + (3, +3)$ channel of Cs 119

7.6 Behaviour of the analytical functions that make the up the Z^c-matrix; the functions $K_l(E)$; the function $\tan\lambda(E)$; and the function $C^{-2}(E)$ 121

7.7 Contour plot of $\sin^2\eta(E, B)$ around the resonance at $B_0 = 226.73$ G in the $(f, m_f) = (3, +3) + (3, +3)$ channel of ^{133}Cs and around the resonance at $B_0 = 543.40$ G in the $(1/2, +1/2) + (1/2, -1/2)$ channel of ^{6}Li 124

7.8 Contour plot of $\sin^2\eta(E, B)$ for $E > 0$ around the resonance at $B_0 = 554$ G in the $(f, m_f) = (3, +3) + (3, +3)$ channel of ^{133}Cs 125

8.1 The energy levels of a spin-1/2 atom in a circularly polarised photon field. . 130

8.2 The energy levels of a spin-1/2 atom in a linearly polarised photon field. . . 131

8.3 rf-coupling diagram 132

8.4 Matrix elements of the rf-dressed Hamiltonian 135

8.5 Bound-state energy levels for ^{85}RbCs with $L = 0$ and $M_F = 4, 5$ and 6. . . . 136

8.6 Asymptotic energy levels of ^{85}RbCs with an applied rf field of $\omega_{\rm rf}$ =100 MHz and $B_{\rm osc} = 5$ G. 137

8.7 Resonance caused by σ_- polarised rf field in the s-wave $(f, m_f) = (2, +2) + (3, +3)$ channel of ^{85}RbCs with varying $\omega_{\rm rf}$ strength 138

8.8 Resonance caused by σ_+ polarised rf field in the s-wave $(f, m_f) = (2, +2) + (3, +3)$ channel of ^{85}RbCs with varying $\omega_{\rm rf}$ strength 139

8.9 Resonance caused by σ_+ polarised rf field in the s-wave $(f, m_f) = (2, +2) + (3, +3)$ channel of ^{85}RbCs with varying $B_{\rm osc}$ strength 140

D.1 Comparison of the s-wave scattering lengths of the $(f, m_f) = (3, +3) + (3, +3)$ channel of ^{133}Cs, the $(2, +2) + (2, +2)$ and $(2, -2) + (2, -2)$ channels of ^{85}Rb and the $(2, -2) + (3, +3)$ channel of ^{85}RbCs 163

D.2 Comparison of the s-wave scattering lengths of the $(f, m_f) = (3, +3) + (3, +3)$ channel of ^{133}Cs, the $(2, +2) + (2, +2)$ and $(2, -2) + (2, -2)$ channels of ^{85}Rb and the $(2, -2) + (3, -3)$ channel of ^{85}RbCs 164

E.1 Scattering length of the $(f, m_f) = (2, +2) + (3, +0)$ channel of ^{85}Rb. 166

E.2 Scattering length of the $(f, m_f) = (2, +2) + (3, +1)$ channel of ^{85}Rb. 166

E.3 Scattering length of the $(f, m_f) = (2, +2) + (3, +2)$ channel of ^{85}Rb. 167

F.1 Triplet fraction of the products of the field-dressed atomic eigenfunctions of ^{85}RbCs 169

F.2 Triplet fraction of the products of the field-dressed atomic eigenfunctions of ^{85}RbCs 170

F.3 Triplet fraction of the products of the field-dressed atomic eigenfunctions of ^{85}RbCs 171

List of Tables

4.1 Location and assignment of Feshbach resonances for ^{85}Rb$_2$ in the $(f, m_f) = (2, -2) + (2, -2)$ channel in the field range between 0 and 1000 G. 38

4.2 Location and assignment of Feshbach resonances for ^{85}Rb$_2$ in the $(f, m_f) = (2, +2) + (2, +2)$ channel in the field range between 0 and 1000 G 43

4.3 Location and assignment of Feshbach resonances for ^{87}Rb$_2$ in the $(f, m_f) = (1, +1) + (1, +1)$ channel in the field range between 0 and 1008 G 51

5.1 Dipole moment, rotational constants and reaction stability for heteronuclear bi-alkali molecules. 57

5.2 Full listing of s-wave Feshbach resonances for ^{85}Rb $|2, +2\rangle$ + ^{133}Cs $|3, +3\rangle$ in the field range 0 to 1000 G 60

5.3 Experimentally observed p-wave Feshbach resonances in ^{85}RbCs. 64

5.4 Full listing of s-wave Feshbach resonances for ^{87}Rb $|1, +1\rangle$ + ^{133}Cs $|3, +3\rangle$ in the field range 0 to 1000 G 71

5.5 All s,d-wave Feshbach resonances with widths $>$ 1 mG for ^{39}KCs in the field range 0 to 1000 G. 78

5.6 All s,d-wave Feshbach resonances with widths $>$ 1 mG for ^{40}KCs in the field range 0 to 1000 G. 80

5.7 All s,d-wave Feshbach resonances with widths $>$ 1 mG for ^{41}KCs in the field range 0 to 1000 G. 81

5.8 Intraspecies and interspecies scattering lengths at fields that bound the regions where $40\ a_0 \lesssim a_{\rm Cs} \lesssim 250\ a_0$. 88

7.1 Parameters of Eq. (7.2.4) that characterize $r_{\rm eff}$ in the vicinity of resonances of different types. 114

7.2 Parameters for effective-range calculations 118

7.3 The resonance parameters required for two-channel formula 123

B.1 Complete list of Feshbach resonances due to p,f-wave bound states in the scattering volume of the incoming $L = 1, M_L = +1$ channel of ^{85}RbCs . . . 156

B.2 Complete list of Feshbach resonances due to p,f-wave bound states in the scattering volume of the incoming $L = 1, M_L = 0$ channel of ^{85}RbCs 156

B.3 Complete list of Feshbach resonances due to p,f-wave bound states in the scattering volume of the incoming $L = 1, M_L = -1$ channel of ^{85}RbCs . . . 157

C.1 Complete list of Feshbach resonances due to s-wave and d-wave states in ^{39}KCs 159

C.2 Complete list of Feshbach resonances due to s-wave and d-wave states in ^{40}KCs 160

C.3 Complete list of Feshbach resonances due to s-wave and d-wave states in ^{41}KCs 161

Declaration

I confirm that no part of the material offered has previously been submitted by myself for a degree in this or any other University. Where material has been generated through joint work, the work of others has been indicated.

Acknowledgements

Firstly, I would like to thank my supervisor Jeremy Hutson for all his patience, advice and support throughout my PhD. I'd also like to thank Paul Julienne and Simon Cornish who have always been willing to share their expertise with me and who have helped me immensely.

I'd like to thank everyone I've worked with in the Hutson group throughout my PhD.; Daniel Brue, Maykel González-Martínez, James Croft, Jesse Lutz, Matthew Frye, George McBane, Dermot Green, Morita Masato, Hannah Patel, Christophe Vaillante, Daniel Owens, Maja Lenz, and in particular Ruth Le Sueur who helped guide me through the RbCs work.

A lot of my research has involved collaborations with Simon Cornish's group and in particular those who work on the RbCs experiment so I'd like to thank Hung-Wen Cho, Danny McCarron, Daniel Jenkins, Peter Molony, Phil Gregory, Bo Lu and Zhonghua Ji. A special thank you goes to Michael Köppinger who patiently explained, many times, how the experiment worked. I'd also like to thank Christoph Weiss for involving me in his work on Solitons.

Finally, I need to say a big thank you to my family and to James, without whom I would have never made it this far.

To Mum, Dad, and Richard

Chapter 1

Introduction

1.1 Ultracold atoms and molecules

In the day-to-day world we encounter three different types of objects: solid, liquids and gases. Each has their own characteristics and properties that defines what it is and how it behaves. However, with the advancement of scientific techniques we have become aware that more states of matter exist which exhibit novel behaviour. At very low temperatures we observe phenomena such as superconductivity, superfluidity, and Bose-Einstein condensates.

The first person to introduce the idea of a minimum temperature was Guillaume Amontons in 1703, when he was working on an air-thermometer. He suppositioned that a minimum temperature must exist where the “spring” of the air disappears [1]. Lord Kelvin put a more definite number on this limit, in 1848, by asserting that *“a unit of heat descending from a body A at the temperature T of this scale, to a body B at the temperature $(T-1)$, would give out the same mechanical effect, whatever be the number T”* [2]; he calculated this point, at which no further heat could be transferred, to be independent of the substance, and to occur at $-273°$C or 0 K. Temperatures as low as 194 K were reached in 1835 with the invention of dry ice [3], and in 1899 hydrogen was solidified at temperatures of 14 K [4]. In 1911 superconductivity was first observed when Heike Kamerlingh-Onnes cooled mercury to 4 K using liquid helium [5]. The phenomenon of superfluidity was first observed in 1937 by Kapitza, Allen and Misener [6, 7] who cooled liquid Helium to 2.2 K. With laser-cooling techniques atomic clouds can be cooled to temperatures in the μK range; W. Phillips, S. Chu and C. Cohen-Tannoudji were awarded the Nobel prize in Physics in 1997 for their work on methods of cooling and trapping atoms with laser light [8–10]. In the following work we refer to temperatures below 1 K as "cold" and below 1 mK as "ultracold".

Ultracold atoms

The phenomenon of Bose-Einstein Condensation was first predicted by Satyendra Nath Bose and Albert Einstein in the 1920's [11, 12]. The Bose-Einstein Condensate (BEC) refers to a new state of matter which occurs when particles are cooled close to absolute zero. At low enough temperatures a group of dilute atoms can be described as a wave packet, rather than a particle. The length of the wave packet is described by the de Broglie wavelength, $\lambda_{\mathrm{dB}} = \sqrt{2\pi\hbar/(mk_{\mathrm{B}}T)}$, where m is the particle mass and T is the temperature. As the particles are cooled their deBroglie wavelengths eventually become larger then the inter-particle spacing. At a critical temperature the wavelengths begin to overlap and eventually, at condensation, bosonic particles form a single coherent matter wave. The onset of the BEC can be quantised in terms of the phase-space density (PSD), $\mathrm{PSD} = n\lambda_{\mathrm{dB}}^3$, where n is the number density of the particles. Fermionic particles display a different behaviour and instead are modelled as a Fermi gas, which has a non-zero pressure even at zero temperature, due to the 'degeneracy pressure' associated with the Pauli exclusion principle; this phenomenon can be used to describe the behaviour of white dwarfs and neutron stars.

The first dilute BECs were observed experimentally in 1995 by E. Cornell and C. Wieman [13] and by W. Ketterle [14], who were awarded the Nobel Prize in Physics for their discoveries in 2001. The first quantum-degenerate gases of fermions were achieved later, in 2003, by DeMarco and Jin [15]. The BECs were created by using laser-cooling techniques followed by evaporative cooling [13]. Laser-cooling techniques combined with magnetic traps can be used to create ultracold clouds of atoms with temperatures in the μK range. Using evaporative cooling the hottest atoms are released from the trap and cooler atoms allowed to rethermalise, thus lowering the average temperature of the atomic cloud to tens of nK where condensation can be achieved.

Since the first successful BEC formations the field of ultracold atoms has rapidly expanded. Among others, condensates of hydrogen, lithium, sodium, rubidium and cesium have been created [16–20] as well as condensates of more exotic atoms such as erbium and ytterbium [21,22]. As the field moves rapidly forward the cooling and trapping of ultracold molecules provides the next challenge.

Applications of ultracold molecules

The creation of ultracold polar molecules is of great interest as they provide numerous new and exciting avenues of research. They offer a wide range of applications including: studies of few-body quantum physics, high-precision spectroscopy, quantum simulators for many-body phenomena and controlled chemistry [23–25]. The low temperature of ultracold molecules correlates with a reduced Doppler broadening of the spectral lines [26]. This makes ultracold molecules ideal candidates for use in high-precision measurements such as measurements of the electric dipole moment (EDM) of the electron [27, 28] and measurements of the possible time-variation of fundamental constants such as the fine structure constant and the electron-to-proton mass ratio [26]. Below 1 K the thermal motion of molecules becomes small compared to perturbations from electric and magnetic fields, and so reactions could be controlled and manipulated by the application of external fields [29]. At ultra-low temperatures the dynamics of molecular reactions change, as quantum mechanical effects dominate, and reaction processes can be dramatically enhanced by quantum threshold phenomena [30, 31]. Different trapping geometries have also been shown to have strong effects on reaction processes in the ultracold regime [29]. Ultracold polar molecules have permanent electric dipole moments which give rise to anisotropic, long-range dipole-dipole interactions. These dipole-dipole interactions can operate over a larger range then optical lattice spacings and could be used in quantum simulation, quantum information processing and to create novel quantum phases.

Methods of forming ultracold molecules

The laser-cooling technique used to produce ultracold atoms requires a well-defined absorption and emission cycle. In general, laser cooling does not work on molecules which have a much more complex energy-level structure; although, there is a small sub-class of molecules, with a large Franck-Condon overlap between the relevant levels of the absorption and emission cycle, where it has been shown to be effective [32]. The first molecule to be successfully cooled and trapped was the radical CaH, in 1998, using a cold buffer gas of ^{3}He [33]. Ultracold bialkali molecules have been successfully produced using both photoassociation and magnetoassociation techniques [34, 35]. There are two main classes of techniques which have been developed to produce cold molecules;

- Direct cooling: Methods designed to directly cool a sample of high temperature molecules to low temperatures such as sympathetic cooling and laser cooling.

- Indirect cooling: Methods designed to associate pre-cooled atoms to form molecules at low temperatures such as photoassociation and magnetoassociation.

Direct Cooling

Direct cooling techniques include a versatile group of techniques which can be used to cool many different types of molecules to 'cold' temperatures. Sympathetic cooling works by mixing a cloud of higher-temperature molecules with a cloud of cold atoms. Collisions between the two species result in thermalisation of the two species which lowers the temperature of the molecules; if there is a large enough cloud of atoms, or if the atoms can be continuously cooled, then the temperature of the molecules can be lowered to the temperature of the atoms. This technique relies upon there being a favourable ratio of elastic (thermalising) collisions to inelastic collisions, which lead to loss from the trap. Molecules can only be trapped if their translational energy is lower than the depth of the trap. Buffer-gas cooling is a technique pioneered by the Doyle group [33, 36, 37] which typically uses a cold buffer gas of liquid helium to cool molecules down to a few Kelvin. The technique does not depend on any particular molecular properties and so can be applied to a wide range of molecules, and has been demonstrated successfully on molecules such as CaH, CrH, MnH, ND and NH [38]. Another technique in this category is the sympathetic cooling of molecular ions: molecules are sympathetically cooled via coulomb interactions with laser-cooled atomic ions when both species are simultaneously trapped in an ion trap [39]. This technique can produce molecular ions below 100 mK [40].

Laser cooling requires a complex set-up of lasers, that are utilised in the same manner as for atomic cooling, to cool molecules with relatively simple energy levels, such as metal hydrides. The first cooling of molecules using lasers was reported by Djeu *et al.*, [41] in 1981, and remained the only successful experiment for over a decade. They used spontaneous anti-Stokes scattering and managed to drop the temperature of CO_2 molecules by 1 K [41]. In 1996, Bahns *et al.* published a method for the laser cooling of molecules based on sequential steps, first lowering the rotational energy, then the translational energy, and finally the vibrational energy to produce cold molecules in the ground state [42]. The first experimental success of laser-cooled cold molecules came in 2010, when SrF was successfully cooled to ≈ 1 K [32]. Recently, Zhelyazkova *et al.* have demonstrated cooling of CaF down to temperatures around 300 mK [43] and Hummon *et al.* have demonstrated the cooling and trapping of YO in a 2-d MOT [44]. In 2014 Barry *et al.* produced a 3-d MOT of SrF via laser cooling at a temperature of 2.5 mK which is the lowest temperature that has currently been achieved via direct cooling methods [45]. However the laser cooling of molecules, will always be restricted to simple molecular structures, with large Franck-Condon overlap between the required molecular sub-levels and a small overlap between all others.

A method of slowing molecules, in order to trap them, is via Stark deceleration. In an inhomogenous electric field the Stark effect splits the energy levels of the molecule into high-field seeking and low-field seeking states. Low-field seeking states will experience a decrease in energy as they moves towards a high-field region of space. In a Stark decelerator first the correct state of the molecule has to be selected, then the molecules travel down the decelerator which generates time-dependent inhomogeneous fields at a series of stages so that the molecule always experience an increasing potential. Using pulsed fields, molecules can be grouped into bunches and at the end of the decelerator molecules can be caught using a quadrupole trap. The first experimental demonstration of Stark deceleration was performed on a beam of metastable CO molecules [46] in 1999. Since then it has been used to cool a variety of molecules including OH radicals [47], ND_3 which was cooled to 250 μK [48, 49] and YbF [50]. Zeeman deceleration techniques, using magnetic fields, have also been successfully demonstrated [51–53], as well as Rydberg decelerators [54, 55] and optical Stark decelerators [56].

Indirect Cooling

Indirect methods combine two ultracold atoms to form an ultracold molecule. This approach is limited by the fact that only atoms which can be laser cooled can be used to form molecules. Additionally, both photoassociation and magnetoassociation require substantial spectroscopic knowledge of the specific molecular sub-levels involved, which means the techniques cannot be generally applied. The benefit of the techniques is that the molecules formed are at the same translational temperature as the constituent atoms and are therefore ultracold.

Photoassociation uses a laser pulse to excite two cold atoms into an excited bound state. The association occurs as two colliding atoms absorb a photon which excites them to a bound level, $X + Y + h\nu_1 \rightarrow XY^*$. The technique was first proposed by Thorsheim *et al.* in 1987 [57]. The excited-state molecule is very unstable and can rapidly decay back into the constituent atoms. To prevent this either spontaneous emission or a second laser pulse can be used to transfer the molecules into the ground state (or lower triplet state). The probability of this transition is governed by the Franck-Condon factors between the two levels, $|\langle\Psi_{v'}^{\mathrm{exc}}|\Psi_{v''}^{\mathrm{ground}}\rangle|^2$. Photoassociation has been used successfully to produce ultracold homonuclear alkali-metal dimers in their vibrational ground state such as K_2 [58] and Cs_2 [59]; it has also been used to produce ultracold heteronuclear alkali-metal dimers such as LiCs [60], KRb [61] and RbCs [62].

Currently the most successful method of ultracold molecule formation is magnetoassociation of ultracold atoms to create Feshbach molecules, followed by stimulated Raman adiabatic passage (STIRAP) to transfer the Feshbach molecules into their rovibrational ground state. A Feshbach resonance occurs when the energy of the two separated atoms is degenerate with the energy of a bound molecular state. The atoms can then be 'tuned' through the resonance into molecules [35]. This process is discussed in further detail in Section 2.4. The most common method used for associating Feshbach molecules is via a 'Feshbach ramp' where the magnetic field is tuned adiabatically across the width of the resonance [63–65]. Another method of forming Feshbach molecules uses an oscillating field to modulate the applied magnetic field which induces a stimulated transition of two colliding atoms into a bound molecular state [35]. The molecules can then be separated from the atomic cloud using Stern-Gerlach separation or optical methods; this should be performed quickly following molecule formation to reduce losses [35]. The ramp can also be reversed, and the molecules will dissociate into atoms; this process is typically used to detect Feshbach molecules.

Feshbach molecules formed by magnetoassociation are very weakly bound and have a short lifetime in the range of 100 ms. The Feshbach molecules can be transferred into a ground-state level using STIRAP. STIRAP is a two-photon transition process that transfers molecules from the short-lived Feshbach state $|F\rangle$ to a long-lived deeply bound state ($|G\rangle$) via an intermediate excited state ($|E\rangle$). Transitions between $|E\rangle$ and $|G\rangle$ are driven by the Stokes laser, with coupling strengths derived from the Rabi frequency Ω_{S}. Transitions between $|F\rangle$ and $|E\rangle$ are driven by the pump laser, with coupling strengths derived from the Rabi frequency Ω_{P}. The Stokes laser is applied first, coupling the unpopulated $|E\rangle$ and $|G\rangle$ states, then the pump laser is switched on. The molecules transfer through a dark superposition of states $|F\rangle$ and $|G\rangle$, $|D\rangle = \cos\theta\,|F\rangle - \sin\theta\,|G\rangle$, where $|D\rangle$ is an eigenstate of the dressed system on two-photon resonance [66]. The mixing angle θ is $\theta = \Omega_{\mathrm{P}}(t)/\Omega_{\mathrm{S}}(t)$. The excited state does not appear in the eigenstate $|D\rangle$ and so by varying the values of $\Omega_\mathrm{P}(t)$ and $\Omega_\mathrm{S}(t)$ the molecules can be transferred adiabatically from $|F\rangle$ to $|G\rangle$. Bypassing $|E\rangle$ means that losses from the excited state do not have to be considered and the transfer efficiency can theoretically be 100% [35].

Magnetoassociation followed by STIRAP has the advantage of being able to produce large numbers of molecules at ultracold temperatures. The first ultracold absolute ground-state polar molecules produced by this method were KRb [67]. Homonuclear Cs_2 [68] and triplet Rb_2 [69] have also been produced in the ground state using these methods. Recently ultracold ground-state molecules of ^{87}RbCs have been produced at both Innsbruck [70] and Durham [71]. This Thesis presents detailed calculations on the scattering lengths and bound states of various alkali-metal systems and an outlook to using these systems for ultracold molecule formation. We also use different basis sets to describe the quantum numbers of the bound states and assess the energy-dependence of the scattering length around Feshbach resonances. Finally, we briefly describe the effects of additional external fields on alkali-alkali collisions.

1.2 Outline of Thesis

This Thesis is organised as follows:

- Chapter 2 gives a brief summary of scattering theory and introduces notation that will be used throughout the Thesis. A description of how the programs MOLSCAT, BOUND and FIELD work is also given.

- Chapter 3 introduces the Hamiltonian for collisions of alkali-metal atoms under the influence of an external magnetic field and the basis sets, and corresponding matrix elements, used in the calculations presented in this Thesis.

- In Chapter 4 scattering and bound-state calculations on ^{85}Rb, ^{87}Rb and ^{133}Cs are presented. The work on ^{85}Rb is published in Ref. [72]. This work involved a close collaboration between experiment and theory; where relevant, the experimental results are discussed alongside the theoretical calculations. The experimental results were all measured by Simon Cornish's group at Durham University. This Chapter also uses the results to develop a proposal to use solitons of ^{85}Rb to generate mesoscopic Bell states; this proposal is the work of Gertjerenken *et al.* [73] and Billam *et al.* [74], my contribution was to identify areas with the requisite scattering properties.

- In Chapter 5 scattering and bound-state calculations of the isotopologues of RbCs and KCs are presented. The work on ^{85}RbCs was published in Ref. [75]. This work involved a close collaboration between experiment and theory; where relevant, the experimental results are discussed alongside the theoretical calculations. The experimental results were all measured by Simon Cornish's group at Durham University. The work on ^{87}RbCs was published in Refs. [71,76]; this work was performed in close collaboration with Dr. Ruth Le Sueur, who produced the scattering length, resonance position and widths, and quantum number assignments. The work on KCs was published in Ref. [77]; this work was performed in collaboration with Hannah Patel.

- In Chapter 6 the matrix elements of a molecular basis $|SIFM_F\rangle\,|LM_L\rangle$ are derived. An analysis of the singlet and triplet character of the bound states of ^{85}RbCs is given. A derivation of the transformation of the product states of the field-dressed Hamiltonian to the $|SM_S m_{i,a} m_{i,b}\rangle$ basis set is also derived and the field-dressed states of ^{85}RbCs are analysed.

- In Chapter 7 we use accurate coupled-channel calculations on ^{6}Li, ^{39}K and ^{133}Cs to explore the behaviour of the effective range in the vicinity of both broad and narrow Feshbach resonances. We present an alternative parametrization of the effective range that is accurate through both the pole and the zero-crossing and demonstrate that an analytical form of an energy- and magnetic-field-dependent phase shift, based on multichannel quantum defect theory, gives accurate results for the energy-dependent scattering length. This work was published in Ref. [78].

- In Chapter 8 the Hamiltonian for collisions of alkali-metal atoms under the influence of an external magnetic field and external rf-fields is introduced. The implementation of rf-fields in MOLSCAT and the results obtained for rf-dressing of the aa channel of ^{85}RbCs are presented.

- Chapter 9 gives a summary of the conclusions drawn in each of the previous chapters, and an outlook into the future directions for work of this nature is given.

1.3 List of Publications

- Hung-Wen Cho, Daniel J. McCarron, Michael P. Köppinger, Daniel L. Jenkin, Kirsteen L. Butler, Paul S. Julienne, Caroline L. Blackley, C. Ruth Le Sueur, Jeremy M. Hutson, and Simon L. Cornish,
  Feshbach spectroscopy of an ultracold mixture of ^{85}Rb and ^{133}Cs.
  Phys. Rev. A **87**, 010703(R) (2013)

- Caroline L. Blackley, C. Ruth Le Sueur, and Jeremy M. Hutson, Daniel J. McCarron, Michael P. Köppinger, Hung-Wen Cho, Daniel L. Jenkin, and Simon L. Cornish,
  Feshbach resonances in ultracold ^{85}Rb.
  Phys. Rev. A **87**, 033611 (2013)

- Bettina Gertjerenken, Thomas P. Billam, Caroline L. Blackley, C. Ruth Le Sueur, Lev Khaykovich, Simon L. Cornish, and Christoph Weiss,
  Generating Mesoscopic Bell States via Collisions of Distinguishable Quantum Bright Solitons.
  Phys. Rev. Lett. **111**, 100406 (2013)

- Michael P. Köppinger, Daniel J. McCarron, Daniel L. Jenkin, Peter K. Molony, Hung-Wen Cho, Simon L. Cornish, C. Ruth Le Sueur, Caroline L. Blackley and Jeremy M. Hutson,
  Production of optically trapped ^{87}RbCs Feshbach molecules.
  Phys. Rev. A **89**, 033604 (2014)

- Caroline L. Blackley, Paul S. Julienne and Jeremy M. Hutson,
  Effective-range approximations for resonant scattering of cold atoms.
  Phys. Rev. A **89**, 042701 (2014)

- Thomas P. Billam, Caroline L. Blackley, Bettina Gertjerenken, Simon L. Cornish and Christoph Weiss,
  Entangling two distinguishable quantum bright solitons via collisions.
  J. Phys.: Conf. Ser. **497**, 012033 (2014)

- Hannah J. Patel, Caroline L. Blackley, Simon L. Cornish, and Jeremy M. Hutson,
  Feshbach resonances, molecular bound states, and prospects of ultracold-molecule formation in mixtures of ultracold K and Cs.
  Phys. Rev. A **90**, 032716 (2014)

- Peter K. Molony, Philip D. Gregory, Zhonghua Ji, Bo Lu, Michael P. Köppinger, C. Ruth Le Sueur, Caroline L. Blackley, Jeremy M. Hutson, and Simon L. Cornish, **Creation of Ultracold ^{87}Rb^{133}Cs Molecules in the Rovibrational Ground State**.
  Phys. Rev. Lett. **113**, 255301 (2014)

Chapter 2

Scattering Theory

In the following Chapter a brief introduction to scattering theory is presented, along with the notation that will be used in the rest of this Thesis. A more detailed treatment of scattering theory can be found in Ref. [79–81]. Low-energy scattering and resonant behaviour are specifically addressed with a description of the meaning and behaviour of the s-wave scattering length, and a description of scattering and bound-state behaviour around zero-energy Feshbach resonances. A brief summary of coupled-channel methods and a discussion of the workings of the programs MOLSCAT, BOUND and FIELD is also presented. A more complete description of the capabilities and workings of these programs can be found in Ref. [82]

2.1 Wavefunction Scattering

The collisional behaviour of two particles is described by the time-dependent Schrödinger Equation,

$$i\hbar\frac{\partial}{\partial t}\Psi(\vec{r},t) = \left[\frac{-\hbar^2}{2\mu}\nabla^2 + V(\vec{r},t)\right]\Psi(\vec{r},t). \tag{2.1.1}$$

where μ is the reduced mass of the system. If the potential is time independent, $V(\vec{r},t) = V(\vec{r})$, then the time-dependent wavefunction can be written as $\Psi(\vec{r},t) = \psi(\vec{r})\exp(-iEt/\hbar)$, where $\psi(\vec{r})$ is a solution of time-independent Schrödinger equation.

The initial wavefunction of the stationary system, in the absence of interactions, is typically described by a plane wave $\psi_0 = e^{i\vec{k}_i\cdot r}$ with energy $E = \hbar^2k^2/2\mu$. When the plane wave scatters around a particle, it can be represented as an interference by outgoing spherical waves, see Figure 2.1. If the interaction potential decreases faster than $1/r$ at

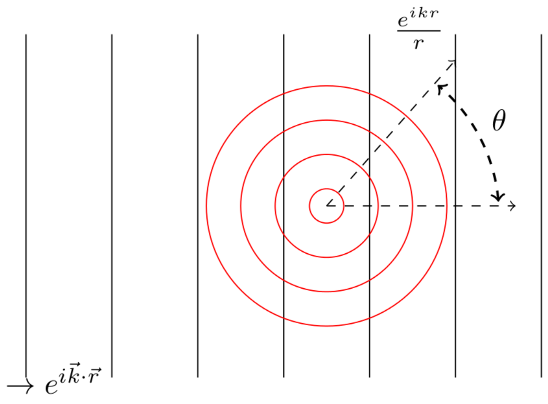

Figure 2.1: The incoming plane wave (black) describes the incident particles and the spherical wave (red) describes the scattered particles. The azimuthal angle, ϕ, is not shown.

long range then the scattering wavefunction behaves asymptotically as,

$$\psi^{+}_{\vec{k}_0}(\vec{r}) \overset{r\to\infty}{\sim} A\left[e^{i\vec{k}\cdot\vec{r}} + f(\theta,\phi)\frac{e^{ikr}}{r}\right], \tag{2.1.2}$$

where $e^{i\vec{k}\cdot\vec{r}}$ is the incoming plane wave, $f(\theta,\phi)$ is the scattering amplitude and e^{ikr}/r is the spherical wave. The scattering amplitude $|f(\theta,\phi)|$ describes the angular distribution of the scattering and is related to the particle flux density. The integral cross-section of the collision is given in terms of the scattering amplitude as,

$$\sigma^{\text{tot}} = \int_0^{\pi}\int_0^{2\pi} |f(\theta,\phi)| \sin\theta d\theta d\phi. \tag{2.1.3}$$

The incident plane wave can be expanded in terms of the Legendre polynomials to give,

$$e^{i\vec{k}\cdot\vec{r}} = \sum_{L=0}^{\infty}(2L+1)i^L P_L(\cos\theta) j_L(kr), \tag{2.1.4}$$

where $j_L(kr)$ are the spherical Bessel functions, shown in Fig. 2.2. The angular momentum is quantised in terms of L, but relates to the classical angular momentum, $\vec{L} = b\vec{p}$, where b is the impact parameter and $\vec{p}$ is the particle momentum.

2.1.1 The partial-wave expansion

The time-independent Hamiltonian in spherical polar coordinates is,

$$\hat{H} = -\frac{\hbar^2}{2\mu}\left[\frac{1}{r^2}\frac{\partial}{\partial r}\left(r^2\frac{\partial}{\partial r}\right) + \frac{1}{r^2\sin(\theta)}\frac{\partial}{\partial\theta}\left(\sin(\theta)\frac{\partial}{\partial\theta}\right) + \frac{1}{r^2\sin^2(\theta)}\frac{\partial^2}{\partial\phi^2}\right] + V(\vec{r}), \tag{2.1.5}$$

which can be simplified using the orbital angular momentum operator $\hat{L} = r \times \hat{p}$, with $\hat{p} = -i\hbar\nabla$.

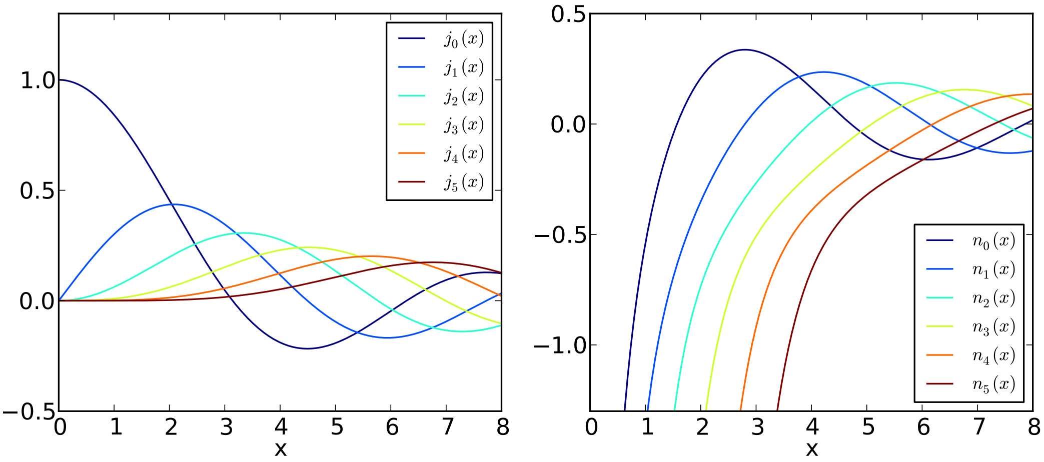

Figure 2.2: Spherical Bessel functions of the first kind (left) and second kind (right) for $L = 0, 1 \ldots 5$.

The orbital-angular-momentum operators in polar coordinates are,

$$\hat{L}_x = -i\hbar\left(y\frac{\partial}{\partial z} - z\frac{\partial}{\partial y}\right) = i\hbar\left(\sin\phi\frac{\partial}{\partial\theta} + \cot\theta\cos\phi\frac{\partial}{\partial\phi}\right), \tag{2.1.6a}$$

$$\hat{L}_y = -i\hbar\left(z\frac{\partial}{\partial x} - x\frac{\partial}{\partial z}\right) = i\hbar\left(-\cos\phi\frac{\partial}{\partial\theta} + \cot\theta\sin\phi\frac{\partial}{\partial\phi}\right), \tag{2.1.6b}$$

and

$$\hat{L}_z = -i\hbar\left(x\frac{\partial}{\partial y} - y\frac{\partial}{\partial x}\right) = i\hbar\frac{\partial}{\partial\phi}, \tag{2.1.6c}$$

with

$$\hat{L}^2 = \hat{L}_x^2 + \hat{L}_y^2 + \hat{L}_z^2 = -\hbar^2\left(\frac{1}{\sin\theta}\frac{\partial}{\partial\theta}\left(\sin\theta\frac{\partial}{\partial\theta}\right) + \frac{1}{\sin^2\theta}\frac{\partial^2}{\partial\phi^2}\right). \tag{2.1.6d}$$

Substituting Eq. (2.1.6d) into Eq. (2.1.5) the Hamiltonian can be re-written as

$$\hat{H} = -\frac{\hbar^2}{2\mu}\left[\frac{1}{r^2}\frac{\partial}{\partial r}\left(r^2\frac{\partial}{\partial r}\right) - \frac{\hat{L}^2}{\hbar^2 r^2}\right] + V(\vec{r}). \tag{2.1.7}$$

Using the partial-wave expansion of the scattering wavefunction,

$$\Psi(\vec{r}) = r^{-1}\sum_{L=0}^{\infty}\Psi_L(r)P_L(\cos\theta), \tag{2.1.8}$$

allows for the separation of a radially dependent Schrödinger Equation

$$\left[\frac{-\hbar^2}{2\mu}\frac{d^2}{dr^2} + \frac{\hbar^2 L(L+1)}{2\mu r^2} + V(r)\right]\psi_L(r) = E\psi_L(r), \tag{2.1.9}$$

which can be solved, subject to appropriate boundary conditions.

Typical boundary conditions are based on a potential which is non-zero at short range and which tends to zero at long range. This gives short-range boundary conditions $\Psi_L \to 0$ as $r \to 0$ and long-range boundary conditions,

$$\Psi_L(k,r) \overset{r\to\infty}{\sim} A_l(k) \left[j_L(kr) - \tan \delta_L n_L(kr) \right], \tag{2.1.10}$$

where j_L and n_L are spherical Bessel functions of the first and second kind (shown in Fig. 2.2), $A_l(k)$ is an energy-dependent normalisation factor, and δ_L is the phase shift. Using the properties of the spherical Bessel functions as $r \to \infty$ [83] Eq. (2.1.10) can be re-written as,

$$\Psi_L(k,r) \overset{r\to\infty}{\sim} \sin(kr - \frac{L\pi}{2} + \delta_L), \tag{2.1.11}$$

where the phase shift δ_L can be interpreted as the shift in the scattered wavefunction compared to the free-particle solution, caused by the interaction potential.

By similarly expanding the scattering wavefunction, and substituting in the expansion of the plane wave, we find an expression for the scattering amplitude as a sum of the Legendre polynomials,

$$f(\theta, \phi) = \frac{1}{2ik} \sum_{L=0}^{\infty} (2L+1)(e^{2i\delta_L} - 1) P_L(\cos\theta). \tag{2.1.12}$$

The differential cross-section is $d\sigma/d\Theta = |f(\theta,\phi)|^2$, and the integral cross-section σ_{tot} is given by,

$$\sigma_{\text{tot}} = \int_0^{\pi} d\theta \sin(\theta) \int_0^{2\pi} d\phi |f(\theta,\phi)|^2 = \frac{4\pi}{k^2} \sum_L (2L+1) \sin^2(\delta_L). \tag{2.1.13}$$

2.1.2 Scattering S-matrix

The boundary conditions of Eq. (2.1.11) can also be defined in terms of incoming and outgoing waves. Following Mott and Massey [79] the functions $f_l(\pm k, r)$ are defined as

$$f_l(\pm k, r) \sim \exp\left(\mp ikr + 1/2 il\pi\right). \tag{2.1.14}$$

Re-writing Eq. (2.1.11) using these functions gives

$$\Psi_L(r) \overset{r\to\infty}{\sim} \frac{1}{2} i \left(f_l(k,r) + (-1)^{l+1} S_l(k) f_l(-k,r) \right). \tag{2.1.15}$$

The scattering matrix, S-matrix, acts as an operator which transforms the coefficients of the incoming wave to the outgoing wave. In terms of the scattering phase shift, the S-matrix has elements

$$S_l(k) = \exp 2i\delta_l. \tag{2.1.16}$$

For collisions in which the number of particles is conserved then the S-matrix is unitary. If there is a single open channel then the S-matrix is single valued; if there is more than one open channel the S-matrix is an $N \times N$ matrix, where N is the number of open channels and the diagonal element corresponding to the incoming channel is denoted S_{00}.

2.2 Low-energy scattering

In the low-energy regime the centrifugal barrier limits the contribution of partial waves with $L > 0$ and s-wave scattering dominates. For elastic scattering the s-wave phase shift at low energy is given by the Wigner threshold laws [84] as,

$$\tan \delta_0(k) \sim k \tag{2.2.1}$$

where k is the wavenumber of the incoming channel. The s-wave scattering length is defined as [85],

$$a_0(k) = \frac{-\tan \delta_0}{k} = \frac{1}{ik}\frac{1 - S_{00}}{1 + S_{00}}, \tag{2.2.2}$$

which can be real or complex. In the s-wave scattering regime the elastic cross-section is [85],

$$\sigma_{\mathrm{el}}(k) = \frac{\pi}{k^2}|1 - S_{00}|^2 = \frac{4\pi|a_0(k)|^2}{1 + |a_0(k)|^2k^2 + 2k\beta(k)}, \tag{2.2.3}$$

and the total inelastic cross-section is,

$$\sigma_{\mathrm{inel}}(k) = \frac{\pi}{k^2}\left(1 - |S_{00}|^2\right) = \frac{4\pi\beta}{k}\left(1 + |a_0(k)|^2k^2 + 2k\beta(k)\right), \tag{2.2.4}$$

with $a_0(k) = \alpha(k) - i\beta(k)$, where $\alpha(k)$ is the real part of the scattering length and $-i\beta(k)$ is the imaginary part of the scattering length.

At limitingly low energies, using the small argument limit, then $\delta_0(k) \approx -ka_0(k)$ and the dependence of a_0 on k becomes negligible. The long-range form of the wavefunction can be rewritten as $\sim \sin(k(r - a_0))/\sqrt{k}$. The sine function is zero when $r = a_0$ and the scattering length thus defines the point at which a linear extrapolation of the long-range tail of the wavefunction crosses the r-axis, as shown in Fig. 2.3. Physically, the asymptotic form of the wavefunction corresponds to the wavefunction caused by scattering of a hard-sphere potential with a radius equal to the scattering length.

The scattering length is correlated to the position of the highest-lying bound state supported by the potential. If no bound state is supported then the scattering length is negative. If there is a bound state exactly at threshold then $a = \infty$, as the state becomes

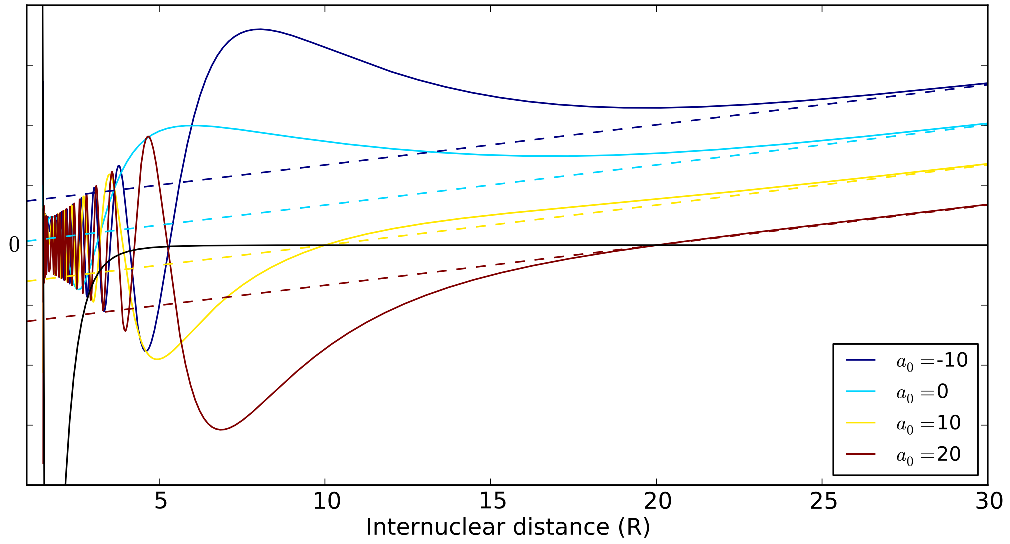

Figure 2.3: Diagram showing the asymptotic behaviour of a wavefunction at zero energy (solid, coloured). The black line (solid) shows a van der Waals potential that tends to zero as R tends to infinity. The dashed lines show the extrapolation of the scattering length for a variety of values.

more deeply bound the scattering length decreases, eventually passing through zero. As the state becomes even more deeply bound the scattering length becomes negative, tending towards $a = -\infty$.

When the long-range interactions of the system can be described by a van der Waals potential then various universal behaviours of the system can be defined based on the long-range C_6 coefficient. It is helpful to define a characteristic length and energy scale of the system, [35]

$$R_{\text{vdW}} = \frac{1}{2}\left(\frac{2\mu C_6}{\hbar^2}\right)^{1/4} \qquad \text{and} \qquad E_{\text{vdW}} = \frac{\hbar^2}{2\mu}\frac{1}{R_{\text{vdW}}^2}, \tag{2.2.5}$$

or alternatively the scales as defined by Gribakin and Flambaum [86]

$$\bar{a} = \frac{4\pi}{\Gamma(1/4)^2} R_{\text{vdW}} \qquad \text{and} \qquad \bar{E} = \frac{\hbar^2}{2\mu}\frac{1}{\bar{a}^2}, \tag{2.2.6}$$

where $\Gamma(x)$ is the gamma function and μ is the reduced mass of the system. When $R > R_{\text{vdW}}$ then the wavefunction approaches its asymptotic form [87].

The characteristic energy and length scales also give information about the bound states of the system. Gao [88] has calculated the energies of the bound states of all partial waves as a function of the scattering length which can be used to define a set of "energy bins" based on the value of E_{vdW}. For s-wave scattering there will be a bound state corresponding to $n = -1$ between $-39.5\ E_{\text{vdW}}$ and 0, a bound state corresponding to $n = -2$ between $-272\ E_{\text{vdW}}$ and $-39.5\ E_{\text{vdW}}$, and so on, where n is the vibrational quantum number counted down from the threshold energy. For near-threshold bound states, when $a \gg \bar{a}$, then the energy of the bound state, E_b is given by the scattering length [35] as,

$$E_b = \frac{\hbar^2}{2\mu a^2}. \tag{2.2.7}$$

Information of this nature can give important insight into the scattering behaviour of the system before full coupled-channel calculations are undertaken.

2.3 Scattering resonances

There are two different classifications of scattering resonances. Shape resonances are caused by a quasi-bound state supported by the incoming channel; Feshbach resonances are caused by a quasi-bound state from a different channel becoming degenerate with the incoming channel. Away from resonance the phase shift is a slowly varying function of the collision energy but near resonance it becomes quickly varying. Its behaviour can be split into two components,

$$\delta(E) = \delta_{\text{bg}}(E) + \delta_{\text{res}}(E), \tag{2.3.1}$$

where $\delta_{\text{bg}}(E)$ represents the slowly varying background term and $\delta_{\text{res}}(E)$ represents the resonance contribution. If the system has a single open channel then the resonance behaviour, of either kind of resonance, is characterised by a sharp variation of π in the phase shift δ_L. The phase shift, as a function of energy, follows the Breit-Wigner form,

$$\delta_L(E) = \delta_{\text{bg}} + \tan^{-1}\left(\frac{\Gamma_E}{2(E_{\text{res}} - E)}\right), \tag{2.3.2}$$

where E_{res} is the resonance position, and Γ_E is the resonance width in energy space. The equivalent formula for the phase shift as a function of magnetic field at constant energy is,

$$\delta_L(B) = \delta_{\text{bg}} + \tan^{-1}\left(\frac{\Gamma_B}{2(B_0 - B)}\right), \tag{2.3.3}$$

where B_0 is the resonance position and $\Gamma_B = \Gamma_E/\delta\mu$. $\delta\mu$ represents the rate at which the energy of the state causing the resonance, E_{res}, tunes with respect to the energy of the open-channel threshold, E_{thres}. The S-matrix element, $S = \exp 2i\delta$, for an elastic scattering resonance, describes a circle of radius one in the complex plane as a function of magnetic field or energy [89].

The variation of the scattering length around a resonance is described by [90]

$$a(B) = a_{\mathrm{bg}} \left(1 - \frac{\Delta}{B - B_0}\right), \tag{2.3.4}$$

where a_{bg} is the background scattering length which corresponds to the background phase shift and the width Δ is related to Γ_B by $\Gamma_B = -2a_{\mathrm{bg}}k\Delta_B$ [89].

2.3.1 Inelastic scattering

Inelastic collisions occur when multiple outgoing channels are present during the collision. The scattering S-matrix element of the incoming channel can be written in terms of a complex phase shift as,

$$S_{00} = \exp 2i\delta_0. \tag{2.3.5}$$

In the low-energy limit the complex phase shift translates into a complex scattering length [91]

$$a = \alpha - i\beta. \tag{2.3.6}$$

With several open channels present, the quantity that follows the Breit-Wigner form across threshold is not the phase shift of a particular channel but rather the S-matrix eigenphase sum. The S-matrix eigenphase sum is the sum of the phase shifts obtained from the eigenvalues of the S-matrix and is real, as the S-matrix is unitary. The variation of the individual elements of the S-matrix, $S_{jj'}$, across a resonance, in either energy or magnetic field, each describe a circle in the complex plane with radius ≤ 1. As a function of magnetic field at constant energy the individual S-matrix elements are [89],

$$S_{jj'}(B) = S_{\mathrm{bg},jj'} - \frac{\mathrm{i} g_{Bj} g_{Bj'}}{B - B_{\mathrm{res}} + i\Gamma_B/2}, \tag{2.3.7}$$

where $g_{Bj}^2 = \Gamma_{Bj} \exp 2j\phi_j$. The radius of the circle is $|g_{Bj}g_{Bj'}|/\Gamma_B$ and ϕ_j describes its direction in the complex plane. The total width Γ_B is given by the sum over all partial widths Γ_{Bj}. A reduced partial width, which is independent of energy, can be defined for the incoming channel as $\gamma_{B0} = \Gamma_{B0}/2k$.

The complex scattering length around a resonance can be described by,

$$a(B) = a_{\mathrm{bg}} + \frac{a_{\mathrm{res}}}{2(B - B_{\mathrm{res}})/\Gamma_B^{\mathrm{inel}} + \mathrm{i}}, \tag{2.3.8}$$

where a_{res} characterises the strength of the resonance and is defined as [89],

$$a_{\mathrm{res}} = \frac{2\gamma_{B0}}{\Gamma_B^{\mathrm{inel}}} \exp 2\mathrm{i}(\phi_0 + k\alpha_{\mathrm{bg}}). \tag{2.3.9}$$

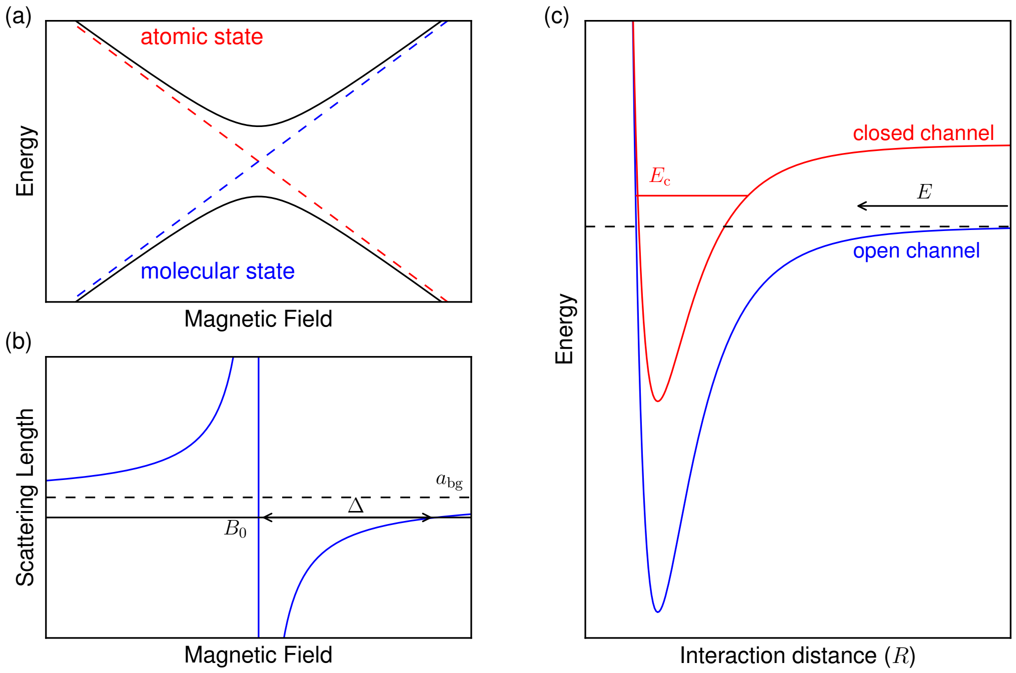

Figure 2.4: (a) an avoided crossing between the separated atoms and a molecular bound state; (b) scattering length around a resonance caused by a molecular bound state becoming degenerate with the scattering state; (c) potential energy curves denoting the relative energies of the incoming scattering channel and bound states in the closed channel when the energy of a bound state in the closed channel becomes degenerate with the energy of the scattering state then a Feshbach resonance occurs.

Across a resonance the real part of the scattering length displays an oscillation of magnitude $a_{\mathrm{res}}/2$ and the imaginary part of the scattering length shows a corresponding peak of height a_{res}. If the background scattering length a_{bg} is real then the lineshapes are symmetrical, however if a_{bg} has an imaginary component then the lineshapes can be assymetrical [92].

2.4 Zero-energy Feshbach resonances

Feshbach resonances occur when the energy of a bound state in a closed channel becomes degenerate with the energy of the scattering state in the incoming channel. Historically, Feshbach resonances were first predicted by both Fano and Feshbach, separately, around 1960 [93–95]. The first examples found experimentally were in high-energy systems where the resonance was caused by tuning the energy of the scattering state [96, 97]. The first prediction of zero-energy Feshbach resonances, where tuning of the magnetic field causes the energy of a molecular bound state to become degenerate with a low-energy scattering state, were by Stwalley [98] in 1976, and the first use for them was suggested by Tiesinga *et al.* [99] who showed that they could be used to tune the scattering length. The first experimental discoveries, of these type of resonances, were by Inouye *et al.* [100] in a BEC of ^{23}Na and by Courteille *et al.* [101] in a BEC of ^{85}Rb. In the following work whenever Feshbach resonances are referred to we are referring to zero-energy Feshbach resonances.

The incoming scattering state has some small energy E with respect to the zero-energy set by the energy of the individual atoms at infinite separation. The incoming channel is therefore an 'open channel', with an asymptotic energy less than E. Within the system there may also exist closed channels, with asymptotic energies greater than E, which support bound states whose energies lie close to the energy of the incoming scattering state. Fig. 2.4 (c) describes such a situation. The bound state with energy, E_c, is supported by a closed channel. The energy of this state depends on magnetic field and so it can be tuned with respect to the scattering state, as shown in Fig. 2.4 (a). Fig. 2.4 (b) shows the scattering length of the system, which varies strongly with the position of the bound state. When the molecular state is above the the scattering state then there is no bound state close to threshold and the scattering length is large and negative. The bound state and the scattering state will become degenerate at the magnetic field denoted by B_0, after this point there is a near-threshold bound state and the scattering length is large and positive.

Each resonance is caused by coupling between the scattering state and a bound state the strength of which can be represented by $V = \langle\phi_{\rm scat}|\hat{H}|\phi_{\rm bound}\rangle$ where $\hat{H}$ includes all the terms which can couple the two states. The strength of this coupling is important to characterise the resonance. If the resonance is open-channel dominated then the scattering and bound states have the spin character of the open channel over a large fraction of the resonance width Δ. If the resonance is closed-channel dominated then the scattering and bound states have the spin character of the closed channel over a large fraction of the resonance width Δ. Resonances that are open-channel dominated are also referred to as broad resonances and tend to have a large value of Δ, and be caused by s-wave bound states. Resonances can be defined as open-channel or closed-channel dominated based on the parameter $s_{\rm res}$ [35],

$$s_{\rm res} = \frac{a_{\rm bg}}{\bar{a}}\frac{\delta\mu\Delta}{\bar{E}}, \tag{2.4.1}$$

where a_{bg} is the “local” background scattering length, $\delta\mu$ is the difference between the magnetic moment of the bound state and the magnetic moment of the separated atoms, and Δ is the width of the resonance. An open (closed) channel resonance corresponds to $s_{\mathrm{res}} \gg 1$ ($s_{\mathrm{res}} \ll 1$).

One of the methods of magnetoassociation involves a linear magnetic field ramp across a Feshbach resonance [102]. The speed at which the magnetic field is ramped requires a balance between transferring the atoms slowly enough that the transfer is adiabatic and quickly enough that significant three-body losses are not sustained. The efficiency of the atom-molecule conversion has a Landau-Zener-like behaviour [34, 35]

$$\frac{P}{P_{\mathrm{max}}} = 1 - \exp\left(-\alpha n \frac{\hbar}{2\mu}\left|\frac{\Delta a_{\mathrm{bg}}}{\dot{B}}\right|\right), \tag{2.4.2}$$

where n is the atomic number density, α is a dimensionless prefactor given in Ref. [34], P_{max} is the maximum conversion efficiency determined by the PSD of the atomic cloud as this determines the number of atomic pairs available, and $\dot{B}$ is the ramp speed [34].

The location of Feshbach resonances can be determined experimentally by measuring atom loss from the trapped sample. The three-body loss rate scales as $\sim a^4$ leading to a drastically enhanced loss rate around the pole of a resonance where $|a|$ is large. If inelastic collisions exist then there is also a two-body loss rate, due to dipolar relaxations caused by the spin-spin coupling and second order spin-orbit interactions. This loss rate $K^{(2)}_{\mathrm{loss}}$ is proportional to the imaginary part of the scattering length β [91],

$$K^{(2)}_{\mathrm{loss}} = \frac{2\hbar}{\mu} g_n \beta, \tag{2.4.3}$$

where $g_n = 2$ for a thermal gas of identical bosons, and 1 otherwise.

2.5 Coupled-Channel methods

In a multi-channel scattering problem numerical methods are essential to solve the Hamiltonian of the interacting system. The total Hamiltonian for a general system of colliding particles in Jacobi coordinates is,

$$\hat{H} = -\frac{\hbar^2}{2\mu} R^{-1} \frac{d^2}{dR^2} R + \frac{\hat{L}^2}{2\mu R^2} + \hat{H}_{\mathrm{int}} + V(R,\theta) \tag{2.5.1}$$

where R is the radial separation coordinate, θ represents all other coordinates in the system, $V(R,\theta)$ is the interaction potential and $\hat{H}_{\mathrm{int}}$ represents the R-independent internal Hamiltonians of the particles. Using the coupled-channel approach the radial coordinate

R is handled by direct numerical propagation on a grid, and all other coordinates using a basis set [82]. The total wavefunction of the n^{th} state of the system is

$$\Psi_n(R,\theta) = R^{-1} \sum_j \Psi_j(\theta) F_{jn}(R), \tag{2.5.2}$$

where the functions $\Psi_j(\theta)$ form a complete orthonormal basis of the channels and the radial channel function $F_{jn}(R)$ describes the wavefunction for each channel j. The differential equation for each channel function $F_{in}(R)$ is

$$\frac{d^2 F_{in}(R)}{dR^2} = \sum_j \left[W_{ij}(R) - E\delta_{ij}\right] F_{jn}(R), \tag{2.5.3}$$

where E is the energy scaled by $2\mu/\hbar^2$ and $W_{ij}(R)$ are the elements of the coupling matrix given by

$$W_{ij}(R) = \frac{2\mu}{\hbar^2} \int \Psi_i^*(\theta) \left[H_{\text{int}} + V(R,\theta) + \frac{\hat{L}^2}{R^2} \right] \Psi_j(\theta) d\theta. \tag{2.5.4}$$

The coupled-channel Schrödinger equation can be expressed more simply in the matrix form,

$$\frac{d^2 \mathbf{F}}{dR^2} = \left[\mathbf{W}(R) - E\mathbf{I}\right] \mathbf{F}(R), \tag{2.5.5}$$

where, in a basis consisting of N channels, $\mathbf{W}$ is an $N \times N$ matrix with elements W_{ij} and $\mathbf{F}$ is an $N \times N$ matrix made up of column vectors $\mathbf{F}_n$ of order N, with elements F_{jn} each of which represents a linearly independent solution.

The wavefunction matrix $\mathbf{F}(R)$ can be propagated from short range to long range using appropriate boundary conditions for each channel. At short range, inside the classically forbidden region, all channels are closed and $\mathbf{F}(R) \to 0$ as $R \to 0$. At long range, when the effects of $V(R)$ are negligible, the solutions are given by

$$\mathbf{F}(R) \overset{r\to\infty}{\sim} \mathbf{J}(R) + \mathbf{N}(R)\mathbf{K}, \tag{2.5.6}$$

where $\mathbf{J}$ and $\mathbf{N}$ are diagonal matrices with open-channel elements made up of Ricatti-Bessel functions [83]

$$J_{ij}(R) = \delta_{ij} k_j^{-1/2} \hat{j}_{l_j}(k_j R), \tag{2.5.7}$$

$$N_{ij}(R) = \delta_{ij} k_j^{-1/2} \hat{n}_{l_j}(k_j R), \tag{2.5.8}$$

and closed-channel elements made up of modified spherical Bessel functions of the first and third kinds

$$J_{ij}(R) = \delta_{ij} k_{i,r}^{1/2} I_{l_j+1/2}(k_j R), \tag{2.5.9}$$

$$N_{ij}(R) = \delta_{ij} k_{i,r}^{1/2} K_{l_j+1/2}(k_j R). \tag{2.5.10}$$

The reaction matrix $\mathbf{K}$ is defined by the asymptotic behaviour of the wavefunction and contains elements connecting the closed and open channels,

$$\mathbf{K} = \begin{pmatrix} \mathbf{K}_{\text{oo}} & \mathbf{K}_{\text{oc}} \\ \mathbf{K}_{\text{co}} & \mathbf{K}_{\text{cc}} \end{pmatrix}. \tag{2.5.11}$$

The S-matrix can be expressed in terms of the open-channel part of the K-matrix, $\mathbf{K}_{\text{oo}}$, as

$$\mathbf{S} = (\mathbf{I} + i\mathbf{K}_{\text{oo}})^{-1} (\mathbf{I} - i\mathbf{K}_{\text{oo}}), \tag{2.5.12}$$

from which the scattering length can be determined using Eq. (2.2.2).

2.5.1 Propagators

Direct propagation of the wavefunction matrix $\mathbf{F}$ is numerically unstable, as any closed channel elements increase exponentially and destroy the linear independence of the solutions. In the following sections two methods which avoid this problem are detailed, the renormalised Numerov propagator and the method of log-derivative propagation.

2.5.1.1 Renormalised Numerov propagator

The renormalised Numerov propagator allows for the stable propagation of closed channels by propagating the ratio of Ψ_n/Ψ_{n+1} [103]. It is derived by taking a series expansion about the wavefunction, $\psi(x_n \pm h)$,

$$\psi_{n+1} = \psi(x_n + h) = \psi_n + h\psi'_n + \frac{h^2}{2}\psi''_n + \frac{h^3}{6}\psi'''_n + \frac{h^4}{24}\psi''''_n + \frac{h^5}{5!}\psi'''''_n + \mathcal{O}(h^6), \tag{2.5.13}$$

and

$$\psi_{n-1} = \psi(x_n - h) = \psi_n - h\psi'_n + \frac{h^2}{2}\psi''_n - \frac{h^3}{6}\psi'''_n + \frac{h^4}{24}\psi''''_n - \frac{h^5}{5!}\psi'''''_n + \mathcal{O}(h^6). \tag{2.5.14}$$

These two expansions can be combined to give

$$\frac{1}{2}[\psi_{n+1} + \psi_{n-1}] = \psi_n + \frac{h^2}{2}\psi''_n + \frac{h^4}{24}\psi''''_n + \mathcal{O}(h^6), \tag{2.5.15}$$

which can be differentiated twice to give

$$\frac{1}{2}[\psi''_{n+1} + \psi''_{n-1}] = \psi''_n + \frac{h^2}{2}\psi''''_n + \frac{h^4}{24}\psi''''''_n + \mathcal{O}(h^6). \tag{2.5.16}$$

Multiplying through Eq. (2.5.16) by $h^2/12$ and subtracting it from Eq. (2.5.15) gives

$$[\psi_{n+1} + \frac{h^2}{12}\psi''_{n+1}] + [\psi_{n-1} + \frac{h^2}{12}\psi''_{n-1}] = 2\psi_n + \frac{10h^2}{12}\psi''_n + \mathcal{O}(h^6). \tag{2.5.17}$$

Using our initial second-order differential equation we can substitute in $\psi'' = f(x)\psi(x)$ which gives the three-term recurrence relation

$$[1 - T_{n+1}]\psi_{n+1} + [1 - T_{n-1}]\psi_{n-1} = [2 + 10T_n]\psi_n + \mathcal{O}(h^6), \tag{2.5.18}$$

where T_n is $h^2/12f(x)$. To reduce the number of matrix multiplication steps required one substitutes in $C_n = [1 - T_n]\psi_n$ which makes Eq. (2.5.18)

$$C_{n+1} - U_n C_n + C_{n-1} = 0, \tag{2.5.19}$$

where $U_n = (1 - T_n)^{-1}(2 + 10T_n)$. The recurrence relation can be reduced from three to two terms by replacing $C_{n+1}/C_n = R_n$, and $C_n/C_{n-1} = R_{n-1}$. The propagation then becomes

$$R_n = U_n - R_{n-1}^{-1}. \tag{2.5.20}$$

The quantity R_n that is being propagated is stable in the energetically forbidden regions as it is the ratio of the wavefunction to the wavefunction at the next step [103]. The actual wavefunction can be recovered at any point in the propagation by keeping track of the ratios and the corresponding normalisations at each step.

2.5.1.2 Log-Derivative propagators

An alternative solution to propagating the wavefunction matrix is to propagate the log-derivative matrix which is numerically stable in the presence of closed channels. The log-derivative matrix is defined as,

$$\mathbf{Y}(R) = \mathbf{F}'(R)\mathbf{F}^{-1}(R). \tag{2.5.21}$$

Substituting the log-derivative matrix into the matrix form of the coupled Schrödinger, Eq. (2.5.5), results in the matrix Ricatti equation [104],

$$\mathbf{Y}'(R) = \mathbf{W}(R) - \mathbf{Y}(R)^2. \tag{2.5.22}$$

The log-derivative matrix cannot be propagated directly using standard numerical techniques as it is undefined wherever $\mathbf{F}(R) = 0$; it is instead propagated by invariant-imbedding techniques. The imbedding propagator $\mathcal{Y}$ is defined on the interval $[r_1, r_2]$ by [105]

$$\begin{bmatrix} \mathbf{F}'(r_1) \\ \mathbf{F}'(r_2) \end{bmatrix} = \begin{bmatrix} \mathcal{Y}_1(r_1, r_2) & \mathcal{Y}_2(r_1, r_2) \\ \mathcal{Y}_3(r_1, r_2) & \mathcal{Y}_4(r_1, r_2) \end{bmatrix} \begin{bmatrix} -\mathbf{F}(r_1) \\ \mathbf{F}(r_2) \end{bmatrix}. \tag{2.5.23}$$

Post-multiplying the first equation by $\mathbf{F}^{-1}(r_1)$ and the second equation by $\mathbf{F}^{-1}(r_2)$, then solving the first equation for $\mathbf{F}(r_1)\mathbf{F}^{-1}(r_2)$ and substituting it into the second equation, gives a recursion relation for the log-derivative matrix,

$$\mathbf{Y}(r_2) = \mathcal{Y}_4(r_1, r_2) - \mathcal{Y}_3(r_1, r_2) \times [\mathbf{Y}(r_1) + \mathcal{Y}_1(r_1, r_2)]^{-1} \mathcal{Y}_2(r_1, r_2). \tag{2.5.24}$$

At the end of the propagation the reaction matrix $\mathbf{K}$ is given by [104],

$$\mathbf{K} = -\left[\mathbf{Y}(R)\mathbf{N}(R) - \mathbf{N}'(R)\right]^{-1} \left[\mathbf{Y}(R)\mathbf{J}(R) - \mathbf{J}'(R)\right]. \tag{2.5.25}$$

Various methods of log-derivative propagation have been derived, which define the imbedding propagator in different ways. The original log-derivative propagator was published by Johnson [104]; its derivation was not published in the original paper but was re-derived by Mruguła and Secrest [106] and later by Manolopoulos [107]. Two improved versions of log-derivative propagation methods were published by Manolopolous [105, 108] and a further improvement which uses an Airy propagator at long range was published by Alexander and Manolopoulos [109]. The Airy propagator allows a varying step size to be used at long range which significantly decreases the computational time required for the calculation.

2.5.2 MOSLCAT, FIELD, BOUND

The MOLSCAT [110], BOUND [111] and FIELD [112] packages solve the set of coupled-channel equations for N channels by propagating the solutions over a grid in R, with appropriate bound state and scattering conditions applied at $R_{\rm min}$ and $R_{\rm max}$. Both programs have multiple propagators available, however all calculations in this Thesis were performed using the diabatic modified log-derivative method of Manolopoulos [105] and the hybrid modified log-derivative/Airy propagator of Alexander and Manolopoulos [109].

In MOLSCAT propagations were performed using the diabatic modified log-derivative method from a value of $R_{\rm min}$ to a value of $R_{\rm mid}$ using a fixed step size and then from $R_{\rm mid}$ to $R_{\rm max}$ using the Airy propagator. The log-derivative matrix can be propagated in any specified basis set, however the boundary conditions described in Sec. 2.5 are only appropriate for a basis set in which the asymptotic Hamiltonian is diagonal. At $R_{\rm max}$ the log-derivative matrix is transformed into the basis which satisfies this condition. The log-derivative is then matched to the long-range solutions, as described in Section 2.5.1.2, and the scattering length is extracted.

In BOUND the bound states of the potential are calculated with respect to energy and field. The log-derivative matrix is propagated outwards, denoted $\mathbf{Y}^+$, from a point R_{min}, which is chosen to be inside the inner-classically forbidden region, to a point R_{mid}. The log-derivative matrix is also propagated inwards, denoted $\mathbf{Y}^-$, from a point R_{max}, which is chosen to be in the outer-classically forbidden region, to a point R_{mid}. If E is an eigenvalue of the coupled equations then the condition

$$\left[\mathbf{Y}^+(R_{\mathrm{mid}}) - \mathbf{Y}^-(R_{\mathrm{mid}})\right]\mathbf{F}(R_{\mathrm{mid}}) = 0, \tag{2.5.26}$$

will be satisified [82]. A non-trivial solution to this equation only exists if the determinant $|\mathbf{Y}^+ - \mathbf{Y}^-| = 0$ at R_{mid}. From Eq. (2.5.26) it can be seen that when a non-trivial solution exists then $\mathbf{F}(R_{\mathrm{mid}})$ is an eigenvector of the log-derivative matching matrix $\mathbf{Y}_+ - \mathbf{Y}_-$ with an eigenvalue of zero. The version of BOUND used in this Thesis [111] locates bound states by converging on energies where the log-derivative matching matrix has an eigenvalue of zero. BOUND has been adapted to work in external fields [113, 114]; all bound states within a designated energy range are located for a specific magnetic field value. FIELD works in the same manner as BOUND but locates all states within a designated magnetic field range for a specific energy value. The program FIELD is particularly useful for locating all Feshbach resonances in a system regardless of width, as it can be used to find all bound states immediately below threshold, which correlate with the position of resonances in the scattering length.

Chapter 3

Alkali-Alkali Scattering

In this Chapter we introduce the general Hamiltonian for collisions of alkali-metal atoms under the influence of an external magnetic field, which is used for the calculations presented in the following Chapters. The basis sets, and corresponding matrix elements, used in the calculations presented in this Thesis are also described, and the relevant quantum numbers are defined.

3.1 Collision Hamiltonian in a static magnetic field

The collision Hamiltonian for a pair of alkali-metal atoms in an external magnetic field is,

$$\frac{\hbar^2}{2\mu}\biggl(-R^{-1}\frac{d^2}{dR^2}R+\frac{\hat{L}^2}{R^2}\biggr)+\hat{H}_1+\hat{H}_2+\hat{V}(R) \tag{3.1.1}$$

where R is the internuclear distance, μ is the reduced mass, $\hat{L}$ is the rotational angular momentum operator and $\hat{V}$ is the interaction operator. $\hat{H}_1$ and $\hat{H}_2$ are the monomer Hamiltonians of the free atoms in a magnetic field,

$$\hat{h_j}=\zeta_{\rm hfs}^{j}\hat{\imath}_j\cdot\hat{s}_{\rm j}+\Bigl(g_e\mu_{\rm B}\hat{s}_{jz}+g_{\rm n}\mu_{\rm B}\hat{\imath}_{jz}\Bigr)B_z, \tag{3.1.2}$$

where $\zeta_{\rm hfs}^{j}$ is the hyperfine coupling constant of atom j, $g_{\rm e}$ and $g_{\rm n}$ are the electron and nuclear g-factors, $\hat{s}$ and $\hat{\imath}$ are the electron and nuclear spin operators and B is the magnetic field. $\hat{s}_z$ and $\hat{\imath}_z$ are the projections of $\hat{s}$ and $\hat{\imath}$, respectively, along a space-fixed z-axis defined by the magnetic field B. The monomer Hamiltonian provides the energies of the separated atoms, in their respective hyperfine states, which is used as the threshold energy in collision calculations.

3.1.1 Monomer Hamiltonian

The Hamiltonian of a single atom in a magnetic field, Eq. (3.1.2), is known as the Breit-Rabi Hamiltonian. For an alkali-metal atom, which has an electron spin $s = 1/2$ and orbital angular momentum $l = 0$, the energy of the atom in a magnetic field is [115]

$$E_{|s=1/2 m_s, i m_i\rangle} = \frac{-\Delta E_{\rm hfs}}{2(2i+1)} + g_{\rm n}\mu_B m_f B \pm \frac{\Delta E_{hfs}}{2}\left(1 + \frac{4m_f x}{2I+1} + x^2\right)^{1/2}, \tag{3.1.3}$$

where $m_f = m_s + m_i$,

$$x = \frac{(g_{\rm e} - g_{\rm n})\mu_B B}{\Delta E_{\rm hfs}}, \tag{3.1.4}$$

and

$$\Delta E_{\rm hfs} = \zeta_{\rm hfs}(i + \frac{1}{2}). \tag{3.1.5}$$

The ± sign is taken to be the same as the sign of m_s. In the spin-stretched case when $m_f = |s + i|$, then Eq. (3.1.3) is written more simply as,

$$E_{|s m_s, i m_i\rangle} = \Delta E_{\rm hfs}\frac{i}{2(2i+1)} \pm (g_{\rm e} + 2g_{\rm n} i)\mu_B B. \tag{3.1.6}$$

The Breit-Rabi diagram for ^{85}Rb is shown in Fig. 3.1. In the low-field region, where the magnetic field splitting has a linear dependence, the hyperfine sub-levels are grouped by quantum number f, where f is the atomic total spin quantum number given by the coupling of s and i. However, in the high-field region they are grouped by the spin-projection quantum number m_s. The only conserved quantum number, for an alkali-metal atom in a magnetic field, is m_f, the projection of f along the magnetic-field axis.

3.1.2 Interaction Potentials

The interaction between the two atoms, $\hat{V}(R)$ in Eq. (3.1.1), is given by the sum of two terms [116],

$$\hat{V}(R) = \hat{V}^{\rm c}(R) + \hat{V}^{\rm d}(R), \tag{3.1.7}$$

where $\hat{V}^{\rm c}(R)$ is an isotropic potential operator that depends on the singlet and triplet electronic potential curves and $\hat{V}^{\rm c}(R)$ represents small spin-dependent couplings due to the magnetic dipole-dipole interaction and the second-order spin orbit interaction. The potential operator $\hat{V}^{\rm c}(R)$,

$$\hat{V}^{\rm c}(R) = V_0(R)\hat{\mathcal{P}}^{(0)} + V_1(R)\hat{\mathcal{P}}^{(1)}, \tag{3.1.8}$$

depends on the potential energy curves $V_0(r)$ and $V_1(R)$ for the respective $X^1\Sigma_g^+$ singlet and $a^3\Sigma_u^+$ triplet states of the diatomic molecule. The singlet and triplet projectors $\hat{\mathcal{P}}^{(0)}$

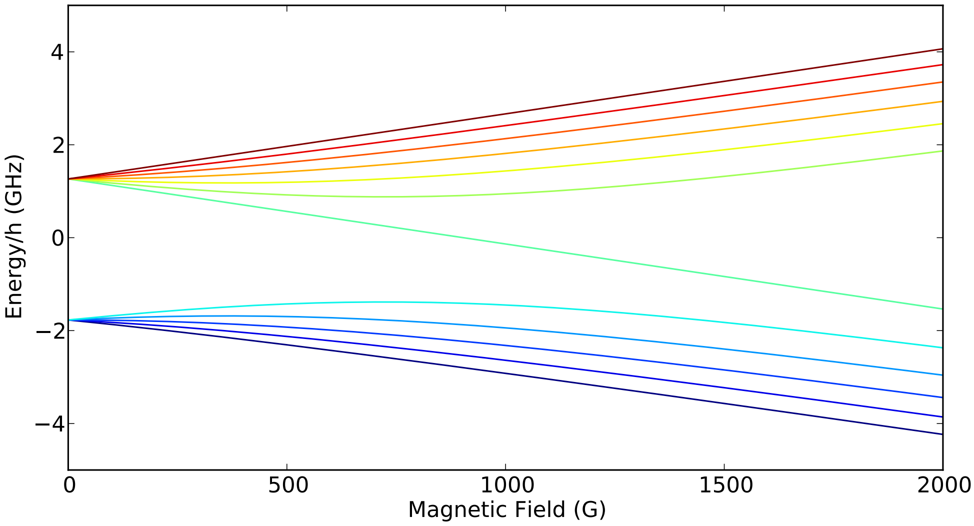

Figure 3.1: The hyperfine structure of ^{85}Rb in an external magnetic field. At zero field the states are grouped into two manifolds the upper one corresponding to $f = 3$ and the lower one corresponding to $f = 2$. The magnetic field lifts the degeneracy of these states and they split into m_f sublevels. In the upper manifold, $f = 3$, the states run, in order of increasing energy, from $m_f = -3 \dots 3$; in the lower manifold, $f = 2$, the states run from $m_f = 2 \cdots -2$.

and $\hat{\mathcal{P}}^{(1)}$ project onto the subspaces with total electron spin quantum numbers 0 and 1 respectively.

The potential energy curves used in this Thesis are defined in three different sections based on the internuclear separation R: short range, intermediate and long range. In the short-range region, at $R < R^{\mathrm{SR}}$ the potential is dominated by a repulsive wall, which is given by an inverse power in R,

$$V^{\mathrm{SR}}(R) = A + \frac{B}{R^N}, \tag{3.1.9}$$

where A, B and N are fitted parameters, which are chosen to match the short-range and mid-range parts of the potential at R^{SR}. The intermediate region, $R^{\mathrm{SR}} \leq R \geq R^{\mathrm{LR}}$, is represented by a finite power expansion of a non-linear function ξ,

$$V^{\mathrm{IR}}(R) = \sum_{i=0}^{n} a_i \xi^i(R), \tag{3.1.10}$$

where,

$$\xi(R) = \frac{R - R_{\mathrm{m}}}{R + bR_{\mathrm{m}}}, \tag{3.1.11}$$

where a_i, b and R_{m} are fitting parameters, and R_{m} is chosen to be close to the equilibrium value R_e. The long-range region, $R > R^\mathrm{LR}$ is represented by

$$V^\mathrm{LR} = -\frac{C_6}{R^6} - \frac{C_8}{R^8} - \frac{C_{10}}{R^{10}} \mp E_\mathrm{exch}, \tag{3.1.12}$$

where C_n are the dispersion coefficients and are the same for both the singlet and triplet potentials, and the exchange contribution is [117]

$$E_\mathrm{exch} = A_\mathrm{exch} R^\gamma \exp\left(-\beta R\right). \tag{3.1.13}$$

The exchange energy adjusts for the tendency of electrons of the same spin to avoid each other and is attractive for the singlet potential and repulsive for the triplet potential. β and γ are related via $\gamma = 7/(\beta - 1)$ and are obtained from the ionization energies of the individual atoms and A_exch is a fitting parameter. The potential energy curves used for RbCs [118] and KCs [119] are shown in Figures 3.2 and 3.3. The zero-energy of the potential curves correlates with the energy of two separated ${}^2S_{1/2}$ ground-state atoms and at long range the hyperfine splittings of the various isotopologues are shown.

The spin-dependent couplings of $\hat{V}^\mathrm{d}(R)$ both have the same tensor form such that $\hat{V}^\mathrm{d}(R)$ can be expressed as,

$$\hat{V}^\mathrm{d}(R) = \lambda(R)\left(\hat{s}_1 \cdot \hat{s}_2 - 3\left(\hat{s}_1 \cdot \vec{e}_R\right)(\hat{s}_2 \cdot \vec{e}_R)\right), \tag{3.1.14}$$

where $\vec{e}_R$ is a unit vector along the internuclear axis, and $\lambda(R)$ is an R-dependent coupling constant,

$$\lambda(R) = E_\mathrm{h}\alpha^2 \left(A \exp\left(-\beta R\right) + \frac{1}{R^3}\right), \tag{3.1.15}$$

where $\alpha \approx 1/137$ is the atomic fine-structure constant. The coupling at long range is dominated by the magnetic dipole-dipole term which has a $1/R^3$ dependence [90,116]. For lighter atoms such as lithium this is a sufficient description of the R-dependent coupling. For the heavier alkali-metals, such as rubidium and caesium, the second-order spin-orbit coupling, represented by an exponential, provides an important contribution in the short-range region of chemical bonding [120–123]. The parameters A and β in the spin-orbit coupling are obtained by fitting to electronic structure calculations.

3.2 Matrix elements of the Hamiltonian

Most of the calculations presented in this Thesis are performed using a fully decoupled basis set. The fully decoupled basis set is defined as

$$\left|s_a, m_{s,a}\right\rangle \left|i_a, m_{i,a}\right\rangle \left|s_b, m_{s,b}\right\rangle \left|i_b, m_{i,b}\right\rangle \left|L, m_L\right\rangle . \tag{3.2.1}$$

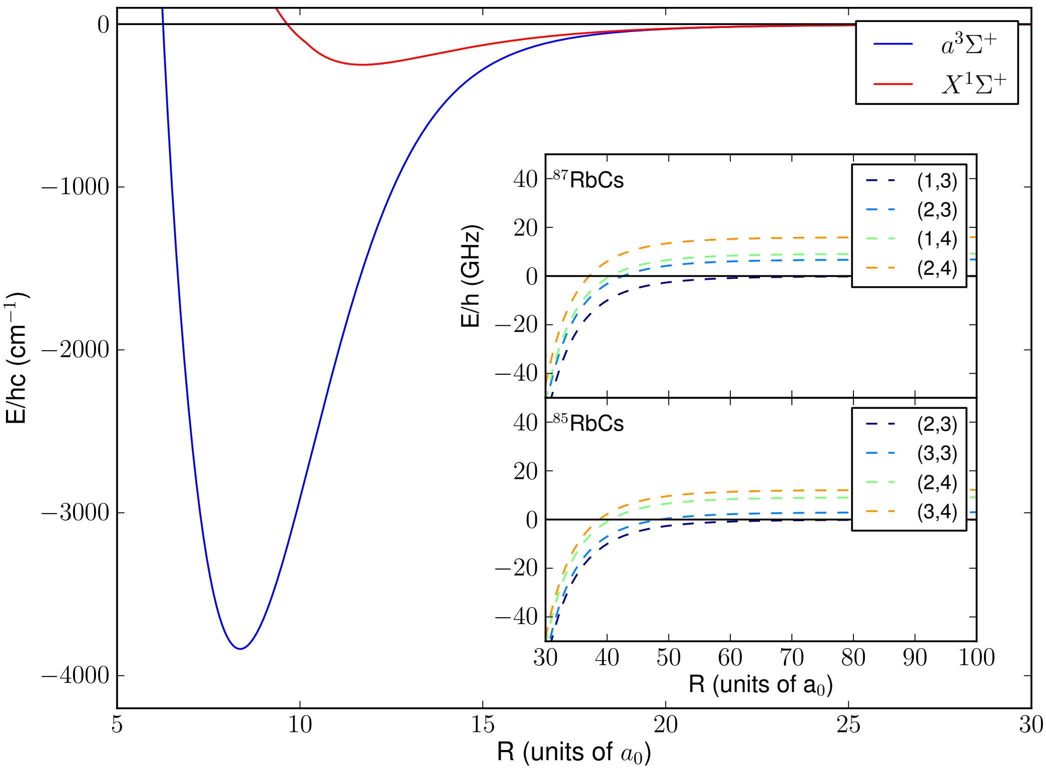

Figure 3.2: Main: Molecular potential energy curves $V_0(R)$ and $V_1(R)$ for the singlet and triplet states of RbCs, respectively [118]. Inset: An expanded view of the hyperfine splittings in the long-range part of the potentials for both isotopologues of RbCs; at this range the singlet and triplet potentials are effectively equal. Zero energy correlates to the energy of two separated $^2S_{1/2}$ ground-state atoms in the lowest hyperfine manifold.

The matrix elements of the Hamiltonian, Eq. (3.1.1), were first presented in Ref. [123]. Details of the rules of angular momentum coupling pertaining to the derivation of the matrix elements can be found in Appendix A; only the results are presented in this Section. The matrix elements of the $\hat{V}^{\mathrm{c}}(R)$ isotropic potential operator are

$$\begin{aligned}&\langle s_a m_{s,a} i_a m_{i,a} s_b m_{s,b} i_b m_{i,b} L M_L | \hat{V}^{\mathrm{c}}(R) | s_a m'_{s,a} i_a m'_{i,a} s_b m'_{s,b} i_b m'_{i,b} L' M'_L \rangle = \\ &\delta_{L,L'}\delta_{M_L,M'_L}\delta_{m_{i,a},m'_{i,a}}\delta_{m_{i,b},m'_{i,b}} \sum_S V_S(R)(-1)^{2s_a-2s_b+m_{s,a}+m_{s,b}+m'_{s,a}+m'_{s,b}} \\ &\times (2S+1)\begin{pmatrix} s_a & s_b & S \\ m_{s,a} & m_{s,b} & -m_{s,a}-m_{s,b}\end{pmatrix}\begin{pmatrix} s_a & s_b & S \\ m'_{s,a} & m'_{s,b} & -m'_{s,a}-m'_{s,b}\end{pmatrix}.\end{aligned} \tag{3.2.2}$$

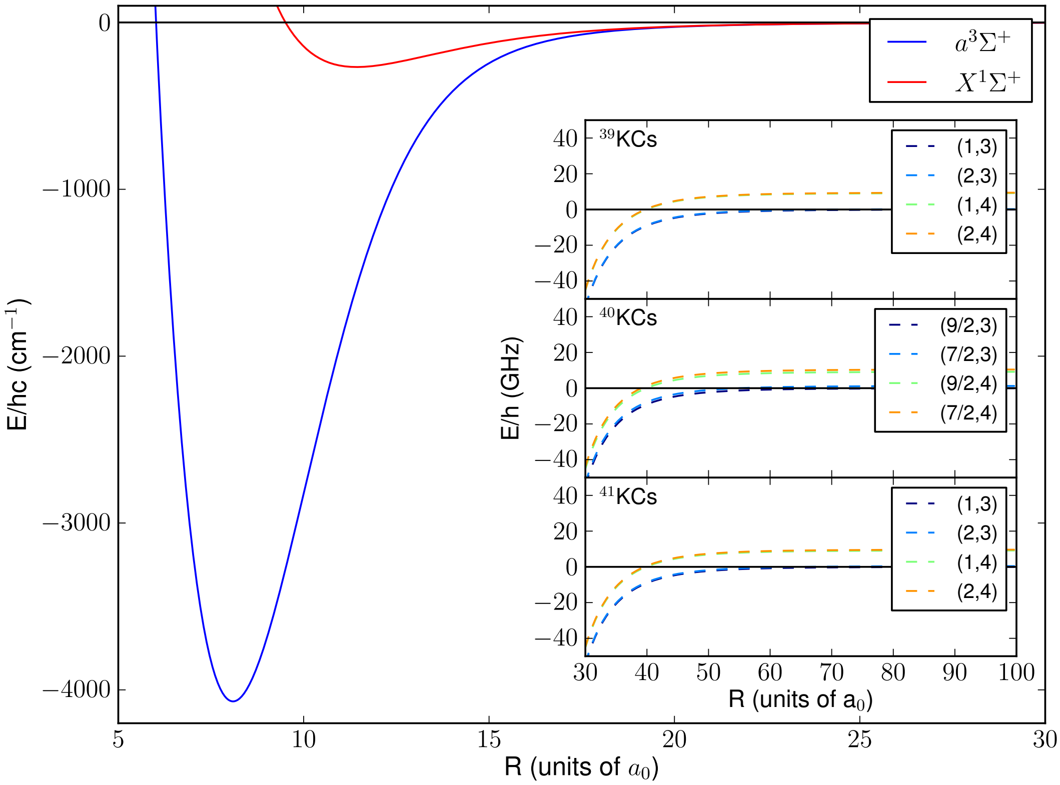

Figure 3.3: Main: Molecular potential energy curves $V_0(R)$ and $V_1(R)$ for the singlet and triplet states of KCs, respectively [119]. Inset: An expanded view of the hyperfine splittings in the long range part of the potentials for all three isotopologues of KCs; at this range the singlet and triplet potentials are effectively equal. Zero energy correlates to the energy of two separated $^2S_{1/2}$ ground-state atoms in the lowest hyperfine manifold.

The matrix elements of the $\hat{V}^{\mathrm{d}}(R)$ dipolar spin-spin operator are

$$\begin{aligned}
&\langle s_a m_{s,a} i_a m_{i,a} s_b m_{s,b} i_b m_{i,b} L M_L |\, \hat{V}^{\mathrm{d}}(R) \,| s_a m'_{s,a} i_a m'_{i,a} s_b m'_{s,b} i_b m'_{i,b} L' M'_L \rangle = \\
&\delta_{m_{i,a},m'_{i,a}} \delta_{m_{i,b},m'_{i,b}} (-\sqrt{30}) \lambda(R) (-1)^{s_a - s_b - m_{s,a} - m_{s,b} - M_L} \\
&\times \left[s_a(s_a+1)(2s_a+1) s_b(s_b+1)(2s_b+1)(2L+1)(2L'+1) \right]^{1/2} \begin{pmatrix} L & 2 & L' \\ 0 & 0 & 0 \end{pmatrix} \\
&\times \sum_{q_a,q_b} \begin{pmatrix} L & 2 & L' \\ -M_L & -q_a - q_b & M'_L \end{pmatrix} \begin{pmatrix} 1 & 1 & 2 \\ q_a & q_b & -q_a - q_b \end{pmatrix} \begin{pmatrix} s_a & 1 & s_a \\ -m_{s,a} & q_a & m'_{s,a} \end{pmatrix} \begin{pmatrix} s_b & 1 & s_b \\ -m_{s,b} & q_b & m'_{s,b} \end{pmatrix} .
\end{aligned} \tag{3.2.3}$$

The matrix elements of $\hat{L}^2$ are

$$\begin{aligned}
&\langle s_a m_{s,a} i_a m_{i,a} s_b m_{s,b} i_b m_{i,b} L M_L |\, \hat{L}^2 \,| s_a m'_{s,a} i_a m'_{i,a} s_b m'_{s,b} i_b m'_{i,b} L' M'_L \rangle = \\
&\delta_{L,L'} \delta_{M_L,M'_L} \delta_{m_{s,a},m'_{s,a}} \delta_{m_{i,a},m'_{i,a}} \delta_{m_{s,b},m'_{s,b}} \delta_{m_{i,b},m'_{i,b}} L(L+1).
\end{aligned} \tag{3.2.4}$$

The matrix elements of the hyperfine interaction in the monomer Hamiltonians, for atom a, are

$$\begin{aligned}&\langle s_a m_{s,a} i_a m_{i,a} s_b m_{s,b} i_b m_{i,b} L M_L |\, \zeta^{a}_{\text{hfs}} \hat{i}_a \cdot \hat{s}_a \,| s_a m'_{s,a} i_a m'_{i,a} s_b m'_{s,b} i_b m'_{i,b} L' M'_L \rangle = \\ &\delta_{L,L'} \delta_{M_L,M'_L} \delta_{m_{s,b},m'_{s,b}} \delta_{m_{i,b},m'_{i,b}} \zeta^{j}_{\text{hfs}} \langle s_a m_{s,a} i_a m_{i,a} |\, \hat{i}_a \cdot \hat{s}_a \,| s_a m'_{s,a} i_a m'_{i,a} \rangle \,,\end{aligned} \tag{3.2.5}$$

where

$$\begin{aligned}&\langle s_a m_{s,a} i_a m_{i,a} |\, \hat{i}_a \cdot \hat{s}_a \,| s_a m_{s,a} i_a m_{i,a} \rangle = m_{i,a} m_{s,a}; \\ &\langle s_a m_{s,a} i_a m_{i,a} |\, \hat{i}_a \cdot \hat{s}_a \,| s_a m_{s,a} \pm 1 i_a m_{i,a} \pm 1 \rangle = \\ &\qquad [s_a(s_a+1) - m_{s,a}(m_{s,a} \pm 1)]^{1/2} \, [i_a(i_a+1) - m_{i,a}(m_{i,a} \pm 1)]^{1/2} \,.\end{aligned}$$

The matrix elements of the Zeeman operator, for atom a, are

$$\begin{aligned}&\langle s_a m_{s,a} i_a m_{i,a} s_b m_{s,b} i_b m_{i,b} L M_L |\, g_{\text{e}} \mu_{\text{B}} B \hat{s}_{z,a} + g_{\text{n}} \mu_{\text{B}} B \hat{i}_{z,a} \,| s_a m'_{s,a} i_a m'_{i,a} s_b m'_{s,b} i_b m'_{i,b} L' M'_L \rangle = \\ &\delta_{L,L'} \delta_{M_L,M'_L} \delta_{m_{s,a},m'_{s,a}} \delta_{m_{i,a},m'_{i,a}} \delta_{m_{s,b},m'_{s,b}} \delta_{m_{i,b},m'_{i,b}} (g_{\text{e}} \mu_{\text{B}} B m_{s,a} + g_{\text{n}} \mu_{\text{B}} B m_{i,a}).\end{aligned} \tag{3.2.6}$$

The matrix elements of the monomer Hamiltonian, for atom b, are given by swapping the indices a and b in both the Zeeman and Hyperfine terms.

In the case of homonuclear scattering the basis functions are symmetrised for the exchange of two identical particles. The symmetrised basis functions are

$$\frac{|s m_{s,a} i m_{i,a} s m_{s,b} i m_{i,b}\rangle \pm (-1)^L \, |s m_{s,b} i m_{i,b} s m_{s,a} i m_{i,a}\rangle}{\sqrt{2}}, \tag{3.2.7}$$

where the (+) sign is applied for bosons and the (−) is applied for fermions.

There is also a partly coupled basis set available in the MOLSCAT, BOUND and FIELD programs. The partly coupled basis set is defined as

$$|(s_a, i_a) f_a\rangle \, |(s_b, i_b) f_b\rangle \, |F, M_F\rangle \, |L, m_L\rangle \,. \tag{3.2.8}$$

where f_j is given by the coupling of s_j and i_j and F is given by the coupling of f_a and f_b. The matrix elements of the partly coupled basis set are defined in Appendix A.2.

In Chapter 6 we define a molecular basis set,

$$|(s_a, s_b) S\rangle \, |(i_a, i_b) I\rangle \, |F, M_F\rangle \, |L, m_L\rangle \,. \tag{3.2.9}$$

where S is the molecular electron spin quantum number and I is molecular nuclear spin quantum number. The matrix elements for this basis set are derived in Section 6.1.

The only truly conserved quantum numbers, during collisions in the presence of a magnetic field, are the projection of the total angular momentum $M_{\rm tot} = m_{f,a} + m_{f,b} + M_L = m_{s,a} + m_{i,a} + m_{s,b} + m_{i,b} + M_L$ and the total parity $(-1)^L$. This means that the basis set for any collision system technically spans an infinite number of channels, as the expansion over L is unbounded. However, both L and $M_F = m_{f,a} + m_{f,b}$ are very good approximate quantum numbers because the only term in the Hamiltonian that is off-diagonal in them is $\hat{V}^{\rm d}$, which is small. Calculations are therefore restricted by limiting L to a subset of values. In this Thesis calculations are typically performed by including subsets of $L = 0$ and 2, some calculations are also performed by restricting M_F. Calculations using different basis sets give the same scattering properties and bound-state energies but allow for different views of the bound states.

Chapter 4

Homonuclear Scattering

In this Chapter, scattering calculations on homonuclear alkali-metal atom pairs are presented, and the prospects for ultracold homonuclear molecule formation are considered. Three different atomic species are considered, ^{85}Rb, ^{87}Rb, and ^{133}Cs. In ^{85}Rb both the ground $(f, m_f) = (2, +2) + (2, +2)$ channel and the excited $(2, -2) + (2, -2)$ channel are considered as well as spin mixtures from the zero-field $F = (2, 3)$ hyperfine manifold. The interaction of the spin mixtures is proposed as a possible method for mesoscopic Bell state formation via soliton collisions. In ^{87}Rb the ground state is considered to gain a complete understanding of its behaviour and its possible interactions with ultracold ^{87}RbCs molecule formation. Likewise, the ground state of ^{133}Cs is also examined and its Feshbach resonances and bound states are detailed.

4.1 85-Rubidium

^{85}Rb is a promising species for ultracold atomic gas experiments, though it has often been overlooked due to the challenges of forming a Bose-Einstein condensate (BEC) [124, 125]. Recent work shows the benefits of ^{85}Rb for RbCs production [75], discussed in Sec. 5.1.1. However, for these experiments a full understanding of the scattering behaviour of ^{85}Rb is required. Most previous work on ^{85}Rb has focused on the wide resonance near 155 G in the $(f, m_f) = (2, -2) + (2, -2)$ channel [126]. This resonance is suitable for experiments that require precise tuning of the scattering length and has been used extensively in studies of condensate collapse [125, 127–129], the formation of bright matter wave solitons [130], and few-body physics [131]. Further work using ^{85}Rb includes spectroscopic studies of photoassociation [101, 132] and measurements of inelastic collision rates [133, 134], molecular binding energies [135], molecule formation [136–140] and Efimov states [129, 131, 141].

In the following Sections we discuss the results of coupled-channel calculations to predict Feshbach resonances in both the $(2,-2)+(2,-2)$ channel (designated ee), and $(2,+2)+(2,+2)$ channel (designated aa) and the experimental confirmation of 16 of the resonances. In addition, we calculate the scattering length of the mixed spin channel $(2,+2)+(3,+3)$, and discuss one resonance which was experimentally confirmed, and look at the possibility of using other mixed spin channels to study soliton collisions.

For ^{85}Rb the coupled-channel scattering calculations are performed using MOLSCAT [110], as described in Sec. 2.5.2. Calculations are carried out with a fixed-step log-derivative propagator [105] from 0.3 nm to 2.1 nm and a variable-step Airy propagator [142] from 2.1 nm to 1,500 nm. The wavefunctions are matched to their long-range solutions, the Ricatti-Bessel functions, at 1,500 nm to find the S-matrix elements, and hence the scattering length from Eq. (2.2.2). The scattering and bound-state calculations are carried out using the potential curves and magnetic-dipole-coupling function from Ref. [143]. The R-dependent coupling function consists of the magnetic dipole-dipole interaction and a small second-order spin-orbit contribution,

$$\lambda(R) = E_h\alpha^2\left(A_{\rm SO}\exp(-\beta_{\rm SO}(R-R_{\rm SO})/a_0)+\frac{1}{R^3/a_0^3}\right), \tag{4.1.1}$$

where $\alpha \approx 1/137$ is the atomic fine-structure constant, $\beta_{\rm SO}$ and $R_{\rm SO}$ are adopted from theoretical calculations by Mies *et al.* [120], and $A_{\rm SO}$ was determined in Ref. [143] The singlet and triplet potentials were obtained by fitting to spectroscopic data on both the singlet [144] and triplet states of ^{87}Rb$_2$ and the triplet state of ^{85}Rb$_2$, together with several Feshbach resonances in ^{87}Rb$_2$, ^{87}Rb^{85}Rb and ^{85}Rb$_2$. The singlet and triplet scattering lengths for ^{85}Rb on the potentials of Ref. [143] are $a_{\rm S} = 2735\ a_0$ and $a_{\rm T} = -386\ a_0$, respectively.

Quantum numbers are assigned by carrying out approximate calculations with either M_F or F and M_F restricted to specific values. For a homonuclear diatomic molecule, F is a nearly good quantum number in the low-field region where the free-atom energies vary linearly with B. ^{85}Rb has $s = 1/2$ and $i = 5/2$ giving it $f = 1$, 2 in the molecular state there are three hyperfine manifolds (2,2), (2,3) and (3,3). The energy levels of the hyperfine/Zeeman states are shown in Fig. 3.1.

The theoretical calculations presented in this Section are discussed alongside experimental results obtained by Simon Cornish's group at Durham. Details of the experimental apparatus and cooling scheme are presented in Refs. [72, 75, 76, 145, 146].

4.1.1 Scattering in the $(f, m_f) = (2, -2) + (2, -2)$ channel

The highest excited state in the $F = 2$ hyperfine manifold of ^{85}Rb is the $(f, m_f) = (2, -2)$ level; the incoming scattering channel for two atoms in this state has $M_{\rm tot} = -4$. The background scattering length of this channel is $-450\ a_0$. A large and negative background scattering length means there is no high-lying bound state; the first $L = 0$ bound state occurs around -200 MHz. As described in Sec. 2.3.1, for an excited-state channel, where inelastic scattering can occur, the scattering length $a(B)$ is complex, $a(B) = \alpha(B) - i\beta(B)$. The two-body inelastic loss rate is proportional to $\beta(B)$. The upper panels of Figure 4.1 show the real and imaginary parts of $a(B)$ for s-wave collisions in the ee channel. In this case the inelastic collisions produce atoms in lower magnetic sublevels, with $m_{f,a}$ and/or $m_{f,b} > -2$. The lower panel shows the corresponding molecular bound states for $M_F = -4$, -5 and -6, obtained from calculations with M_F fixed. We also carried out calculations of the quasibound states with $M_F = -2$ and -3 near the ee threshold in order to identify the states responsible for the remaining resonances. These calculations use the FIELD program with propagation to reduced distances around 100 nm in order to reduce interference from continuum states.

In the presence of inelastic scattering, $a(B)$ does not show actual poles at resonance [89]. If the background inelastic scattering is negligible, the real part $\alpha(B)$ shows an oscillation of amplitude $a_{\rm res}$, while the imaginary part shows a peak of height $a_{\rm res}$. The resonant scattering length $a_{\rm res}$ is determined by the *ratio* of the couplings from the quasibound state responsible for the resonance to the incoming and inelastic channels [89]. If there is significant background scattering, then there is a more complicated asymmetric lineshape that may show a substantial dip in the inelastic scattering near resonance [92]. Fig. 4.1 shows resonances of all these different types: the resonances due to bound states with $M_F = m_{f,a} + m_{f,b} = -4$, -5 and -6 are pole-like, with values of at least $a_{\rm res} > 20$ a_0 and with most $a_{\rm res} > 1000\ a_0$. These resonances produce pronounced features in $\alpha(B)$ and sharp peaks in $\beta(B)$, off scale in Figure 4.1.

By contrast, resonances due to states with $M_F = -2$ and -3 show much weaker features with $a_{\rm res} < 15\ a_0$ and some lower than $0.01\ a_0$. These are barely perceptible in $\alpha(B)$ on the scale of Fig. 4.1 and produce broader, weaker peaks in $\beta(B)$. The distinction occurs because all the inelastic channels have $M_F > -4$: bound states with $M_F = -2$ and -3 are generally more strongly coupled to inelastic channels with the same M_F than to the incoming channel with $M_F = -4$, whereas the reverse is true for bound states with

Incoming s-wave (2,−2)+(2,−2) state							
Experiment		Theory					
B_0	δ	Assignment		B_0	Δ	a_{res}	a_{bg}
(G)	(G)	L	M_F	(G)	(mG)	(bohr)	(bohr)
156(1)	10.5(5)	0	-4	155.3	10900	$\geq$10000	-441
-	-	2	-6	215.5	5.5	4000	-374
219.58(1)	0.22(9)	0	-4	219.9	9.1	4000	-379
232.25(1)	0.23(1)	2	-4	232.5	2.0	400	-393
248.64(1)	0.12(2)	2	-5	248.9	2.9	5000	-406
297.42(1)	0.09(1)	2	-4	297.7	1.8	5000	-432
382.36(2)	0.19(1)	2	-3	382	-	15	-457
532.3(3)	3.2(1)†	0	-4	532.9	2300	$\geq$10000	-474
604.1(1)	0.2(1)	2	-4	604.4	0.03	700	-466
-	-	2	-5	854.3	0.002	25	-481
924.52(4)	2.8(1)	2	-3	924	-	9	-476

Table 4.1: Location and assignment of Feshbach resonances for $^{85}\mathrm{Rb}_2$ in the $(f, m_f) = (2, -2) + (2, -2)$ channel in the field range between 0 and 1000 G. All resonances shown satisfy $a_{\mathrm{res}} \geq 1\ a_0$. All quantum numbers in the table refer to the molecular states. The experimental errors shown are statistical uncertainties resulting from the fits as described in the text. The experimental width labeled † was determined from the difference between the minima and maxima in the measured atom number. Additional systematic uncertainties of 0.1 G and 0.5 G apply to resonance positions in the field ranges 0 to 400 G and 400 to 1000 G respectively. The resonances near 155 G and 220 G have been measured previously [135, 147].

$M_F = -4$, -5 and -6. Many of the features show quite pronounced asymmetry in the shape of the inelastic peaks.

Overall 18 resonances were found in the ee channel, the positions of which are marked in Fig. 4.1. Of these 18 resonances, 11 were found to have $a_{\mathrm{res}} > 1.0\ a_0$ and are listed in Table 4.1 along with their widths and approximate a_{res} values. Nine of the predicted resonances were confirmed experimentally; the experimental determination of the resonance pole positions and widths are also listed in Table 4.1. All but two of the predicted pole-like resonances were confirmed experimentally, together with two of the inelastically dominated features. The pole-like resonances produce sharp drops in atom number which are due to both the 3-body recombination rate, which scale as a^4 and also by inelastic loss through 2-body processes. As these mechanisms depend on the density of the atomic cloud then there is a concomitant heating of the cloud observed alongside the atom loss.

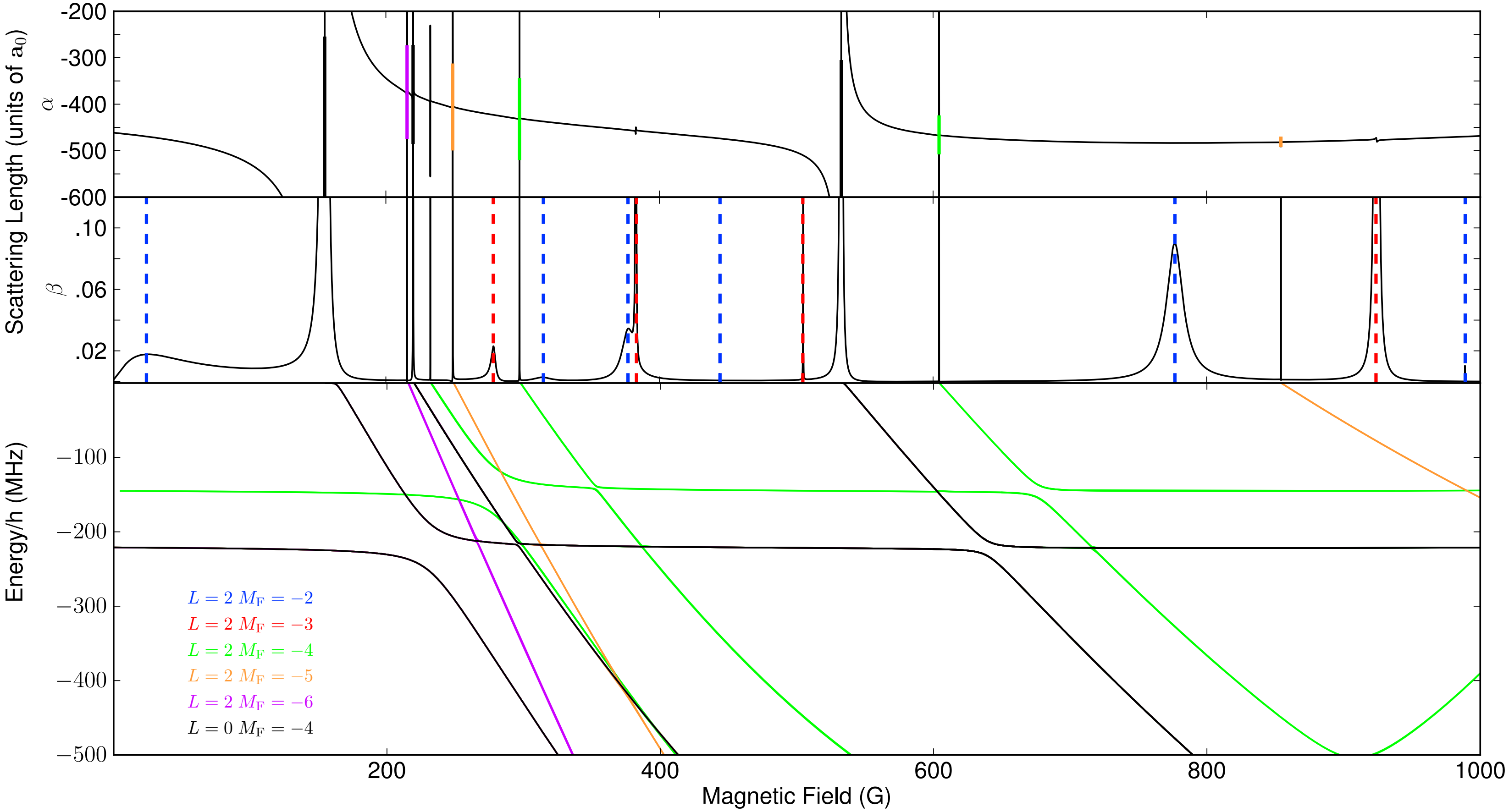

Figure 4.1: Top: The s-wave scattering length in the $(f, m_f) = (2, -2) + (2, -2)$ of $^{85}\mathrm{Rb}_2$, with $L = 0$ and 2 functions. Bottom: The energies of weakly bound molecular states. Only states with no continuum interference ($M_F \leq -4$) are shown in the bound-state map, but all resonances are included in the scattering length. Resonance widths greater than 1 μG are shown as vertical bars with lengths proportional to $\log_{10} \Delta/\mu\mathrm{G}$. Inelastically dominated resonances are not always evident in α but appear as peaks in β and are indicated by dashed vertical lines.

In Fig. 4.2, fine scans of the atom loss signal for a broad and narrow Feshbach resonance are shown. For a narrow resonance the final experimental determination of the position of the resonance is determined by the weighted average of Lorentzian fits to both the atom loss data and to temperature data. The experimental width is determined by a fit to the loss feature and is an entirely different quantity to the theoretical widths. In the broad Feshbach resonance the experimental measurements form a noticeably different shape, there is both a trough and a peak that can be located rather than a single peak. The trough (loss maximum) corresponds to the resonance position and the peak (loss minimum) occurs near the zero-crossing of the scattering length; the experimental widths reported for broad resonances were determined by the difference between these two points, this is similar to but not exactly the same as the way theoretical widths are calculated and there are still some discrepancies in the reported widths due to this and other factors, such as 3-body recombination.

In the ee channel, the two inelastically dominated features that are seen experimentally are those with the largest a_{res} values. The experimental atom loss signal measurements are shown in Figure 4.3(a) and (b). The inelastic collisions also lead to an increase in temperature, as shown in Figure 4.3 (c) and (d). The rate coefficient for 2-body losses due to inelastic collisions, calculated by Eq. (2.4.3), for the two resonances are shown in panels (e) and (f); they peak around 1×10^{-11} cm^3/s, which is an order of magnitude higher than for any of the other inelastically dominated features.

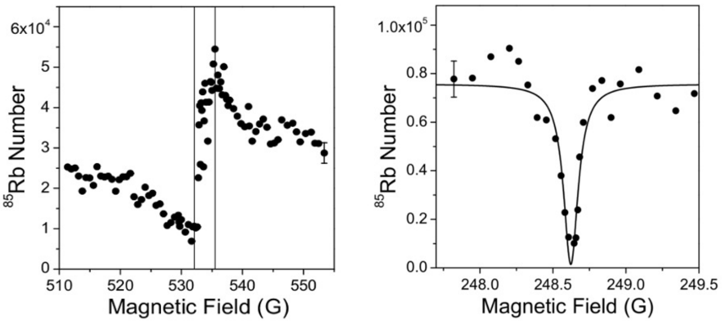

Figure 4.2: Left: Atom loss measurements around a broad resonance in the $(f, m_f) = (2, -2) + (2, -2)$ channel of ^{85}Rb, with width $\Delta > 1$ G. Right: Atom loss measurements around a narrow resonance in the $(f, m_f) = (2, -2) + (2, -2)$ channel of ^{85}Rb. The error bars show the standard deviation for multiple control shots at specific magnetic fields.

An understanding of the collisional behavior of ^{85}Rb, as described here, is essential for the production of the high phase-space density mixtures required for efficient molecule

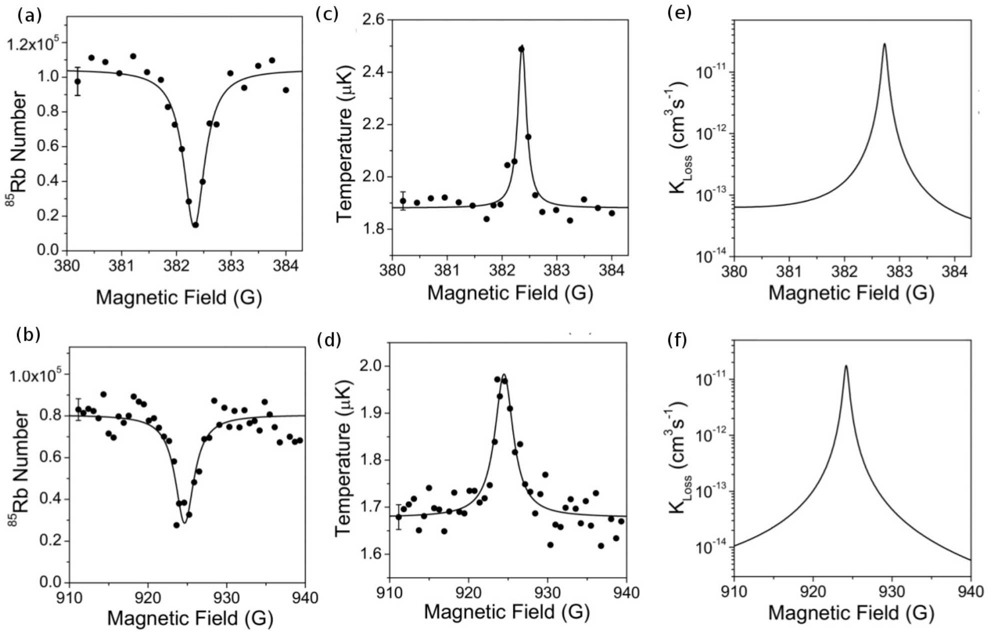

Figure 4.3: The two inelastically dominated features observed in the $(2, -2)$ state. Figures (a) and (b) show the atom number while (c) and (d) show temperature. Error bars show the standard deviation for multiple control shots at specific magnetic fields. (e) and (f) show the calculated rate coefficient for two-body loss K_{loss}.

formation. The previously unmeasured broad resonance in the ee channel offers a new magnetic field region for evaporative cooling. The elastic to inelastic collision ratio in the vicinity of this feature is potentially more favorable for evaporative cooling than near the, previously measured, 155 G resonance, where direct evaporation of ^{85}Rb to BEC is possible [125, 148]. Figure 4.4 compares the scattering properties around the 532 G resonance with those near the 155 G resonance. The results for the 532 G resonance show a pronounced dip in the rate coefficient for 2-body loss near 570 G, due to interference between the resonant and background contributions to the inelastic scattering [89, 92], which offers a range of magnetic fields where more efficient cooling may be possible. No such dip in the 2-body loss rate is present near the 155 G resonance.

4.1.2 Scattering in the ground state

The lowest hyperfine/Zeeman sub-level of ^{85}Rb is the (f, m_f)=(2,+2) level and therefore the incoming scattering channel for two atoms in this state has $M_{\mathrm{tot}} = 4$. The background scattering length of this channel is $-400\ a_0$. A large and negative background scattering length means there is no high-lying bound state; the first $L = 0$ bound state occurs around

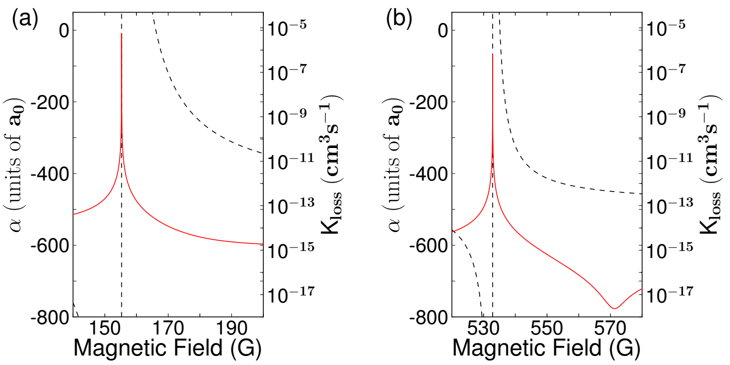

Figure 4.4: The rate coefficient for 2-body loss K_{loss} (red solid lines), which is proportional to the imaginary part of the scattering length, and the corresponding real part of the scattering length (dashed lines) for the two resonances with $\Delta > 1$ G in the $(f, m_f) = (2, -2) + (2, -2)$ channel. Note the dip in K_{loss} on the high-field side the 532 G resonance.

−200 MHz. The calculated s-wave scattering length for the aa channel is shown in the top panel of Figure 4.5 and the binding energies of the near-threshold molecular states responsible for the resonances are shown in the lower panel. The resonance positions are given in Table 4.2, along with their widths. Figure 4.5 shows one wide resonance near 851 G ($\Delta = 1.2$ G) that offers attractive possibilities for precise tuning of the scattering length, and many narrower resonances that may be useful for molecule formation.

Along with the wide resonance, 11 narrow resonances are also predicted. These narrow resonances range in width from 5 mG to 0.4 nG. In the ground state seven of the predicted resonances, listed in Table 4.2, were confirmed experimentally. All the widest calculated resonances are seen experimentally, with the exception of the two high-field resonances where the experimental field is less reproducible [72].

In the ground state both F and (f_a, f_b) quantum numbers were assigned to the resonances. The F quantum numbers are assigned by performing restricted calculations in the partly coupled basis set, $|f_a, m_{f,a}\rangle\,|f_b, m_{f,b}\rangle\,|F, M_F\rangle$. The (f_a, f_b) quantum numbers were assigned by comparison of bound-state calculations performed using a basis restricted only in L to bound-state calculations performed using a basis restricted to individual values of F, and by considering the possible hyperfine states of $^{85}\text{Rb}_2$. The (3,3) manifold will give rise to bound states of $F = 6, 5, 4, 3, 2, 1, 0$ states although some of these will be restricted by our choice of M_{tot}. Likewise the (2,3) manifold will give rise to bound states of $F = 5, 4, 3, 2, 1$ and the (2,2) manifold will give rise to bound states of $F = 4, 3, 2, 1, 0$. By searching for these patterns, in the bound-state energy levels, then the correct (f_a, f_b)

levels can be assigned, as well as the F quantum number. However, it should be noted that f_a and f_b are not good quantum numbers, and whilst we assign them to each resonance they apply predominately only at low magnetic fields, below 400 G.

The wide resonance offers the prospect of evaporative cooling free from two-body loss. Although the background scattering length is moderately large and negative for ground-state atoms (see Figure 4.5), the broad resonance at 851 G may be used to tune the scattering length to modest positive values, improving the evaporation efficiency and offering the prospect of BEC formation directly in the absolute ground state.

Incoming s-wave (2,2)+(2,2) state								
Experiment		Theory						
B_0	δ	Assignment				B_0	Δ	a_{bg}
(G)	(G)	L	(f_a,f_b)	F	M_F	(G)	(mG)	(bohr)
164.74(1)	0.08(2)	2	(2,2)	4	2	164.7	-0.0006	-432
171.36(1)	0.12(2)	2	(2,2)	2	2	171.3	-0.02	-431
368.78(4)	0.4(1)	2	(2,2)	4	3	368.5	-0.06	-413
-	-	2	(2,3)	3	2	594.9	-0.4×10^{-6}	-401
-	-	2	(2,3)	5	3	685.0	-0.4×10^{-4}	-396
-	-	2	(2,3)	5	2	750.8	-0.0003	-392
770.81(1)	0.11(2)	2	(2,3)	5	4	770.7	-0.5	-390
809.65(3)	0.3(1)	2	(2,3)	3	3	809.7	-0.09	-383
819.8(2)	0.7(5)	2	(2,3)	5	5	819.0	-5.4	-380
852.3(3)	1.3(4)†	0	(2,3)	5	4	851.3	-1199	-393
-	-	2	(2,3)	2	2	961.8	-0.01	-390
-	-	2	(2,3)	4	4	980.5	-0.7	-387

Table 4.2: Location and assignment of Feshbach resonances for $^{85}\text{Rb}_2$ in the $(f, m_f) = (2, +2) + (2, +2)$ channel in the field range between 0 and 1000 G. All quantum numbers in the table refer to the molecular states. The experimental errors shown are statistical uncertainties resulting from the fits as described in the text. The experimental width labelled † was determined from the difference between the minima and maxima in the measured atom number. Additional systematic uncertainties of 0.1 G and 0.5 G apply to resonance positions in the field ranges 0 to 400 G and 400 to 1000 G respectively.

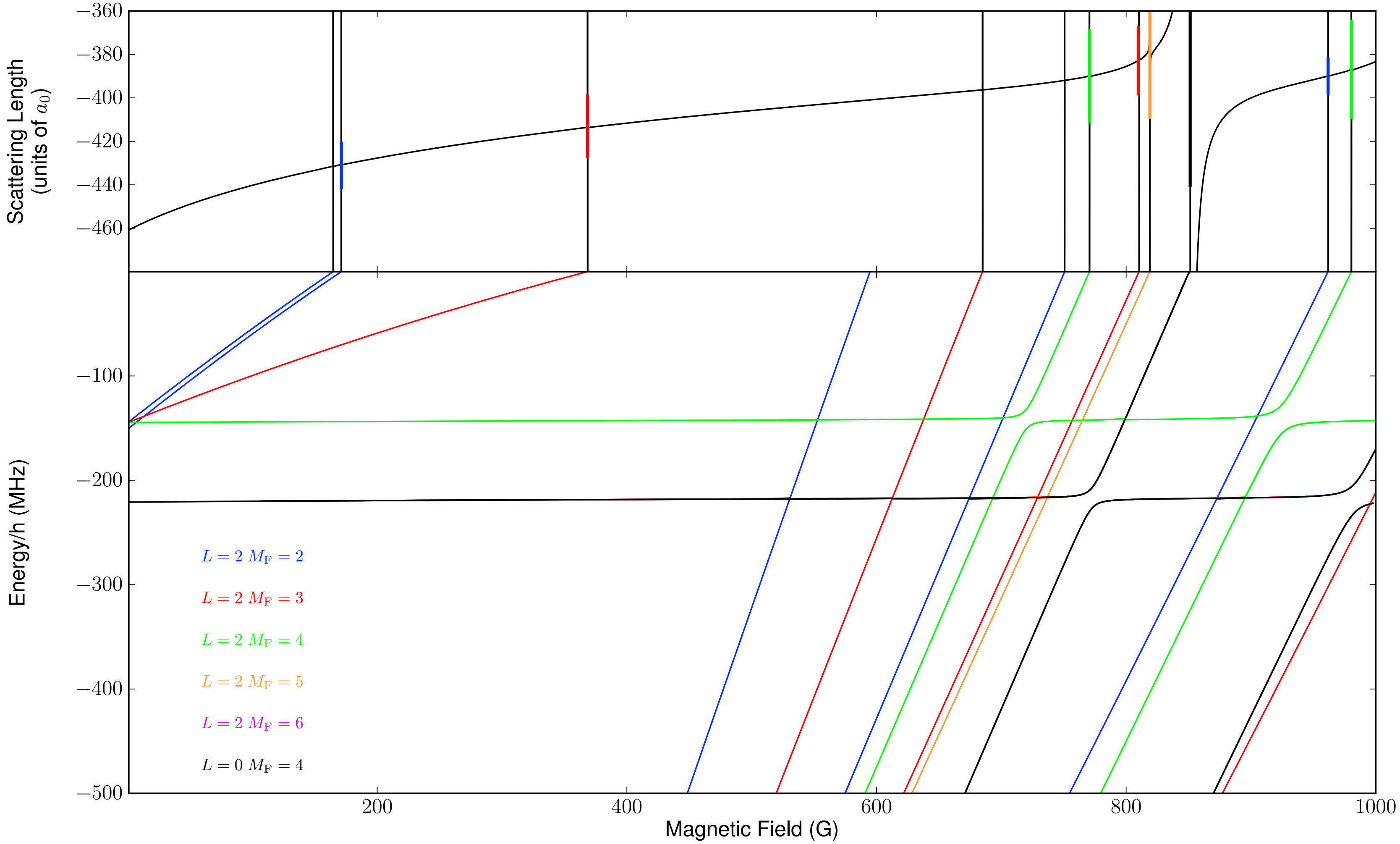

Figure 4.5: Top: The s-wave scattering length in the $(f, m_f) = (2, +2) + (2, +2)$ channel of $^{85}\mathrm{Rb}_2$, with $L = 0$ and 2 functions. Bottom: The energies of weakly bound molecular states. Resonance widths greater than 1 μG are shown as vertical bars with lengths proportional to $\log_{10} \Delta/\mu\mathrm{G}$.

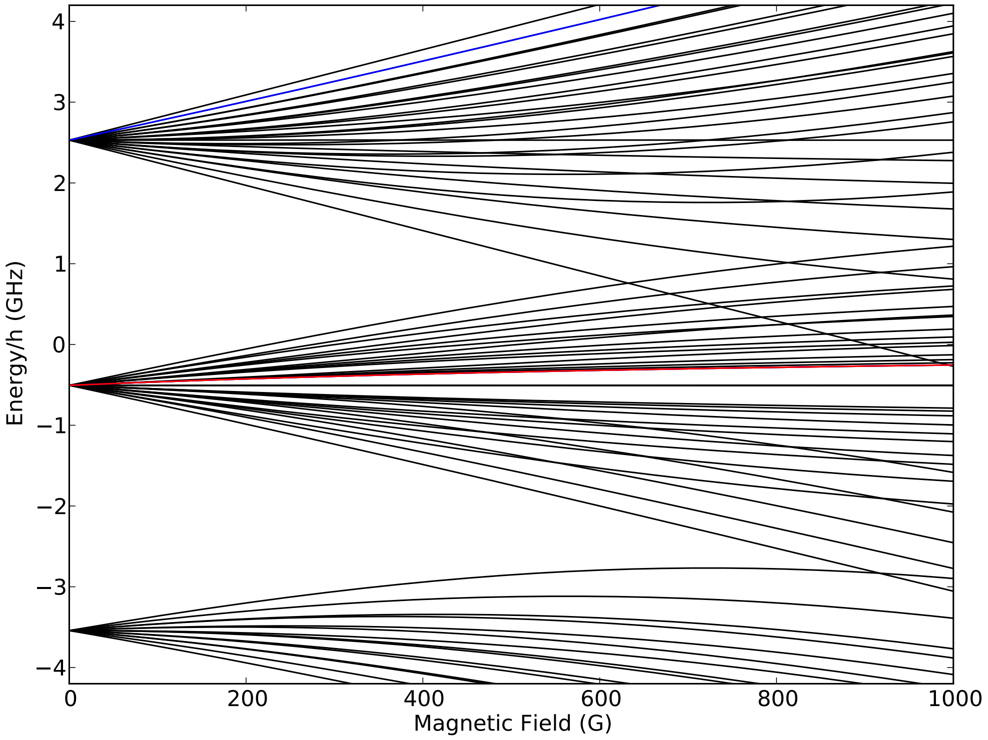

Figure 4.6: Breit-Rabi diagram showing the hyperfine sub-levels of $^{85}\mathrm{Rb}_2$. The black lines show all possible asymptotic energy levels; the red line shows the state corresponding to $(f_a m_{f_a}, f_b m_{f_b}) = (2, +2, 3, +3)$ at low field and the blue line shows a different state which also has $M_{\mathrm{tot}} = 5$.

4.1.3 Scattering in mixed states

We have also investigated the scattering length for a series of mixed spin channels from the $(f_a, f_b) = (2, 3)$ hyperfine manifold, with the aim of identifying broad resonances suitable for tuning interactions. By tuning the scattering length from positive to negative (or vice-versa) using a Feshbach resonance then the overall behaviour of the condensate switches between repulsive and attractive.

The energy of the state, which corresponds to the desired $(f_a m_{f_a}, f_b m_{f_b})$ state at low field, can be calculated exactly. The asymptotic energy levels of $^{85}\mathrm{Rb}_2$ are shown in Fig. 4.6, as black lines. Each MOLSCAT calculation is run for a specific projection of total angular momentum for each mixed state, $M_{\mathrm{tot}} = m_{f_a} + m_{f_b} + m_L$. Limiting the asymptotic energy levels of $^{85}\mathrm{Rb}_2$ to those corresponding to $M_{\mathrm{tot}} = 5$ reduces the number of states in the $L = 0$ basis to two, as shown by the blue and red lines in Fig. 4.6. The lower in energy of these two states is the one which corresponds to the $(2, +2, 3, +3)$ channel at low field. The scattering length and associated plot of K_{loss}, for the $(2, +2, 3, +3)$ channel,

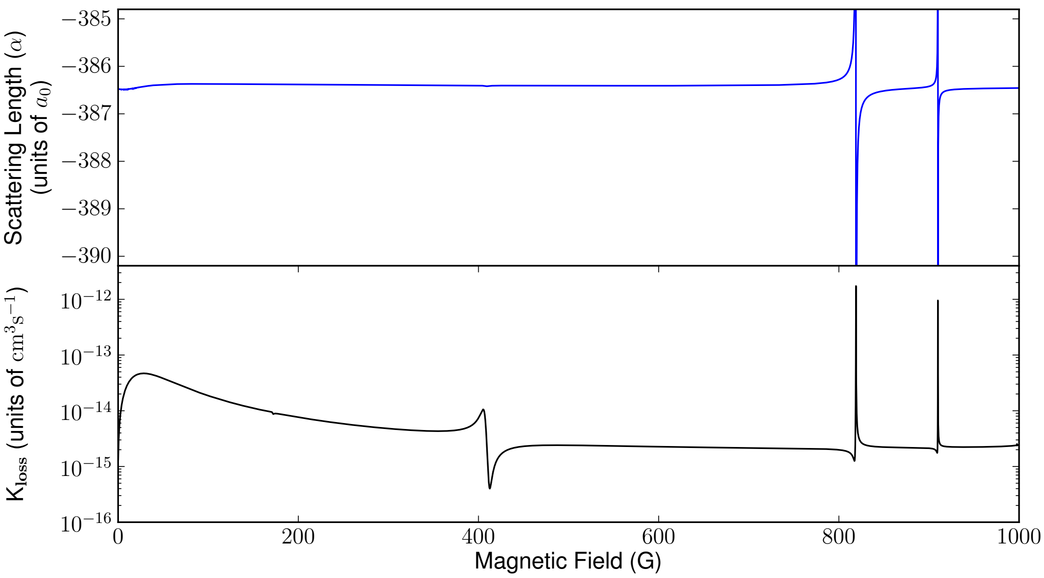

Figure 4.7: Scattering length of the $(f, m_f) = (2, +2) + (3, +3)$ channel of ^{85}Rb. Top: Real part of the scattering length. Bottom: The coefficient of the two body loss rate.

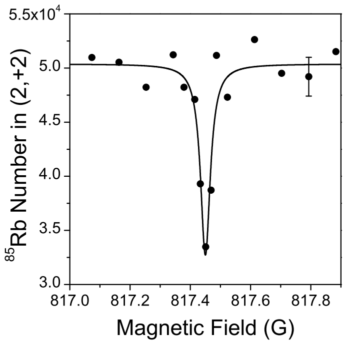

Figure 4.8: A resonance measured between the $(2, +2)$ and $(3, +3)$ spin states in ^{85}Rb at 817.45(5) G. On resonance the increased inelastic collision rate in the mixture results in a loss feature in the $(2, +2)$ atom number as a function of magnetic field.

are shown in Fig. 4.7. All the states originating from the same hyperfine mainfold have similarly large and negative background scattering lengths. Wide tunable resonances were also found in the $(f_a m_{f_a}, f_b m_{f_b}) = (2, +2, 3, +2)$, $(2, +2, 3, +1)$ and $(2, +2, 3, 0)$ states; the scattering lengths for these states are shown in Appendix E.

Most channels exhibit strong inelastic decay with measured trap lifetimes of ∼ 100 ms. However, the $(2, +2) + (3, +3)$ channel is immune to inelastic spin exchange collisions, resulting in trap lifetimes of ∼ 5 s. The scattering length in the mixed spin channel, $(2, +2) + (3, +3)$ shows two pole-like resonances at 818.8 G and 909.9 G, both with widths of 2 mG, and $a_{\rm res}$= 1600 a_0 and 800 a_0 respectively.

The resonance at 818.8 G was also measured experimentally. The experimental results are presented in Figure 4.8 where a loss feature in the ^{85}Rb $(2, +2)$ number reveals the location of the resonance. The experimentally determined resonance position and width are 817.45(5) G and 0.031(1) G, respectively.

4.1.4 Potential application of a spin mixture

Solitons are non-dispersive solitary wave, which can be considered to behave in a particle-like manner [130, 149]. Solitons have been suggested as promising candidates to study quantum entanglement on a mesoscopic scale. In particular, solitons have been suggested as a route to create mesoscopic Bell states in Refs. [74, 150]. A Bell state is

$$|\psi_{\mathrm{Bell}}\rangle \equiv \frac{1}{\sqrt{2}}\left(|\mathrm{A},\mathrm{B}\rangle + e^{i\alpha}|\mathrm{B},\mathrm{A}\rangle\right), \tag{4.1.2}$$

where $|A, B\rangle$ ($|B, A\rangle$) signifies that the BEC A is on the left (right) and the BEC B is on the right (left). The initial proposal by Gertjerenken *et al.* [150] called for a dual-species BEC of ^{85}Rb and ^{133}Cs. However, the use of a BEC of different hyperfine states of the same atomic species, proposed by Billam *et al.* [74], fulfils the requirement that the solitons are distinguishable whilst removing the need of creating a dual-species BEC, and adjusting for the different atomic masses.

The general behaviour for a mean-field bright soliton in a soliton-barrier or soliton-soliton collision is for the soliton considered to break into two parts, with only a fraction of the atoms transmitted depending on the interaction potential [150–152]. However, it was shown in Refs. [73, 153] that at very low kinetic energies the solitons are energetically forbidden from breaking apart and a mesoscopic superposition can be realised as a result of the collision. Highly entangled states are characterised by a roughly 50:50 chance of finding the soliton A (B) on the left/right when soliton B is on the right/left side. The correlation function is,

$$\gamma(\delta) \equiv \int_{\delta}^{\infty} dx_A \int_{-\infty}^{-\delta} dy_B |\Psi|^2 + \int_{-\infty}^{-\delta} dx_A \int_{\delta}^{\infty} dy_B |\Psi|^2 \,, \tag{4.1.3}$$

where Ψ is the many-particle wavefunction (normalised to one) and Bell states (4.1.2) are characterised by $\gamma \simeq 1$.

The behaviour of a BEC, with a large number of particles, is usually modelled using the mean-field Gross-Pitaevskii Equation [154–156]

$$\begin{aligned} i\hbar\partial_t\varphi_{\mathrm{A}}(x,t) &= \left[-\frac{\hbar^2}{2m_{\mathrm{A}}}\partial_x^2 + \frac{g_{\mathrm{A}}}{2}|\varphi_{\mathrm{A}}(x,t)|^2\right]\varphi_{\mathrm{A}}(x,t) \\ &+ \left[V_{\mathrm{A}}(x) + \frac{g_{\mathrm{AB}}}{2}|\varphi_{\mathrm{B}}(x,t)|^2\right]\varphi_{\mathrm{A}}(x,t) \\ i\hbar\partial_t\varphi_{\mathrm{B}}(x,t) &= \left[-\frac{\hbar^2}{2m_{\mathrm{B}}}\partial_x^2 + \frac{g_{\mathrm{B}}}{2}|\varphi_{\mathrm{B}}(x,t)|^2\right]\varphi_{\mathrm{B}}(x,t) \\ &+ \left[V_{\mathrm{B}}(x) + \frac{g_{\mathrm{AB}}}{2}|\varphi_{\mathrm{A}}(x,t)|^2\right]\varphi_{\mathrm{B}}(x,t)\ , \end{aligned}$$

where $V(x) = \frac{1}{2}m_{\mathrm{S}}\omega^2x^2$ is the harmonic confinement potential and the single-particle density $|\varphi_{\mathrm{S}}(x,t)|^2$ is normalised to N_{S}, where S = A,B. The interaction parameters g_S (S = A,B or AB) are set by the scattering lengths a_S where (S = A,B or AB) and the radial trapping frequency, $f_\perp$ [157]. In the description of low-kinetic-energy collisions of bright solitons the GPE is combined with the Truncated Wigner Approximation (TWA) for the centre of mass degree of freedom in order to model the true quantum behaviour, as described in [150]. The TWA approximation accounts for quantum noise, not present in the GPE equation, by modelling the noise classically. It is often used to model thermal noise, however in this situation it is used to account for noise in the soliton centre-of-mass wavefunction. The correlation function can then be calculated using Eq. (4.1.3) with $|\Psi|^2 = |\Psi_{\mathrm{A}}|^2|\Psi_{\mathrm{B}}|^2$ where $|\Psi_S|^2$ is the single particle density of soliton $S = \mathrm{A},\mathrm{B}$, and $\delta \geq 0$ serves as an indication of entanglement.

The physical requirements for the experiment are a negative background scattering length for each of the two distinguishable soliton states, and a wide Feshbach resonance in the mixed-state scattering length. Coupled-channels calculations were performed as detailed previously on each of the $(fa, fb) = (2,\ 3)$ hyperfine manifold. A wide tunable resonance was found in the $(f, m_f) = (2,2){+}(3,2)$ channel. The resonance has a calculated width of $\Delta = 14$ G. Whilst excited-state resonances are subject to decay from inelastic collisions [89], the resonance has $a_{\mathrm{res}} > 10{,}000\ a_0$ making it pole-like from an experimental point of view. The real part of the scattering length and associated plots of K_{loss}, of both the mixed-state and the individual states, are shown in Fig. 4.9. The three-dimensional scattering can be converted into a one dimensional interaction parameter g by taking account of the trapping frequency $(f_\perp)$. g_{1D} is given in terms of a_{3D} as [157, 158]

$$g_{\mathrm{1D}} = \frac{2\hbar a}{\mu a_\perp^2}\frac{1}{(1 - Ca/a_\perp)} \approx \frac{2\hbar a}{\mu a_\perp^2}, \tag{4.1.4}$$

where $C = -\zeta(1/2) = 1.4603\ldots$ and $a_\perp = \sqrt{\hbar/(2\pi\omega f_\perp)}$. $a_\perp$ is the harmonic oscillator length for a particle of mass m and trapping frequency $f_\perp$. With the introduction of

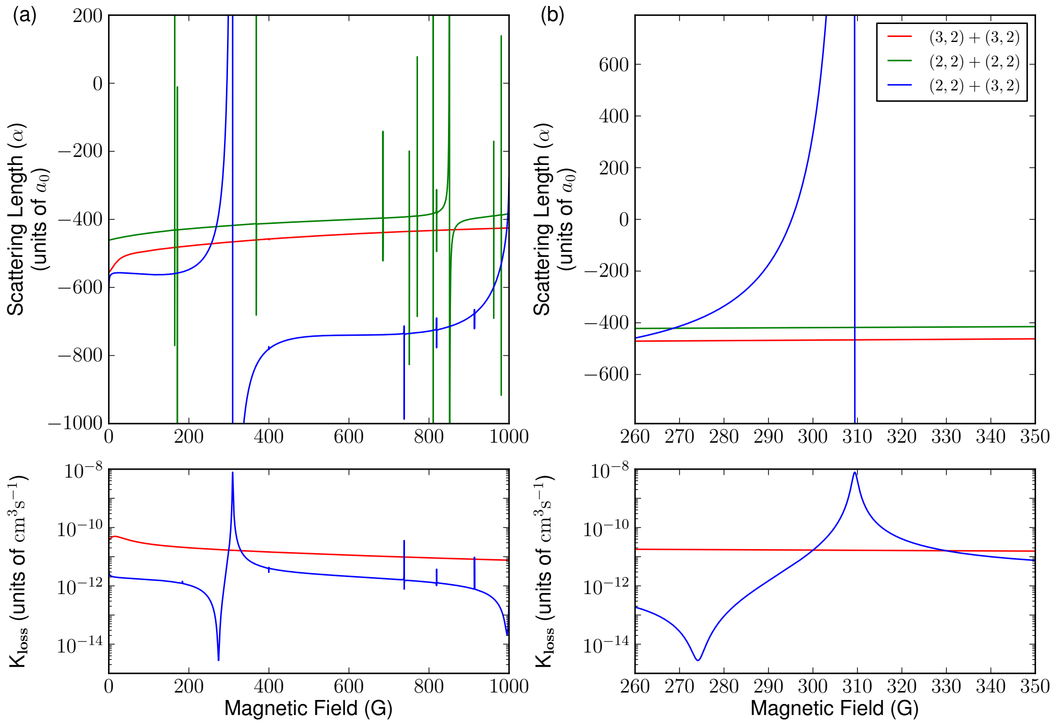

Figure 4.9: The s-wave scattering length for the $(f, m_f) = (2, 2) + (3, 2)$, $(2, 2) + (2, 2)$ and $(3, 2) + (3, 2)$ channels of ^{85}Rb. (a) The real part of the scattering length is shown in the top plot, the imaginary part is proportional to the inelastic decay-rate coefficient, K_{loss}, which is shown in the bottom plot. (b) Zoom of (a), the wide resonance in the mixed spin state allows for tuning of the scattering length.

harmonic confinement it is possible to cause a confinement induced resonance (CIR) as predicted in [158]. A CIR occurs when the 3D scattering length approaches the same length scale as $a_\perp$, namely at $a_\perp \approx C a_{3\text{D}}$. The CIR is caused when the incoming scattering channel becomes degenerate with a transversally excited molecular bound state supported by the trapping potential [157, 159]. Given the confinement parameters used in Ref. [74], $f_\perp = 50$ Hz and $f = 2$ Hz, the CIR would occur when $a_{3\text{D}} \approx 3.5 \times 10^5\ a_0$ which would not interfere with any practical implementation of the proposed scheme.

Using the Feshbach resonance described above, centre-of-mass TWA-GPE simulations were performed by Billam *et al.* [74] using the $(f, mf) = (2, +2)$ and $(3, +2)$ hyperfine states of ^{85}Rb as the two components of the mixture. The resulting calculations showed a high (≈ 1) value of γ subsequent to the first collision, which indicates the formation of a Bell state with high fidelity [74]. Compared to the scheme suggested in Ref. [150], the scheme in Ref. [74] is feasible at higher atom numbers, less sensitive to magnetic bias field strength, and generates higher-fidelity Bell states.

4.2 87-Rubidium

It is important to have a complete understanding of the behaviour of the ground state of ^{87}Rb in order to fully understand the mechanisms contributing to the magnetoassociation of ^{87}RbCs, which is presented in Section 5.1.2. The same potentials are used for ^{87}Rb as were used for ^{85}Rb, as the potentials can be 'mass-scaled' for use with all Rb isotopes. 'Mass-scaling' refers to changing the reduced mass used in the scattering calculation but using the same potential curves. This method works well with the heavier alkali elements [75,160], but not as well with lighter elements such as lithium where corrections due to the breakdown of the Born-Oppenheimer approximation are important [161–163]. ^{87}Rb has a different hyperfine structure to that of ^{85}Rb; its nuclear spin is $i = 3/2$ giving atomic quantum numbers $f = 1, 2$. The energy levels of a single rubidium atom in an external magnetic are shown in Fig. 4.10. The singlet and triplet scattering lengths for ^{87}Rb are $a_{\rm S} = 90\ a_0$ and $a_{\rm T} = 99\ a_0$, respectively.

The lowest-energy hyperfine/Zeeman sub-level of ^{87}Rb is the $(f, m_f) = (1, +1)$ level

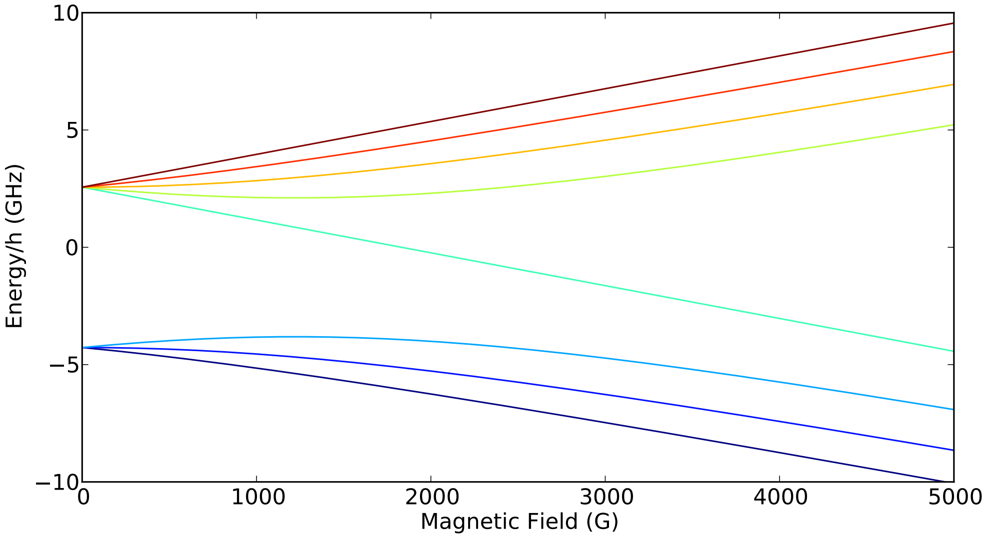

Figure 4.10: The hyperfine structure of ^{87}Rb in an external magnetic field. At zero-field the states are grouped into two manifolds the upper one corresponding to $f = 2$ and the lower one corresponding to $f = 1$. The magnetic field lifts the degeneracy of these states and they split into m_f sublevels. In the upper manifold, $f = 2$, the states run, in order of increasing energy, from $m_f = -2 \ldots 2$; in the lower manifold, $f = 1$, the states run from $m_f = 1 \cdots -1$.

and therefore the incoming scattering channel for two atoms in this state has $M_{\text{tot}} = 2$. Calculations were carried out using the methods described for ^{85}Rb. The background scattering length of the ground-state channel is 100 a_0 and the scattering has little variation with magnetic field. The calculated s-wave scattering length for the $(f, m_f) = (1, +1) + (1, +1)$ channel is shown in the top panel of Fig. 4.11 and the binding energies of the near-threshold molecular states responsible for the resonances are shown in the lower panel. The resonance positions are given in Table 4.3, along with their widths. The widest known resonance in the system occurs just above the magnetic field range we include at around 1007 G; the scattering length at the high-field end of Fig. 4.11 can be seen to be turning upwards which is the start of this resonance. The position and width of this resonance are included in Table 4.3 for completeness. This resonance has been used to create Feshbach molecules of ^{87}Rb$_2$ [164]. Experimental results on the resonance positions are available in Ref. [165], as well as previous theoretical calculations, and we find good agreement with these results.

Overall the moderately positive and relatively constant background scattering length of ^{87}Rb makes it an ideal component of heteronuclear mixtures, as it can be cooled to degeneracy at almost any magnetic field. In Section 5.1.2 its use in the formation of ground state ^{87}RbCs is discussed.

Incoming s-wave (1,1)+(1,1) state									
B_0 (G)	Δ (mG)	a_{bg} (bohr)	L	M_F	B_0 (G)	Δ (mG)	a_{bg} (bohr)	L	M_F
248.45	5×10^{-5}	100.3	2	1	631.81	2	100.3	2	4
305.67	1×10^{-5}	100.3	2	0	685.57	7	100.3	0	2
319.3	0.1	100.3	2	2	718.65	0.9	100.3	2	3
377.76	1×10^{-6}	100.3	2	0	819.32	3	100.4	2	1
387.25	0.1	100.3	2	1	830.33	0.2	100.4	2	2
391.56	0.5	100.3	2	3	857.22	4×10^{-3}	100.4	2	1
395.32	9×10^{-4}	100.3	2	0	911.12	2	100.5	0	2
406.33	0.5	100.3	0	2	929.57	4×10^{-2}	100.5	2	2
532.6	0.08	100.3	2	0	977.69	3×10^{-2}	101	2	1
551.36	0.3	100.3	2	2	1007.37	200	100.3	0	2

Table 4.3: Location and assignment of Feshbach resonances for ^{87}Rb$_2$ in the $(f, m_f) = (1, +1) + (1, +1)$ channel in the field range between 0 and 1008 G. All quantum numbers in the table refer to the molecular states.

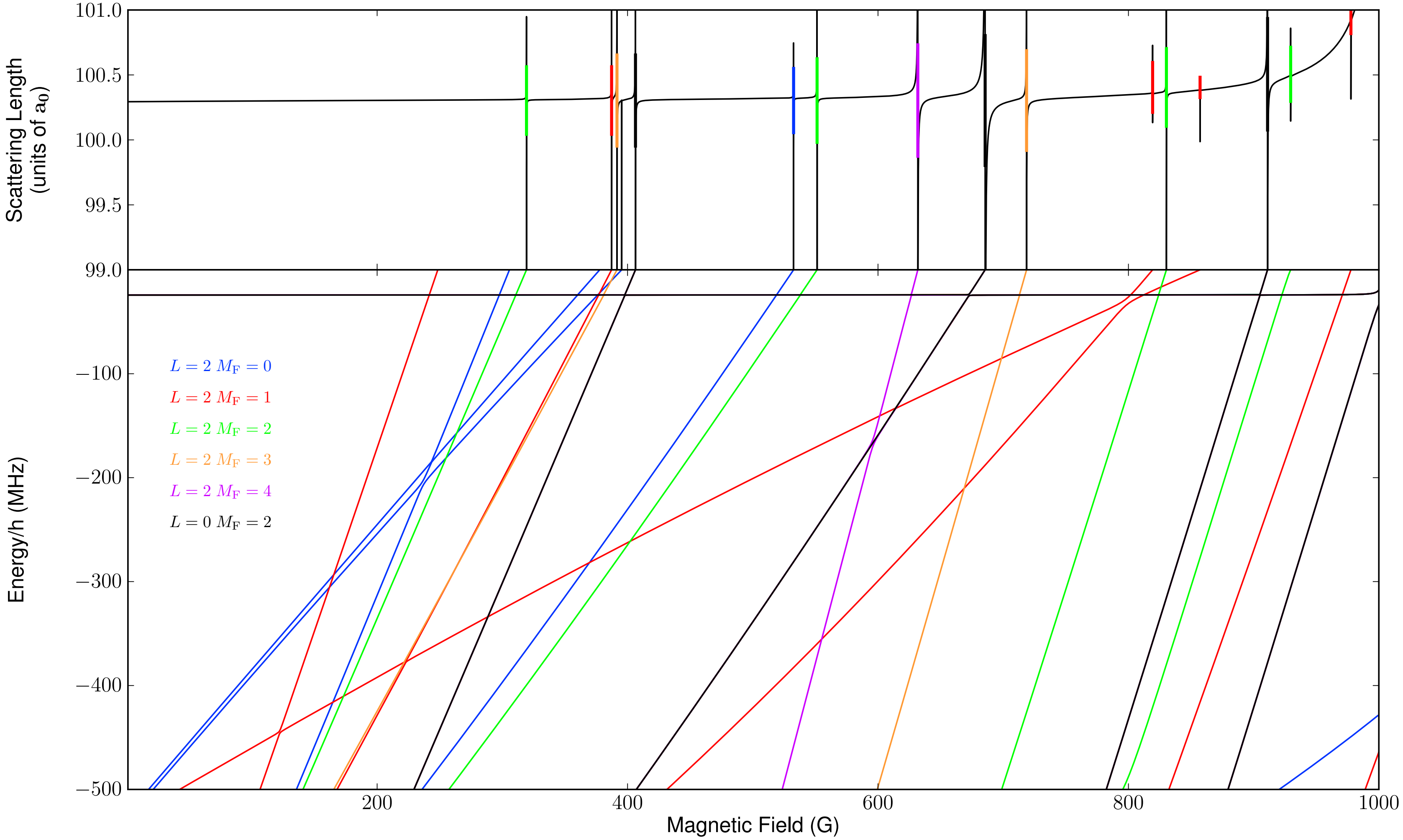

Figure 4.11: Top: The s-wave scattering length in the $(f, m_f) = (1, +1) + (1, +1)$ channel of $^{87}\text{Rb}_2$, with $L = 0$ and 2 functions. Bottom: The energies of weakly bound molecular states. Resonance widths greater than 1 μG are shown as vertical bars with lengths proportional to $\log_{10} \Delta/\mu\text{G}$.

4.3 133-Cesium

The scattering properties and bound states of cesium are well known, and results from the most recent potentials are presented in Ref. [166]. However, calculations using these potentials are presented in the following Section for completeness, and to aid in the discussion of their interactions as part of a heteronuclear mixture, which is discussed in the following Chapter. The only stable isotope of cesium is ^{133}Cs, which is the isotope considered. The large nuclear charge of ^{133}Cs gives rise to a large second-order spin-orbit contribution in short-range interactions, which is fitted to experimental results from electronic structure calculations [122] in Ref. [166]. For accurate representations of the scattering properties of Cs we use a basis set that includes $L = 0, 2$ and 4 basis functions, as the second-order spin-orbit contribution strengthens the higher-order L contributions.

The ground state of ^{133}Cs is the (f, m_f)=(3,+3) level and therefore the incoming scattering channel for two atoms in this state has $M_{\text{tot}} = 6$. The calculated s-wave scattering length for the ground-state channel including $L = 0, 2$ and 4 functions, an sdg-basis set, is shown in the top panel of Figure 4.13 and the binding energies of the near-threshold molecular states responsible for the resonances are shown in the lower panel. Detailed information on the position, character and width of the Feshbach resonances can be found in Ref. [166]. It is noted in [166] that the resonances around $490 - 510$ G are mixed as they cross threshold. In Fig. 4.13 the states are labelled with the colour which corresponds to the colour of the bound state closest in position to the resonance, so that the width of the resonance may still be shown; however, as explained in [166] the M_F labelling of these states should not be taken as exact.

The background scattering length for the incoming s-wave $(f, m_f) = (3, +3) + (3, +3)$ channel of ^{133}Cs is around 3000 a_0 and there is a corresponding very high-lying bound state at around -50 kHz. This bound state contributes to two wide resonances in the scattering length around 548 G and 782 G. The large scattering length of Cs means that BECs can only be formed in very specific magnetic field ranges around the wide resonances when the scattering length can be tuned to an acceptable value, typically around $40 \lesssim |a| \lesssim 250$ a_0 [16, 17, 21, 167]. There is also a wide resonance around -12 G which gives rise to the negative divergence of the scattering length which can be seen at low magnetic fields. The variation in scattering length due to this resonance creates a region where the scattering length is only moderately positive. This region was used to produce the first Cs BEC [168] just above the zero-crossing at 17 G. Magnetoassociation of Cs_2

has been performed at the nearby resonance at 19.89 G [169], making use of the moderate background scattering length. In Köppinger *et al.* [170] an optically trapped BEC of Cs is used to show that repeated sweeps of the magnetic field over the 19.89 G resonance can be used to produce multiple groups of ultracold molecules. The weakly bound molecular states can be controlled by using the magnetic field to guide the molecules down to a state with the desired magnetic moment, which can be determined from the the slope of the bound states shown in Fig. 4.13. Feshbach molecules of Cs_2 have also been used to form ground-state homonuclear molecules [171].

Cesium has also been used to study Efimov states, which are high-lying bound states of triatomic molecules that appear when the two-body interaction has a bound state near to threshold [172]. Efimov predicted an infinite series of three-body bound states each with a successive size of $a_-^{(n)} = 22.7^n a_-^{(0)}$, where $a_-^{(0)}$ is the position of the first Efimov state and commonly referred to as the three-body parameter, and a binding energy which is a factor of 22.7^{2n} weaker than the first resonance. Several Efimov features have been observed in Cs [173,174] including a resonance identified as the second Efimov resonance [175]. Efimov states have generated great interest as a test of universality as the states should occur in the same patterns for any system, once the three-body parameter is determined.

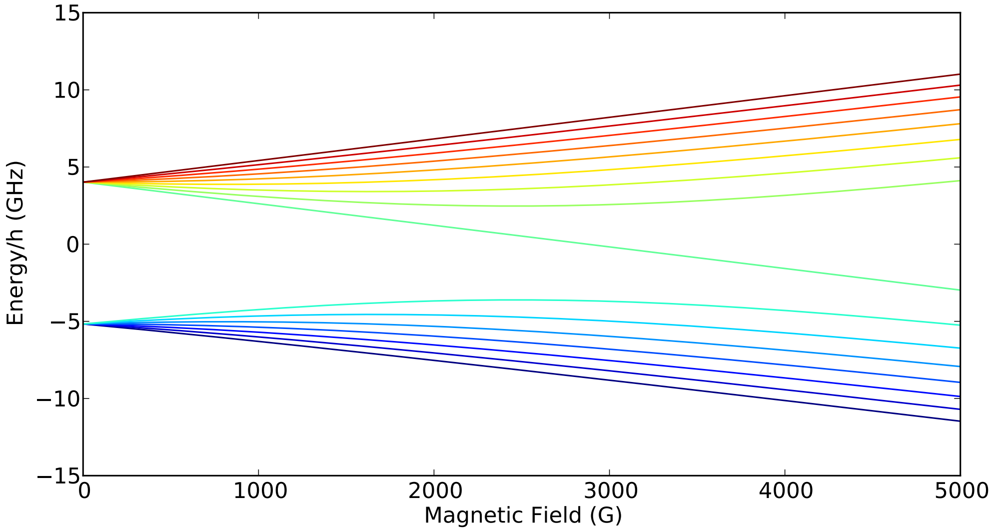

Figure 4.12: The hyperfine structure of ^{133}Cs in an external magnetic field. At zero-field the states are grouped into two manifolds, the upper one corresponding to $f = 4$ and the lower one corresponding to $f = 3$. The magnetic field lifts the degeneracy of these states and they split into m_f sublevels. In the upper manifold, $f = 4$, the states run, in order of increasing energy, from $m_f = -4 \ldots 4$; in the lower manifold, $f = 3$, the states run from $m_f = 3 \cdots -3$.

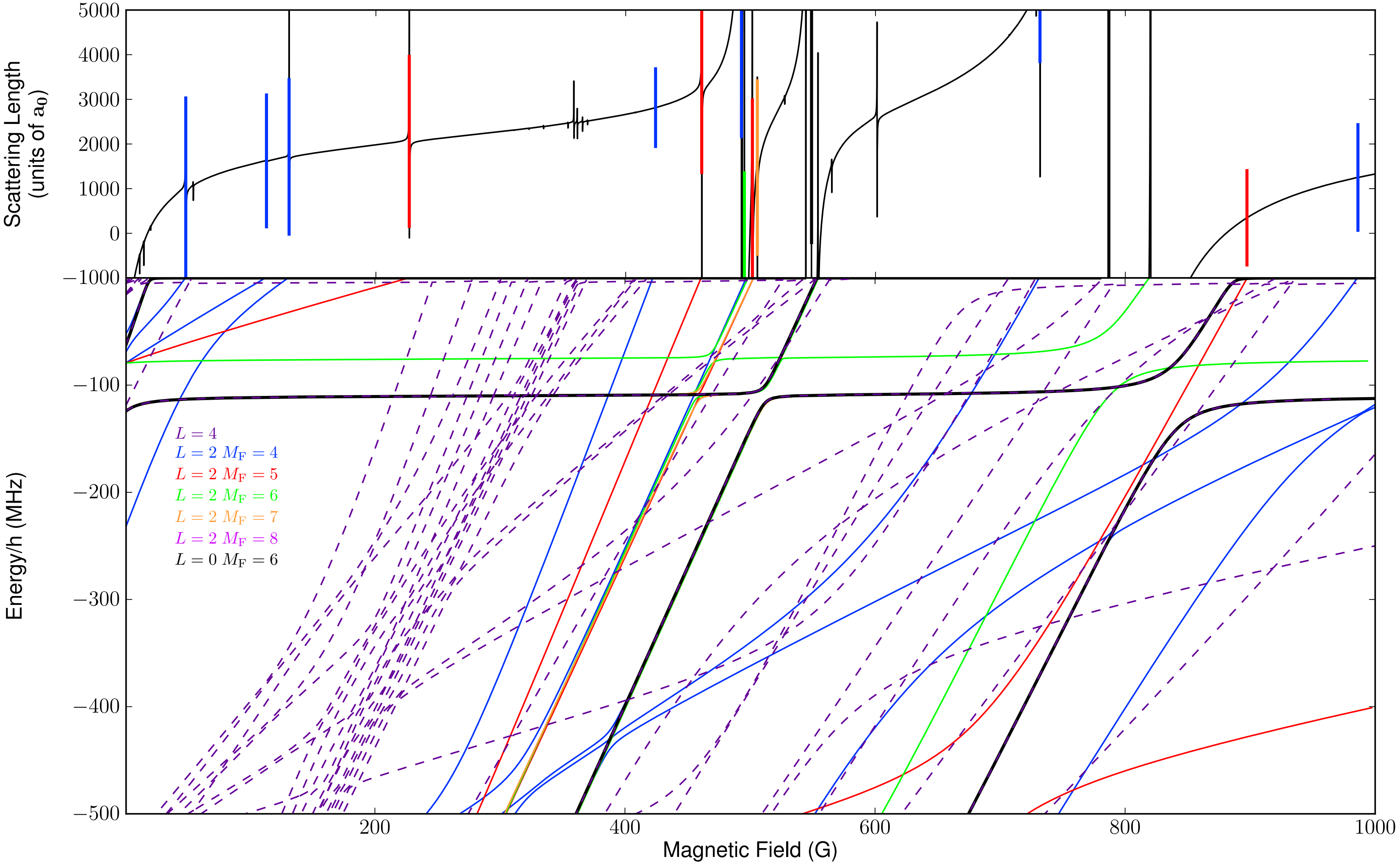

Figure 4.13: Top: The s-wave scattering length in the $(f, m_f) = (3,3) + (3,3)$ channel of $^{133}\mathrm{Cs}_2$, with $L = 0$ and 2 functions. Bottom: The energies of weakly bound molecular states. Resonance widths greater than 1 μG are shown as vertical bars with lengths proportional to $\log_{10} \Delta/\mu\mathrm{G}$.

Chapter 5

Heteronuclear Molecule Formation

The motivation for the formation of ultracold polar molecules was discussed in the Introduction. The interesting uses of ultracold heteronuclear polar molecules require a strong long-range, anisotropic dipole-dipole interaction. The maximal dipole-dipole interaction energy, for a pair of aligned dipoles, is [176]

$$V_{\mathrm{dd}} = \frac{C_{\mathrm{dd}}}{4\pi} \frac{1 - 3\cos^2\theta}{r^3} \tag{5.0.1}$$

where r is the distance between molecules and θ is the angle between the axis connecting the molecules and the direction of polarisation. The coupling constant $C_{\mathrm{dd}} = d^2/\epsilon_0$ where d is the electric dipole and ϵ_0 is the permittivity of free space. If a polar molecule is left to rotate freely the average dipole moment in the lab frame is zero, but an applied electric field can be used to orient the dipoles and create a fixed dipole moment. The applied electric field required to reach 1/3 of the permanent dipole moment of the molecule is referred to as E_{crit} and is given by $E_{\mathrm{crit}} = B_{\mathrm{rot}}/d$, where B_{rot} is the rotational constant. Molecules generally have the strongest dipole moment in the rovibrational ground state. Table 5.1 shows the dipole moments, rotational constants and E_{crit} values for the ground state of various possible alkali-alkali combinations.

Another consideration in choosing a possible system of heteronculear molecules is their reactivity. All possible alkali combinations are stable with respect to atom transfer reactions such as $XY + XY \to X_2Y + Y$ or $XY_2 + Y$ [177]; however, some of the alkalis are not stable with respect to the exchange reaction

$$XY + XY \to X_2 + Y_2.$$

Table 5.1 shows which alkali-alkali combinations are stable.

In the following Chapter we consider isotopologues of RbCs and KCs, both of which have large dipole moments and are stable to the exchange reaction. The scattering lengths and near-threshold bound states are calculated and relevant experimental details are discussed. The formation of ultracold molecules of ^{87}RbCs is detailed as well as the possibility for molecule formation in KCs.

Species	Dipole moment (D)	B_{rot} $\times 10^{-2}$cm^{-1}	E_{crit} (kV cm^{-1})	Stable
RbCs	1.24	1.66	0.8	Yes
KCs	1.91	3.10	1.0	Yes
NaCs	4.61	5.93	0.8	Yes
LiCs	5.52	19.4	2.1	No
KRb	0.62	3.86	3.7	No
NaRb	3.31	7.11	1.3	Yes
LiRb	4.17	22.0	3.1	No
NaK	2.58	9.62	2.2	Yes
LiK	3.57	26.1	4.4	No
LiNa	0.57	38.0	39.9	No

Table 5.1: Permanent dipole moment, rotation constant and E_{crit} for various alkali-metal heteronuclear molecule combinations in the lowest vibrational level of the singlet ground state. Molecules labelled as stable are stable to exchange reactions. (Data taken from [60, 177, 178])

5.1 RbCs

RbCs is a good candidate for ultracold molecule formation as condensates of both Rb and Cs have been successfully produced, as discussed in the previous Chapter. Table 5.1 shows the beneficial properties of ultracold RbCs molecules. The ground state of RbCs has a relatively small rotational constant, $B_{\mathrm{rot}} = 1.66 \times 10^{-2}$ cm^{-1}, and therefore a small electric field is required to achieve E_{crit}.

Additionally, ultracold-scattering calculations require highly accurate scattering potentials. In the case of RbCs highly accurate potentials were determined in Ref. [118], and these potentials are used for all RbCs calculations in this Thesis. The singlet and triplet potential curves, and the parameters of $\lambda(R)$, were fitted to experimental results, of both Feshbach resonance positions and bound-state measurements on ^{87}RbCs, to produce high-accuracy potentials [118]. The potentials were ‘mass-scaled’, as described for rubidium, for use in ^{85}RbCs scattering calculations. The change in reduced mass between the two isotopes of rubidium shifts the bound-state energy levels in both the singlet and triplet wells; this effect, combined with the different hyperfine structure, results in drastically different scattering length behaviours for the two species.

5.1.1 ^{85}RbCs

In the following sections scattering and bound-state calculations on ^{85}RbCs are presented. The calculated results are compared to experimental findings from Feshbach spectroscopy on the system, and the outlook for molecule formation is discussed. The theoretical calculations presented in this Section are discussed alongside experimental results obtained by Simon Cornish's group at Durham.

5.1.1.1 Resonances and bound states in the s-wave incoming channel

The hyperfine splitting of ^{85}Rb is smaller than that of ^{133}Cs, $\Delta E_{\rm hfs}^{\rm Rb} = 3.04$ GHz and $\Delta E_{\rm hfs}^{\rm Cs} = 9.19$ GHz, therefore the order of the hyperfine manifolds, with increasing energy, are $(f_{\rm Rb}, f_{\rm Cs})$ = (2,3), (3,3), (2,4) and (3,4). The lowest-energy hyperfine sublevel of ^{85}RbCs is the $(f, m_f) = (2, 2) + (3, 3)$ state; the s-wave incoming scattering channel therefore has $M_{\rm tot} = 5$. Coupled-channel scattering calculations are performed for this $M_{\rm tot}$, including $L = 0$ and 2 basis functions, using MOLSCAT [110], as described in Sec. 2.5.2. Calculations are carried out with a fixed-step log-derivative propagator [105] from 0.3 nm to 1.9 nm and a variable-step Airy propagator [142] from 1.9 nm to 1,500 nm. The wavefunctions are matched to their long-range solutions, the Ricatti-Bessel functions, at 1,500 nm to find the S-matrix elements, and hence the scattering length from Eq. (2.2.2).

The background scattering length of the ground-state channel is 15 a_0 and there is a rich Feshbach structure. Between 0 and 100 G, 32 resonances are predicted in the s-wave scattering length. Of these resonances 5 are caused by $L = 0$ bound states and the other 27 are caused by $L = 2$ bound states. The calculated s-wave scattering length is shown in the top panel of Figure 5.4 and the binding energies of the near-threshold molecular states responsible for the resonances are shown in the lower panel. An expanded view of the highest-lying-bound states is shown in Fig. 5.5. The interaction of the bound states, which cause the resonances, with each other provides important information about which states Feshbach molecules can be produced in. The resonance positions are given in Table 5.2, along with their widths.

The small background scattering length causes wide resonances, due to the definition of

Δ. This causes complications in fitting the widths of the resonances at 109 G and 642 G via Eq. (2.3.4), as the two resonances overlap with each other. The theoretical widths of the resonances at 109 G and 642 G are instead given by the difference between the resonance pole position, B_0, and the closest zero-crossing of the scattering length following the resonance pole, B_*. The widths of the other resonances in Table 5.2 are calculated by fitting to Eq. (2.3.4). For an exact fit to all the overlapping resonances of a system a more complex model is required which takes into account the interference effects caused by the overlapping resonances [179]. The wide resonances provide important regions where the scattering length can be tuned, allowing precise control over the interatomic interactions which dictate the miscibility of the atomic condensates and can be of use in studies of Efimov physics in heteronuclear systems. The narrow resonances can be used for molecule formation through magnetoassociation.

In ^{85}RbCs the singlet and triplet scattering lengths calculated on the potentials of Ref. [118] are $a_{\rm S} = 585.6\ a_0$ and $a_{\rm T} = 11.27\ a_0$ respectively. Due to the large difference in scattering length, and corresponding difference in bound-state energy levels, the singlet and triplet vibrational levels are very strongly mixed. This makes identification of the vibrational quantum number of the bound states impossible. The first five vibrational levels of the singlet well that appear below the $(2,2) + (3,3)$ threshold are $E_{\nu,S=0} = -0.2$, -196.2, -1273.4, -4002.9 and -9179.8 MHz. The first five vibrational levels of the triplet well are $E_{\nu,S=1} = -68.8$, -761.4, -2834.2, -7052.9 and -14182.3 MHz. The F state quantum numbers are obtained by performing calculations using the $|(f_a, f_b)FM_{\rm F}\rangle$ basis set and restricting the F quantum number, as shown in Fig. 5.1. The resonances are assigned approximate F quantum numbers based on their low-field assignments, although as the deviations between the states of Fig. 5.4 and the restricted basis set results of Fig. 5.1 show the F quantum number is not exact at high field. An attempt was made to assign (f_a, f_b) quantum numbers by studying the patterns of the F bound states at zero-field. The (3,4) manifold will give rise to bound states of $F = 7, 6, 5, 4, 3, 2, 1$ states although some of these will be restricted by our choice of $M_{\rm tot}$. Likewise the (2,4) manifold will give rise to bound states of $F = 6, 5, 4, 3, 2$, the (3,3) manifold will give rise to bound states of $F = 6, 5, 4, 3, 2, 1, 0$, and the (2,3) manifold will give rise to bound states of $F = 5, 4, 3, 2, 1$. In Fig. 5.4 the states originating between -1.8 and -2.6 GHz correspond to the (3,4) manifold and the states originating between -0.7 and -0.8 GHz correspond to the (2,3) manifold. The states originating above -0.3 GHz are strongly mixed with

Experiment		Theory							
B_0	δ	Assignment				B_0	B_*	Δ	a_{bg}
(G)	(G)	L_{i}	L	F	M_F	(G)	(G)	(G)	(bohr)
		s	2	5	3	3.1	3.1	5×10^{-5}	27.5
		s	2	5	4	4.27	4.27	3×10^{-4}	27.8
		s	2	5	5	6.8	6.8	9×10^{-4}	28.6
		s	2	3	3	66.36	66.36	0.002	71.6
		s	2	4	3	77.51	77.52	0.01	93.6
		s	2	5	3	82.75	82.75	1×10^{-4}	115
107.13(1)	0.6(2)	*s*	0	5	5	109.28	161.78	53	9.6
112.6(4)	28(5)	*s*	6	6	6	112.29	112.12	−0.2	−628
		s	2	4	4	114.33	114.21	−0.1	−246
		s	2	6	5	117.4	117.35	−0.05	−169
		s	2	6	4	128.29	128.28	−0.005	−139
		s	2	6	3	131.09	131.09	-6×10^{-4}	−121
		s	2	5	4	141.87	141.87	−0.001	−78.3
187.66(5)	1.7(3)	*s*	0	6	5	187.07	182.97	−4.0	−30.4
370.39(1)	0.08(4)	*s*	2	7	7	370.41	374.31	4.0	1.57
395.20(1)	0.08(1)	*s*	2	7	6	395.11	395.56	0.4	3.4
		s	2	7	5	425.11	425.16	0.04	6.1
		s	2	7	4	460.4	460.4	0.004	9.4
		s	0	7	5	477.47	477.48	0.008	11.2
		s	2	6	6	494.08	494.08	0.003	13.1
		s	2	7	3	501.68	501.68	4×10^{-5}	14.1
		s	2	6	5	525.86	525.86	1×10^{-4}	17.8
		s	2	6	4	563.66	563.66	0.001	27.8
		s	2	5	5	568.62	568.66	0.04	29.8
577.8(1)	1.1(3)	*s*	0	6	5	578.37	578.71	0.3	32.2
		s	2	6	3	607.32	607.32	1×10^{-5}	57.5
		s	2	5	4	625.29	625.3	0.01	123
641.8(3)	6(2)	*s*	0	5	5	642.35	901.35	259	9.6
		s	2	5	3	660.61	660.61	−0.002	−96.1
		s	2	4	4	665.89	665.89	-6×10^{-4}	−74.5
		s	2	4	3	691.73	691.73	−0.002	−33.7
		s	2	3	3	708.7	708.68	−0.02	−23.9

Table 5.2: Full listing of s-wave Feshbach resonances for ^{85}Rb $|2,+2\rangle$ + ^{133}Cs $|3,+3\rangle$ in the field range 0 to 1000 G. The experimental errors δ are statistical uncertainties resulting from the fits as described in the text. Additional systematic uncertainties of 0.1 G and 0.5 G apply to the experimental resonance positions in the field ranges 0 to 400 G and 400 to 1000 G respectively.

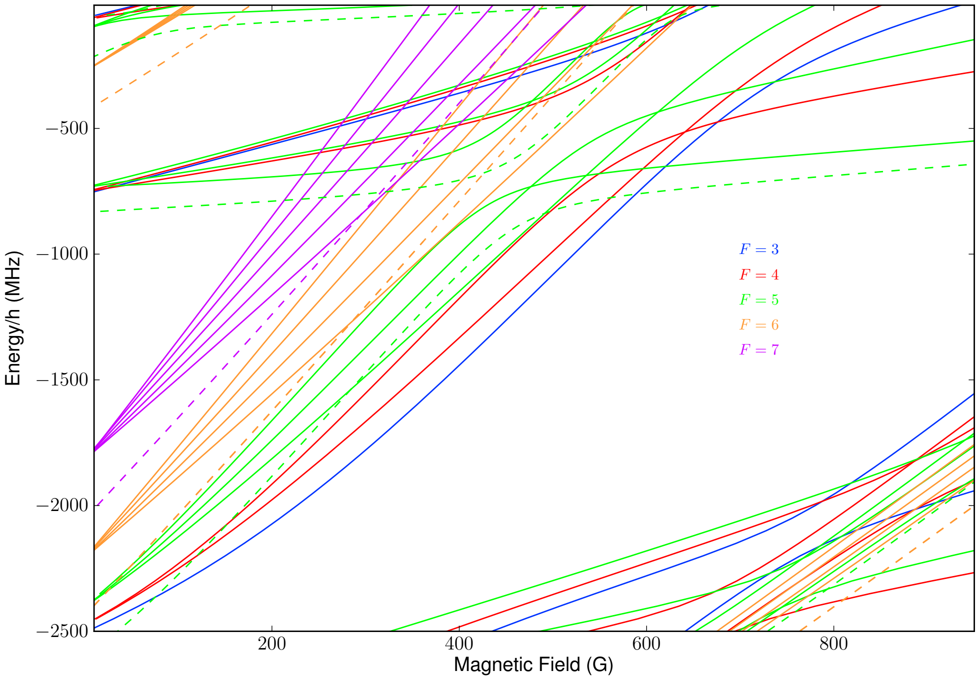

Figure 5.1: The bound states of ^{85}RbCs calculated by restricting the F quantum number using the $|(f_a, f_b)F, M_F\rangle$ basis set. Calculations were performed using $L = 0$ (dashed lines) and 2 (solid lines) states. The states are coloured according to their F quantum number. As F is not an exact quantum number the bound states shown are not the true bound states of the system. They are almost exact at low field but deviate significantly from the true states at high field.

a set of states above threshold that cannot be identified. Additionally the states which cross threshold between 400 and 900 G are mixed with a different and unidentified (f_a, f_b) manifold above threshold. Due to these unknown factors the (f_a, f_b) assignments are not given in Table. 5.2.

Seven of the predicted resonances, in the s-wave scattering length, were confirmed experimentally in Ref. [75]. Details of the experimental set-up can be found in Ref. [178,180]. A cloud of each species is prepared in the ground state and held within a dipole trap. In previous experiments the location of Feshbach resonances has been determined by an observation of atom loss at a fixed magnetic field. In the case of ^{85}RbCs a different method is possible as because of the small background scattering length the species do not thermalise with each other off resonance. The Cs trap is ~ 1.35 times deeper than the Rb trap, due to their different polarisablities, therefore the two gases are at different temperatures after the evaporation stage. The ^{85}Rb temperature after evaporation is 1.50(3) μK and the Cs temperature is 2.4(1) μK. When the magnetic field is used to tune

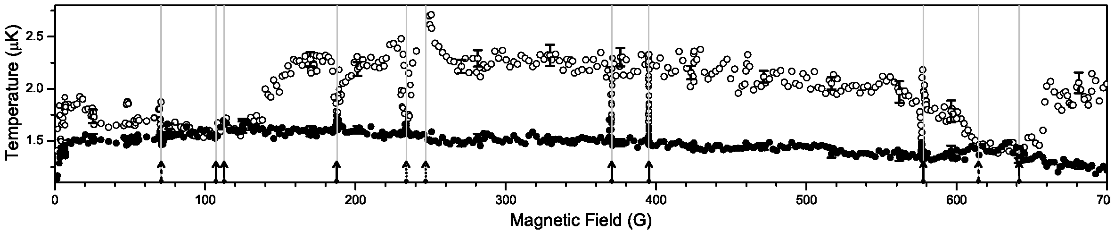

Figure 5.2: Temperature data for a mixture of ^{85}Rb (closed circles) and ^{133}Cs (open circles) in the (2,+2) and (3,+3) state, respectively, evaporated at different magnetic bias fields from 0 to 700 G. The positions of observed Feshbach resonances are marked with arrows, where solid (dashed) arrows mark s-wave (p-wave - see Sec. 5.1.1.2) resonances. The dotted arrows mark features generated by the dipole trap lasers (see Sec. 5.1.1.3). The standard deviation at representative magnetic fields is shown with error bars.

the scattering length to a value $a > 60\ a_0$ then interspecies interactions thermalise the two species. To locate resonances the evaporation process is undertaken at varying magnetic fields between $0 - 700$ G and thermalisation of the two species is used to detect the location of Feshbach resonances. The experimental measurements from a coarse magnetic field scan are shown in Fig. 5.2. As ^{85}Rb, Cs and ^{85}RbCs all have rich Feshbach structures in the magnetic field range examined, it is important to distinguish intra and interspecies resonances. Figure 5.3 shows experimental measurements for the temperature of both clouds and the atom number of ^{85}Rb around an intraspecies resonance at 368.8 G and an interspecies resonance at 370.4 G. At the intraspecies resonance there is a peak in temperature for ^{85}Rb and a drop in atom number but there is no effect on the temperature of the Cs cloud. At the interspecies resonance there is a drop in atom number for ^{85}Rb and a peak in temperature for ^{85}Rb with a corresponding drop in temperature for Cs. The experimentally determined widths and positions of the resonances, found in the s-wave scattering length, are given in Table 5.2. The widths and positions are determined by the same methods described in Sec. 4.1. The resonances found correspond to most of the wider theoretically predicted resonances, especially those at lower fields. The discrepancy in theoretical and experimental measurements of B_0 for the resonances around 109 G occurs because not all the resonances in this region can be resolved experimentally.

5.1.1.2 Resonances and bound states in the p-wave incoming channel

In higher-temperature experiments, although the s-wave scattering regime dominates the interaction behaviour, resonances in higher L incoming channels can also be seen. The

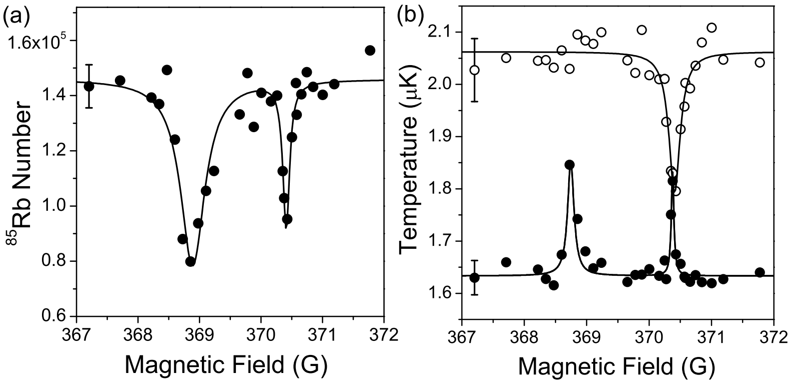

Figure 5.3: An intraspecies ^{85}Rb resonance at 368.78(3) G neighbouring an interspecies resonance at 370.39(1) G. Closed (open) symbols indicate ^{85}Rb (^{133}Cs) data. (a) Loss of ^{85}Rb reveals both resonances. (b) Temperature data allows the resonances to be distinguished as intra- or interspecies. The ^{133}Cs temperature is unchanged at the ^{85}Rb alone resonance in contrast to the interspecies resonance at higher field due to interspecies collisions causing sympathetic cooling. Error bars show the standard deviation for multiple control shots at a specific magnetic field.

centrifugal barrier height is given by

$$V_L(r_{\text{barrier}}) = \left(\frac{\hbar^2 L(L+1)}{2\mu}\right)^{3/2} (54\ C_6)^{-1/2}\,. \tag{5.1.1}$$

For ^{85}RbCs the barrier heights are $V_{L=1} = 55\ \mu$K, $V_{L=2} = 290\ \mu$K and $V_{L=3} = 810\ \mu$K; however, resonances in these channels can appear at lower temperatures due to quantum tunnelling effects.

Scattering calculations were performed for the p-wave incoming channel at 1 μK, including $L = 1, 3$ (a p,f-basis) states, at collision energies of $E_{\text{coll}} = 1\ \mu$K. This collision energy is close to the corresponding temperature measured in the experimental set-up. The bound states relative to the lowest energy incoming threshold were calculated using a $L = 1$ basis set. The calculated p-wave scattering volumes are shown in Fig. 5.6; there are three separate components corresponding to the projection of the L quantum number, $M_L = -1$, 0 and 1. The bound states causing the resonances due to $L = 1$ states are also shown as well as the M_L quantum number of the bound states. The background scattering volumes of the $M_L = \pm 1$ are the same, but there are resonances in different locations for each M_L. The background scattering volume of the $M_L = 0$ channel is significantly different.

Two of the predicted p-wave resonances are observed experimentally. The experimental measurements and theoretical predictions are shown in Table 5.3. The two resonances which are observed experimentally have calculated widths > 6 G; all other resonances in

Experiment		Theory		
B_0 (G)	Δ (G)	B_0 (G)	Δ (G)	L
70.68(4)	0.8(1)	70.54	-12	1
614.8(3)	1.1(4)	614.98	-7	1

Table 5.3: Experimentally observed p-wave Feshbach resonances in ^{85}RbCs.

this channel have calculated widths < 0.3 G. A complete list of the resonances calculated in the p-wave incoming channel can be found in Appendix B.

5.1.1.3 Dipole-trap induced features

In the course of the ^{85}RbCs experiment an additional two loss features were observed experimentally that were not predicted by theory. These resonances were shown to be artifacts of the dipole trap. The features were measured at 233.9(2) G and 246.5(3) G [178], and are responsible for the large dip in atom number around these field values (marked by dotted arrows) in Fig. 5.2. It was determined that these features only appeared when the dipole lasers, which are detuned from each other by 100 MHz, have perpendicular polarisations. It was further determined that when the dipole lasers had parallel polarisations the features could be induced by applying a 100 MHz radio-frequency magnetic field perpendicular to the quantisation axis of the static magnetic field. Calculations of the position of bound states with $M_{\rm tot} = 4, 5$ and 6 within 100 MHz of the (2,+2)+(3,+3) state threshold show that around these magnetic field values coupling to both the $M_F = 4$ and $M_F = 6$ states is possible. Different polarisations of light allow for different couplings which explains the appearance and disappearance of the features.

5.1.1.4 Outlook for molecule formation

The two wide resonances at 112.2 and 642.1 G can be used to tune the interspecies interactions, giving precise control over the behaviour of the atomic mixtures. The resonances could also be used to study Efimov physics in heteronuclear systems. The many narrow resonances could be used for molecule formation, via magnetoassociation. The small interspecies background scattering length reduces the losses due to three-body collisions in ^{85}RbCs and allows for a good overlap of the atomic clouds. In the Durham group's experimental set-up, presented in Ref. [75], the phase-space density (PSD) of the two atomic clouds is not yet high enough to allow for efficient magnetoassociation. A new dipole trap set-up which increases the initial number of ^{85}Rb is being considered. With an increased PSD in each of the atomic clouds then the production of ^{85}RbCs Feshbach molecules should be possible. The agreement between the experimental and theoretical resonance predictions confirms the accuracy of the RbCs potential and validates the mass-scaling approach. The bound states shown in Fig. 5.5 provide a detailed map of the possible molecular states that could be reached via magnetoassociation.

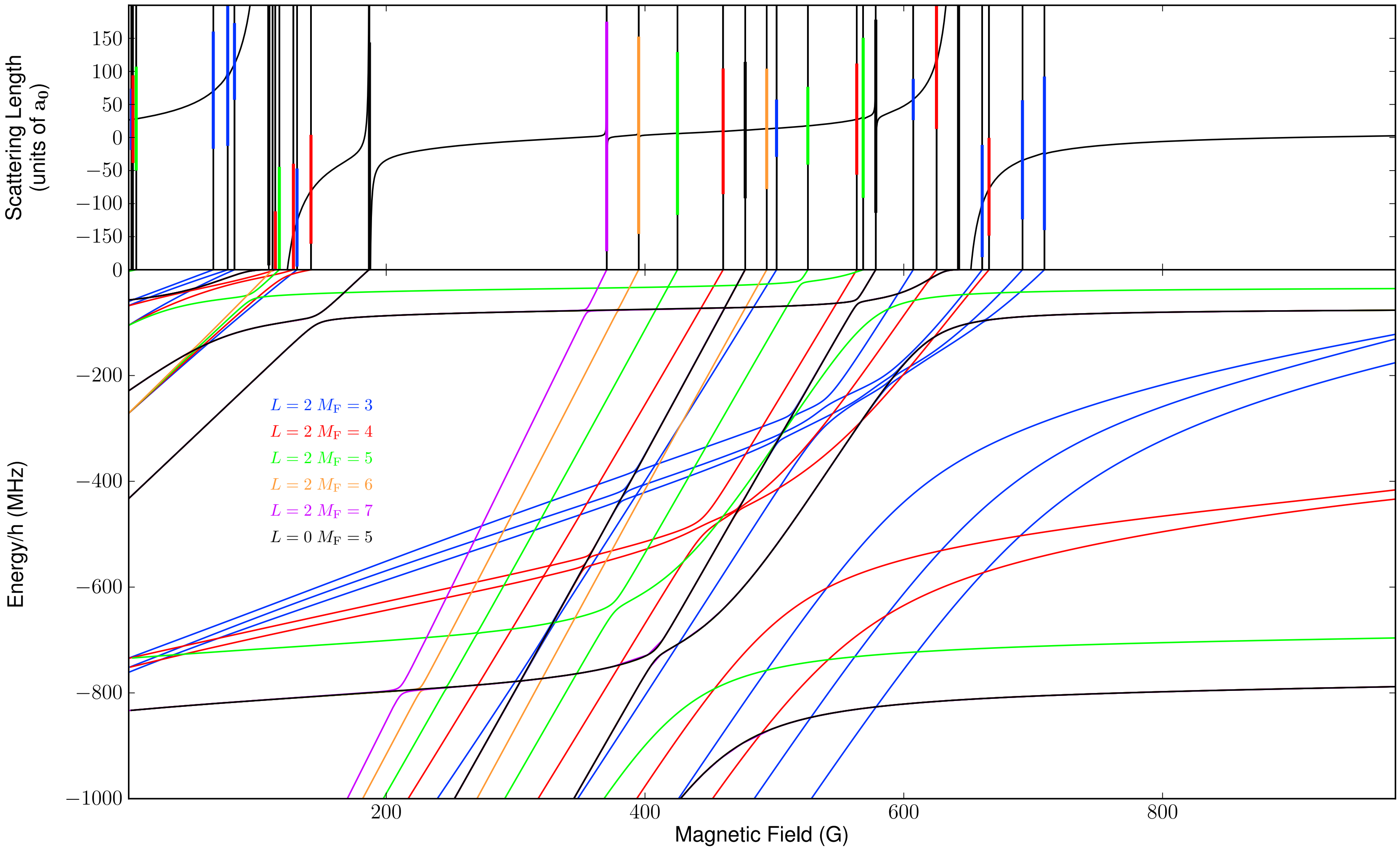

Figure 5.4: Top: The s-wave scattering length in the $(f, m_f) = (2,2) + (3,3)$ channel of ^{85}RbCs, with $L = 0$ and 2 functions. Bottom: The energies of weakly bound molecular states. Resonance widths greater than 1 μG are shown as vertical bars with lengths proportional to $\log_{10} \Delta/\mu$G.

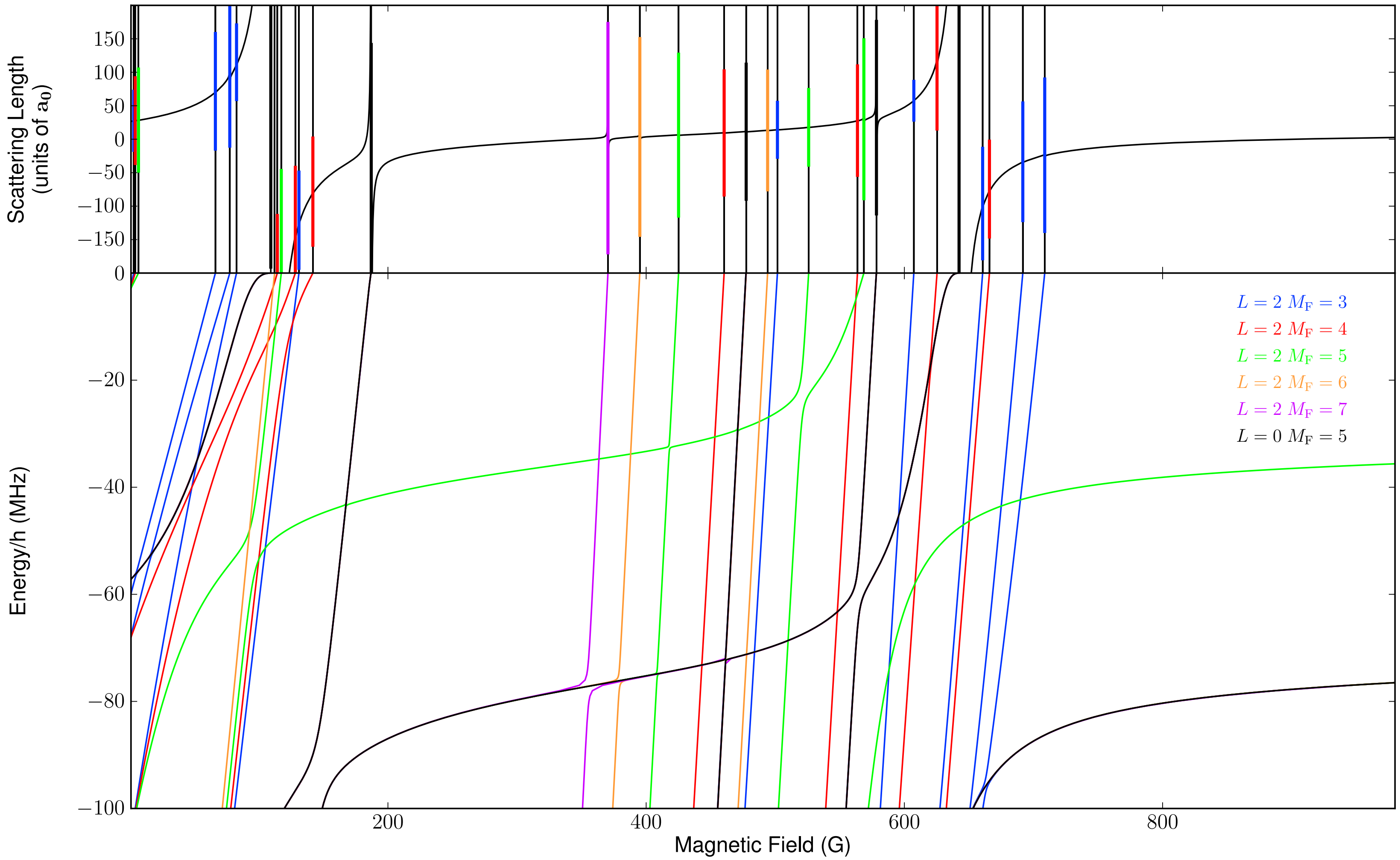

Figure 5.5: Top: The s-wave scattering length in the $(f, m_f) = (2, 2) + (3, 3)$ channel of ^{85}RbCs, with $L = 0$ and 2 functions. Bottom: The energies of very weakly bound molecular states. Resonance widths greater than 1 μG are shown as vertical bars with lengths proportional to $\log_{10} \Delta/\mu$G.

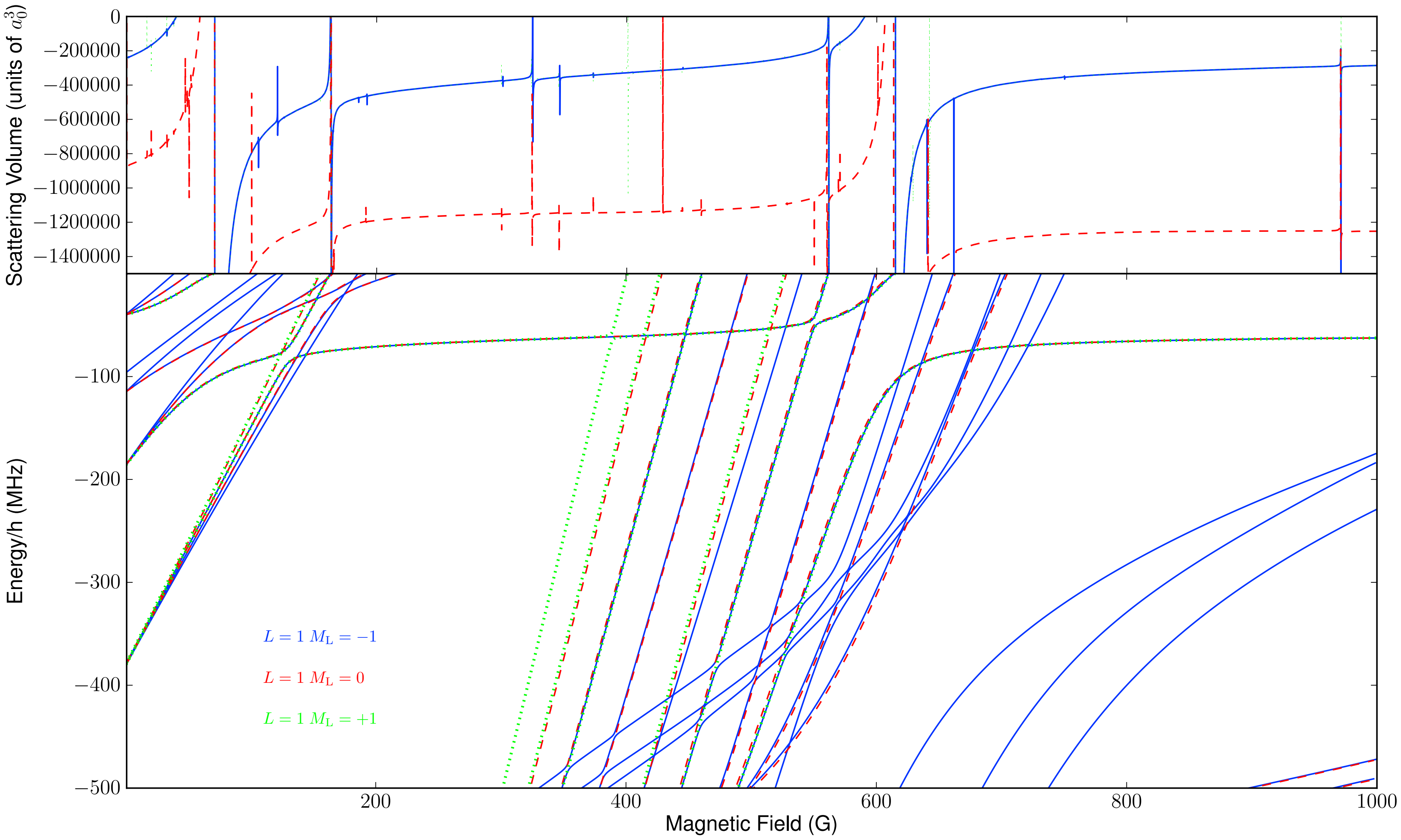

Figure 5.6: Top: The p-wave scattering volumes corresponding to the $(f, m_f) = (2, 2) + (3, 3)$ state of ^{85}RbCs, with $L = 1$ and 3 functions. Bottom: The energies of weakly bound states from $L = 1$.

5.1.2 ^{87}RbCs

The scattering and bound-state calculations on ^{87}RbCs presented in this Thesis are an extension of the work which had already been done as part of Ref. [118]. During this earlier work high-accuracy potentials were fitted to the results of experimentally determined resonance positions. Between 0 and 700 G, 30 resonances in incoming s- and p-wave channels were calculated and experimentally determined. The bound states calculated in this work were assigned $|n(f_{\rm Rb}, f_{\rm Cs})L(m_{\rm f_{Rb}}, m_{\rm f_{Cs}})\rangle$ quantum numbers, where $n = -1$ represents the least-bound state with respect to threshold. The following sections detail the extension of this earlier work to a set of higher-field resonances the results of which are presented in Ref. [76]. A route to ultracold molecule formation through magnetoassociation and STIRAP is also discussed, followed by the results of successful ultracold polar molecule formation [71].

5.1.2.1 Feshbach resonances and bound states

The results of calculations on the scattering length, and resonance positions and widths of ^{87}RbCs are included in this Thesis for completeness; however, they are not submitted as part of the degree material. A full list of calculated resonance positions and widths between $0 - 1000$ G, as detailed in Refs. [118] and [76], is given in Table 5.4. There are a total of 31 resonances predicted in the s-wave scattering length between 0 and 1000 G. Four of the resonances are caused by $L = 0$ bound states and the other 27 by $L = 2$ bound states. Table 5.4 also contains the experimentally measured resonance positions and widths from Refs. [118] and [76]. Data for an additional high-field resonance at 1115 G from Ref. [76] are also included.

The (f_a, f_b) quantum numbers of the bound states were identified during the work in Ref. [118]. Additionally a vibrational quantum number of the bound state was assigned. For near-dissociation levels a vibrational quantum n was assigned by comparing the zero-field hyperfine threshold energy levels to the energy levels of the "bin" boundaries which are derived from $E_{\rm vdW}$ [35]. Using these methods $|n(f_{\rm Rb}, f_{\rm Cs})L(m_{\rm f_{Rb}}, m_{\rm f_{Cs}})\rangle$ quantum numbers were assigned to each of the resonances listed in Ref. [118] and to the additional resonances between $700 - 1000$ G; all the resonances in Table 5.4 are listed with their quantum numbers assignments, as given in Refs. [118] and [76].

The scattering length and corresponding near-threshold bound states for the full calculation including $L = 0$ and 2 states, from 0 to 1000 G, are shown in Fig. 5.9. Fig.

5.10 shows the interactions between the highest-lying bound states just below threshold. This provides an important picture of which states can be reached following magnetoassociation. There is a high-lying bound state which runs parallel to threshold at -110 kHz this complicates magnetoassociation as molecules made in this state would have the same magnetic moment to mass ratio as the disassociated atoms and therefore could not be separated from the atomic clouds. Magnetoassociation can still be performed by transferring the molecules via avoided crossings in the bound-state energy levels to different molecular quantum states. Details of the magnetoassociation route used by Köppinger *et al.* [76] are given in Section 5.1.2.3.

5.1.2.2 Magnetic moments of bound states

The magnetic moment of a molecular state is an important quantity to know in order to trap the Feshbach molecules and separate them from the remaining atomic clouds. If the molecules have the same magnetic moment to mass ratio as the individual atoms then Stern-Gerlach separation of the molecules from the atoms is not possible. The magnetic moment of a molecular state is given by the slope of the bound state with energy $\mu = \partial E/\partial B$ where μ is the magnetic moment of the bound state. The magnetic moment of the molecular states that appear in the bound-state diagram are calculated by finite-difference methods on the bound-state data,

$$\mu(B') \approx \frac{E(B' + \Delta B) - E(B')}{\Delta B}, \tag{5.1.2}$$

where ΔB is a small step in magnetic field. The bound states near threshold and corresponding magnetic moments, between 180 and 185 G, are shown in Fig. 5.7. At an avoided crossing the bound state changes character and correspondingly has a change in magnetic moment; these transitions are smooth but not instantaneous.

5.1.2.3 Molecule formation

Details of the Durham group's experimental route to ultracold molecule formation, using the information from the previous sections, are presented in Refs. [76] and [71] and details of the Innsbruck group's experimental route are presented in Refs. [70], and only a brief summary is given here. Efficient magnetoassociation was performed in both experiments on the resonance at 197 G. This resonance is caused by the $|-6(2,4)d(2,3)\rangle$ molecular state, however, due to the least bound state at -110 kHz molecules formed at this resonance are

Experiment				Theory			
Durham		Innsbruck					
B_0 (G)	δ (G)	B_0 (G)	δ (G)	B_0 (G)	a_{bg} (bohr)	Δ (G)	Assignment
				87.25	355.0	1×10^{-4}	$-2(1,3)d(-1,3)$
				123.09	357.5	2×10^{-6}	$-2(1,3)d(0,2)$
181.55(5)		181.64(8)	0.27(10)	181.63	360.3	0.2	$-6(2,4)d(2,4)$
		185.34		185.24	343.0	1×10^{-5}	$-2(1,3)d(0,3)$
		189.66		189.47	353.7	3×10^{-5}	$-2(1,3)d(1,1)$
197.10(3)	0.1(1)	197.06(5)	0.09(1)	197.07	356.0	0.05	$-6(2,4)d(2,3)$
		217.34(5)	0.06(1)	217.33	358.3	0.009	$-6(2,4)d(2,2)$
		225.43(3)	0.16(1)	225.47	358.9	0.03	$-6(2,4)d(1,4)$
		242.29(5)		242.25	361.7	0.001	$-6(2,4)d(2,1)$
		247.32(5)	0.09(3)	247.28	361.9	0.02	$-6(2,4)d(1,3)$
		272.80(4)		272.81	369.9	3×10^{-4}	$-6(2,4)d(2,0)$
		273.76(4)		273.69	369.6	0.002	$-6(2,4)d(1,2)$
279.03(1)	0.11(1)	279.12(5)		279.02	369.5	0.03	$-6(2,4)s(2,2)$
		286.76(5)	0.09(3)	286.68	370.9	0.01	$-6(2,4)d(0,4)$
		308.44(5)		308.45	472.2	0.004	$-6(2,4)d(1,1)$
310.72(2)	0.70(3)	310.69(6)		310.71	374.4	0.6	$-6(2,4)s(1,3)$
		314.74(11)	0.60(4)	314.56	311.1	0.09	$-6(2,4)d(0,3)$
352.7(2)	2.9(5)	352.65(34)	0.18(10)	352.74	345.9	2.2	$-6(2,4)s(0,4)$
		381.34(5)	2.70(47)	353.57	−580.5	−0.001	$-6(2,4)d(0,2)$
		421.93(5)		381.28	321.1	0.02	$-6(2,4)d(-1,4)$
				408.63	334.4	2×10^{-4}	$-2(1,3)d(1,2)$
				422.04	337.4	0.002	$-6(2,4)d(-1,3)$
				552.75	346.6	6×10^{-7}	$-6(2,4)d(-2,4)$
				585.65	347.9	2×10^{-7}	$-5(2,3)d(2,0)$
				651.02	351.5	1×10^{-4}	$-5(2,3)d(2,1)$
				722.63	362.6	3×10^{-4}	$-5(2,3)d(2,2)$
790.2(2)	6.8(2)			791.79	343.5	4.2	$-5(2,3)s(2,2)$
				799.90	160.6	0.07	$-5(2,3)d(1,1)$
				808.02	250.2	0.005	$-5(2,3)d(2,3)$
				818.08	286.1	7×10^{-7}	$-3(1,3)d(-1,3)$
910.6(8)				909.35	332.7	0.006	$-5(2,3)d(1,2)$
1115.2(2)	10.0(6)			1116.55		9	$-5(2,3)s(1,3)$

Table 5.4: Full listing of s-wave Feshbach resonances for ^{87}Rb $|1,+1\rangle$ + ^{133}Cs $|3,+3\rangle$ in the field range from 0 to 1000 G. The theoretical widths are calculated as described in the text and the quantum number assignments correspond to $|n(f_{\mathrm{Rb}}, f_{\mathrm{Cs}})L(m_{f_{\mathrm{Rb}}}, m_{f_{\mathrm{Cs}}})\rangle$. The Innsbruck experimental data is taken from Ref. [118], the magnetic field uncertainties in these results arise from noise in atom number and an estimated field calibration error of 0.03 G.

Table 5.4 *(previous page)*: The Durham experimental data is taken from Ref. [76], the experimental errors δ are statistical uncertainties resulting from the fits, additional systematic uncertainties of 0.1 G and 0.5 G apply to the experimental resonance positions in the field ranges 0 to 400 G and 400 to 1200 G respectively.

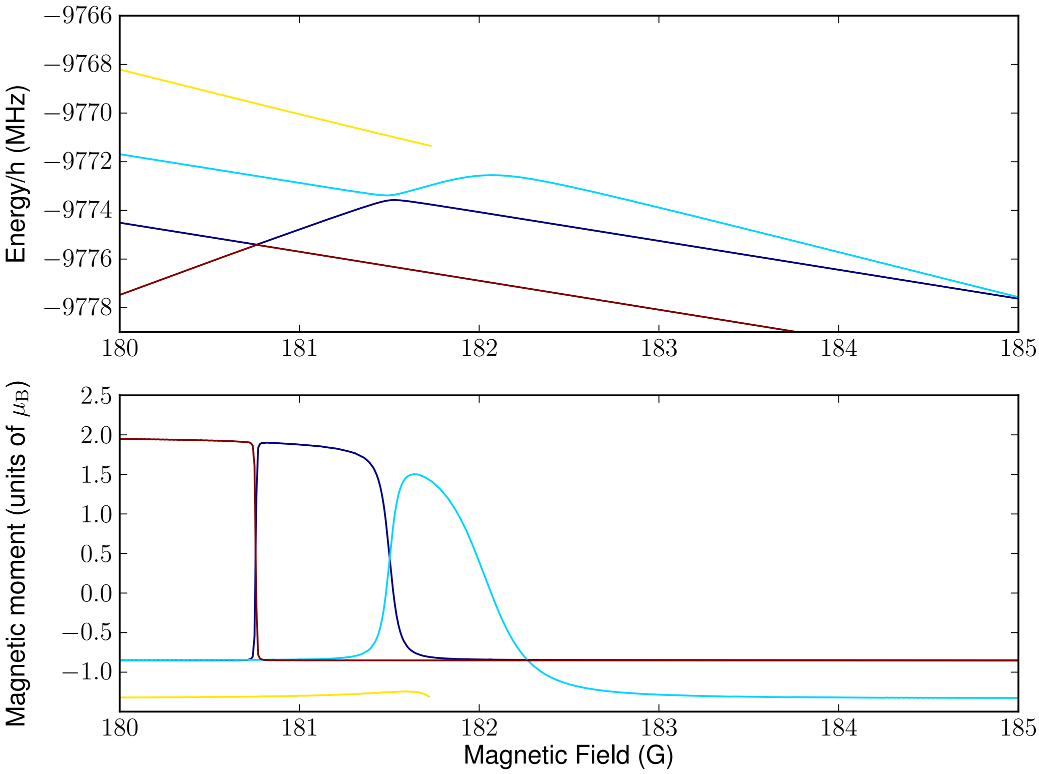

Figure 5.7: ^{87}RbCs: (top) Bound states of ^{87}RbCs, with $L = 0$ and 2 functions; (bottom) the magnetic moments of the bound states of the corresponding colour as shown in (top).

transferred directly into the $|-1(1,3)s(1,3)\rangle$ state. As discussed, Stern-Gerlach separation cannot be used to separate the molecules when they are in this state so the molecules are transferred, via a magnetic field sweep, to a state with a different magnetic moment. The path of the magnetoassociation sequence, and the molecular moments of the bound states, is shown in Fig. 5.8. Molecules are transferred to the $|-6(2,4)d(2,4)\rangle$ molecular state, which is a weak-field-seeking state, to the high-field-seeking state $|-2(1,3)d(0,3)\rangle$, using the avoided crossing around 181 G and -2.7 MHz. The probability of the molecules being transferred adiabatically (p) can be described by the Landau-Zener model $p = 1 - \exp\left(-\dot{B}_c/|\dot{B}|\right)$ [102] where $\dot{B}$ is rate of change of the magnetic field and

$$\dot{B}_c = \frac{2\pi V^2}{\hbar|\Delta\mu|}. \tag{5.1.3}$$

Calculations on the relevant bound states show that this avoided crossing has a coupling strength $V = 0.08$ MHz and $\Delta\mu = 3.7\ \mu_\mathrm{B}$. In the experiment at Durham up to ~ 5000 molecules are observed with an observed lifetime of 0.21(ms) [76].

To create ground-state molecules Feshbach molecules are transferred from their highly excited vibrational level to the ro-vibrational ground state via STIRAP. The Feshbach molecules are transferred from their weakly bound state, $|F\rangle$, to the ground state, $|G\rangle$, via coupling to an excited level of the $A^1\Sigma^+ + b^3\Pi$ manifold, $|E\rangle$ [71]. Details of the STIRAP methods used by both Durham and Innsbruck are presented in Refs. [71] and [70], respectively.

For the observation of strong interaction effects, in an ultracold gas, the dipole-dipole interaction energy must be comparable to, or greater than, the thermal energy. This requires a system of high PSD and with a large dipole moment. Experiments at Durham [71] have achieved a laboratory-frame dipole moment of 0.355(2)(4) D at an electric field of 765 Vcm^{-1}. These developments highlight the possibility of using stable ultracold molecular gases to observe strong dipolar interactions in the near future.

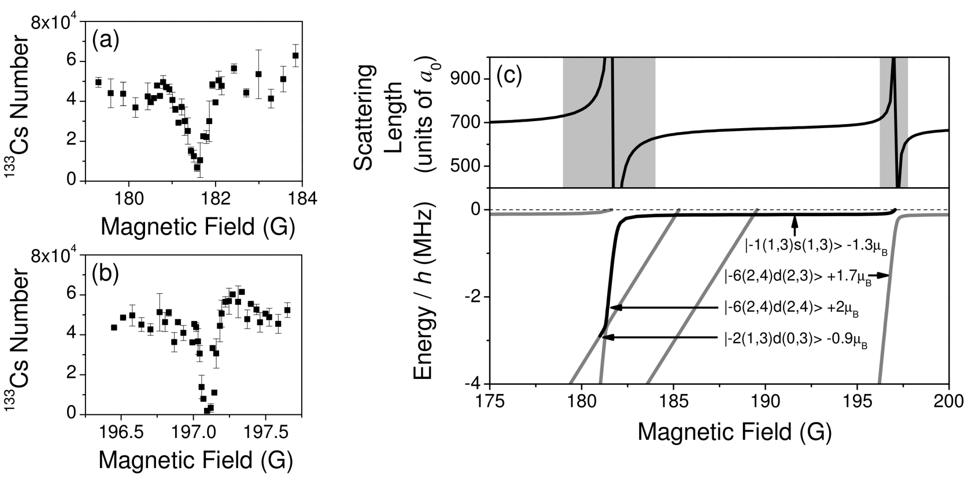

Figure 5.8: Experimental ^{87}RbCs magnetoassociation sequence from Ref. [76]. Experimental determination of the interspecies Feshbach resonances at (a) 181.55(5) G and (b) 197.10(3) G detected through loss in the ^{133}Cs atom number. (c) Upper panel: The ^{87}Rb^{133}Cs s-wave scattering length in the relevant magnetic field range. The grey shaded areas mark the field ranges shown in (a) and (b). Lower panel: The weakly bound molecular states relevant to the magnetoassociation sequence. Also shown are the magnetic moments for each bound state. Molecules are produced at the Feshbach resonance at 197.10(3) G and then transferred into the $|-2(1,3)d(0,3)\rangle$ state at 181 G following the path shown by the solid black line.

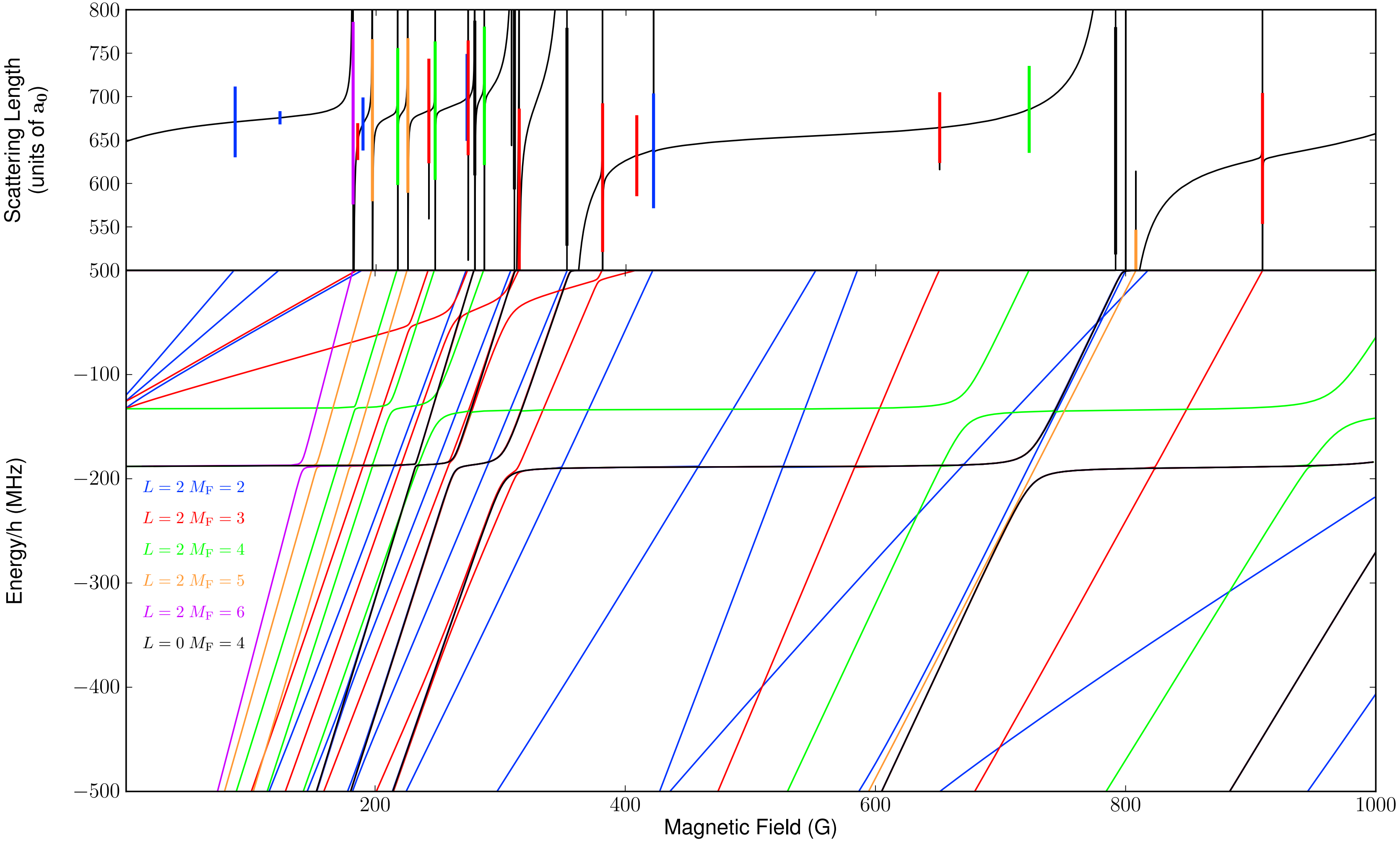

Figure 5.9: Top: The s-wave scattering length in the $(f, m_f) = (1, 1) + (3, 3)$ channel of ^{87}RbCs, with $L = 0$ and 2 functions. Bottom: The energies of weakly bound molecular states. Resonance widths greater than 1 μG are shown as vertical bars with lengths proportional to $\log_{10} \Delta/\mu$G.

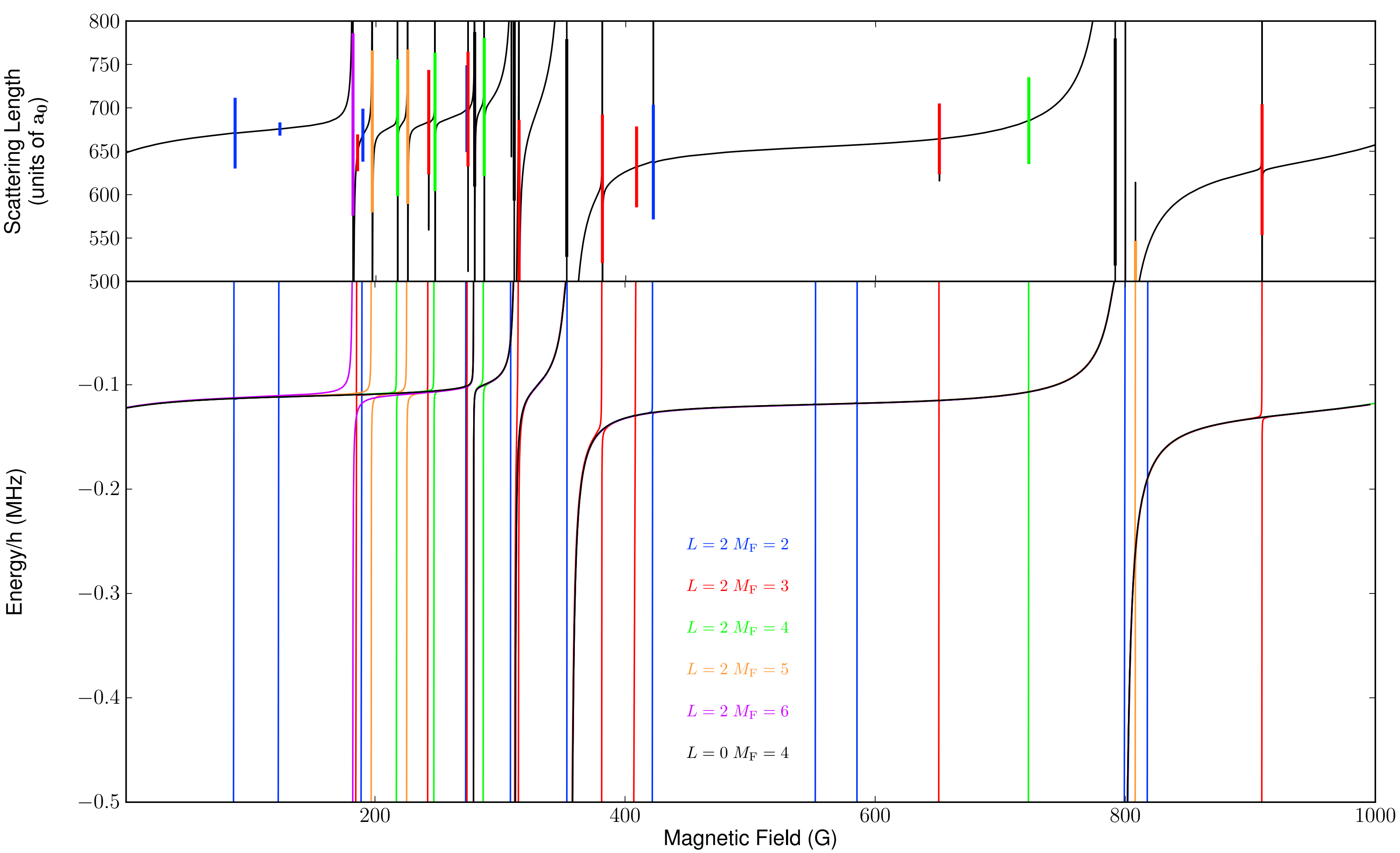

Figure 5.10: Top: The s-wave scattering length in the $(f, m_f) = (1, 1) + (3, 3)$ channel of ^{87}RbCs, with $L = 0$ and 2 functions. Bottom: The energies of very weakly bound molecular states. Resonance widths greater than 1 μG are shown as vertical bars with lengths proportional to $\log_{10} \Delta/\mu$G.

5.2 KCs

Other promising candidates for producing ultracold ground-state polar molecules are the isotopologues of KCs. Like RbCs, KCs is energetically stable to all possible two-body reactions. KCs also has a larger dipole moment than KRb or RbCs (1.92 D) [181]. There are three different isotopes of potassium, including bosonic and fermionic species, which can be used: ^{39}K, ^{40}K and ^{41}K. Each isotope requires a different ‘mass scaling’ of the potential and therefore will exhibit a unique scattering behaviour. The singlet and triplet potential curves used for KCs are taken from Ferber *et al.* [119]. Ferber *et al.* [119] carried out calculations to identify Feshbach resonances using an $L = 0$ basis set, we have extended these calculations to include $L = 0$ and 2 states. Unlike the RbCs potentials, these potentials have not been fitted to Feshbach resonances therefore they are not as accurate. Remaining uncertainties in the potentials may shift the resonances positions calculated in the following sections by a few Gauss, but the qualitative picture of the systems should be accurate.

5.2.1 ^{39}KCs

The hyperfine splitting of ^{39}K is smaller than that of ^{133}Cs therefore the order of the hyperfine manifolds, with increasing energy, is $(f_{\rm K}, f_{\rm Cs})$ = (1,3), (2,3), (1,4) and (2,4). The lowest-energy hyperfine sublevel of ^{39}KCs is the $(f, m_f) = (1, 1)+(3, 3)$ state; therefore, the s-wave incoming scattering channel has $M_{\rm tot} = 4$. Coupled-channel scattering calculations are performed for this channel, as described in Sec. 2.5.2. Calculations are carried out with a fixed-step log-derivative propagator [105] from 2.5 a_0 to 15 a_0 and a variable-step Airy propagator [142] from 15 a_0 to 15,000 a_0. The wavefunctions are matched to their long-range solutions, the Ricatti-Bessel functions, at 15,000 a_0 to find the S-matrix elements, and hence the scattering length from Eq. (2.2.2).

For heavy atoms it is known that second-order spin-orbit coupling provides an additional contribution to the dipolar spin-spin operator that has the same tensor form as the dipole-dipole term. This contribution dominates at short range for species containing Cs [120, 122] and has a large effect on the widths of resonances due to states with $L > 0$. The dipolar spin-spin operator of KCs, $\hat{V}^{\rm d}(R)$, takes the form described by Eq. (3.1.14), where λ is an R-dependent coupling constant. For both Cs$_2$ [122] and RbCs [118], electronic structure calculations showed that the second-order spin-orbit splitting can be represented by a biexponential form, so that the overall form of $\lambda(R)$ is

$$\begin{aligned}\lambda(R) &= E_{\mathrm{h}}\alpha^2\Big[A_{\mathrm{2SO}}^{\mathrm{short}}\exp\left(-\beta_{\mathrm{2SO}}^{\mathrm{short}}(R/a_0)\right) \\ &+ A_{\mathrm{2SO}}^{\mathrm{long}}\exp\left(-\beta_{\mathrm{2SO}}^{\mathrm{long}}(R/a_0)\right) + \frac{1}{(R/a_0)^3}\Big],\end{aligned} \tag{5.2.1}$$

where $\alpha \approx 1/137$ is the atomic fine-structure constant. The second-order spin-orbit coupling has not been calculated for KCs, but an estimate may be made from the values for Cs_2 and RbCs. It is physically reasonable to suppose that the coupling comes principally from the Cs atom(s) and (for chemically similar species) does not depend strongly on the identity of the other atom. Evaluating the second-order spin-orbit contribution to $\lambda(R)$ [118, 122] at the inner turning point of the triplet curve at zero-energy gives values per Cs atom within about 40% of one another for Cs_2 and RbCs. In the present work, we simply shifted the RbCs function inwards 0.125 a_0, to give the same value at the inner turning point for KCs as for RbCs. We thus use $\beta_{\mathrm{2SO}}^{\mathrm{short}} = 0.80$ and $\beta_{\mathrm{2SO}}^{\mathrm{long}} = 0.28$, as for RbCs [118], with $A_{\mathrm{2SO}}^{\mathrm{short}} = -45.5$ and $A_{\mathrm{2SO}}^{\mathrm{long}} = -0.032$. Figure 5.11 shows the scattering length for ^{39}KCs.

When only $L = 0$ basis functions are included (Fig. 5.11(a)), the scattering length shows 5 resonances below 1000 G. These agree within 1 G with those calculated by Ferber *et al.* [119]. When $L = 2$ basis functions are included, an additional 30 bound states cross threshold below 1000 G. These are colour-coded according to M_F in Fig. 5.11 (b) and (c). If only the long-range spin-spin coupling is included (the R^{-3} term in Eq. 5.2.1), the resonances due to d-wave states are quite narrow (Fig. 5.11(b)). However, if second-order spin-orbit coupling is included, most of them become significantly broader, as shown in Fig. 5.11(c) (note the logarithmic scale of the vertical bars used to indicate the resonance widths). Some of the resonances have widths suitable for use in molecule formation.

The scattering length and corresponding near-threshold bound states, for the full calculation including $L = 0$ and 2 basis functions and with spin-orbit coupling included, are shown in Fig. 5.12. The positions and widths of some of the broader resonances are given in Table 5.5, and a complete tabulation (all resonances, with and without second-order spin-orbit coupling for ^{39}KCs) is included in Appendix C. The effect of the spin-orbit contribution on the width of the resonances we calculate show that it is an important factor. Calculations on the other isotopes of KCs in the following sections all use the spin-orbit coupling described here.

B_0 (G)	Δ (G)	$a_{\rm bg}$ (bohr)	L	M_F
49.57	0.001	73.2	2	4
341.90	4.8	79.0	0	4
375.35	0.006	68.5	2	4
421.36	0.4	74.7	0	4
697.02	0.03	80.0	2	6
760.13	0.004	80.3	2	5
813.14	3×10^{-4}	81.0	0	4
860.52	0.05	82.0	0	4
907.54	0.02	92.7	2	3
915.56	1.2	80.1	0	4

Table 5.5: Listing of all s-wave Feshbach resonances and d-wave Feshbach resonances with widths > 1 mG for ^{39}KCs in the field range 0 to 1000 G.

5.2.2 ^{40}KCs

^{40}K is the only alkali-metal isotope with an ‘inverted’ hyperfine structure. It is a fermionic species with a nuclear spin of $i = 4$, giving atomic quantum numbers $f = 7/2$ and $9/2$. The larger of the two f values corresponds to the lower-energy manifold and the lowest-energy hyperfine sublevel, in a magnetic field, is the $(f, m_f) = (9/2, -9/2)$ state. The incoming s-wave scattering channel, for $(9/2, -9/2) + (3, +3)$ state has $M_{\rm tot} = -3/2$. Scattering and bound-state calculations are performed for this channel using the methods described in Sec. 5.2.1.

The background scattering length for this channel is $-40\ a_0$ and there is a very dense Feshbach structure. The scattering length and corresponding near-threshold bound states are shown in Fig. 5.13. There are 84 Feshbach resonances in the region from 0 to 1000 G. 14 of the resonances are caused by $L = 0$ bound states and the other 70 are caused by $L = 2$ bound states. There is a dense set of bound states which originate between -555 and -570 MHz at zero-field and cause a number of the resonances between 100 and 300 G. Most of the resonances in ^{40}KCs are incredibly narrow; the widest s-wave resonance has a width of 0.1 G, the widest d-wave resonances has a width of 0.01 G, and many of the resonances have widths < 1 nG. A tabulation of the calculated positions and widths of all s-wave resonances and d-wave resonances with $\Delta > 1$ mG is given in Table 5.6 and a complete list of all the resonances is given in Appendix C.

The narrowness of the resonances can be explained by the similarity in the singlet

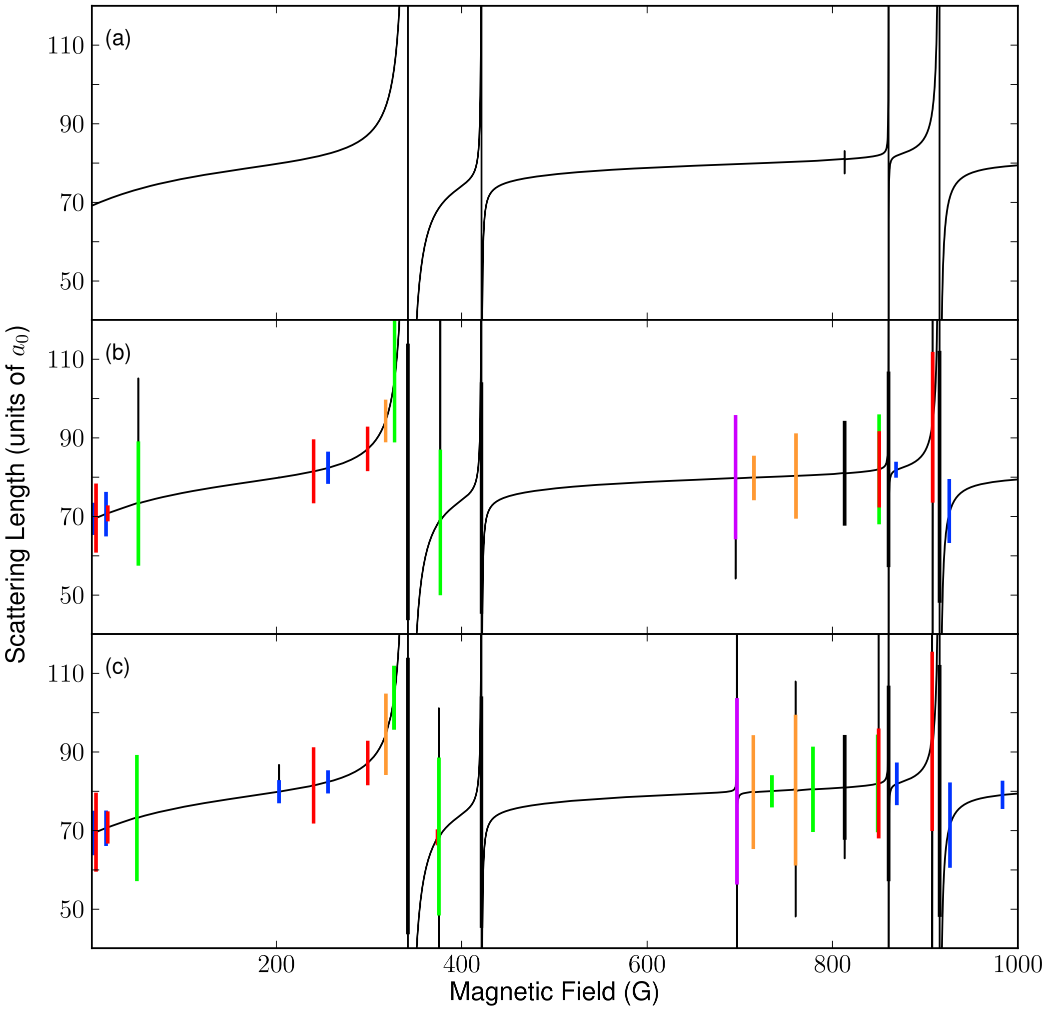

Figure 5.11: ^{39}K^{133}Cs: (a) $L = 0$ functions only; (b) $L = 0$ and 2 functions, but 2nd-order spin-orbit coupling not included; (c) scattering length with $L = 0$ and 2 functions, and approximate model of 2nd-order spin-orbit coupling included. Resonance widths greater than 1 μG are shown as vertical bars with lengths proportional to $\log \Delta/\mu$G.

and triplet scattering lengths, $a_{\rm S} = -52\ a_0$ and $a_{\rm T} = -41\ a_0$ respectively, which directly reduces the strength of $L = 0$ resonances and indirectly reduces the strength of $L = 2$ resonances [182]. A similar effect is seen in LiNa [183] and in ^{87}Rb [182, 184]. There are still some resonances, however, which are wide enough for molecule formation. Fig. 5.14 shows the interactions between the highest-lying bound states just below threshold.

B_0 (G)	Δ (G)	$a_{\rm bg}$ (bohr)	L	M_F
57.59	< 1 nG	-40.3	0	$-3/2$
69.85	< 1 nG	-40.3	0	$-3/2$
89.01	< 1 nG	-40.3	0	$-3/2$
122.77	< 1 nG	-40.3	0	$-3/2$
192.18	-0.001	-40.2	2	$-3/2$
196.71	-3×10^{-7}	-40.2	0	$-3/2$
215.96	-0.01	-40.2	2	$-1/2$
230.24	< 1 nG	-40.2	0	$-3/2$
234.15	< 1 nG	-40.1	0	$-3/2$
239.55	< 1 nG	-40.1	0	$-3/2$
246.44	-4×10^{-7}	-40.0	0	$-3/2$
254.52	-1×10^{-4}	-39.8	0	$-3/2$
264.34	-0.1	-40.3	0	$-3/2$
379.60	-0.002	-40.3	2	$-5/2$
470.25	-0.01	-40.2	0	$-3/2$
677.44	< 1 nG	-40.2	0	$-3/2$
902.84	< 1 nG	-40.2	0	$-3/2$

Table 5.6: Listing of all s-wave Feshbach resonances and d-wave Feshbach resonances with widths > 1 mG for ^{40}KCs in the field range 0 to 1000 G.

5.2.3 ^{41}KCs

^{41}K has the same nuclear spin as ^{39}K and therefore a similar hyperfine structure. The incoming s-wave scattering channel, for $(f, m_f) = (1, +1) + (3, +3)$, has $M_{\rm tot} = 4$. Scattering and bound-state calculations are performed for this channel using the methods described in Sec. 5.2.1. The singlet and triplet scattering lengths are $a_{\rm S} = -73\ a_0$ and $a_{\rm T} = 205\ a_0$, respectively.

The background scattering length for this channel is 200 a_0 and there is a rich Feshbach structure. The scattering length and corresponding near-threshold bound states are shown in Fig. 5.15. The Feshbach resonances in ^{41}KCs are clustered into two groups, one group is between 0 and 200 G and the other group is between 600 and 1000 G. There are 42 resonances in total and 27 occur below 130 G. Seven of the resonances are caused by s-wave states and two of these have widths > 1 G; the other 35 resonances are caused by d-wave states and the widest of these has $\Delta = 0.03$ G. A list of the calculated positions and widths of all s-wave resonances and d-wave resonances with $\Delta > 1$ mG is given in

Table 5.7 and a complete list of all the resonances is given in Appendix C.

Some of the narrow resonances below 130 G offer good prospects for molecule formation. There are three resonances around 30 G where the intraspecies scattering lengths of ^{41}K and Cs mean that both can be cooled to degeneracy. The resonances have similar widths to the resonance at 19.8 G in Cs which has been used successfully to create Cs_2 molecules [170, 185, 186]. Although the combination of intra- and interspecies scattering lengths at these fields would lead to phase separation of the condesates, molecules could still be formed by the use of thermal gases, as in ^{87}RbCs [76]. Fig. 5.16 shows the interactions between the highest-lying bound states just below threshold. A further discussion of the required scattering length combinations for optimal routes to magnetoassociation is presented in the following Section.

B_0 (G)	Δ (G)	a_{bg} (bohr)	L	M_F
23.89	0.02	193.0	2	6
25.68	0.03	189.3	2	5
28.41	0.007	188.7	2	4
87.38	0.003	201.6	2	4
90.10	0.008	201.1	2	5
94.28	0.001	201.5	2	3
109.86	0.002	204.5	2	2
111.04	4.00×10^{-4}	204.3	0	4
113.93	3.00×10^{-4}	205.3	0	4
120.89	0.02	206.0	0	4
168.19	0.6	262.6	0	4
171.20	1.2	151.3	0	4
861.03	0.03	247.7	2	5
884.92	4.1	211.4	0	4
966.89	0.1	201.5	0	4

Table 5.7: Listing of all s-wave Feshbach resonances and d-wave Feshbach resonances with widths > 1 mG for ^{41}KCs in the field range 0 to 1000 G.

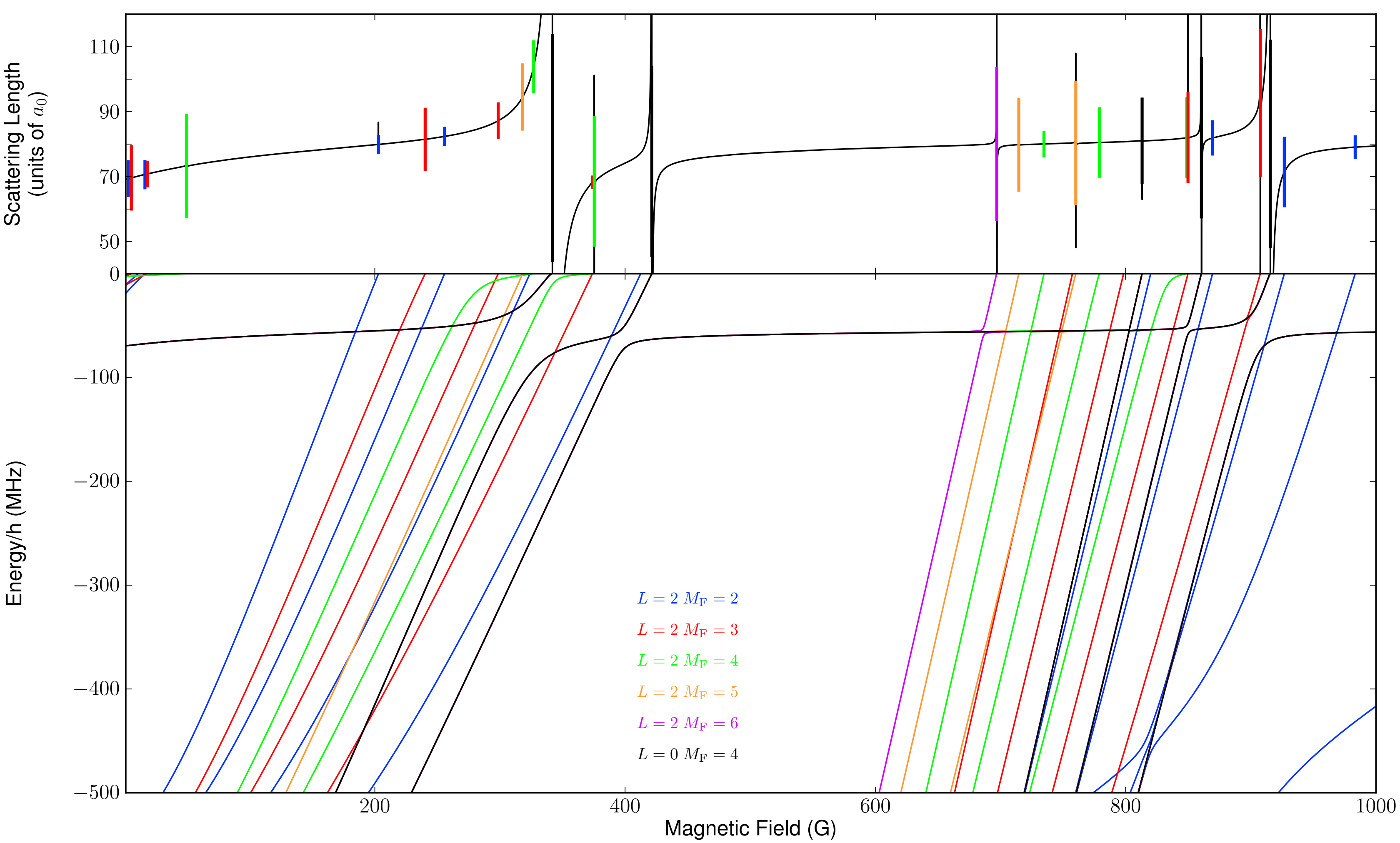

Figure 5.12: Top: The s-wave scattering length in the $(f, m_f) = (1, 1) + (3, 3)$ channel of ^{39}KCs, with $L = 0$ and 2 functions. Bottom: The energies of weakly bound molecular states. Resonance widths greater than 1 μG are shown as vertical bars with lengths proportional to $\log_{10} \Delta/\mu$G.

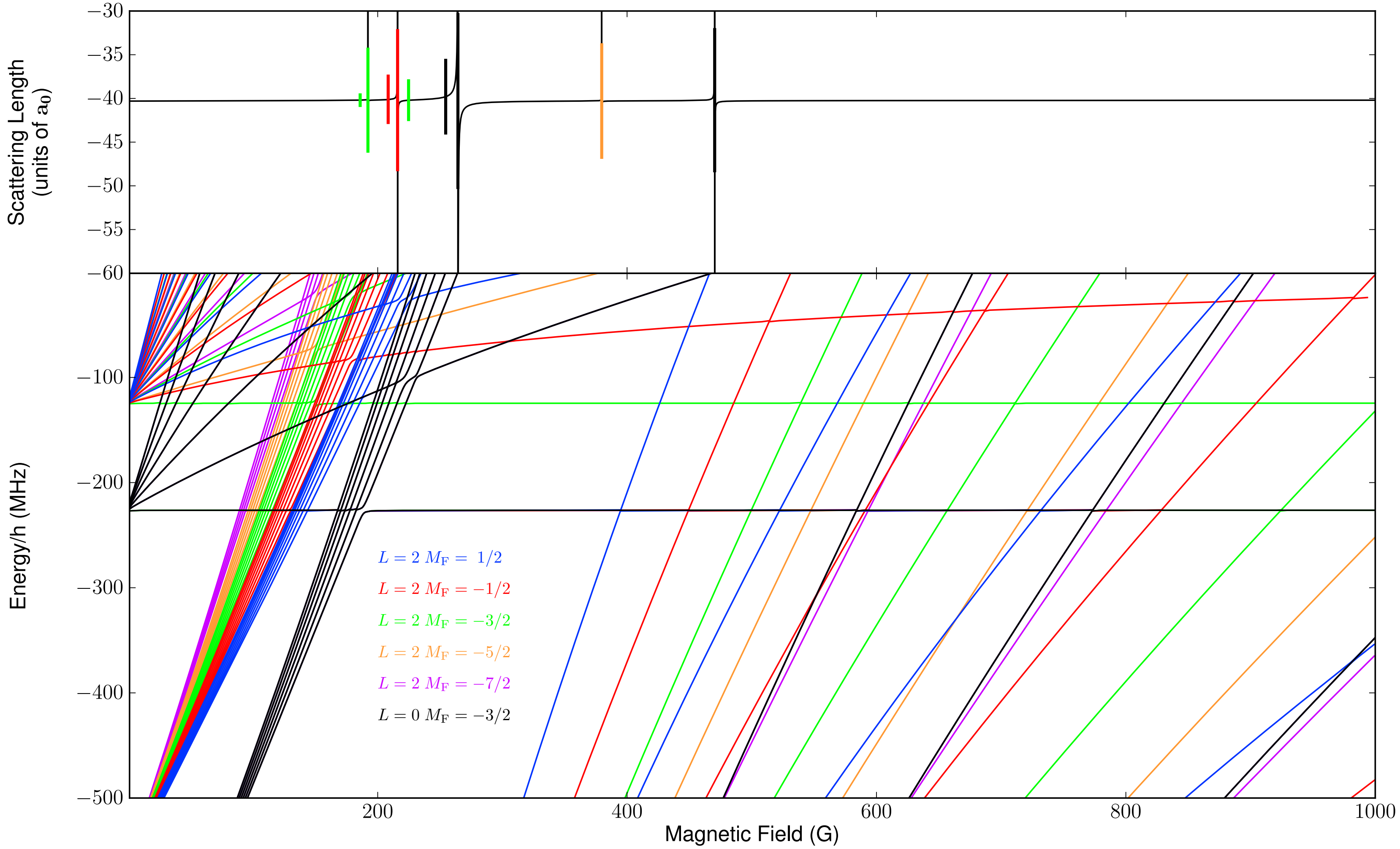

Figure 5.13: Top: The s-wave scattering length in the $(f, m_f) = (9/2, -9/2) + (3, 3)$ channel of ^{40}KCs, with $L = 0$ and 2 functions. Bottom: The energies of weakly bound molecular states. Resonance widths greater than 1 μG are shown as vertical bars with lengths proportional to $\log_{10} \Delta/\mu$G.

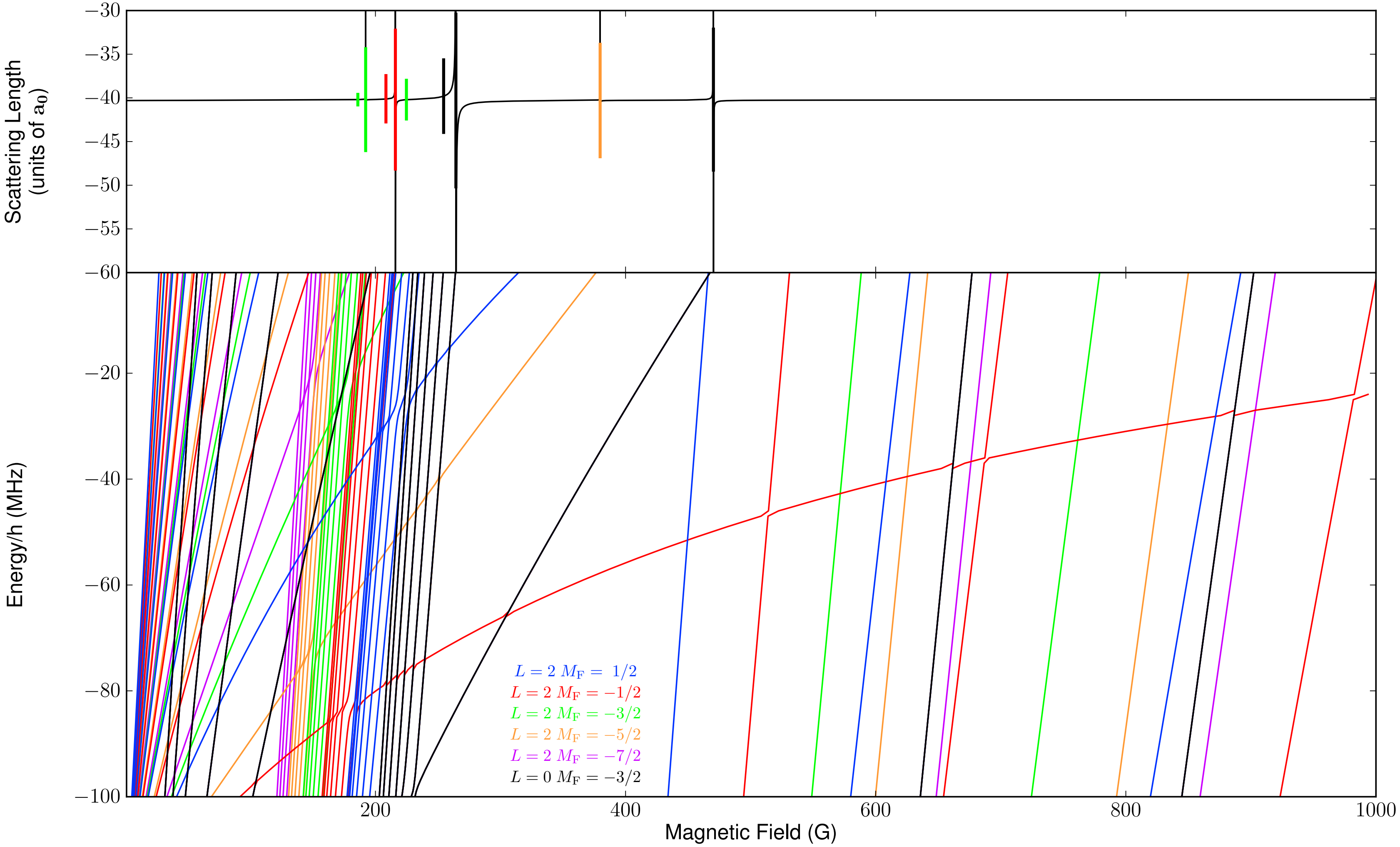

Figure 5.14: Top: the s-wave scattering length in the $(f, m_f) = (9/2, -9/2) + (3, 3)$ channel of ^{40}KCs, with $L = 0$ and 2 functions. Bottom: The energies of very weakly bound molecular states. Resonance widths greater than 1 μG are shown as vertical bars with lengths proportional to $\log_{10} \Delta/\mu$G.

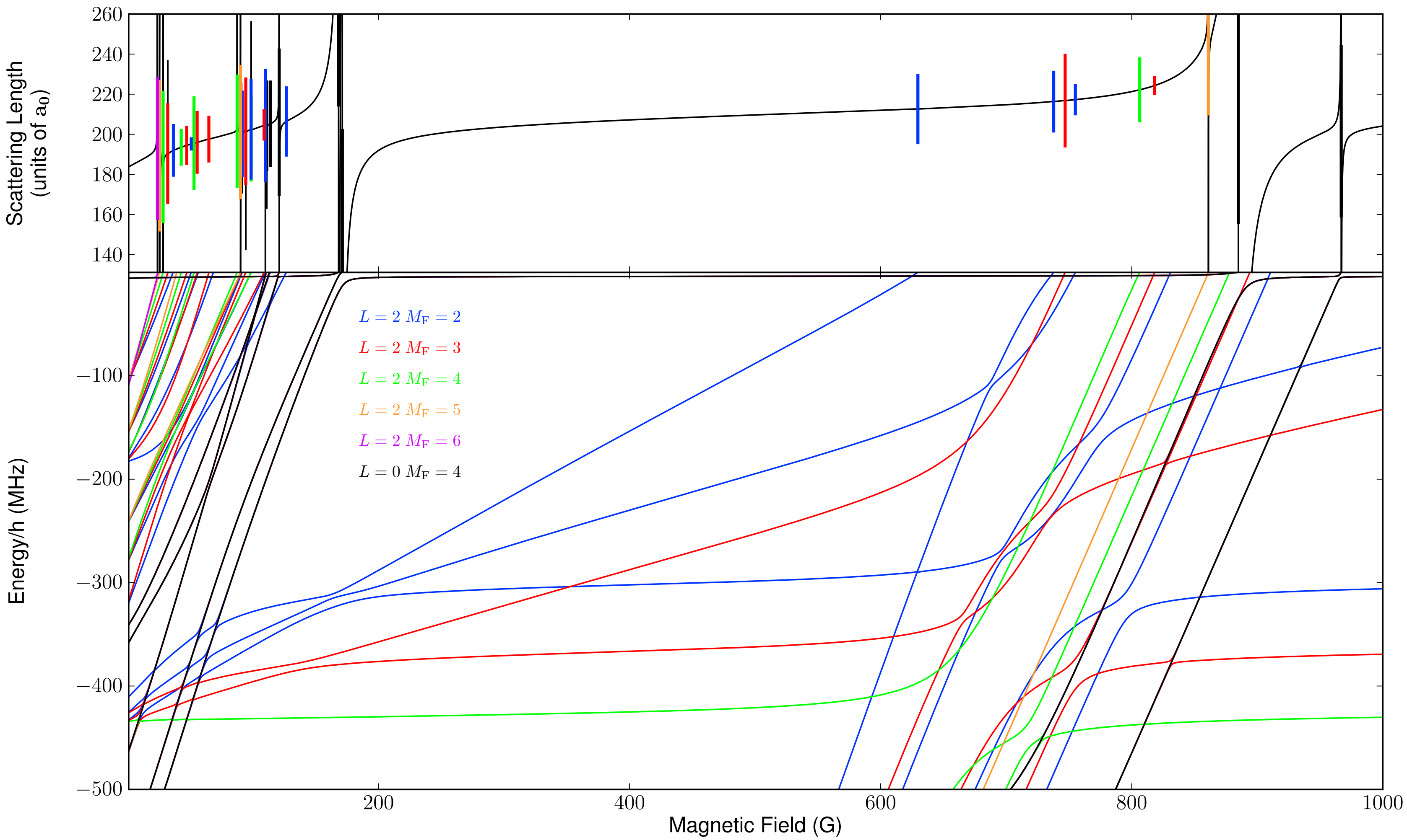

Figure 5.15: Top: The s-wave scattering length in the $(f, m_f) = (1, 1) + (3, 3)$ channel of ^{41}KCs, with $L = 0$ and 2 functions. Bottom: The energies of weakly bound molecular states. Resonance widths greater than 1 μG are shown as vertical bars with lengths proportional to $\log_{10} \Delta/\mu$G.

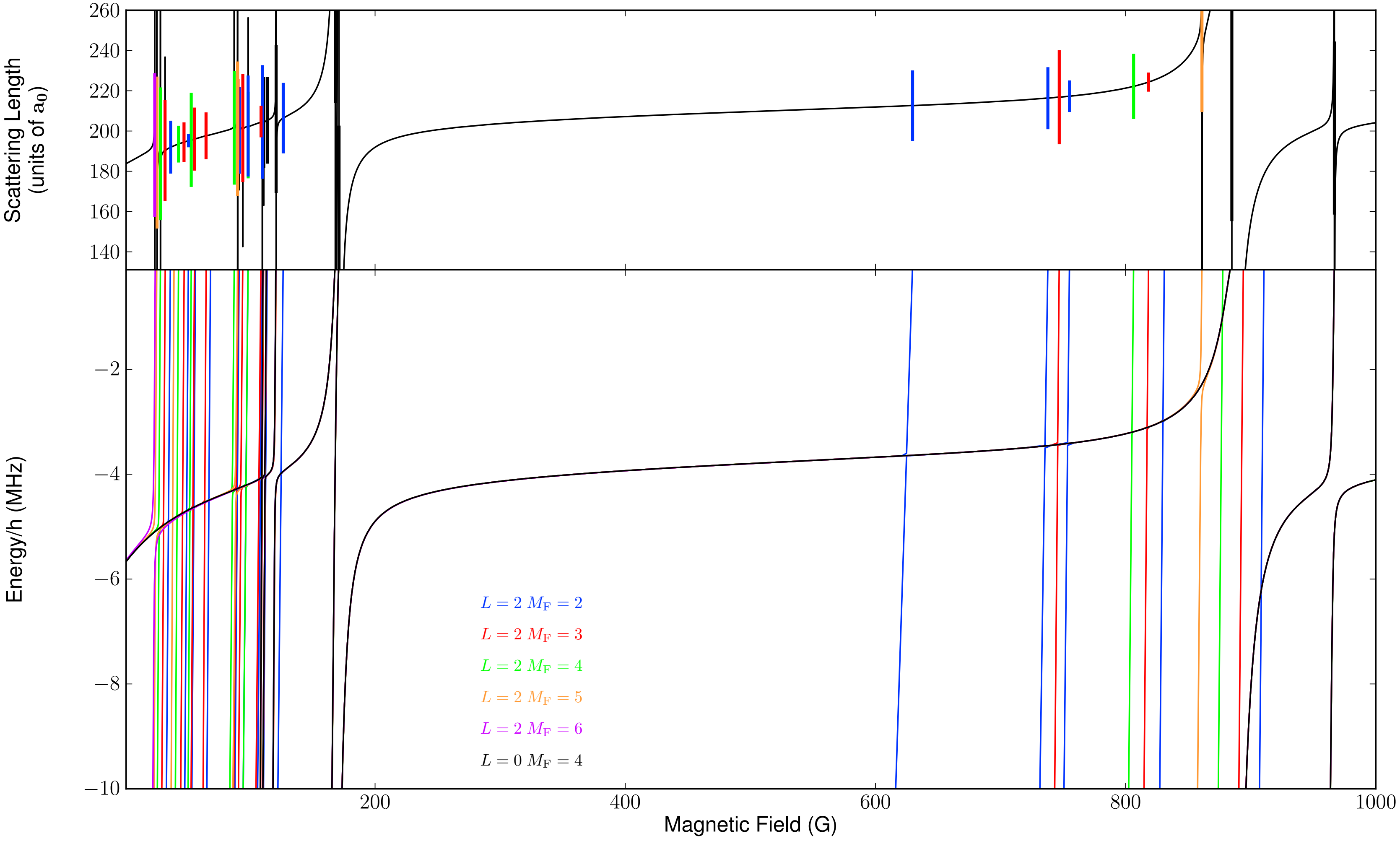

Figure 5.16: Top: The s-wave scattering length in the $(f, m_f) = (1,1) + (3,3)$ channel of ^{41}KCs, with $L = 0$ and 2 functions. Bottom: The energies of very weakly bound molecular states. Resonance widths greater than 1 μG are shown as vertical bars with lengths proportional to $\log_{10} \Delta/\mu$G.

5.3 Prospects for alkali-alkali ultracold molecule formation

Magnetoassociation of Feshbach molecules has been performed successfully using ultracold gases close to degeneracy. However, the maximum conversion efficiency is dictated by the PSD of the atomic gas; therefore, using quantum-degenerate gases is always preferable. To achieve degeneracy in an atomic gas requires the right balance of elastic and inelastic collisions for evaporative cooling [187, 188] typically it requires an s-wave scattering length such that $40 \lesssim |a| \lesssim 250\ a_0$ [16, 17, 21, 167]. In a mixed-species experiment there are several different possible cooling routes. If the intraspecies scattering length of one of the species (a_{11}) is in the desired range and the interspecies scattering length (a_{12}) is also in the desired range then species 1 can be cooled directly and species 2 can be cooled via interspecies collisions, provided a_{22} is positive and has a moderate value [189–194], as in the case of ^{87}RbCs [76]. If both the intraspecies scattering lengths are in the desired range but the interspecies scattering length is not then the two species can be cooled separately and spatially overlapped only after cooling [75, 118]. If neither of these scenarios are possible then the species can potentially be cooled in different hyperfine states.

Once degeneracy is reached the behaviour of a two-species degenerate mixture is described by a pair of coupled Gross-Pitaevskii equations with an additional non-linear term which represents interspecies interactions [195],

$$\left[\frac{-\hbar^2}{2m_1}\nabla^2 + V_1(r) + g_{11}|\psi_1(r)|^2 + g_{12}|\psi_2(r)|^2\right]\psi_1(r) = \mu_1\psi_1(r) \tag{5.3.1}$$

$$\left[\frac{-\hbar^2}{2m_2}\nabla^2 + V_2(r) + g_{22}|\psi_2(r)|^2 + g_{21}|\psi_1(r)|^2\right]\psi_2(r) = \mu_2\psi_2(r) \tag{5.3.2}$$

where ψ_i is the wavefunction of species $i = 1$ or 2, and μ_i is the corresponding chemical potential. The interaction coupling constants that govern the intraspecies interactions are

$$g_{11} = \frac{4\pi\hbar^2 a_{11}}{m_1} \quad \text{and} \quad g_{22} = \frac{4\pi\hbar^2 a_{22}}{m_2} \tag{5.3.3}$$

and the interaction coupling constants that govern the interspecies interactions are

$$g_{12} = g_{21} = 2\pi\hbar^2 a_{12}\frac{m_1 + m_2}{m_1 m_2}. \tag{5.3.4}$$

For an individual condensate to be stable the scattering length must be positive ($g_{ii} > 0$). Assuming both of the individual species have positive scattering lengths then the behaviour of the mixture is determined by the relative strengths of the intraspecies interactions (g_{ii}) and the interspecies interactions (g_{ij}) and can be characterised in terms of the interaction

	Scattering length (a_0)										
Field (G)	^{133}Cs	^{39}K	^{39}KCs	^{41}K	^{41}KCs	^{40}K	^{40}KCs	^{85}Rb	^{85}RbCs	^{87}Rb	^{87}RbCs
17.7	35.2	−34.0	70.8	63.1	189.6	169.6	−40.3	−456.2	32.1	100.3	655.7
21.7	252.5	−30.7	71.1	62.9	192.2	169.9	−40.3	−455.2	33.8	100.3	657.2
556.2	28.2	−40.0	78.2	60.5	210.9	165.7	−40.3	−402.9	24.6	100.3	655.2
556.9	253.6	−40.0	78.2	60.5	210.9	165.8	−40.3	−402.9	24.6	100.3	655.2
882.3	39.3	−34.5	83.1	60.3	539.9[a]	167.8	−40.2	−406.6	−81.8[b]	100.4	619.5
892.2	251.3	−34.5	84.5	60.3	93.2	167.8	−40.2	−402.3	0.4	100.4	623.4

Table 5.8: Intraspecies and interspecies scattering lengths at fields that bound the regions where $40\ a_0 \lesssim a_{\mathrm{Cs}} \lesssim 250\ a_0$.

[a] ^{41}KCs has a resonance at 884.9 G that substantially affects its scattering length in this region.

[b] ^{85}RbCs has a resonance at 642 G that substantially affects its scattering length in this region.

parameter Δ_{int},

$$\Delta_{\mathrm{int}} = \frac{g_{12}}{\sqrt{g_{11}g_{22}}} = \frac{a_{12}}{\sqrt{a_{11}a_{22}}}\sqrt{\frac{(m_1+m_2)^2}{4m_1m_2}} \approx \frac{a_{12}}{a_{11}a_{22}} \tag{5.3.5}$$

If $|\Delta_{\mathrm{int}}| < 1$ then the mixture is both stable and miscible. If $\Delta_{\mathrm{int}} > 1$ then repulsive interspecies interactions dominate and there is a phase separation of the two species, and if $\Delta_{\mathrm{int}} > -1$ then attractive interspecies interactions dominate and the mixture becomes unstable against collapse. If these conditions cannot be fulfilled then a thermal gas close to degeneracy must be used instead, or the instabilities avoided by loading the two species into an optical lattice to form a Mott-insulator phase with one atom of each species per lattice site [196].

Given the parameters discussed above, the scattering lengths of the isotopologues of KCs and RbCs are examined. Three different criteria are defined for comparison:

- If $40 \lesssim |a_{11}| \lesssim 250\ a_0$ and $40 \lesssim |a_{21}| \lesssim 250\ a_0$ and $|a_{22}| \lesssim 600\ a_0$ (or vice-versa replacing species 1 with species 2) then one species can be cooled directly and the other evaporatively and the region is marked in blue on Figures 5.18 and 5.19.
- If $40 \lesssim |a_{11}| \lesssim 250\ a_0$ and $40 \lesssim |a_{22}| \lesssim 250\ a_0$ then both species can be cooled directly and the region is marked in red on Figures 5.18 and 5.19.
- If $a_{11} > 0$, $a_{22} > 0$ and $g_{12}^2 < g_{11}g_{22}$ then the condensates are stable and miscible and the region is marked in green on Figures 5.18 and 5.19.

The intraspecies scattering length of Cs has a very large background scattering length which severely limits the regions in which Cs can be evaporatively cooled. Condensates

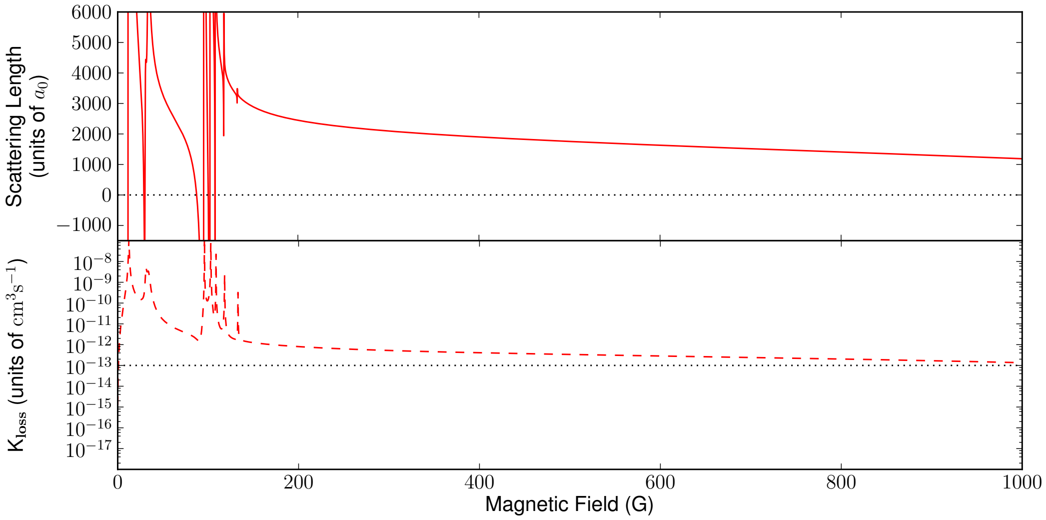

Figure 5.17: Top: Real part of the scattering length of Cs in the s-wave incoming $(f, m_f) = (3,-3)+(3,-3)$ channel. Bottom: Loss-rate coefficient associated with the imaginary part of the scattering length of Cs in the s-wave incoming $(3,-3)+(3,-3)$ channel. The horizontal line at 1×10^{-13} denotes experimentally acceptable loss rates for efficient evaporative cooling.

of Cs are usually produced just above the zero-crossing of the scattering length associated with a broad resonance [20,166,197,198] due to the reduction in three-body loses in these regions [174]. There are three such windows that appear in the region from $0-1000$ G: around 21 G above the zero-crossing in the scattering length at 17 G, around the zero-crossing at 556 G associated with the resonance at 549 G, and around the zero-crossing at 881 G associated with the resonance at 894 G. The intraspecies and interspecies scattering lengths of the isotopologues of KCs and RbCs at the boundaries of the regions of moderate positive Cs scattering length are summarised in Table 5.8.

For ^{87}RbCs the scattering lengths of ground state ^{87}Rb, Cs and ^{87}RbCs are compared, shown in Fig. 5.18. There are several regions where the condensates are stable and miscible, most notably a large region between 700 and 800 G; however, there is nowhere both species can be cooled to degeneracy. In the molecule formation of ^{87}RbCs described in Section 5.1.2 the species are cooled to between $200-700$ nK, just above degeneracy, before the magnetoassociation stage [76] to prevent phase separation of the condensates. In Refs. [70,118] the species are cooled to around 200 nK and a 1D optical lattice is applied to reduce species interactions. Both of these methods succeed in making several thousand Feshbach molecules, which are then transferred into the ground state.

For ^{85}RbCs the scattering lengths of ^{85}Rb in the $(f, m_f) = (2,+2)+(2,+2)$ and

$(2,-2)+(2,-2)$ states are compared with the ground state of Cs and the ground state of ^{85}RbCs, shown in Fig. 5.18. For the excited states an additional restriction of $K_{\rm loss} < 1\times10^{-13}$ cm^{3}s^{-1} is applied to the regions where evaporative cooling is possible. This number is based on the successful formation of condensates of ^{85}Rb around 161 G where $K_{\rm loss} = 5\times10^{-14}$ cm^{3}s^{-1} [148]. The excited-state scattering length of the $(3,-3)+(3,-3)$ state of Cs, shown in Fig. 5.17, is not considered in the possible combinations as there is no significant field region in the range from $0-1000$ G with $K_{\rm loss} < 1\times10^{-13}$ cm^{3}s^{-1}. The ground and excited-state scattering lengths of ^{85}Rb are compared along with the ground state of Cs to the ground state of ^{85}RbCs. The excited state of ^{85}Rb can be compared to the ground state of ^{85}RbCs because the time required to change the hyperfine state is on the order of milliseconds [199] allowing this to be performed without sustaining significant losses or causing condensate collapse. This means that other hyperfine states of ^{85}RbCs can also be considered and comparisons to the $(2,-2)+(3,+3)$ and the $(2,-2)+(3,-3)$ scattering lengths are given in Appendix D; as these states all have associated inelastic losses, molecule formation in the ground state is always preferable. Unfortunately, for ground state ^{85}RbCs there is only a very small region where the species can both be cooled (around 48 G) and no region where the condensates are stable and miscible. In the excited state of ^{85}Rb the wide resonance at 155 G creates a small window between $155-166$ G where the condensates are stable and miscible, however there is still only a very small region where both species can be cooled. The large background scattering length of Cs combined with the negative intra-species background scattering length of both the ground and excited-states of ^{85}Rb and the small interspecies scattering length of ^{85}RbCs causes a dearth in suitable cooling regions. Any molecule formation process involving these two species would most likely have to involve the use of thermal mixtures rather than degenerate gases.

For ^{39}KCs the scattering lengths of ground state ^{39}K, Cs and ^{39}KCs are compared, shown in Fig. 5.19. The background intraspecies scattering length of ^{39}K, Fig. 5.19 (b), is small and negative (around -35 a_0) except near a wide Feshbach resonance at 402 G; this makes a single-species condensate of ^{39}K unstable at most fields. Condensation of ground-state ^{39}K has previously been achieved by sympathetic cooling with ^{87}Rb [200] by using the resonance at 402 G [201]. There is a wide region on the low-field side of the 402 G resonance in ^{39}K, between the zero-crossing of the scattering length (353 G) and the pole of the resonance, where the condensates are stable and miscible. There

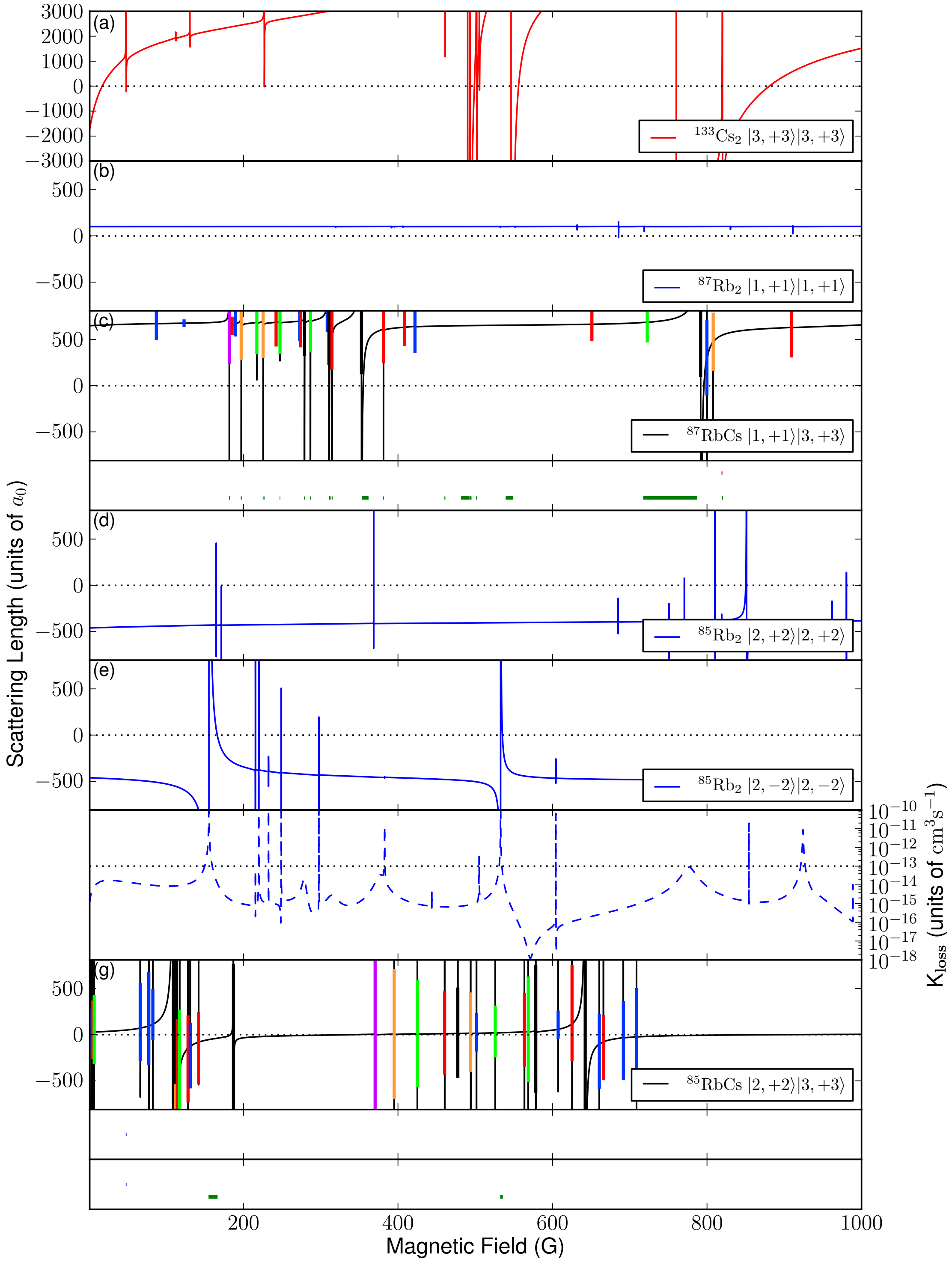

Figure 5.18: Scattering lengths for isotopologues of RbCs, together with those of the corresponding isotopes of Rb and Cs. The scattering lengths are shown with the same magnetic field axis, to facilitate the identification of regions where the combination is conducive to molecule formation. Resonance widths greater than 1 μG are shown as vertical bars with lengths proportional to $\log_{10} \Delta/\mu$G.

Figure 5.18 ***(previous page)*:** The coloured bars beneath each interspecies scattering length indicate the fields at which both species can be cooled evaporatively (red, top), the fields at which one species can be cooled evaporatively and the other sympathetically (blue, center), and the fields at which the condensates are miscible (green, bottom). For ^{85}RbCs two comparison bars are shown: the top bar corresponds to comparison with the (2,+2) state of ^{85}Rb and the lower bar to the (2,-2) state.

are two resonances with widths < 1 μG in the ^{39}KCs scattering length in this region; the wider of the two resonances, which has a pole at 375 G and a width of 6 mG, is a promising option for magnetoassociation. There is also a resonance just below this region, which has a pole at 342 G and a width of 4.8 G, that could possibly be used for molecule formation if the magnetic field sweep can be performed before the ^{39}K condensate collapses. The background scattering length of ^{39}KCs is around 70 a_0, Fig. 5.19 (c), which may allow for sympathetic cooling of ^{39}K by Cs, in the three regions where Cs can be efficiently cooled. The widest of these regions is the high field region around 894 G. There are three resonances in ^{39}KCs around this region at 861, 908, and 916 G where the Cs scattering length is -630, 510 and 630 a_0 respectively. These regions offer the potential for magnetoassociation using thermal gases.

In the case of ^{40}KCs the s-wave scattering length of identical ^{40}K atoms in the ground state is undefined due to their fermionic character, instead the scattering length of the $(9/2, -9/2) + (9/2, -7/2)$ is shown in Fig. 5.19 (f) and compared to the ground state of Cs and ^{40}KCs. The background scattering length of ^{40}K is around 170 a_0, Fig. 5.19 (f), and the background scattering length of ^{40}KCs is around -40 a_0, Fig. 5.19 (g). In the regions where Cs can be cooled evaporatively it may be possible to use Cs to sympathetically cool ^{40}K in the $(9/2, -9/2)$ state removing the need for the second spin state of ^{40}K. There are no resonances in the ^{40}KCs scattering length near to regions where the two species can be cooled, however there are resonances with suitable widths at 192, 216, 264 and 470 G.

For ^{41}KCs the scattering lengths of ground state ^{41}K, Cs and ^{41}KCs are compared, shown in Fig. 5.19. The background scattering length of ^{41}K is around 63 a_0, Fig. 5.19 (d). Similarly to ^{87}Rb, the scattering length has little variation in the field range from $0 - 1000$ G therefore efficient evaporation should be possible at most magnetic field values. The background interspecies scattering length of ^{41}KCs is around 200 a_0, Fig. 5.19 (e), which allows for sympathetic cooling of Cs using ^{41}K in the regions around 21, 558 and 894 G. There is a large region in which the condensates will be stable and miscible from

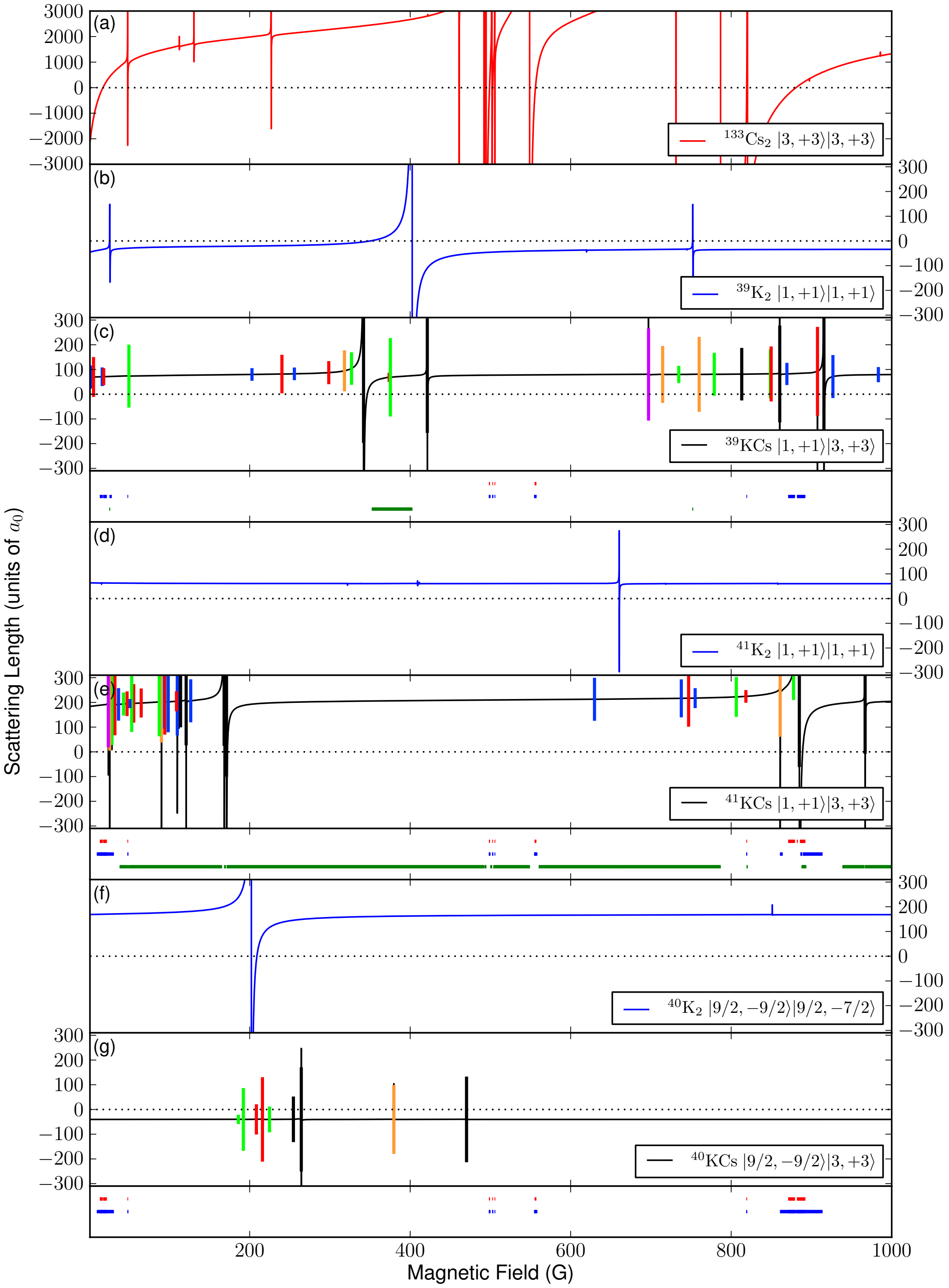

Figure 5.19: Scattering lengths for isotopologues of KCs, together with those of the corresponding isotopes of K and Cs. The scattering lengths are shown with the same magnetic field axis, to facilitate the identification of regions where the combination is conducive to molecule formation. Resonance widths greater than 1 μG are shown as vertical bars with lengths proportional to $\log_{10} \Delta/\mu$G.

Figure 5.19 ***(previous page)*:** The coloured bars beneath each interspecies scattering length indicate the fields at which both species can be cooled evaporatively (red, top), the fields at which one species can be cooled evaporatively and the other sympathetically (blue, center), and the fields at which the condensates are miscible (green, bottom, not shown for ^{40}K).

$38 - 786$ G and above 939 G. There is also a small (5 G) region of miscibility immediately above the broad ^{41}KCs resonance at 885 G ($\Delta = 4.1$ G), where $a_{^{40}\mathrm{K}} = 63\ a_0$ and a_{Cs} is around 200 a_0. These properties make this resonance a very promising option for cooling a mixed gas directly to degeneracy, followed by magnetoassociation. There are also a set of three ^{41}KCs resonances below 30 G which lie close to a region where evaporative cooling of both species is possible and which have comparable widths to the width of the Cs resonance at 19.8 G where magnetoassociation is very effective.

Chapter 6

Analysis of singlet and triplet character

The character of the molecular bound states is important when considering which states are best for STIRAP transfer. In the following Chapter different methods for analysing the singlet and triplet character of molecular bound states and of asymptotic energy levels are discussed.

6.1 A molecular basis

Depending on the system studied and the various regions looked at different basis sets give the most appropriate description of the system. For example at zero magnetic field the $|(s_a, i_a)f_a(s_b, i_b)f_bF\rangle$ quantum numbers are well defined, whereas at high field the $|m_{s,a}m_{i,a}, m_{s,b}, m_{i,b}\rangle$ quantum numbers better represent the system. Calculations in different basis sets also allow for different views of the molecular bound states and the bound-state wavefunctions. Bound-state wavefunctions allow for the calculation of transition intensities and expectation values; therefore, finding a basis in which they are simply represented can be useful. In the following sections we define the matrix elements of basis set described by the molecular quantum numbers,

$$|(s_1, s_2)S\rangle\,|(i_1, i_2)I\rangle\,|F, M_F\rangle\,|L, M_L\rangle \tag{6.1.1}$$

where S is the molecular electron spin quantum number, I is molecular nuclear spin quantum number, F is the molecular total spin quantum number given by the coupling of S and I and M_F is the projection of F. This basis set is known to describe the ^{6}Li system well and we will examine how useful it can be in describing the bound states of ^{85}RbCs and of ^{6}Li$_2$.

6.1.1 The isotropic potential operator

In this basis, as the molecular electronic spin is a given quantum number, then the projection operator will be diagonal in S and the matrix elements of $\hat{V}^{\mathrm{c}}$ are

$$\begin{aligned}\langle S(s_1,s_2), I(i_1,i_2), FM_F, LM_L|\hat{V}^{\mathrm{c}}|S'(s_1,s_2), I'(i_1,i_2), F'M'_F, L'M'_L\rangle \equiv \\ \delta_{L,L'}\delta_{M_L,M'_L}\delta_{I,I'}\delta_{F,F'}V_S(R)\delta_{S,S'}.\end{aligned} \tag{6.1.2}$$

6.1.2 The spin-spin interactions

In ground-state alkali-alkali interactions the $\hat{V}^{\mathrm{d}}$ operator takes the form,

$$\hat{V}^{\mathrm{d}}(R) = \lambda(R)[\hat{s}_1\cdot\hat{s}_2 - 3(\hat{s}_1\cdot\vec{e}_R)(\hat{s}_1\cdot\vec{e}_R)],$$

describing the spin-dipolar coupling. This can be rewritten in irreducible tensor form as [202]

$$\hat{V}^d(R) = -\lambda(R)g_{\mathrm{e}}^2\mu_B^2(\mu_0/4\pi)\sqrt{6}T^2(s_1,s_2)\cdot T^2(\mathbf{C}).$$

The two second rank tensors can be separated using the scalar product identity [203]

$$T^k(\hat{A})\cdot T^k(\hat{B}) \equiv W_0^0 \equiv \sum_q (-1)^q T_q^k(\hat{A})T_{-q}^k(\hat{B}).$$

Applying this operator to the basis set one can separate out the terms based on $|L, M_L\rangle$ so that the expression for $\langle S(s_1,s_2), I(i_1,i_2), FM_F, LM_L|\hat{V}^{\mathrm{d}}|S'(s_1,s_2), I'(i_1,i_2), F'M'_F, L'M'_L\rangle$, ignoring constants and $\lambda(R)$ which will precede the summation in the complete expression, becomes

$$\begin{aligned}\sum_q (-1)^q \langle S(s_1,s_2), I(i_1,i_2), FM_F|\hat{T}_q^2(s_1,s_2)|S'(s_1,s_2), I'(i_1,i_2), F'M'_F\rangle \\ \times \langle LM_L|\hat{T}_{-q}^2(\mathbf{C})|L'M'_L\rangle\,.\end{aligned}$$

Each of the brakets can now be treated separately and then recombined once evaluated to give the total expressions for $\hat{V}_d$. Using the Wigner-Eckart Theorem

$$\begin{aligned}\langle S(s_1,s_2), I(i_1,i_2), FM_F|\hat{T}_q^2(s_1,s_2)|S'(s_1,s_2), I'(i_1,i_2), F'M'_F\rangle \equiv \\ (-1)^{F-M_F}\begin{pmatrix} F & 2 & F' \\ -M_F & q & M'_F\end{pmatrix}\sqrt{2F+1}\,\langle SIF||T^2(s_1,s_2)||S'I'F'\rangle\,.\end{aligned}$$

As the operator $T^2(s_1, s_2)$ acts only on the electron spin components of the basis set we can further simplify $\langle SIF||T^2(s_1, s_2)||S'I'F'\rangle$ to

$$\delta_{I,I'}\sqrt{(2F'+1)(2S+1)}(-1)^{2+I+F'+S}\begin{Bmatrix} F & F' & 2 \\ S' & S & I \end{Bmatrix}\langle S(s_1, s_2)||T^2(s_1, s_2)||S'(s_1, s_2)\rangle\,.$$

The component $\langle S(s_1, s_2)||T^2(s_1, s_2)||S'(s_1, s_2)\rangle$ can be separated into two separate operators $\hat{s}_1$ and $\hat{s}_2$. This reduction results in

$$\langle S(s_1, s_2)||T^2(s_1, s_2)||S'(s_1, s_2)\rangle \equiv$$
$$\sqrt{5(2S'+1)(2s_1+1)(2s_2+1)}\begin{Bmatrix} S & S' & 2 \\ s_1 & s_1' & 1 \\ s_2 & s_2' & 1 \end{Bmatrix}\langle s_1||\hat{s}_1||s_1\rangle\,\langle s_2||\hat{s}_2||s_2\rangle\,,$$

where the reduced tensor elements can each be evaluated as

$$\langle s_a||\hat{s}_a||s_a\rangle \equiv \delta_{s_a,s_a'}\sqrt{s_a(s_a+1)}.$$

The second braket in our spin-spin interaction term $\langle LM_L|T^2_{-q}(\mathbf{C})|L'M_L'\rangle$ can be reduced, again using the Wigner-Eckart Theorem, to

$$\langle LM_L|T^2_{-q}(\mathbf{C})|L'M_L'\rangle \equiv (-1)^{L-M_L}\sqrt{2L+1}\begin{pmatrix} L & 2 & L' \\ -M_L & -q & M_L' \end{pmatrix}\langle L||C^2(\hat{L})||L'\rangle\,,$$

where the reduced tensor element $\langle L||C^2(\hat{L})||L'\rangle$ with $C^k_q \equiv C_{kq}(\theta,\phi) = (\frac{4\pi}{2k+1})^{1/2}Y_{kq}(\theta,\phi)$ is given in our notation as

$$\langle L||C^2(\hat{L})||L'\rangle \equiv -1^L\sqrt{2L'+1}\begin{pmatrix} L & 2 & L' \\ 0 & 0 & 0 \end{pmatrix}.$$

Combining all the above expressions we find the total expression for the spin-spin operator

$$\langle S(s_1, s_2), I(i_1, i_2), FM_F, LM_L|\hat{V}^{\mathrm{d}}|S'(s_1, s_2), I'(i_1, i_2), F'M_F', L'M_L'\rangle \equiv -\lambda(R)\sqrt{30}$$
$$\times\sum_{q=-2}^{2}(-1)^q\sqrt{(2F+1)(2F'+1)(2S+1)(2S'+1)(2s_1+1)(2s_2+1))s_1(s_1+1)s_2(s_2+1)}$$
$$\times\left(\delta_{I,I'}\delta_{s_1,s_1'}\delta_{s_2,s_2'}(-1)^{F-M_F}\begin{pmatrix} F & 2 & F' \\ -M_F & q & M_{F'} \end{pmatrix}\begin{Bmatrix} F & F' & 2 \\ S' & S & I \end{Bmatrix}\begin{Bmatrix} S & S' & 2 \\ s_1 & s_1' & 1 \\ s_2 & s_2' & 1 \end{Bmatrix}\right)$$
$$\times\left((-1)^{-M_L}\sqrt{(2L+1)(2L'+1)}\begin{pmatrix} L & 2 & L' \\ -M_L & -q & M_L' \end{pmatrix}\begin{pmatrix} L & 2 & L' \\ 0 & 0 & 0 \end{pmatrix}\right).\tag{6.1.3}$$

6.1.3 The hyperfine interactions

The hyperfine term $\zeta_{\mathrm{hfs}}\hat{\imath}_a \cdot \hat{s}_a$, for either atom (1) or (2), can be written using the tensor scalar product, and then have the Wigner-Eckart theorem applied such that the reduced tensor elements of the hyperfine interaction can be written,

$$\begin{aligned}&\langle S(s_1,s_2), I(i_1,i_2), FM_F, LM_L|\zeta_{\mathrm{hfs}}\hat{\imath}_a \cdot \hat{s}_a|S'(s_1,s_2), I'(i_1,i_2), F'M'_F, L'M'_L\rangle \equiv \\ &\delta_{F,F'}(-1)^{F-M_F}\begin{pmatrix} F & 0 & F' \\ -M_F & 0 & M_{F'}\end{pmatrix}\sqrt{(2F+1)}\left\langle SIF||\hat{\imath}_a \cdot \hat{s}_a||S'I'F'\right\rangle.\end{aligned}$$

The 3-j symbol in the above equation can be simplified using the expansion

$$\begin{pmatrix} a & b & 0 \\ \alpha & \beta & 0\end{pmatrix} \equiv (2a+1)^{\frac{-1}{2}}\delta_{(a,b)}\begin{pmatrix} a \\ \beta\alpha\end{pmatrix} \equiv (2a+1)^{\frac{-1}{2}}\delta_{(a,b)}\delta(\alpha-\beta)(-1)^{a-\alpha}.$$

The square roots cancel and $-1^{(F-M_F)+(F'-M_{F'})} = 1$ in all non-zero evaluations due to the delta functions, therefore the evaluation of the hyperfine interaction simplifies to

$$\delta_{F,F'}\delta_{M_F,M_{F'}}\left\langle SIF||\hat{\imath}_a \cdot \hat{s}_a||S'I'F'\right\rangle.$$

The dot product in $\langle SIF||\hat{\imath}_a \cdot \hat{s}_a||S'I'F'\rangle$ separates into two reduced components

$$(-1)^{S'+I+F}\begin{Bmatrix} S & S' & 1 \\ I' & I & F\end{Bmatrix}\sqrt{(2S+1)(2I+1)}\left\langle (s_1,s_2)S||\hat{s}_a||(s_1,s_2)S\right\rangle\left\langle (i_1,i_2)I||\hat{\imath}_a||(i_1,i_2)I\right\rangle.$$

The evaluation of these reduced tensor components now depends on whether a refers to atom (1) or (2). Overall we arrive at a total expression for both hyperfine components of

$$\begin{aligned}&\langle S(s_1,s_2), I(i_1,i_2), FM_F, LM_L|\,\zeta_{\mathrm{hfs}}\hat{\imath}_1 \cdot \hat{s}_1 \\ &\qquad\qquad +\zeta_{\mathrm{hfs}}\hat{\imath}_2 \cdot \hat{s}_2\,|S'(s_1,s_2), I'(i_1,i_2), F'M'_F, L'M'_L\rangle \equiv \\ &\quad\delta_{F,F'}\delta_{M_F,M_{F'}}\delta_{s_1,s'_1}\delta_{s_2,s'_2}\delta_{i_1,i'_1}\delta_{i_2,i'_2}(-1)^{S'+I+F}\sqrt{(2S+1)(2I+1)(2S'+1)(2I'+1)} \\ &\quad\begin{Bmatrix} S & S' & 1 \\ I' & I & F\end{Bmatrix}\times\Bigg(\zeta_{\mathrm{hfs}_1}\sqrt{(2s_1+1)(2i_1+1)}\sqrt{s_1(s_1+1)i_1(i_1+1)} \\ &\quad\times(-1)^{s_1+S'+s_2+i_1+I'+i_2}\begin{Bmatrix} S & S' & 1 \\ s'_1 & s_1 & s_2\end{Bmatrix}\begin{Bmatrix} I & I' & 1 \\ i'_1 & i_1 & i_2\end{Bmatrix} \\ &\quad+\zeta_{\mathrm{hfs}_2}\sqrt{(2s_2+1)(2i_2+1)}\sqrt{s_2(s_2+1)i_2(i_2+1)} \\ &\quad\times(-1)^{s_1+S+s'_2+i_1+I+i'_2}\begin{Bmatrix} S & S' & 1 \\ s'_2 & s_2 & s_1\end{Bmatrix}\begin{Bmatrix} I & I' & 1 \\ i'_2 & i_2 & i_1\end{Bmatrix}\Bigg).\end{aligned} \tag{6.1.4}$$

6.1.4 The Zeeman interactions

The magnetic field dependent terms are $g_{\mathrm{e},1}\mu_{\mathrm{B}}\hat{s}_{z,1}$, $g_{\mathrm{n},1}\mu_{\mathrm{B}}\hat{i}_{z,1}$, $g_{\mathrm{e},2}\mu_{\mathrm{B}}\hat{s}_{z,2}$, and $g_{\mathrm{n},2}\mu_{\mathrm{B}}\hat{i}_{z,2}$. Each of the 4 terms can be expressed in the same reduced form

$$\langle (s_1, s_2)S, (i_1, i_2)I, F || g_z \mu_{\mathrm{B}} \hat{j}_{z,a} B || (s_1, s_2)S', (i_1, i_2)I', F' \rangle\,,$$

where $\hat{j}_{z,a}$ represents the appropriate spin operator ($\hat{i}_{z,1}$, $\hat{s}_{z,1}$, $\hat{i}_{z,2}$ or $\hat{s}_{z,2}$) and g_z the appropriate g-factor. Each operator can be dealt with separately and then combined, extracting any common factors. We arrive at a total expression for the magnetic-field dependent terms;

$$\begin{aligned}
&\langle S(s_1,s_2), I(i_1,i_2), FM_F, LM_L|\, (g_{\mathrm{e},1}\mu_{\mathrm{B}}\hat{s}_{z,1} + g_{\mathrm{n},1}\mu_{\mathrm{B}}\hat{i}_{z,1} \\
&\qquad + g_{\mathrm{e},2}\mu_{\mathrm{B}}\hat{s}_{z,2} + g_{\mathrm{n},2}\mu_{\mathrm{B}}\hat{i}_{z,2})B_z | S'(s_1,s_2), I'(i_1,i_2), F'M'_F, L'M'_L\rangle \equiv \\
&\qquad (-1)^{F-M_F+2I+2S}\sqrt{(2F+1)(2F'+1)} \begin{pmatrix} F & 1 & F' \\ -M_F & 0 & M_{F'} \end{pmatrix} \\
&\qquad \times \Bigg[(-1)^{F'+s_a+s_b}\sqrt{(2S+1)(2S'+1)} \begin{Bmatrix} F & F' & 1 \\ S' & S & I \end{Bmatrix} \\
&\qquad\qquad \times \Bigg(g_{e_a}\delta_{s_b,s'_b}(-1)^{S'}\sqrt{s_a(s_a+1)(2s_a+1)} \begin{Bmatrix} S & S' & 1 \\ s'_a & s_a & s_b \end{Bmatrix} \\
&\qquad\qquad + g_{e_b}(\delta_{s_a,s'_a}(-1)^{S}\sqrt{s_b(s_b+1)(2s_b+1)} \begin{Bmatrix} S & S' & 1 \\ s'_b & s_b & s_a \end{Bmatrix} \Bigg) \\
&\qquad + (-1)^{F+i_a+i_b}\sqrt{(2I+1)(2I'+1)} \begin{Bmatrix} F & F' & 1 \\ I' & I & S \end{Bmatrix} \\
&\qquad\qquad \times \Bigg(g_{n_a}\delta_{i_b,i'_b}(-1)^{I'}\sqrt{i_a(i_a+1)(2i_a+1)} \begin{Bmatrix} I & I' & 1 \\ i'_a & i_a & i_b \end{Bmatrix} \\
&\qquad\qquad + g_{n_b}\delta_{i_a,i'_a}(-1)^{I}\sqrt{i_b(i_b+1)(2i_b+1)} \begin{Bmatrix} I & I' & 1 \\ i'_b & i_b & i_a \end{Bmatrix} \Bigg) \Bigg].
\end{aligned} \tag{6.1.5}$$

6.1.5 Bound states of ^{85}RbCs

The bound states of ^{85}RbCs have previously been shown in Sec. 5.1.1. The results that are shown in Sec. 5.1.1 are calculated in the decoupled basis described in Sec. 3.2 and the labelling of the different M_{F} states is enforced by a restriction of the basis set corresponding to each possible M_{F} value. As M_{F} is a nearly good quantum number then the

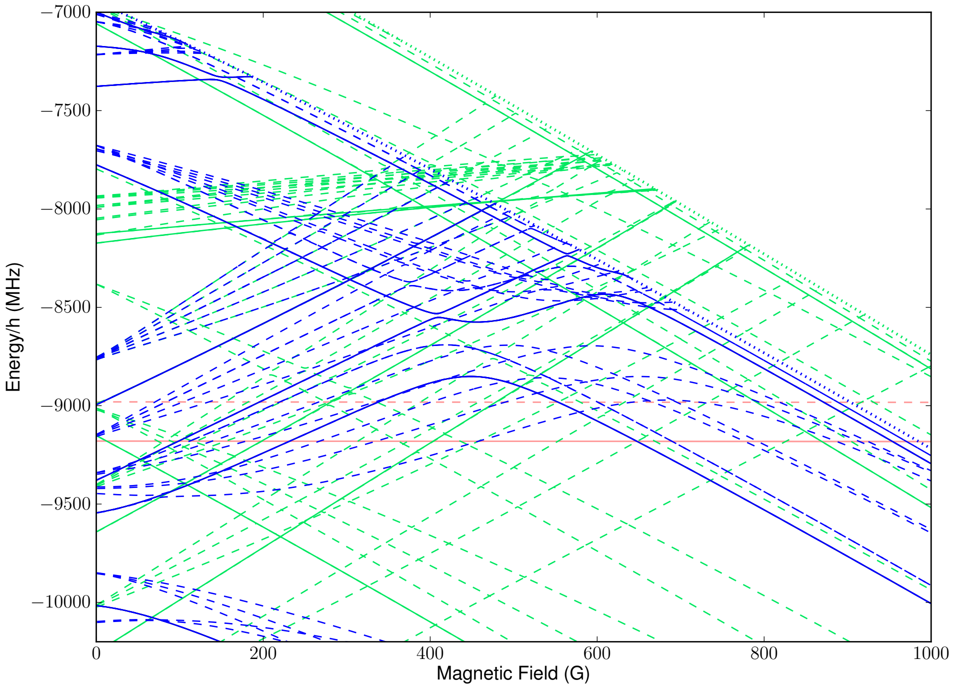

Figure 6.1: Bound states of ^{85}RbCs, including $L = 0$ and 2, calculated from: a complete basis (blue), a restricted basis including $S = 1$ only (green), a restricted basis including $S = 0$ only (pink). Dashed lines indicate states with $L = 2$ and solid lines indicate states with $L = 0$. The thresholds for each basis sent are shown in the corresponding colour with dotted lines (note for $S = 0$ only the threshold does not appear as it occurs at 0 MHz).

restriction has little effect on the calculation of the bound states. Using the $|SIFM_{\rm F}\rangle$ basis the bound states are calculated again. Intially, the bound states were calculated using an unrestricted basis set in the $|SIFM_{\rm F}\rangle$ basis and these results were compared to the results from calculations using and unrestricted basis set in the decoupled basis; the good agreement between these results shows that the matrix elements of the $|SIFM_{\rm F}\rangle$ basis were calculated correctly. The bound states were calculated again, using the $|SIFM_{\rm F}\rangle$ basis, but this time with a restriction to each value of S, where $S = 0$ shows the pure singlet states and $S = 1$ shows the pure triplet states, shown in Fig. 6.1. As the system is not well represented by the $|SIFM_{\rm F}\rangle$ basis this restriction leads to a significant deviation of the bound-state energies calculated. Unlike the previous bound-state figures, in Fig. 6.1 the states are not plotted with respect to the lowest-energy atomic threshold but rather to the zero energy given by the degeneracy-weighted average of the Hamiltonian. The individual thresholds of each calculation are given by the dotted lines of the same colour

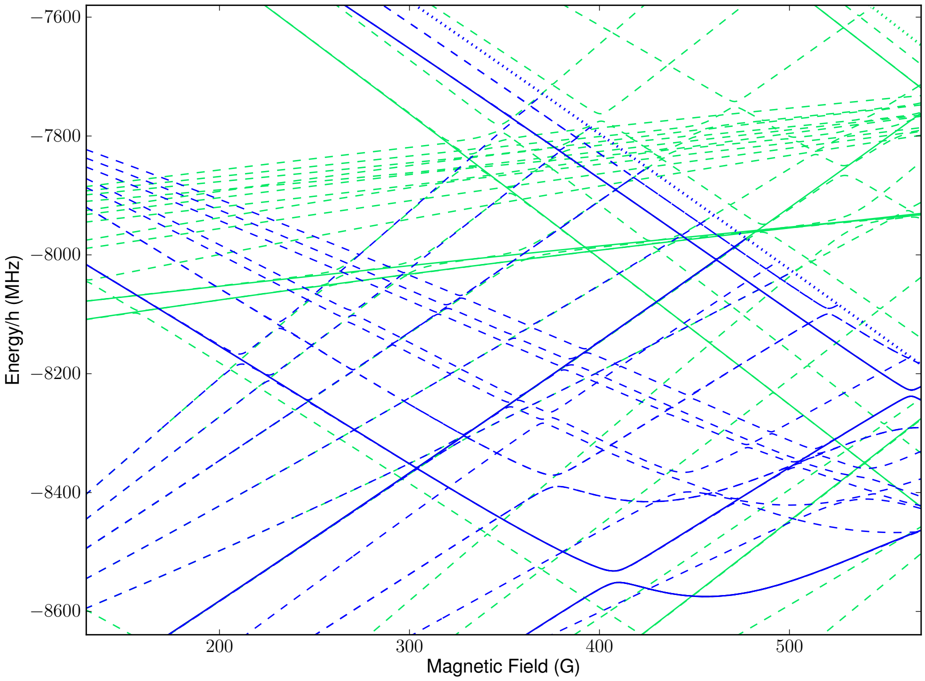

Figure 6.2: Bound states of ^{85}RbCs between 300 and 400 G, including $L = 0$ and 2, calculated from: a complete basis (blue), a restricted basis including $S = 1$ only (green), a restricted basis including $S = 0$ only (pink). Dashed lines indicate states with $L = 2$ and solid lines indicate states with $L = 0$. The thresholds for each basis set are shown in the corresponding colour with dotted lines (note for S=0 only the threshold does not appear as it occurs at 0 MHz).

as the bound states; the $S = 0$ threshold cannot be seen as it is around 0 MHz. The bound states corresponding to $S = 0$ can be seen to have little slope with magnetic field as their slope comes only from the projection of I which is a much smaller contribution then S. The bound states corresponding to $S = 1$ can have three distinct slope: those that correspond to $M_S = +1$ will slope strongly upwards; those that correspond to $M_S = 0$ will be horizontal; and those that correspond to $M_S = -1$ will slope strongly downwards. Fig. 6.2 shows that the group of states, corresponding to $F = 7$ in Fig. 5.1 and which cause resonances between 350 and 500 G, have $M_S = +1$ character, as their slopes match those of the $S = 1$ states. Most of the other high-field resonances also come from states with similar slopes to the $M_S = +1$ states whilst some of the low field resonances, below 200 G, come from $M_S = 0$ states. States with $M_S = -1$ character slope the wrong way from the atomic threshold to cause resonances.

As the basis does not seem to characterise the bound states well, then it does not provide an ideal basis with which to describe the bound-state wavefunctions. For example, the wavefunction of the bound state which causes the resonance around 187 G, shown in Fig. 6.3, is comprised of three main components. The largest component is from the $|SIFM_F\rangle = |1,5,6,5\rangle$ state but there are also significant contributions from the $|1,4,5,5\rangle$ and $|0,6,6,5\rangle$ states. The only state that is well-defined by this basis set is the $M_F = 7$ state which causes the resonance around 370 G. The bound-state wavefunction, shown in Fig. 6.4, consists of a single component corresponding to the $|SIFM_F\rangle = |1,6,7,7\rangle$ state.

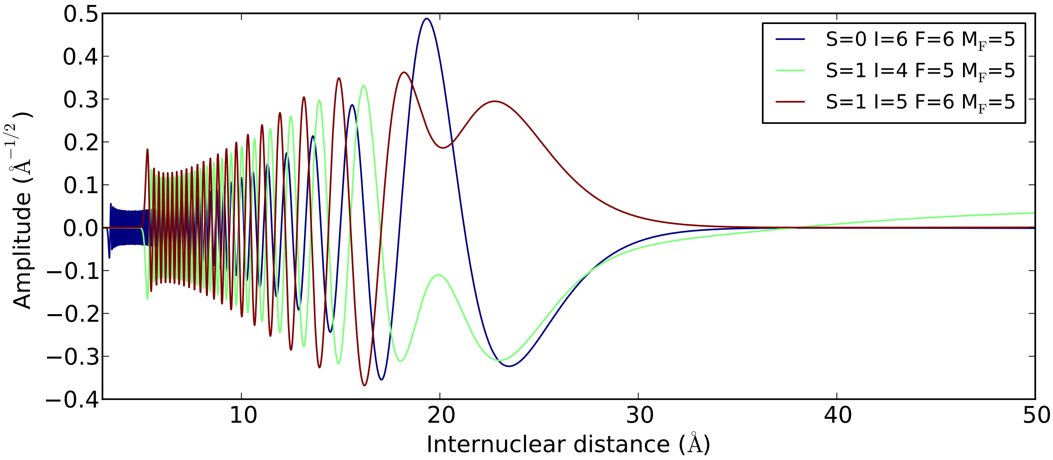

Figure 6.3: ^{85}RbCs bound-state wavefunction for the state which causes the resonance around 187 G. The true wavefunction is a superposition of the different $|SIFM_F\rangle$ states; the three largest components are shown.

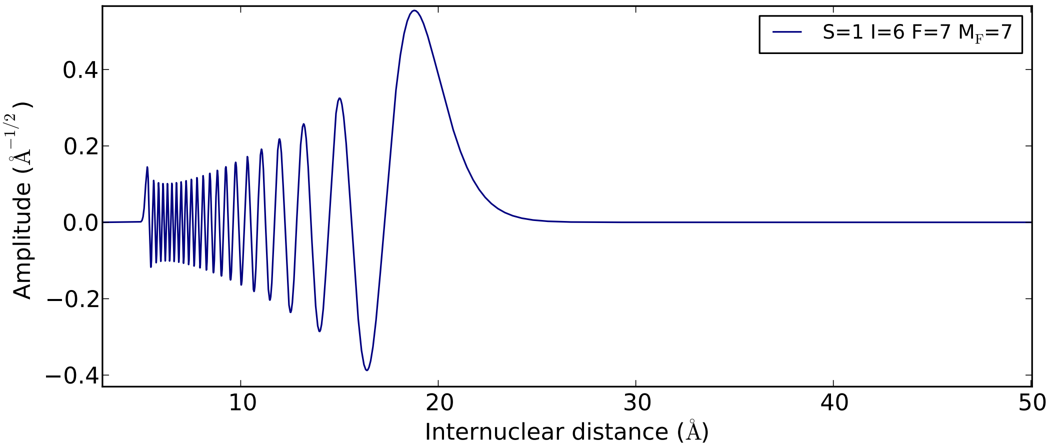

Figure 6.4: ^{85}RbCs bound-state wavefunction for the state which causes the resonance around 370 G. The wavefunction is represented by a single component of the $|SIFM_F\rangle$ basis.

6.1.6 Bound states of ^{6}Li$_2$

Unlike RbCs, the bound states of ^{6}Li$_2$ are well-defined by the $|SIFM_\mathrm{F}\rangle$ quantum numbers. There are two bound states near threshold in the region from 0 to 1000 G. At energies well below threshold then both of the states are strongly singlet in character. The state which appears at slightly lower fields is the $|SIFM_\mathrm{F}\rangle = |0,2,2,0\rangle$ state and the state which appears at slightly higher fields is the $|SIFM_\mathrm{F}\rangle = |0,0,0,0\rangle$ state. The $|0,2,2,0\rangle$ state causes the resonance at 543 G, whereas the $|0,0,0,0\rangle$ state has an avoided crossing with a pure triplet state which exists just above threshold. The bound states, calculated using restricted and unrestricted basis sets, are shown in Fig. 6.5. The states calculated using the $|SIFM_\mathrm{F}\rangle$ basis restricted to $S = 0$ are degenerate and correspond to the $\nu = 38$ vibrational level of the singlet potential. The highest-lying triplet state is around 2000 MHz below threshold and therefore is not shown. The wavefunction of the bound state which causes the resonance around 543 G is shown in Fig. 6.6.

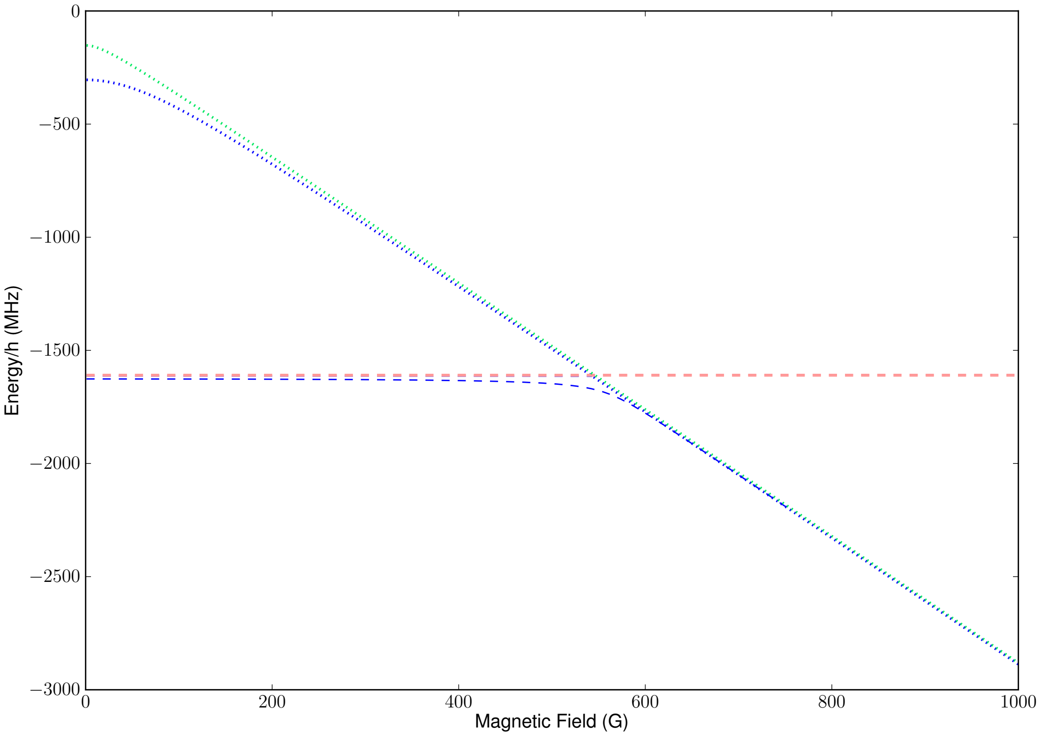

Figure 6.5: Bound states of ^{6}Li$_2$ in an $L = 0$ basis, calculated from: a complete basis (blue dashed), a restricted basis including $S = 1$ only (green dashed - no state exists in the region shown), a restricted basis including $S = 0$ only (pink dashed). The thresholds for each basis set are shown in the corresponding colour with dotted lines (note for $S = 0$ only the threshold does not appear as it occurs at 0 MHz).

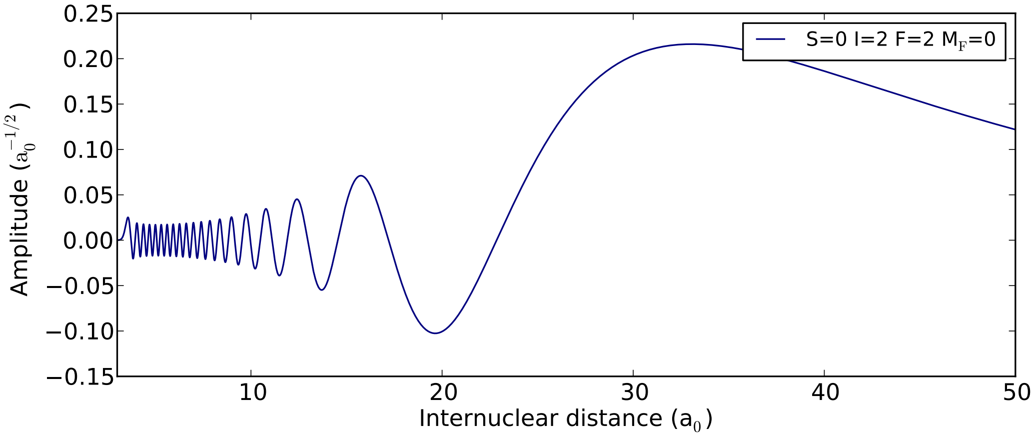

Figure 6.6: ^{6}Li$_2$ bound-state wavefunction for the state which causes the resonance around 543 G. The wavefunction is represented by a single component of the $|SIFM_F\rangle$ basis

6.2 Transformation of the product states of the field-dressed Hamiltonian to the $|SM_S m_{i,a} m_{i,b}\rangle$ basis set

The asymptotic energy levels of an alkali atom in a magnetic field are determined from the eigenvalues of the Breit-Rabi Hamiltonian, which defines a set of field-dressed eigenfunctions for each atom. To calculate the singlet and triplet fraction of the products of field-dressed atomic eigenfunctions, represented by $|\alpha, m_{f,a}\rangle\,|\beta, m_{f,b}\rangle$, we perform a transformation from the field-dressed basis to the $|SM_s m_{i,a} m_{i,b}\rangle$ basis. For a given m_f, each state in the field-dressed basis can be re-written as a superposition of its $|m_s, m_i\rangle$ contributions. The $|m_s, m_i\rangle$ basis can then be transformed using 3-j symbols to the $|SM_s m_{i,a} m_{i,b}\rangle$ basis.

To transform between the asymptotic $|\alpha, m_{f,a}\rangle$ basis and the $|m_s, m_i\rangle$ basis we use the Breit-Rabi hamiltonian,

$$\begin{aligned}\hat{H}_a &= \zeta_{\rm hfs}\hat{\imath}_a \cdot \hat{s}_a + \frac{\mu_{\rm B}}{\hbar}\left(g_s\hat{s}_a + g_n\hat{\imath}_a\right)B \\ &= \zeta_{\rm hfs}\left(\hat{\imath}_{z,a}\hat{s}_{z,a} + \frac{1}{2}\left(\hat{\imath}_+\hat{s}_- + \hat{\imath}_-\hat{s}_+\right) + \frac{\mu}{\hbar}\left(g_s\hat{s}_{z,a} + g_n\hat{\imath}_{z,a}\right)B\right),\end{aligned}$$

where $\hat{j}_\pm$ are the raising and lowering operators and $\hat{j}_z\,|jm\rangle = m\,|jm\rangle$. We restrict ourselves to the case of two alkali-metal atoms such that $m_s = \pm 1/2$ and $m_i = m_f \mp 1/2$. For each m_f we therefore need to calculate a two-by-two Hamiltonian, which will have diagonal terms

$$\langle\pm|\hat{H}|\pm\rangle \equiv \zeta_{\rm hfs}\left(\pm\frac{1}{2}\right)\left(m_f \mp \frac{1}{2}\right) + \frac{\mu_{\rm B}}{\hbar}\left(g_s\left(\pm\frac{1}{2}\right) + g_n\left(m_f \mp \frac{1}{2}\right)\right),$$

and off-diagonal terms

$$\langle\mp|\hat{H}|\pm\rangle \equiv \frac{\zeta_{\rm hfs}}{2}\left(\left(i+\frac{1}{2}\right)^2 - m_f^2\right)^{\frac{1}{2}}.$$

We can then extract the eigenvalues, $\lambda_\pm$, and from them calculate the eigenvectors

$$\begin{pmatrix} \hat{H}_{1,1} & \hat{H}_{1,2} \\ \hat{H}_{2,1} & \hat{H}_{2,2} \end{pmatrix} = \begin{pmatrix} \cos\theta & \sin\theta \\ -\sin\theta & \cos\theta \end{pmatrix} \begin{pmatrix} \lambda_+ & 0 \\ 0 & \lambda_- \end{pmatrix} \begin{pmatrix} \cos\theta & -\sin\theta \\ \sin\theta & \cos\theta \end{pmatrix}$$

such that each $|\alpha, m_f\rangle$ basis can be written as a sum of $|m_s, m_i\rangle$ basis terms,

$$\begin{aligned} |\alpha_+, m_f\rangle &= \cos\theta\,|1/2, m_f - 1/2\rangle + \sin\theta\,|-1/2, m_f + 1/2\rangle \\ |\alpha_-, m_f\rangle &= -\sin\theta\,|1/2, m_f - 1/2\rangle + \cos\theta\,|-1/2, m_f + 1/2\rangle\,. \end{aligned}$$

Combining the results for each atom, in the γ_+ states for example, gives

$$\begin{aligned} |\alpha_+, m_{f_a}\rangle\,|\beta_+, m_{f_b}\rangle = \quad & \cos\theta_a\cos\theta_b\,|1/2, m_{f,a} - 1/2\rangle\,|1/2, m_{f,b} - 1/2\rangle \\ & + \cos\theta_a\sin\theta_b\,|1/2, m_{f,a} - 1/2\rangle\,|-1/2, m_{f,b} + 1/2\rangle \\ & + \sin\theta_a\cos\theta_b\,|-1/2, m_{f,a} + 1/2\rangle\,|1/2, m_{f,b} - 1/2\rangle \\ & + \sin\theta_a\sin\theta_b\,|-1/2, m_{f,a} + 1/2\rangle\,|-1/2, m_{f,b} + 1/2\rangle\,. \end{aligned}$$

Each coefficient of the type $\cos\theta_a \sin\theta_b$ is denoted $C_{m_{s_a} m_{i_a} m_{s_b} m_{i_b}}$. To find the total singlet or triplet percentage in an individual $|\alpha, m_{f_a}\rangle\,|\beta, m_{f_b}\rangle$ requires the sum

$$\begin{aligned} |\alpha, m_{f_a}\rangle\,|\beta, m_{f_b}\rangle &= \sum_{m_{s_{a,b}} m_{i_{a,b}}} C_{m_{s_a} m_{i_a} m_{s_b} m_{i_b}}\,|m_{s_a}, m_{i_a}, m_{s_b}, m_{i_b}\rangle \\ &= \sum_{S, M_S, m_{i,a}, m_{i,b}} |SM_S\rangle\,|m_{i,a}\rangle\,|m_{i,b}\rangle \sum_{m_{s_{a,b}}} C_{m_{s_a} m_{i_a} m_{s_b} m_{i_b}}\,\langle SM_S|m_{s_a} m_{s_b}\rangle\,|m_{i_a}\rangle\,|m_{i_b}\rangle\,, \end{aligned}$$

where $\langle SM_S|m_{s_a} m_{s_b}\rangle$ are Clebsch-Gordan coefficients. In the singlet case, $S = 0$ and $M_{\rm S} = 0$ and the Clebsch-Gordan coefficients are

$$\langle SM_S|s_a m_{s_a}, s_b m_{s_b}\rangle = \langle 00|1/2 m_{s_a}, 1/2 m_{s_b}\rangle = \delta_{m_{s_a}, -m_{s_b}} \frac{(-1)^{1/2 - m_{s_a}}}{\sqrt{2}}.$$

The triplet fraction of each field-dressed atomic eigenfunctions, corresponding to the $(2,3)$ hyperfine manifold at zero field, of ^{85}RbCs is shown in Fig. 6.7. Each state is labelled by its $(m_{f_{\rm Rb}}, m_{f_{\rm Cs}})$ and has $(f_{\rm Rb}, f_{\rm Cs}) = (2,3)$ quantum numbers at zero field although the

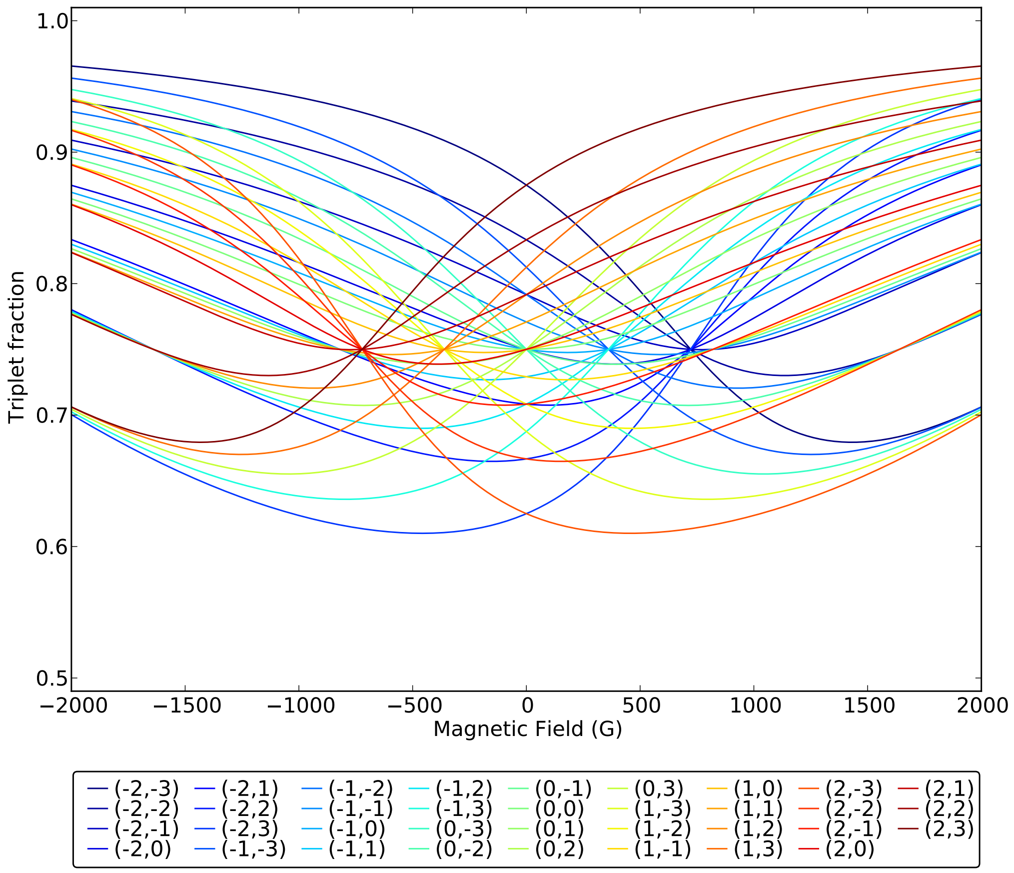

Figure 6.7: Triplet fraction of the products of the field-dressed atomic eigenfunctions of ^{85}RbCs. Each state is labelled by its zero-field $(m_{f_{\rm Rb}}, m_{f_{\rm Cs}})$ quantum number and correlates with $(f_{\rm Rb}, f_{\rm Cs}) = (2, 3)$ at zero field although the different f levels will be mixed at higher fields.

different f levels will be mixed at higher fields. The other eigenfunctions corresponding the higher hyperfine manifolds are shown in Appendix F. All of the states show significant triplet character and tend towards full triplet character at high fields. The average value is centred around 3/4 triplet character at zero field as expected. In the other hyperfine manifolds all states tend towards either 100% or 50% triplet character at high field, and no state ever drops below 50% triplet character. This result was checked by examining the value of each $\langle SM_S|\alpha m_{f,a}\beta m_{f,b}\rangle$ element and verifying that the sum of squares of the rows and columns was equal to one. This results means that all the thresholds of ^{85}RbCs have at least 50% triplet character and that most are triplet dominated. This explains why the background scattering length of different incoming channels is often close to the triplet scattering length, but never close to the singlet scattering length.

Chapter 7

Effective Range Theory

The work presented in this Chapter comes from the work published in [78]. Studies of cold atom collisions and few-body interactions often require the energy dependence of the scattering phase shift, which is usually expressed in terms of an effective-range expansion. In this Chapter we use accurate coupled-channel calculations on ^{6}Li, ^{39}K and ^{133}Cs to explore the behavior of the effective range in the vicinity of both broad and narrow Feshbach resonances and show that commonly used expressions for the effective range break down dramatically for narrow resonances and near the zero-crossings of broad resonances. We present an alternative parametrization of the effective range that is accurate through both the pole and the zero-crossing for both broad and narrow resonances and further demonstrate that an analytical form of an energy and magnetic field-dependent phase shift, based on multichannel quantum defect theory, gives accurate results for the energy-dependent scattering length.

7.1 Introduction to Effective Range Theory

The study of trapped samples of ultracold atomic gases is an extremely fruitful area of experimental and theoretical research. It includes studies of Bose-Einstein condensation (BEC) of bosonic species [204–207], the crossover between the BEC and Bardeen-Cooper-Schrieffer regimes of fermionic species [208–210], the production of ultracold polar molecules [67, 69, 211], the manipulation of atoms in optical lattices [212, 213], and the study of Efimov physics in few-body systems [214–217]. The theory of such phenomena has been greatly simplified by the ability to characterize the zero-energy interaction of two atoms in terms of the s-wave scattering length a. For many species, nearly any desirable value $a(B)$ can be obtained by tuning a magnetic field B near the pole position B_0 of a threshold scattering resonance known as a Feshbach resonance. The scattering length is approximately related to the magnetic field by the formula [90]

$$a(B) = a_{\mathrm{bg}} \left(1 - \frac{\Delta}{B - B_0}\right), \tag{7.1.1}$$

where Δ is the width of the resonance and a_{bg} is the background scattering length far from resonance.

The parametrization of low-energy interactions in terms of $a(B)$ allows the detailed chemical interaction between two ultracold atoms in the limit of zero collision kinetic energy $E \to 0$ to be replaced by a zero-range Fermi pseudo-potential whose strength is proportional to $a(B)$. However, as experimental probes of ultracold systems become more powerful and sophisticated, the variation of atomic interactions as a function of energy away from exactly $E = 0$ must be considered and understood. The usual way to describe the variation with energy of the near-threshold s-wave scattering phase shift $\eta(E)$ is to use an effective-range expansion at small collision momentum $\hbar k$, where $E = \hbar^2 k^2/(2\mu)$ and μ is the reduced mass of the two atoms [218, 219],

$$k \cot \eta(E) = -\frac{1}{a_0} + \frac{1}{2} r_{\mathrm{eff}} k^2 + \dots\,, \tag{7.1.2}$$

where the parameter r_{eff} is called the effective range and a_0 is the zero-energy scattering length. We prefer a modified way of writing this expression and define the energy-dependent scattering length $a(E)$ by [89],

$$a(E) = -\frac{\tan \eta(E)}{k} = \frac{1}{ik} \frac{1 - S(E)}{1 + S(E)}, \tag{7.1.3}$$

where $S = e^{2i\eta}$ is the diagonal element of the unitary S-matrix for the threshold channel in question. With this formulation, both $\eta(E)$ and $a(E)$ are real when only elastic scattering is possible but become complex in the presence of inelasticity. Eq. (7.1.2) becomes

$$a(E)^{-1} = a_0^{-1} - \frac{1}{2} r_{\mathrm{eff}} k^2 + \dots\,, \tag{7.1.4a}$$

or

$$a(E) = a_0 + \frac{1}{2} r_{\mathrm{eff}} a_0^2 k^2 + \dots\,. \tag{7.1.4b}$$

Far from a pole or a zero-crossing in $a_0(B)$, finite-difference equations based on either of these relationships may be used to evaluate r_{eff}. However, those based on (7.1.4a) are numerically unstable near a zero-crossing and those based on (7.1.4b) are numerically unstable near a pole.

Effective-range expansions have been invoked to include the role of collisions at finite energy in few-body phenomena [220–224] and to correct for the zero-point energy in optical lattice physics [225]. The energy-variation of the phase shift is needed to obtain the contribution of two-body collisions to low-energy partition functions and thermodynamic properties of cold gases [226]. The effective range is known to vary around Feshbach resonances [215, 224, 227–230], but there has been no in-depth numerical study of the behaviour of $\eta(E)$, $a(E)$ and $r_{\rm eff}$ as B is tuned across Feshbach resonances of different types. In the present work we use accurate coupled-channels calculations to explore this numerically for both broad and narrow Feshbach resonances. Our calculations demonstrate that the effective-range expansion can fail in some circumstances for low-energy atomic collisions and also elucidate the range of applicability of simple approximations that have been developed to relate the effective range to the scattering length, given the form of the long-range potential [231]. We also present an approach based on multichannel quantum defect theory (MQDT) [231], which gives an analytic form for the energy-dependence of the phase shift that applies even when the effective-range expansion breaks down. We will demonstrate that this analytic representation gives excellent agreement with coupled-channels calculations for both broad and narrow resonances.

We choose to study resonances in ^{6}Li, ^{133}Cs and ^{39}K, in their lowest possible s-wave collision channels, all of which are important in studies of Efimov physics [173, 215–217, 232–236]. The interaction potentials used in the coupled-channels calculations are those of Zürn *et al.* [237] for ^{6}Li, Berninger *et al.* [166, 217] for ^{133}Cs, and Falke *et al.* [238] for ^{39}K. The atomic hyperfine/Zeeman states are labelled using Roman letters a,b,c, etc., in increasing order of energy.

7.2 Behaviour of the effective range near a Feshbach resonance

In this Section we analyse the behaviour of the effective range in the vicinity of Feshbach resonances of different types. A magnetically tunable resonance can be classified as broad or narrow, based on the parameter $s_{\rm res}$ [35], as described in Sec. 2.4 Using these scalings allow us to define dimensionless length and energy parameters, $a/\bar{a}$ and $E/\bar{E}$, respectively.

In the following discussion resonances with $s_{\rm res} > 1$ are referred to as broad resonances, whilst those with $s_{\rm res} < 1$ are narrow resonances.

The effective-range expansion is the leading term in a Taylor series and breaks down at 'high' energies. However, in the present work it is always valid up to at least $E/k_{\rm B} = 50$ nK. We therefore obtain $r_{\rm eff}$ at each magnetic field by performing coupled-channels calculations at 1 pK and 10 nK and fitting the resulting values of $a(E)$ from Eq. (7.1.3) to either Eq. (7.1.4a) or Eq. (7.1.4b). The coupled-channels calculations are performed using the MOLSCAT package [110], adapted to handle collisions in external fields [112]. Calculations are carried out with a fixed-step log-derivative propagator [105] at short range and a variable-step Airy propagator [142] at long range. The wavefunctions are matched to their long-range solutions, the Ricatti-Bessel functions, to find the S-matrix elements; these are related to the energy-dependent scattering length and phase shift by Eq. (7.1.3).

Gao [228] and Flambaum *et al.* [229] have developed an approximate formula relating $r_{\rm eff}$ to a, based on the case of single-channel scattering with an R^{-6} potential,

$$r_{\rm eff} \approx \left(\frac{\Gamma(1/4)^4}{6\pi^2}\right)\bar{a}\left[1-2\left(\frac{\bar{a}}{a_0}\right)+2\left(\frac{\bar{a}}{a_0}\right)^2\right]. \tag{7.2.1}$$

We show below that this formula works well near the pole of a broad resonance, but may break down around a zero-crossing. In particular, Eq. (7.2.1) predicts that $r_{\rm eff}$ is always positive, which is not in fact the case. For narrow resonances, we demonstrate that the parabolic dependence on $1/a_0$ is retained, but quite different coefficients are required.

The scattering length $a(B)$ and effective range $r_{\rm eff}(B)$ for ^{133}Cs, in the $(f, m_f) = (3, +3) + (3, +3)$ s-wave scattering channel (designated aa), are shown in Figure 7.1. In this channel the scattering length has many resonances between 0 and 1000 G which overlap and interfere with each other; however, we highlight three distinct magnetic-field regions that correspond to different scattering-length behaviours. Around 17 G there is a zero-crossing in the scattering length due to a wide resonance, here the effective range diverges to positive values. At the zero-crossing due to a narrow resonance at 227 G the effective range diverges to negative values. Near the pole of the wide resonance at 787 G the effective range is a slowly varying function of magnetic field.

To contrast the behaviour of the effective range across broad and narrow resonances, we consider ^{6}Li in its lowest $(f, m_f) = (1/2, +1/2) + (1/2, -1/2)$ s-wave scattering channel (designated ab). Using an $L = 0$ (s-only) basis set, the scattering length for this channel has only two resonances at fields below 1000 G, one broad near 832 G ($\Delta = -262$ G) and

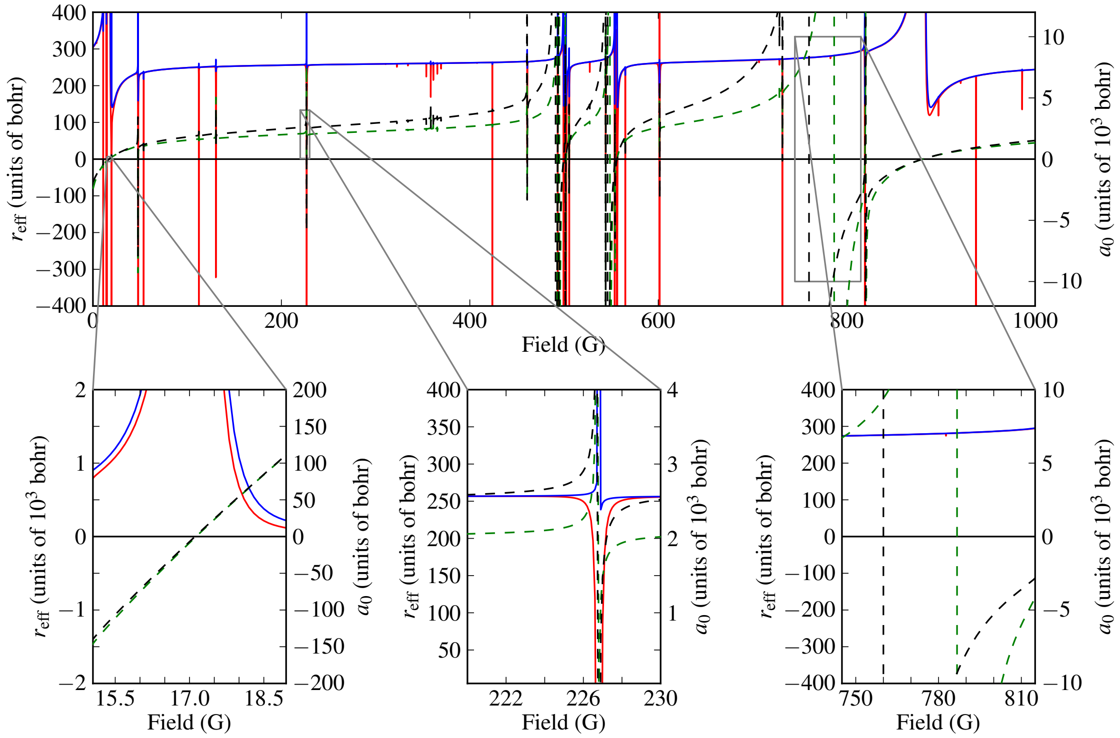

Figure 7.1: Top: The field-dependent effective range for the $(f, m_f) = (3, +3) + (3, +3)$ channel of ^{133}Cs from coupled-channel calculations (red solid) and as calculated from Eq. (7.2.1) (blue solid). The zero-energy s-wave scattering length (green dashed) and the s-wave scattering length at 1 μK (black dashed) are also shown. Bottom left: An expanded view around the zero-crossing of the scattering length at 17 G. Bottom centre: An expanded view around the narrow resonance at 227 G. Bottom right: An expanded view around the pole of the wide resonance at 787 G.

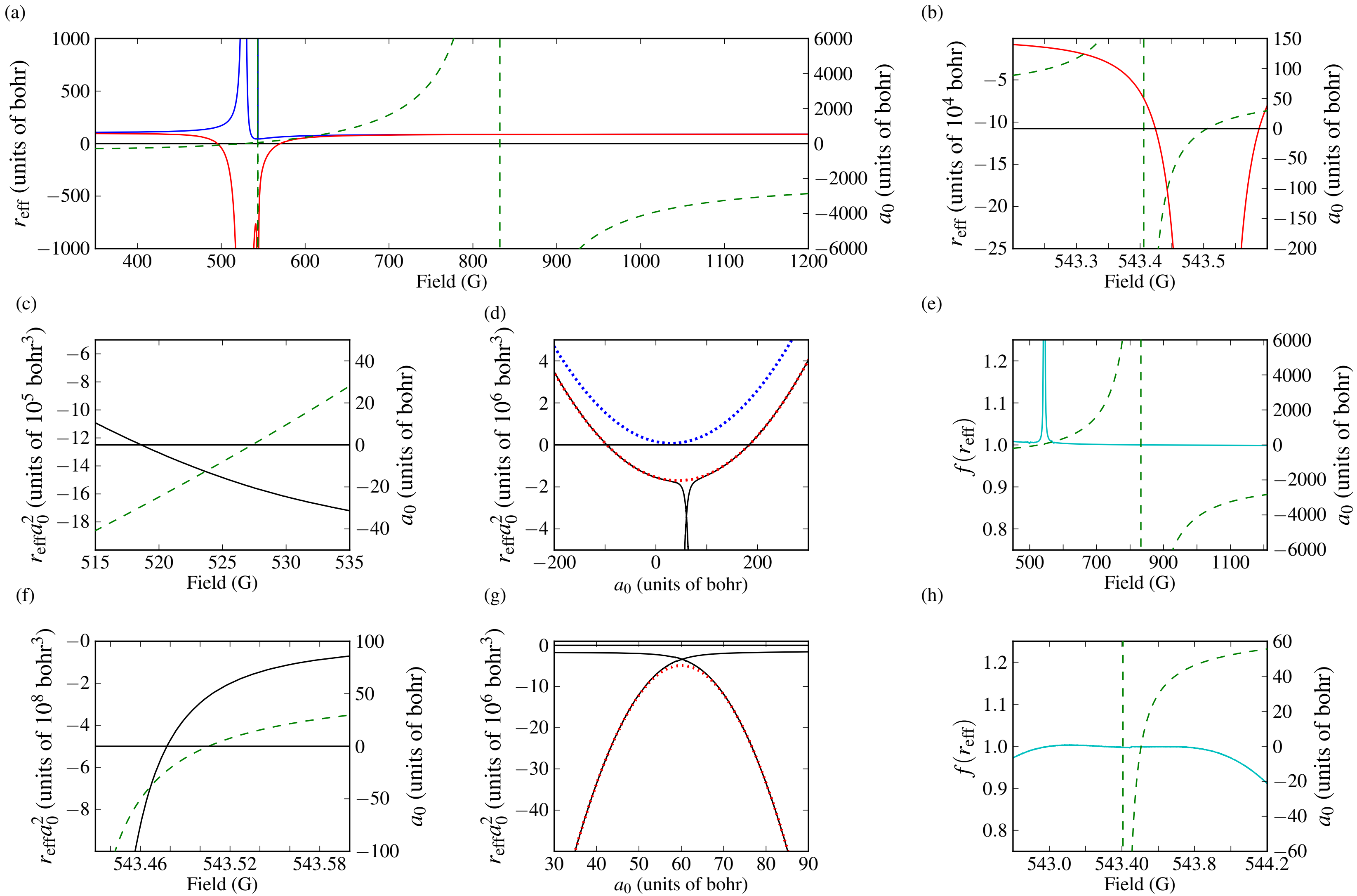
(a)
$r_{\rm eff}$ (units of bohr)
1000
500
0
−500
−1000
6000
4000
2000
0
−2000
−4000
−6000
a_0 (units of bohr)
400
500
600
700
800
900
1000
1100
1200
Field (G)
(b)
$r_{\rm eff}$ (units of 10^4 bohr)
−5
−10
−15
−20
−25
150
100
50
0
−50
−100
−150
−200
543.3
543.4
543.5
Field (G)
(c)
$r_{\rm eff}a_0^2$ (units of 10^5 bohr^3)
−6
−8
−10
−12
−14
−16
−18
40
20
0
−20
−40
515
520
525
530
535
Field (G)
(d)
$r_{\rm eff}a_0^2$ (units of 10^6 bohr^3)
4
2
0
−2
−4
−200
0
200
a_0 (units of bohr)
(e)
$f(r_{\rm eff})$
1.2
1.1
1.0
0.9
0.8
6000
4000
2000
0
−2000
−4000
−6000
500
700
900
1100
Field (G)
(f)
$r_{\rm eff}a_0^2$ (units of 10^8 bohr^3)
−0
−2
−4
−6
−8
100
50
0
−50
−100
543.46
543.52
543.58
Field (G)
(g)
$r_{\rm eff}a_0^2$ (units of 10^6 bohr^3)
0
−10
−20
−30
−40
30
40
50
60
70
80
90
a_0 (units of bohr)
(h)
$f(r_{\rm eff})$
1.2
1.1
1.0
0.9
0.8
60
40
20
0
−20
−40
−60
543.0
543.40
543.8
544.2
Field (G)

Figure 7.2 ***(previous page)*:** (a) The field-dependent effective range for the $(f, mf) = (1/2, 1/2) + (1/2, -1/2)$ channel of ^{6}Li from coupled-channel calculations (red solid or light gray) and as calculated from Eq. (7.2.1) (blue solid or dark gray). The zero-energy s-wave scattering length is also shown (green dashed). (b) An expanded view of (a) showing the narrow resonance at 543.40 G. (c) and (f) The quantity $r_{\mathrm{eff}}a_0^2$ (black solid), which is a smoothly varying function of magnetic field through the zero-crossing of a_0 (green dashed) for both the wide resonance (c) and the narrow resonance (f). (d) The quantity $r_{\mathrm{eff}}a_0^2$ (black), which is parabolic as a function of a_0 across the width of the wide resonance, except around the narrow resonance. The red dotted line shows the parabola $v + r_0(a_0 - a_{\mathrm{ext}})^2$ fitted to the coupled-channel results, while the blue dotted (upper) line shows the corresponding parabola from Eq. (7.2.2). (e) The function $f(r_{\mathrm{eff}})$ of Eq. (7.2.4) (cyan), with parameters appropriate for the wide resonance, which is constant across the width of the wide resonance in a_0 (green dashed) except around the narrow resonance. (g) the quantity $r_{\mathrm{eff}}a_0^2$ (black solid), which is parabolic as a function of a_0 across the width of the narrow resonance; the red dotted line shows the parabola $v + r_0(a_0 - a_{\mathrm{ext}})^2$ fitted to the coupled-channel results. (h) The function $f(r_{\mathrm{eff}})$ of Eq. (7.2.4) (cyan), with parameters appropriate for the narrow resonance, which is constant across the width of the narrow resonance in a_0 (green dashed).

the other narrow near 543.40 G ($\Delta = 0.10$ G) [237]. The system is somewhat unusual because the narrow resonance is close to the zero-crossing of the broad resonance. However, as the spacing in magnetic field between the two features is several orders of magnitude greater than the width of the narrow resonance, the overall behaviour of the two features is still distinct.

The scattering length $a(B)$ and effective range $r_{\mathrm{eff}}(B)$ for ^{6}Li are shown in Figure 7.2(a) between 200 and 1000 G. For the wide resonance, the effective range is a smooth function of magnetic field except near the zero-crossing in $a_0(B)$ close to 527 G, where it diverges to negative values. This may be contrasted with the behaviour of Gao's formula (7.2.1), also shown in Fig. 7.2, which diverges to positive values. The quantity $r_{\mathrm{eff}}a_0^2$, shown in Fig. 7.2(c) as a function of field, is continuous through the zero-crossing, but naturally diverges at the resonance pole, where r_{eff} itself does not. As shown in Fig. 7.2(d), it is close to parabolic as a function of a_0, except close to the narrow resonance. However, the parabola dips below zero between $a_0 = 183$ and -96 bohr, accounting for the fact that r_{eff} is negative in this region. The corresponding parabola from Gao's formula,

$$r_{\mathrm{eff}}a_0^2 \approx \left(\frac{\Gamma(1/4)^4}{6\pi^2}\right)\left[\bar{a}^3 + \bar{a}(a_0 - \bar{a})^2\right], \tag{7.2.2}$$

is also shown in Fig. 7.2(d). It is similar to the true parabola but is offset from it and is

System	$\bar{a}$ (bohr)	B_0 (G)	Δ (G)	$a_{\rm bg}$ (bohr)	$s_{\rm res}$
^{6}Li	29.88	832	−262	−1593	27
^{6}Li	29.88	543.40	0.10	59.0	8.1×10^{-4}
^{39}K	61.77	744.93	−0.005	−33.4	6.2×10^{-4}
^{133}Cs	96.62	226.73	0.076	2062	0.19
System	r_0 (bohr)	$a_{\rm ext}$ (bohr)	v (bohr^3)	$-2R^*$ (bohr)	$r_{\rm eff,bg}$ at $a_0 = a_{\rm bg}$
^{6}Li	87	43	-1.7×10^6	−2.2	90
^{6}Li	−71000	60	-4.9×10^6	−74000	44
^{39}K	−190000	−34	2.2×10^6	−200000	2100
^{133}Cs	−810	2800	1.8×10^9	−1000	260

Table 7.1: Parameters of Eq. (7.2.4) that characterize $r_{\rm eff}$ in the vicinity of resonances of different types.

positive everywhere, with a minimum value of $\bar{a}^3\Gamma(1/4)^4/6\pi^2 = 77840$ bohr^3 at $a_0 = \bar{a}$.

The values of $r_{\rm eff}a_0^2$ from coupled-channel calculations may be fitted to a parabola

$$r_{\rm eff}a_0^2 = v + r_0(a_0 - a_{\rm ext})^2, \tag{7.2.3}$$

with parameters given in Table 7.1. By construction, r_0 is the value of $r_{\rm eff}$ at the resonance pole. The quantity

$$f(r_{\rm eff}) = \frac{r_{\rm eff}a_0^2}{v + r_0(a_0 - a_{\rm ext})^2} \tag{7.2.4}$$

is almost constant across the whole width of the broad resonance, except close to the narrow resonance, as shown in Fig. 7.2(e).

In the narrow-resonance region, the effective range varies very fast with magnetic field even very close to the pole, as shown in Fig. 7.2(b). An expanded view of $r_{\rm eff}a_0^2$ in this region is shown in Fig. 7.2(g). It is clear that $r_{\rm eff}a_0^2$ is actually double-valued as a function of a_0: the narrow resonance contributes a second near-parabolic feature, but it has completely different parameters from the parabola for the broad resonance. We have fitted a parabola of the same form to points away from the region around $a_0 = 59$ bohr, where the narrow resonance reaches its background scattering length and rejoins with the wide resonance, and the resulting curve is shown in Fig. 7.2(g). The parameters of the parabola for the narrow resonance, also given in Table 7.1, bear no resemblance to those from Gao's formula (7.2.2).

Petrov [239] and Bruun *et al.* [240] introduced a parameter R^*, defined as

$$R^* = \frac{\hbar^2}{2\mu a_{\rm bg}\Delta\delta\mu} = \frac{\bar{a}}{s_{\rm res}}. \tag{7.2.5}$$

For narrow resonances, this is large and positive and is related to the effective range at the pole by $R^* \approx -r_0/2$. The values obtained from this expression are included in Table 7.1; it may be seen that R^* is within about 4% of $-r_0/2$ for the narrow resonance in ^{6}Li, but (as expected) bears no resemblance to it for the broad resonance.

To explore further the behaviour of the effective range around narrow resonances, we have carried out additional calculations on the resonances at 744.93 G in the $(f, m_f) = (1, +1) + (1, +1)$ s-wave channel of ^{39}K (designated aa) and at 226.73 G in the aa channel of Cs. The ^{39}K resonance is caused by an $L = 0$ bound state, whereas the Cs resonance is caused by an $L = 2$ bound state. The quantity $r_{\rm eff}a_0^2$ was again found to be close to parabolic in each case, with parameters given in Table 7.1. It may be seen that r_0 and v may have the same or different signs; when they are different, $r_{\rm eff}$ diverges at the zero-crossing with the opposite sign to its value at the pole. For narrow resonances, the position of the extremum in $r_{\rm eff}a_0^2$, $a_{\rm ext}$, is typically close to $a_{\rm bg}$. This is consistent with the expression given by Zinner and Thogerson [227] for $r_{\rm eff}$ in the vicinity of a narrow resonance, $r_{\rm eff} = r_0(1 - a_{\rm bg}/a_0)^2$. However, this expression gives $r_{\rm eff} = 0$ far from resonance. If we add a "background" effective range $r_{\rm eff,bg}$, this may be generalized to

$$r_{\rm eff} = r_{\rm eff,bg} + (r_0 - r_{\rm eff,bg}) \left(\frac{a_0 - a_{\rm bg}}{a_0} \right)^2 . \tag{7.2.6}$$

The resulting parabola for $r_{\rm eff}a_0^2$ is of the form of Eq. (7.2.3), with

$$a_{\rm ext} = a_{\rm bg}(1 - r_{\rm eff,bg}/r_0) \tag{7.2.7a}$$

and

$$v = a_{\rm bg}a_{\rm ext}r_{\rm eff,bg}. \tag{7.2.7b}$$

For resonances that are not very narrow, this effect can make $a_{\rm ext}$ significantly different from $a_{\rm bg}$, as seen for the Cs resonance at 226.73 G in Table 7.1. For the isolated resonances in ^{39}K and Cs, Gao's formula (7.2.1), evaluated for $a_0 = a_{\rm bg}$, gives $r_{\rm eff,bg}$ and hence v and $a_{\rm ext}$ within 10% of the values in Table 7.1.

Using Gao's formula (7.2.1) to define an $r_{\rm eff,bg}(B)$ which varies with magnetic field, Eq. (7.2.6) agrees with that of Werner and Castin [241] and Gao [230] and the resulting parabola $r_{\rm eff} a_0^2$ is of the form of Eq. (7.2.3) with

$$r_0 = -2R^* + \frac{\Gamma(1/4)^4}{6\pi^2}\bar{a}, \tag{7.2.8a}$$

$$a_{\rm ext} = \frac{-2R^* a_{\rm bg}}{r_0} - \frac{\Gamma(1/4)^4}{6\pi^2}\frac{\bar{a}^2}{r_0}, \tag{7.2.8b}$$

and

$$v = \left(-2R^* a_{\rm bg}^2 + 2\frac{\Gamma(1/4)^4}{6\pi^2}\bar{a}^3\right) - a_{\rm ext}^2 r_0. \tag{7.2.8c}$$

We find reasonable agreement with our values in Table 7.1 to those for r_0, $a_{\rm ext}$ and v calculated via Eq. (7.2.8), however there are some discrepancies. As the values in Table 7.1 were fitted around the whole resonance there will be some error introduced in the fitting due to the fact that the resonances are not completely isolated, but in fact overlap. In particular we find discrepancies in the ^{6}Li resonances which overlap each other. Eq. (7.2.3), together with parameters from Eqs. (7.2.1), (7.2.5) and (7.2.8), thus provides a useful approximate expression for $r_{\rm eff}$ in the vicinity of an isolated resonance that does not require coupled-channel calculations.

7.3 Limitations of the effective-range expansion

In this Section, we assess the range of energies over which the effective-range expansion provides an accurate representation of the energy-dependent scattering length. We consider the same 4 resonances as in Section 7.2, at collision energies ranging from 1 nK to 1 mK. For each resonance, we calculate the energy-dependent phase shift at multiple magnetic fields around the zero-energy pole position. For resonances at the lowest atomic threshold, the state responsible for the resonance is always bound on the low-field side of the zero-energy resonance pole. We therefore calculate $\eta(E)$ at one field just below the pole and several fields above it.

Fig. 7.3 compares the energy-dependent phase shift directly from coupled-channels calculations with that from the effective-range expansion, Eq. (7.1.2), using the accurate (field-dependent) values of $r_{\rm eff}$ from the previous Section. The values of the effective range at the specific fields shown are given in Table 7.2. Significant deviations can be seen for energies on the order of 1 μK. For Cs at $B = 226.80$ G, for example, the effective-range expansion is inadequate at energies above 200 nK, corresponding to $E/\bar{E} = 2 \times 10^{-3}$.

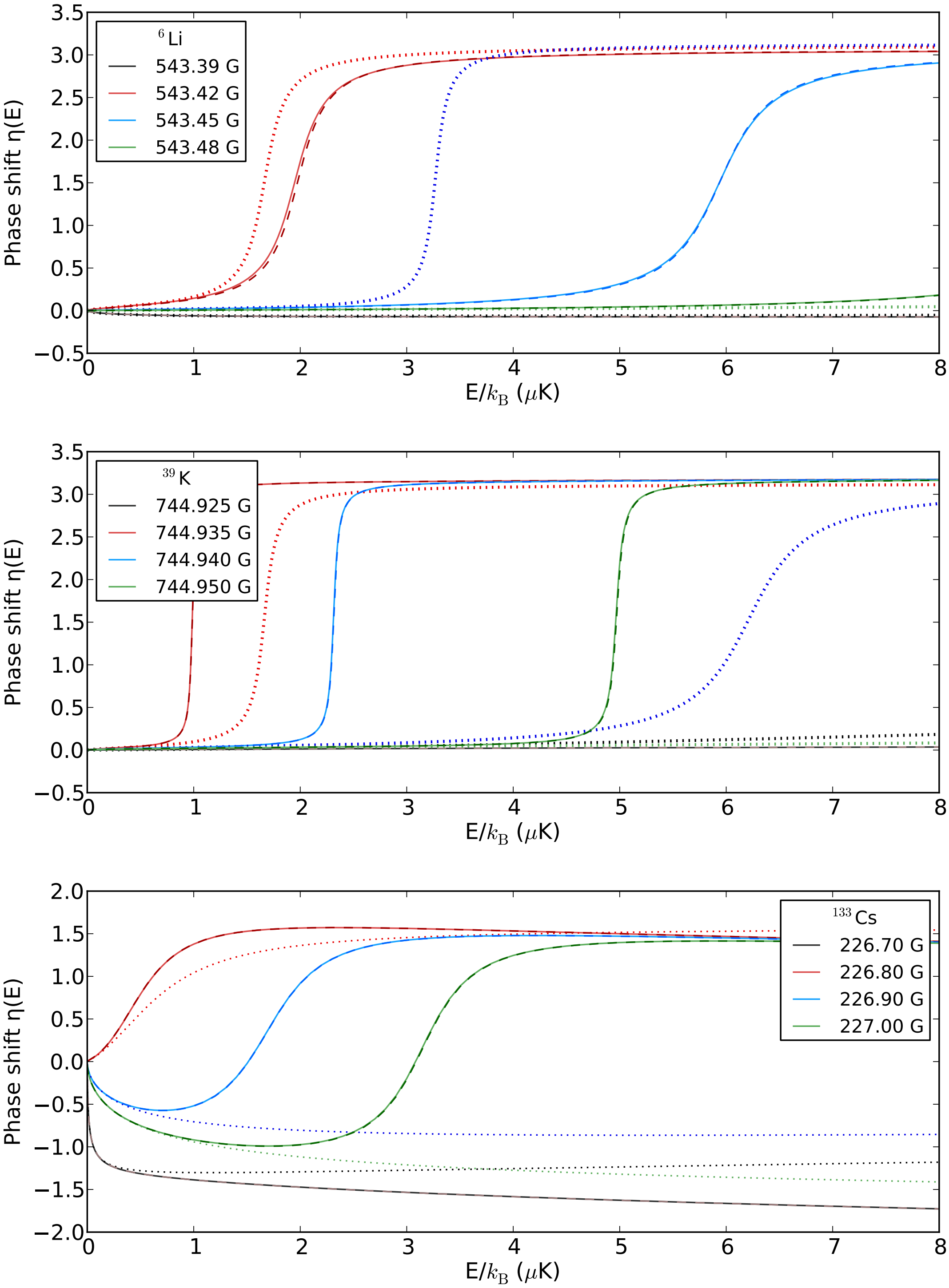

Figure 7.3: Energy dependence of the phase shift $\eta(E)$ at magnetic fields around narrow resonances in ^{6}Li, ^{39}K and ^{133}Cs. Coupled-channels calculations (solid lines) give the actual variation. The effective-range expansions (dotted lines) are given by Eq. (7.1.2), except for those at 543.48 G for ^{6}Li, 744.925 G for ^{39}K, and 226.80 G for ^{133}Cs, which are close to zeroes in $a_0(B)$ and are therefore calculated with the phase-shift form of Eq. (7.1.4b). The effective-range expansions deviate substantially from the coupled-channels results at collision energies on the order of μK.

Figure 7.3 *(previous page)*: The MQDT approach of Section 7.4 (dashed lines) gives an accurate representation of $\eta(E)$ over the full range of collision energies. Top: The resonance at $B_0 = 543.40$ G in the ab channel of ^{6}Li; center: The resonance at $B_0 = 744.93$ G in the aa channel of ^{39}K; bottom: The resonance at $B_0 = 226.73$ G in the aa channel of ^{133}Cs.

	B (G)	$a_0(B)$ (bohr)	$r_{\rm eff}$ (bohr)
^{6}Li	543.39	456.0	-5.4×10^4
	543.42	-362.5	-9.7×10^4
	543.45	-75.3	-2.3×10^5
	543.48	-20.8	-1.1×10^6
^{133}Cs	226.7	7680.6	-290
	226.8	-103.4	-4.6×10^5
	226.9	1152.2	-420
	227.0	1485.6	86
^{39}K	744.925	-4.6	-7.0×10^7
	744.935	-82.0	-6.6×10^4
	744.940	-54.1	-2.7×10^4
	744.950	-43.1	-8000

Table 7.2: Parameters for effective-range calculations. At each magnetic field, the zero-energy scattering length is given along with the effective range as calculated using the effective-range expansion.

On the high-field side of the pole, there is a quasibound state at low collision energy; as the energy passes through this, the phase shift η increases by π, and there is a pole in the energy-dependent phase shift $a(B)$ when $\eta(E) = \pi/2$; the location of this feature is not well captured by the effective-range expansion. This is particularly true for the Cs resonance at 226.73 G, where the non-resonant part of the phase shift has a general downwards trend as a function of energy.

We have also analysed the broad s-state resonance in ^{6}Li at 832 G, which has $s_{\rm res} \gg 1$, and the results are shown in Fig. 7.4. In this case the effective-range expansion is indistinguishable from the results from coupled-channels calculations.

7.4 MQDT approach to an energy-dependent phase shift

A more complete theory of the energy dependence of the phase shift may be formulated in the framework of Multichannel Quantum Defect Theory (MQDT). Julienne and Gao [231]

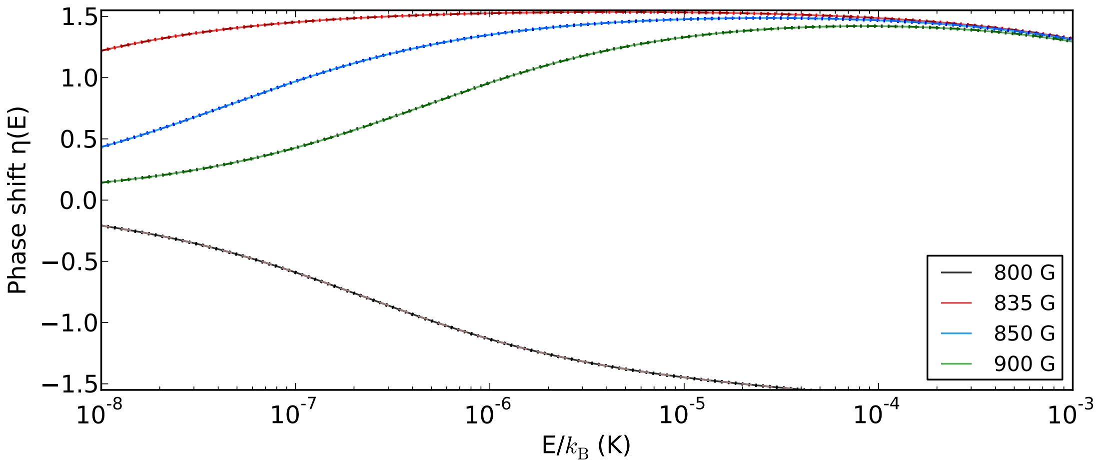

Figure 7.4: Energy dependence of the phase shift $\eta(E)$ at magnetic fields around the broad resonance in ^{6}Li. The results of coupled-channels calculations, the effective-range expansion and the MQDT approach are indistinguishable on this scale.

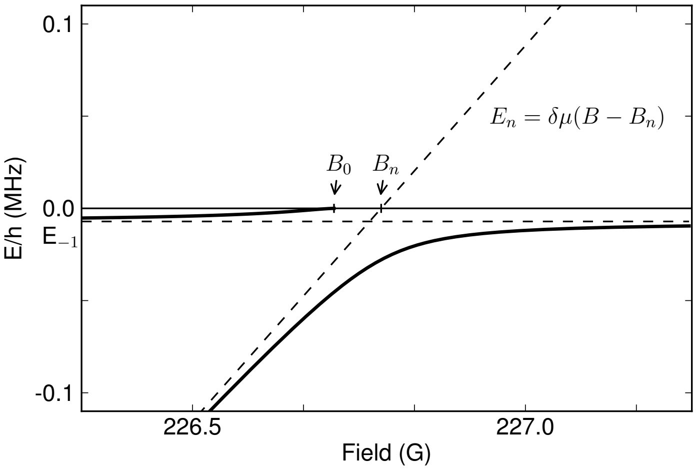

Figure 7.5: The resonance at 226.73 G in the $(f, m_f) = (3, +3) + (3, +3)$ channel of Cs. The two-channel model (dashed lines) includes a bare bound state which crosses threshold at B_n and a reference potential whose first bound level is at E_{-1}. The bound states from the coupled-channels calculations (solid lines) have have an avoided crossing with the resonance pole at B_0.

have described a two-channel MQDT approach to resonant scattering of ultracold atoms, combining the MQDT approach of Julienne and Mies [242, 243] with the analytic van der Waals theory of Gao [88, 228, 244, 245]. A similar theory has been described by Gao [246], but in quite different notation.

For an isolated resonance, the complex set of many coupled channels can be approximated by a two-channel model where the closed channel is represented by a 'bare' bound state with energy E_n and the open channel by a 'bare' continuum state characterized by the background scattering length of the resonance. The key quantities are illustrated in Fig. 7.5 for the ^{133}Cs resonance near 226.73 G. The energy of the bare bound state with respect to threshold is $E_n = \delta\mu(B - B_n)$. The phase shift at fixed magnetic field follows the Breit-Wigner form, $\eta(E) = \eta_{\rm bg} + \eta_{\rm res}(E)$, where $\eta_{\rm bg}$ is the background component and $\eta_{\rm res}$ is the resonant component,

$$\eta_{\rm res}(E) = -\tan^{-1}\left(\frac{\frac{1}{2}\Gamma_n}{E - E_0}\right). \tag{7.4.1}$$

Here Γ_n is the resonance width and the resonance position E_0 differs from E_n by a shift δE_n, with $E_0 = E_n + \delta E_n$. Near threshold, $\eta_{\rm bg}(E)$, $\Gamma_n(E)$ and $\delta E_n(E)$ are strongly energy-dependent and their functional forms may be obtained from MQDT.

MQDT connects the energy-insensitive short-range potential to the energy-sensitive long-range part of the potential, using the solutions for a reference potential that closely resembles the true potential at long range. The solutions for the reference potential are given at short range by WKB-normalized wavefunctions and at long range by asymptotic Bessel functions. However, at energies near threshold the WKB description breaks down at long range and the short-range solutions are connected to the long-range solutions using the MQDT functions $C(E)$ and $\tan\lambda(E)$. $C(E)$ describes the breakdown in the normalization of the WKB wavefunction at long range and scales the short-range solutions to match the long-range ones. In addition the regular and irregular WKB solutions propagated out of the short-range region lose their phase relationship, and this loss is corrected by a phase shift given by $\tan\lambda(E)$ [87]. At sufficiently high energies, the WKB wavefunctions are valid everywhere and $C(E) \to 1$ and $\tan\lambda(E) \to 0$.

The threshold behaviour of the resonance width and shift may be written in terms of the MQDT functions, $C_{\rm bg}(E)$ and $\tan\lambda_{\rm bg}(E)$ [242, 243],

$$\frac{1}{2}\Gamma_n(E) = \frac{1}{2}\bar{\Gamma}_n C_{\rm bg}(E)^{-2}; \tag{7.4.2a}$$

$$\delta E_n(E) = -\frac{1}{2}\bar{\Gamma}_n \tan\lambda_{\rm bg}(E). \tag{7.4.2b}$$

The full expression for the phase shift near a resonance is then

$$\eta(E, B) = \eta_{\rm bg}(E) + \eta_{\rm res}(E, B), \tag{7.4.3}$$

where

$$\eta_{\rm res}(E, B) = -\tan^{-1}\left(\frac{\frac{1}{2}\bar{\Gamma}_n C_{\rm bg}(E)^{-2}}{E - \delta\mu(B - B_n) + \frac{1}{2}\bar{\Gamma}_n \tan\lambda_{\rm bg}(E)}\right). \tag{7.4.4}$$

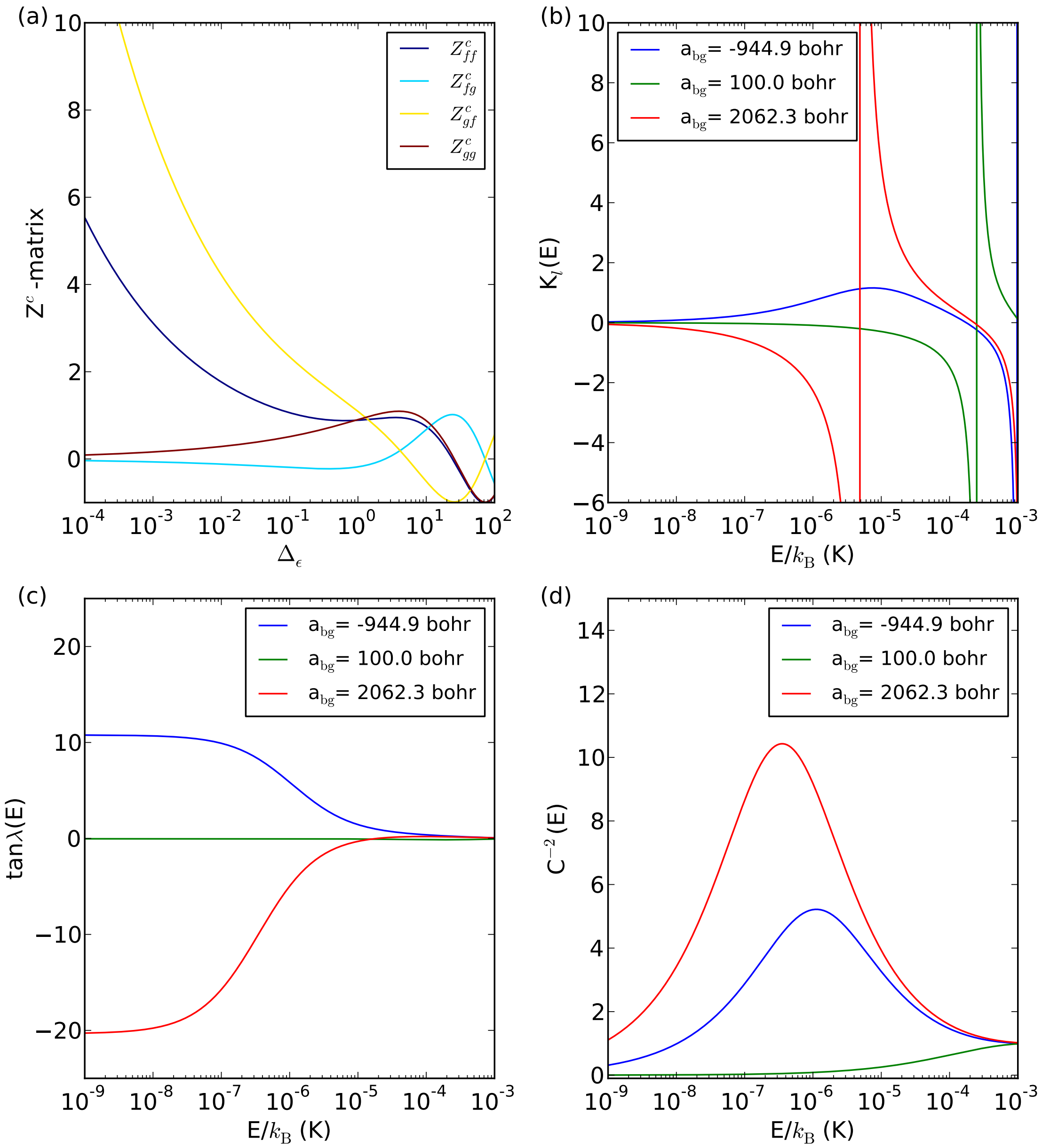

Figure 7.6: (a) The analytical functions that make the up the Z^c-matrix for the s-wave case as given in [88, 228, 244, 245], these functions vary only with scaled energy. (b) The function $K_l(E)$, (c) the function $\tan\lambda(E)$ and (d) the function $C^{-2}(E)$ for Cs, with a variety of different background scattering lengths. The behaviour of these functions is determined by the reduced mass, C_6 co-efficient and the background scattering length.

In the present work we follow Gao's work on analytical van der Waals theory [88, 228, 244, 245, 247, 248] and choose reference functions that have the correct long-range C_6 coefficient and directly reproduce the background scattering length of the resonance. The background phase shift $\eta_{\rm bg}(E)$ and the MQDT functions $C_{\rm bg}^{-2}(E)$ and $\tan\lambda_{\rm bg}(E)$ are then determined analytically by Gao's theory once the background scattering length $a_{\rm bg}$ is specified. The expression for $\eta_{\rm bg}(E)$ is given by [88],

$$K_l(E) = \tan\eta_{\rm bg}(E) = (K^c Z^c_{gg} - Z^c_{fg})(Z^c_{ff} - K^c Z^c_{gf})^{-1}. \tag{7.4.5}$$

K^c is a short-range parameter which results from the matching of the short-range and long-range solutions. Within this model it can be considered to be approximately constant in the region around threshold where its value is proportional to the background scattering length [228]. The $Z^c(E)$ functions are analytical functions of energy which depend only on the scaled energy of the system, shown in Fig. 7.6. The Z functions make up the Z-matrix which is defined as the transformation between the long-range energy normalised solutions and the short-range solutions with energy-independent normalisation [247]. Similar expressions for $C_{\rm bg}^{-2}(E)$ and $\tan\lambda_{\rm bg}(E)$ have been derived and implemented numerically by Gao [249]

$$\tan\lambda(E) = \frac{(Z^c_{ff} - K^c Z^c_{gf})(Z^c_{gf} + K^c Z^c_{ff}) + (Z^c_{fg} - K^c Z^c_{gg})(Z^c_{gg} + K^c Z^c_{fg})}{(Z^c_{ff} - K^c Z^c_{gf})(Z^c_{ff} - K^c Z^c_{gf}) + (Z^c_{fg} - K^c Z^c_{gg})(Z^c_{fg} - K^c Z^c_{gg})} \tag{7.4.6a}$$

$$C_{\rm bg}^{-2}(E) = \frac{1 + (K^c)^2}{(Z^c_{ff} - K^c Z^c_{gf})(Z^c_{ff} - K^c Z^c_{gf}) + (Z^c_{fg} - K^c Z^c_{gg})(Z^c_{fg} - K^c Z^c_{gg})}. \tag{7.4.6b}$$

The energy dependence of $\eta_{\rm bg}(E)$, $C_{\rm bg}^{-2}(E)$ and $\tan\lambda_{\rm bg}(E)$ for ^{133}Cs are shown in Fig. 7.6 for a variety of different $a_{\rm bg}$. The threshold behaviour (accurate for $ka_{\rm bg} \ll 1$) is $C_{\rm bg}^{-2}(E) \to k\bar{a}(1 + (a - r)^2)$ and $\tan\lambda_{\rm bg} \to 1 - r$ as $E \to 0$ [231], where $r = a_{\rm bg}/\bar{a}$. In this notation, $\frac{1}{2}\bar{\Gamma}_n$ is related to the magnetic resonance width Δ by

$$\frac{1}{2}\bar{\Gamma}_n = \frac{r}{1 + (1 - r)^2}\delta\mu\Delta. \tag{7.4.7}$$

To implement Eq. (7.4.4), we first carry out coupled-channel calculations of $a(B)$ and (if necessary) extrapolate to zero energy. We then fit the zero-energy scattering length to Eq. (7.1.1) to find the resonance position B_0, magnetic field width Δ and local $a_{\rm bg}$. Along with the van der Waals coefficient C_6 and the reduced mass μ, this allows us to find the MQDT parameters $C_{\rm bg}^{-2}(E)$ and $\tan\lambda_{\rm bg}(E)$ using Gao's analytic van der Waals routines [249]. The shift between B_n, the crossing of the bare bound state, and the

System	μ ($m_{\rm u}$)	$\bar{E}$ (mK)	$\bar{a}$ (bohr)	C_6 ($E_{\rm h}$bohr^6)	B_0 (G)	B_n (G)	$\delta\mu$ ($\mu_{\rm B}$)
^{6}Li	3.0076	32.3	29.88	1393.39	543.4	543.5	1.97
^{39}K	19.4819	1.17	61.77	3926.9	745.93	744.93	3.95
^{133}Cs	66.4527	0.14	96.62	6890.48	226.73	226.81	0.24

Table 7.3: The resonance parameters required for two-channel formula, along with those in Table 7.1.

coupled-channels resonance pole B_0 is

$$B_0 - B_n = \Delta r \left(\frac{1-r}{1+(1-r)^2} \right). \tag{7.4.8}$$

Lastly, we need $\delta\mu$, the difference between the magnetic moments of the bare bound state and the separated atoms. To obtain this, we carry out coupled-channel calculations on the near-threshold bound states of the system, using the approach described in Ref. [123]. Such calculations give the energies of real bound states rather than bare states, but it is usually straightforward to find a region of magnetic field where the energies are only weakly perturbed by avoided crossings, and to obtain magnetic moments by finite differences in this region. If necessary, pairs of crossing states could be deperturbed to find the properties of the underlying bare states, but this was not necessary in the present work. Typically 2-3 significant figures were found to be sufficient in our calculations.

7.5 Effectiveness of the MQDT formula

The MQDT formula for the energy-dependent phase shift, Eq. (7.4.4), was applied to the same set of narrow resonances discussed in Section 7.3. The parameters obtained for the MQDT approach are given in Table 7.3. Figure 7.3 compares the MQDT results with those obtained directly from coupled-channel calculations at a variety of fields around each resonance. There is excellent agreement in all cases, and MQDT succeeds in reproducing the complicated variation of the phase shift with both energy and field (which the effective-range expansion was unable to do). The MQDT approach also gives results indistinguishable from coupled-channel calculations for the broad resonance in ^{6}Li, shown in Fig. 7.4, although in this case the effective-range expansion is also successful, provided the field-dependence of $r_{\rm eff}$ is taken from coupled-channel calculations and not from an approximate formula.

The MQDT approach can be used to generate a smooth and accurate representation

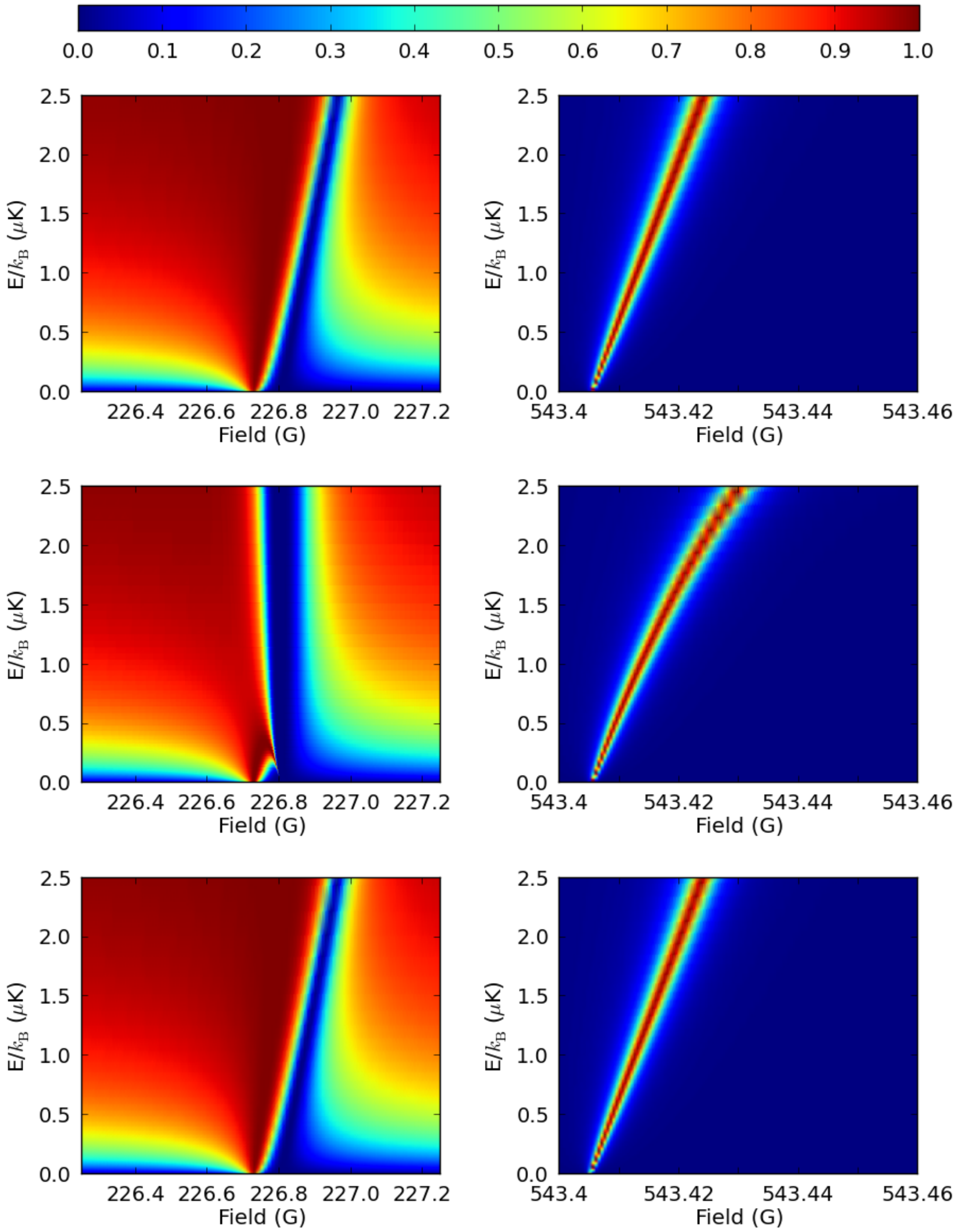

Figure 7.7: Contour plot of $\sin^2 \eta(E, B)$ for $E > 0$ where $E = 0$ is the energy of the two separated atoms. (Left) around the resonance at $B_0 = 226.73$ G in the $(f, m_f) = (3, +3) + (3, +3)$ channel of ^{133}Cs and (right) around the resonance at $B_0 = 543.40$ G in the $(1/2, +1/2) + (1/2, -1/2)$ channel of ^{6}Li. $\eta(E, B)$ is calculated using coupled-channel calculations (top), the effective-range expansion, Eq. (7.1.2), (middle), and the MQDT approach, Eq. (7.4.3), (bottom).

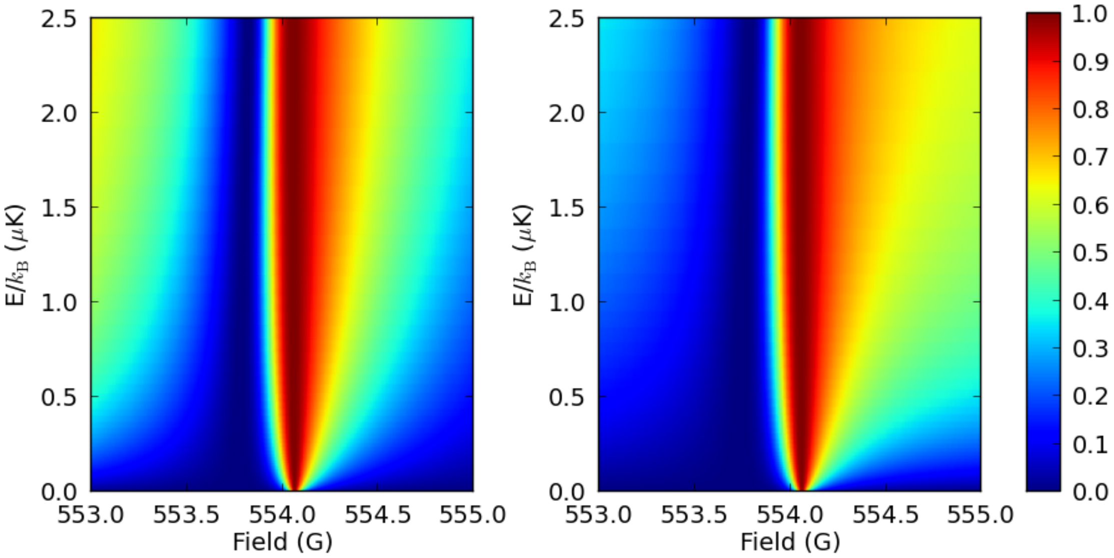

Figure 7.8: Contour plot of $\sin^2\eta(E,B)$ for $E > 0$ around the resonance at $B_0 = 554$ G in the $(f,m_f) = (3,+3)+(3,+3)$ channel of ^{133}Cs, where $E = 0$ is the energy of the two separated atoms. $\eta(E,B)$ is calculated using coupled-channel calculations (left) and the MQDT approach, Eq. (7.4.3), (right). Around the pole of the resonance where the value of $a_{\rm bg}$ fitted by the pole formula is roughly accurate then the MQDT approach works well, towards the edges of the resonance where the value of $a_{\rm bg}$ is shifted the formula breaks down.

of the resonance with magnetic field both near threshold and at higher energies. Figure 7.7 shows contour plots of $\sin^2\eta$ as a function of both magnetic field and energy over the width of the Cs resonance at 226.73 G and the Li resonance at 543.40 G, as obtained from coupled-channel calculations, from the effective range expansion using $r_{\rm eff}$ as given by the parabola determined by Eqs. (7.2.3) and from the MQDT approach. The states that arise in the two-channel model for this resonance are shown in Fig. 7.5. The shift from B_0 to B_n between the dressed and bare state pictures can be clearly seen. It may be seen that the MQDT approach reproduces the coupled-channel results very accurately over the whole range of energy and field, while the effective-range expansion does not. In particular, the peak of the resonance, where $\sin^2\eta = 1$ and $a(B) = \infty$, follows a quite incorrect path as a function of energy in the effective-range expansion.

All the calculations described above were carried out with MQDT functions that represent the 'bare' open channel derived from the local $a_{\rm bg}$ of the resonance, even if it is not the overall $a_{\rm bg}$ of the system. This approach works well for the examples discussed, but it is limited to resonances where $a_{\rm bg}$ remains reasonably constant over the width of the resonance. This is true for most resonances with $s_{\rm res} \ll 1$, unless they sit very close to the pole of a much wider resonance; under such circumstances, however, there can be a substantial variation in $a_{\rm bg}$ over the width of the resonance. As an example of this we consider the resonance at $B_0 = 554$ G in the aa channel of ^{133}Cs, which is close to the pole of a broad resonance at 548 G. In Fig. 7.8 the energy-dependent phase shift from coupled-channel calculations is compared to the results of the MQDT approach with fixed $a_{\rm bg}$. Whilst the MQDT approximation is good at fields close to the pole of the resonance, it quickly starts to fail at fields further away. This is because the two resonances need to be treated together as a pair of interfering, overlapping resonances [179] instead of treating them as independent. In such a case, the assumption of a constant background scattering length is valid only close to the resonance pole.

7.6 Conclusions

An accurate description of the energy dependence of the scattering phase shift and hence the scattering length is crucial to many experiments on few-body phenomena at finite temperatures. We have explored the behaviour of the commonly used effective-range expansion, and shown that is reasonably good at describing the energy dependence around broad resonances and away from zero-crossings in the scattering length. However, around narrow resonances the effective-range expansion can fail badly, even when the full field-dependence of the effective range is taken from coupled-channel calculations.

Gao [228] and Flambaum *et al.* [229] have developed an approximate formula relating the effective range $r_{\rm eff}$ to the scattering length. We have shown that this formula is reasonably accurate near the pole of a broad resonance, but even for broad resonances it breaks down badly near zero-crossings, and may give an effective range of the wrong sign. However, it is possible to write a modified form of the formula (with a different parabolic denominator) that gives a good representation of the effective range across the whole width of the resonance. For narrow resonances, an analogous parabolic form may still be used, but its parameters are completely different from those of Refs. [228] and [229].

To remedy the deficiencies of the effective-range expansion around narrow resonances, we advocate the use of an MQDT approach that fully describes the effect of a resonance as a function of both field and energy. This method entails representing the resonance in a two-channel model in which a bare bound state interacts with a bare continuum channel. The parameters of the model are obtained from coupled-channel calculations on the bound states and scattering length of the system. This MQDT approach successfully characterizes the behaviour of the resonance for both broad and narrow resonances. It can be used to include the role of collision at finite energy, correct for zero-point energy in lattices, and to evaluate thermodynamic properties of cold atoms and molecules.

The MQDT approach described here is accurate only for individual isolated resonances that have a reasonably constant background scattering term across their entire width. It is not uncommon to find cases of overlapping resonances where treating individual resonances as isolated can break down to a lesser or greater extent. A full treatment of overlapping resonances would require a multi-channel treatment such as the generalized MQDT model presented by Jachymski and Julienne [179]. The energy-dependent scattering length of this model should be capable of describing the complicated variation of the scattering phase shift with energy E and magnetic field B even when there are several resonances that overlap within their widths.

Our analytic expressions for the the near-threshold energy-dependent scattering length could benefit a number of active cold atom research areas mentioned in Sec. 7.1, since energies in the μK range are common with cold atom phenomena. This could be especially important for studies of optical lattice structures, where the finite zero-point or band energy can lead to significant corrections to the energy of confinement-induced resonances [225] and accounting for it requires the scattering length at finite energy [250, 251]. Accurate finite-energy corrections to the phase shift could also be significant for the equation of state of cold fermions [252] and for understanding few-body phenomena [220, 222].

Chapter 8

Radio-Frequency dressing of Feshbach resonances

Magnetic fields are often used to manipulate and control the behaviour of atoms and molecules. The prior chapters of this Thesis have dealt with the use of static fields and their effects on atomic interactions; however, oscillating fields such as radio-frequency (rf) fields can also be used to control atomic interactions. Radio-frequency fields have already been demonstrated to be of great use in ultracold gases as a probe of bound-state energies and as a method for associating and dissociating molecules [137, 253–256]. Both radio-frequency and microwave fields have also been used to create trapping potentials and to dress single species traps [257–259]. They have also been used to associate Efimov trimers [260, 261] and to enhance interactions between atoms in different lattice sites [262].

It has also been shown both theoretically and experimentally that radio-frequency fields can be used to create and manipulate Feshbach resonances [263–267], and to modify the background scattering length of a species [266, 268]. As discussed in Ref. [266] the coupling can occur through a variety of different mechanisms. The rf dressing couples additional channels to the incoming scattering channel which can lead to the creation of new resonances; it can also couple bound states together modifying their interaction with the incoming scattering channel; thirdly it causes avoided crossings in the atomic thresholds which modify the incoming channel and can cause significant changes in the background scattering length without a resonance existing.

The field has progressed from dealing with the dressing of atomic states to calculations on the interaction of molecules in radio-frequency and microwave fields. Microwave fields can be used as traps for cold polar molecules [269] and as a means of modifying and controlling molecular collisions [270–273]. In the following Chapter we will discuss the implementation of rf fields in MOLSCAT and the results obtained for rf dressing of the s-wave $(f, m_f) = (2, +2) + (3, +3)$ channel of ^{85}RbCs.

8.1 Collision Hamiltonian in a static magnetic field and radio-frequency field

The Hamiltonian for the interaction of two atoms in a combined static magnetic field B_z and an oscillating radio-frequency (rf) field of frequency ω_rf is

$$\hat{H} = \frac{\hbar^2}{2\mu}\left[-r^{-1}\frac{d^2}{dr^2}r + \frac{\hat{L}^2}{r^2}\right] + \hat{H}_1 + \hat{H}_2 + \hat{V}(r) + \hat{H}_{\omega_\mathrm{rf}}. \tag{8.1.1}$$

The monomer hamiltonians, $\hat{H}_1$ and $\hat{H}_2$, are

$$\hat{H}_i = \zeta_i \hat{i}_i \cdot \hat{s}_i + (g_\mathrm{e}\mu_\mathrm{B}\hat{s}_{iz} + g_\mathrm{n}\mu_\mathrm{B}\hat{i}_{iz})B_z + \hat{H}_{i,\mathrm{rf}}, \tag{8.1.2}$$

where $i = 1, 2$ and $\hat{H}_{i,\mathrm{rf}}$ is the interaction between atom i and the rf field. The rf-field term is given by

$$\hat{H}_{\omega_\mathrm{rf}} = \hbar\omega_\mathrm{rf}(a^\dagger a - N), \tag{8.1.3}$$

where ω_rf is the frequency of the applied field, N is the initial number of photons and $\hat{H}_{w_\mathrm{rf}}\left|N + n\right\rangle = n\hbar\omega_\mathrm{rf}$ where n represents the change in photon number from N. Following Refs. [259, 274] and [275], the interaction of the atom with the rf field is given by the coupling of the magnetic-dipole moment of the atom with the oscillating field such that

$$\hat{H}_{i,\mathrm{rf}} = -\mu_i \cdot B_\mathrm{rf}. \tag{8.1.4}$$

The rf field in quantised notation can be written as

$$B_\mathrm{rf} = \lambda\left(\epsilon a + \epsilon a^\dagger\right), \tag{8.1.5}$$

where $\lambda = B_\mathrm{osc}/\sqrt{2N}$, and ϵ is the polarisation vector of the rf field. Rewriting $\epsilon \cdot \mu_i$, with $\mu = g_\mathrm{e}\mu_\mathrm{B}\hat{s} + g_\mathrm{n}\mu_\mathrm{B}\hat{i}$, gives $\hat{H}_{i,\mathrm{rf}}$ for each polarisation:

$$\hat{H}_{i,\sigma_+} = \lambda g_\mathrm{e}\mu_\mathrm{B}(\hat{s}_{+1}\hat{a} + \hat{s}_{-1}\hat{a}^\dagger) + g_\mathrm{n}\mu_\mathrm{B}(\hat{i}_{+1}\hat{a} + \hat{i}_{-1}\hat{a}^\dagger) \tag{8.1.6}$$

$$\hat{H}_{i,\sigma_-} = \lambda g_\mathrm{e}\mu_\mathrm{B}(\hat{s}_{-1}\hat{a} + \hat{s}_{+1}\hat{a}^\dagger) + g_\mathrm{n}\mu_\mathrm{B}(\hat{i}_{-1}\hat{a} + \hat{i}_{+1}\hat{a}^\dagger) \tag{8.1.7}$$

$$\hat{H}_{i,\sigma_\mathrm{x}} = \frac{\lambda}{\sqrt{2}} g_\mathrm{e}\mu_\mathrm{B}(\hat{s}_{+1} - \hat{s}_{-1})(\hat{a} + \hat{a}^\dagger) + g_\mathrm{n}\mu_\mathrm{B}(\hat{i}_{+1} - \hat{i}_{-1})(\hat{a} + \hat{a}^\dagger). \tag{8.1.8}$$

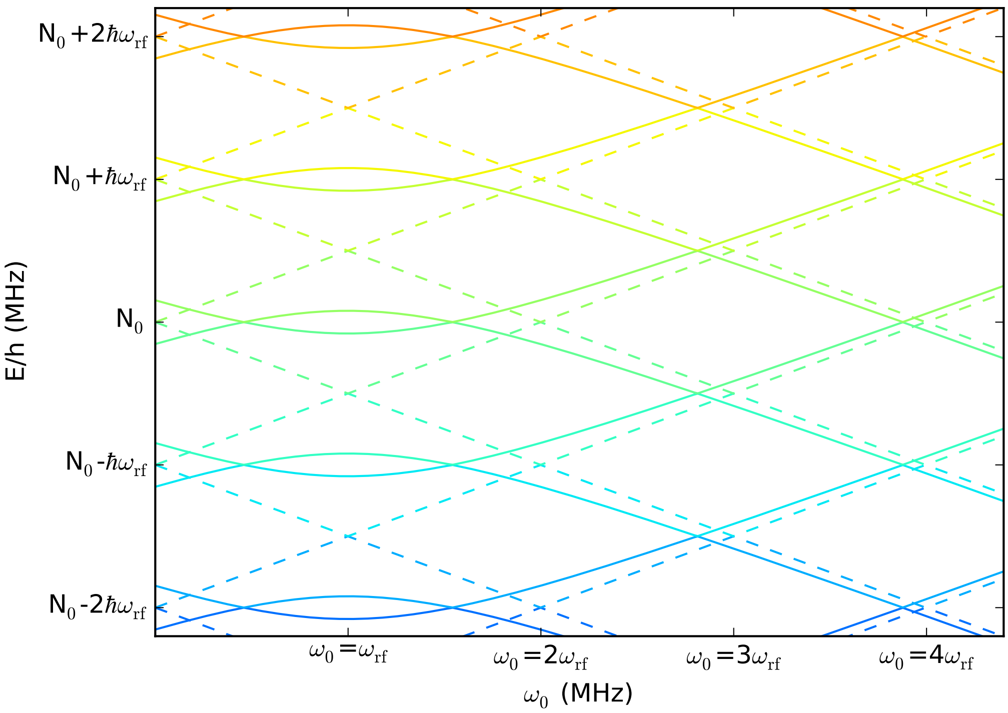

Figure 8.1: The energy levels of a spin-1/2 atom in a static magnetic field of frequency ω_0 and a circularly polarised photon field of frequency $\omega_{\rm rf}$, with a background photon number N_0.

8.2 A spin-1/2 system

In a spin-1/2 system, consisting of a single atom with $s = 1/2$ and $i = 0$, circularly polarised photons only couple together states with the same $m_s + N$ value. Each unique $m_s + N$ value corresponds to a two-dimensional subspace consisting of the states,

$$|\psi_a\rangle = |{-1/2}, N+1\rangle \qquad\qquad |\psi_b\rangle = |{+1/2}, N\rangle\,.$$

Applying the asymptotic part of Eq. (8.1.1), $\hat{H} = \omega_0 \hat{s}_z + \omega_{\rm rf} a^\dagger a + \lambda/\sqrt{2}(a\hat{s}_+ + a^\dagger \hat{s}_-)$ where $\omega_0 \propto B_z$, on the subspace gives

$$\begin{aligned}
\langle\psi_a|\,\hat{H}\,|\psi_a\rangle &= (N+1)\omega_{\rm rf} - \frac{\omega_0}{2},\\
\langle\psi_b|\,\hat{H}\,|\psi_b\rangle &= N\omega_{\rm rf} + \frac{\omega_0}{2},\\
\langle\psi_a|\,\hat{H}\,|\psi_b\rangle &= \frac{\lambda}{\sqrt{2}}\sqrt{N},\\
\langle\psi_b|\,\hat{H}\,|\psi_a\rangle &= \frac{\lambda}{\sqrt{2}}\sqrt{N+1}.
\end{aligned}$$

As $N \gg 1$ then we can make the approximation $\langle\psi_a|\,\hat{H}\,|\psi_b\rangle = \langle\psi_b|\,\hat{H}\,|\psi_a\rangle = \lambda/\sqrt{2}\sqrt{\bar{N}} = \Omega/2$, where Ω is the Rabi frequency, determined from the dipole moment of the ab tran-

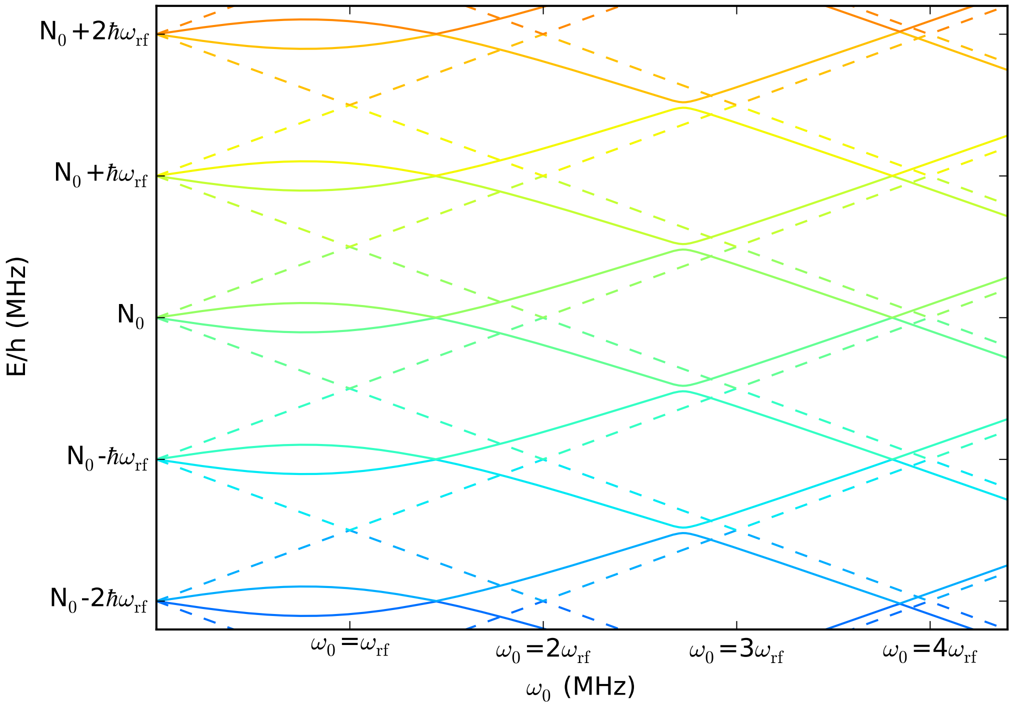

Figure 8.2: The energy levels of a spin-1/2 atom in a static magnetic field of frequency ω_0 and a linearly polarised photon field of frequency ω_{rf}, with a background photon number N_0.

sition. Diagonalising the subspace gives eigenvalues,

$$E_a = (N+1/2)\omega_{\mathrm{rf}} + \sqrt{\left(\frac{\omega_{\mathrm{rf}}-\omega_0}{2}\right)^2 + \left(\frac{\Omega}{2}\right)^2}$$
$$E_b = (N+1/2)\omega_{\mathrm{rf}} - \sqrt{\left(\frac{\omega_{\mathrm{rf}}-\omega_0}{2}\right)^2 + \left(\frac{\Omega}{2}\right)^2}.$$

The energy levels are shown in Fig 8.1. The unperturbed energy levels (dashed lines) follow linear paths, while the dressed-state energy levels (solid lines) form sets of hyperbolas which head asymptotically towards the unperturbed levels.

In the case of circularly polarised light there is an avoided crossing between the states centred at $\omega_0 = \omega_{\mathrm{rf}}$; but there are no crossings between the states at higher values of ω_0, as all other crossings correspond to states of differing $m_s + N$ values. In contrast, a similar diagram for the dressing of a spin-1/2 system by linearly polarised (σ_x) photons shows a series of crossings and avoided crossings at $\alpha\omega_{\mathrm{rf}} = \omega_0$ for even and odd values of α respectively, Fig. 8.2. These additional crossings are the manifestation of the coupling terms that exist in the linearly polarised photon case between $\langle +1/2, N|\,\hat{H}\,|-1/2, N\pm 1\rangle$.

8.3 Building an rf-dressed basis set

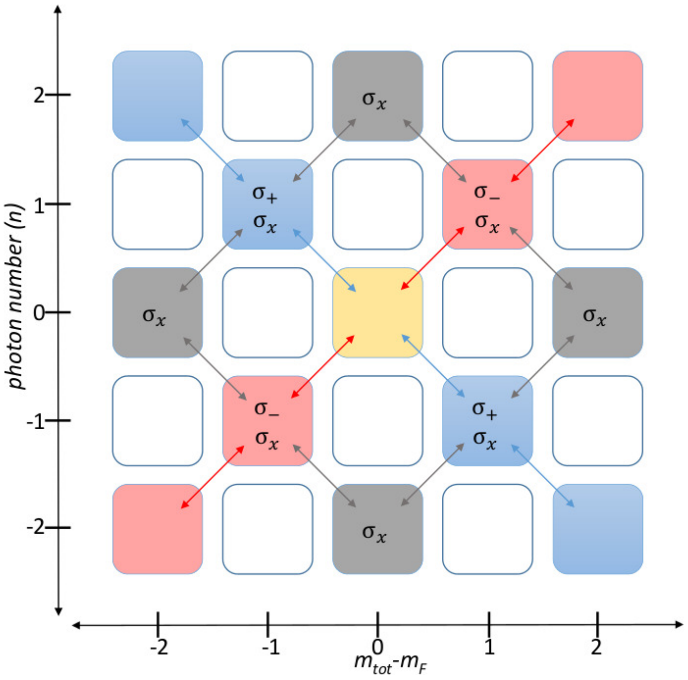

Figure 8.3: Visualisation of the rf coupling from an initial state $(n = 0, M_F = M_{\mathrm{tot}})$ (yellow) for a variety of different polarisations: the blue arrows and squares represent coupling due to σ_+ polarisation; the red arrows and squares represent coupling due to σ_- polarisation; all red, blue and grey arrows and squares represent couplings arising from σ_x polarisation. The white squares indicate states that will never be coupled as for all polarisations considered only states where $n + (M_F - M_{\mathrm{tot}})$ is even can be coupled.

The rf field drives transitions between the atomic Zeeman states, which leads to coupling between the states, and increases the number of channels that must be included in a full scattering calculation. The character of the states that are coupled depends on the polarisation and propagation of the rf field. In the following discussion, we consider an rf field which is propagating in the same direction, z, as the static magnetic field; as such, we conserve the projection of the total angular momentum along the z-axis, M_{tot}, and consider three different types of polarisation σ_+, σ_- and σ_x. The circularly polarised photons, $\sigma_\pm$, couple in states of differing angular momentum such that $M_F \pm n = M_{\mathrm{tot}}$ with the sign corresponding to the same sign as the polarisation. In the case of linearly polarised, σ_x, photons, as σ_x can be written as a superposition of σ_+ and σ_-, then the change in M_F cannot be described by n alone as only the parity $\eta(M_F, n) = (-)^{M_{\mathrm{tot}}+1/2+n}$ is conserved. The couplings arising from each polarisation are shown in Fig 8.3, as well as the M_F block that each includes. For σ_x polarisation a lower-energy channel is always coupled in by the rf field giving rise to loss via inelastic collisions from the system; however, for $\sigma_\pm$ polarisations it is possible to pick an incoming channel of the system such that no lower energy channels are coupled by the rf field, due to the constraints on the change in M_F.

We construct the basis set of rf-dressed channels in the fully decoupled form and represent the change in the number of photons from the initial state with n. Depending on the atomic system and the polarisation of the rf field the number of channels in the basis set can be infinite. In practice we limit the basis set to include $2n+1$ photon states, which results in converged calculations for all systems considered.

The Hamiltonian given in Eq. (8.1.1) has two additional terms compared to that of the static field Hamiltonian Eq. (3.1.1). Applying the basis set $|m_{s,a}, m_{i,a}, m_{s,b}, m_{i,b}\rangle|L, M_L\rangle|n\rangle$ to the terms that both Hamiltonians have in common gives the same results as in Eqs. (3.2.2)–(3.2.6) but with an additional factor of $\delta_{n,n'}$ in each one. The matrix elements of the rf field term, $\hat{H}_{\omega_\mathrm{rf}}$, are

$$\begin{gathered}\langle m_{s,a}m_{i,a}m_{s,b}m_{i,b}, LM_L, n|\hat{H}_{\omega_\mathrm{rf}}\,|m'_{s,a}m'_{i,a}m'_{s,b}m'_{i,b}, L'M'_L, n'\rangle \equiv \\ \omega n\delta_{n,n'}\delta_{L,L'}\delta_{m_L,M'_L}\delta_{m_{s,a},m'_{s,a}}\delta_{m_{s,b},m'_{s,b}}\delta_{m_{i,a},m'_{i,a}}\delta_{m_{i,b},m'_{i,b}}.\end{gathered} \tag{8.3.1}$$

The matrix elements of the $\hat{H}_{i,\mathrm{rf}}$ are given for atom $a = i$ for a given polarisation σ

$$\begin{gathered}\langle m_{s,a}m_{i,a}m_{s,b}m_{i,b}, LM_L, n|\hat{H}_{i,\mathrm{rf}}\,|m'_{s,a}m'_{i,a}m'_{s,b}m'_{i,b}, L'M'_L, n'\rangle \equiv \\ -\frac{B_\mathrm{osc}}{\sqrt{2N}}(g_\mathrm{e}\mu_\mathrm{B}\,\langle m_{s,a}m_{i,a}m_{s,b}m_{i,b}, LM_L, n|\hat{s}_\sigma\hat{a} + \hat{s}^*_\sigma\hat{a}^\dagger\,|m'_{s,a}m'_{i,a}m'_{s,b}m'_{i,b}, L'M'_L, n'\rangle \\ +g_\mathrm{n}\mu_\mathrm{B}\,\langle m_{s,a}m_{i,a}m_{s,b}m_{i,b}, LM_L, n|\hat{i}_\sigma\hat{a} + \hat{i}^*_\sigma\hat{a}^\dagger\,|m'_{s,a}m'_{i,a}m'_{s,b}m'_{i,b}, L'M'_L, n'\rangle)\end{gathered} \tag{8.3.2}$$

The photon creation and annihilation operator terms, $\langle n|\,\hat{a}^\dagger\,|n'\rangle$ and $\langle n|\,\hat{a}\,|n'\rangle$, give expressions of $\delta_{n,n'+1}\sqrt{N+n'+1}$ and $\delta_{n,n'-1}\sqrt{N+n'}$, respectively; as $N \gg 1$ we make the approximation $\sqrt{N+n'+1} \approx \sqrt{N+n'} \approx \sqrt{N}$. The atomic spin operators each have matrix elements of the form

$$\begin{gathered}\langle j, m_j|\hat{j}_q\,|j', m'_j\rangle = \\ \delta_{j,j'}\delta_{m_j,m'_j+q}(-1)^{q+m'_j+j'-1}\sqrt{j(j+1)(2j+1)}\begin{pmatrix} j' & j & 1 \\ -(m_j+q) & m_j & q \end{pmatrix},\end{gathered} \tag{8.3.3}$$

where $q = +1, 0, -1$. The operators can be re-written as raising and lowering operators, rather than in their spherical tensor form, $\hat{j}_{+1} = -\hat{j}_+/\sqrt{2}$ and $\hat{j}_{-1} = \hat{j}_-/\sqrt{2}$, and then their matrix elements are given more simply as

$$= \sqrt{j(j+1) - m_{j'm_j}\delta_{m_j,m'_j\pm1}}. \tag{8.3.4}$$

In the case of homonuclear scattering the basis set consists of the symmetrised functions

$$\frac{|m_{s,a}, m_{i,a}, m_{s,b}, m_{i,b}\rangle|L, M_L\rangle|N\rangle \pm (-1)^L|m_{s,a}, m_{i,a}, m_{s,b}, m_{i,b}\rangle|L, M_L\rangle|N\rangle}{\sqrt{2}}, \tag{8.3.5}$$

with the + sign for bosons and the − sign for fermions. Similar matrix elements can also be derived by treating the rf dressing in a semi-classical manner and using Floquet theory to derive the required terms. Examples of these derivations can be found in Refs. [276,277]; however, the overall result is the same using either a semi-classical or quantised description.

The asymptotic matrix elements of an example case of ^{87}Rb in the $(f, m_f) = (1, +1) + (1, -1)$ channel dressed with σ_+ polarised photons of frequency $\omega_{\rm rf} = 100$ MHz, $B_{\rm rf} = 1$ G, and $B_z = 10$ G, are shown in Fig. 8.4. The thick black lines delineate changes in photon number, n. On the main diagonal each matrix element has a value of at least $n\hbar\omega$. The main diagonal blocks correspond to blocks of a conserved M_F and therefore include the appropriate hyperfine coupling terms. The elements, in these blocks, with the largest magnitude correspond to the hyperfine couplings $\zeta_{\rm hfs}\hat{i} \cdot \hat{s}$, as $\zeta_{\rm hfs}$ is on the order of GHz. The other couplings in these blocks correspond to the static magnetic field terms $g_j\mu_{\rm B}\hat{j}B_z$, where j is s or i, which also appear on the main diagonal but are smaller in magnitude than the other terms. The off-diagonal blocks contain the matrix elements due to $\hat{H}_{i,\rm rf}$. The larger magnitude elements correspond to those from the atomic spin $\hat{s}$ operator and those smaller elements to $\hat{i}$, as $g_{\rm e} \gg g_{\rm n}$.

8.4 RF-induced resonances in RbCs

In the initial investigations of ^{85}RbCs, as detailed in Section 5.1.1, the loss features measured experimentally around 230 G and 245 G were found to have been induced by the off-set in frequency of the dipole-trap lasers and could be reproduced using an applied rf field. This situation is not one which we can model exactly using the current setup for rf fields as the rf field in this instance was applied orthogonally to the static magnetic field. However, we investigate a similar magnetic field range for resonances caused by an applied rf field which propagates in the same direction as the static magnetic field and find resonances induced by both σ_+ and σ_- polarised photons.

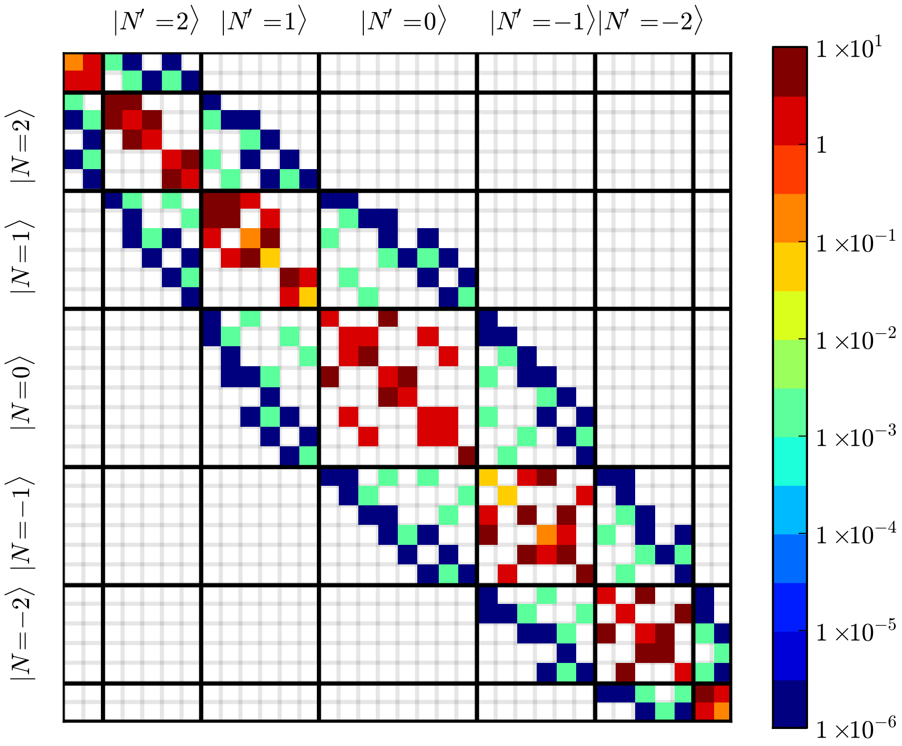

Figure 8.4: Asymptotic matrix elements of the rf-dressed Hamiltonian Eq. (8.1.1) for ^{87}Rb in the $(f, m_f) = (1, +1) + (1, -1)$ channel with σ_+ polarised photons, $B_{\rm rf} = 1$ G, $\omega_{\rm rf} = 100$ MHz and $B_z = 10$ G. The diagonal blocks enclosed in thick black lines show the photon number blocks. The colour of each matrix element corresponds to its absolute magnitude.

The incoming scattering channel in the ground state of ^{85}RbCs has a total angular momentum $M_{\rm tot} = 5$. In the following examples we consider only $L = 0$ (s-wave) basis functions and so $M_{\rm tot} = M_F$ in the absence of photons. This means that absorption or emission of a single photon couples in states with $M_F = 4$ and/or 6. Fig. 8.5 shows the bound-state levels for ^{85}RbCs with $M_F = 4, 5$ and 6. Each of the energy levels is shown with respect to the energy of the $M_F = 5$ threshold. The threshold for each M_F value is given by the dotted lines of the same colour as the bound states; the threshold for $M_F = 6$ is not shown as it occurs around 4000 MHz. Dashed horizontal lines mark the change in energy from the threshold caused by 50 and 100 MHz photons. From these lines we can see that, for a σ_+ polarised field, a resonance is expected around 198 G for an applied field of $\omega_{\rm rf} = 50$ MHz and around 216 G for an applied field of $\omega_{\rm rf} = 100$ MHz. For a σ_- polarised field a resonance is expected around 220 G for an applied field of $\omega_{\rm rf} = 50$ MHz

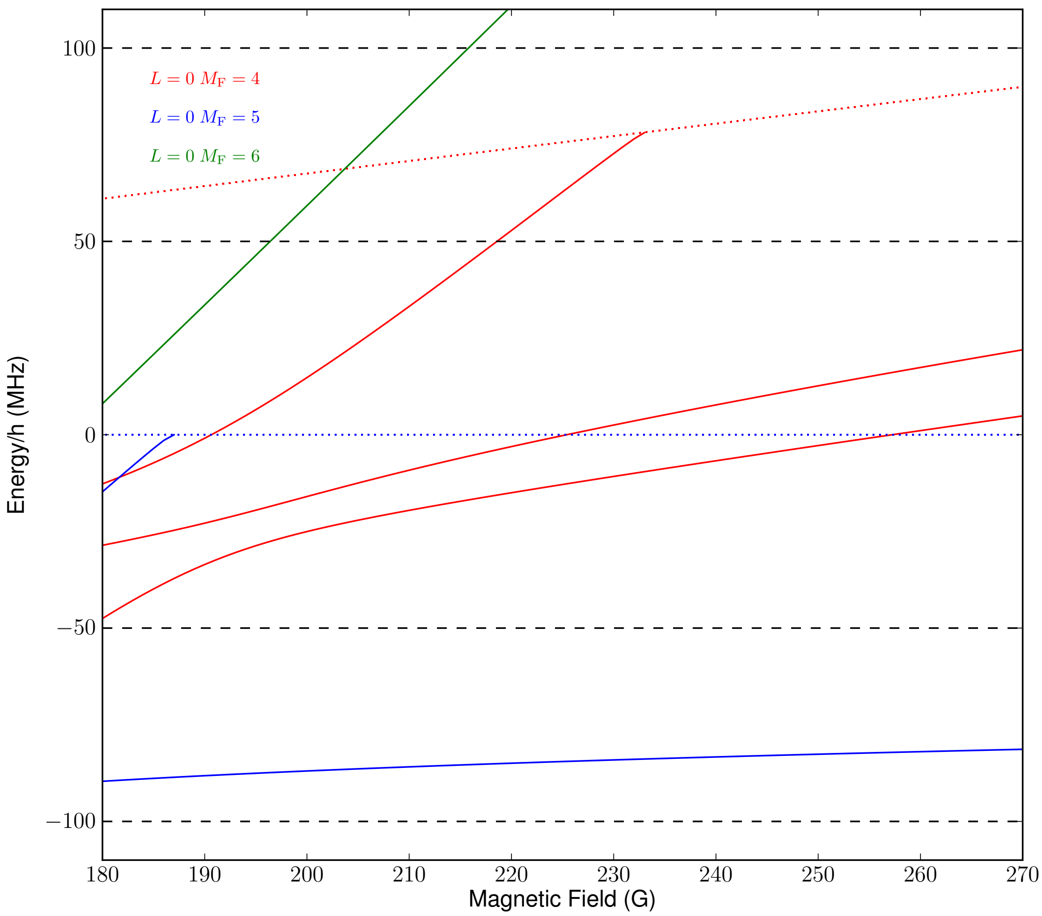

Figure 8.5: Bound-state energy levels for ^{85}RbCs with $L = 0$ and $M_F = 4$ (red), 5 (blue) and 6 (green). The states are plotted with respect to the threshold energy level of the incoming s-wave $(f, m_f) = (2, +2) + (3, +3)$ channel. The thresholds of each M_F is given by the dotted line of corresponding colour; the threshold for $M_F = 6$ is not shown as it occurs around 4000 MHz. Dashed horizontal lines mark the energy transitions that would occur with 50 or 100 MHz photons.

and around 240 G a resonance with a quasi-bound state above the $M_F = 4$ threshold will occur for an applied field of $\omega_{\text{rf}} = 100$ MHz.

In performing MOLSCAT calculations in the rf-dressed basis the threshold should be specified as the energy of the desired incoming channel with $n = 0$ or N_0 photons. This is close to, but not always exactly the same as, the energy of the undressed channel. To find the energy and position of the incoming dressed channel the asymptotic energy levels of the rf-field-dressed Hamiltonian, Eq. (8.1.1), are calculated for ^{85}RbCs. The energy levels are shown in Fig. 8.6; the levels are calculated with respect to the energy of the undressed $(f, m_f) = (2, 2) + (3, 3)$ channel, and only the levels from the lowest hyperfine threshold are shown. This example is calculated using a σ_x polarised rf field, propagating in the same direction as the static field, with $\omega_{\rm rf} = 50$ MHz and $B_{\rm osc} = 5$ G and for up to $n = \pm 3$ photons. The line which appears to be horizontal at 0 MHz corresponds to

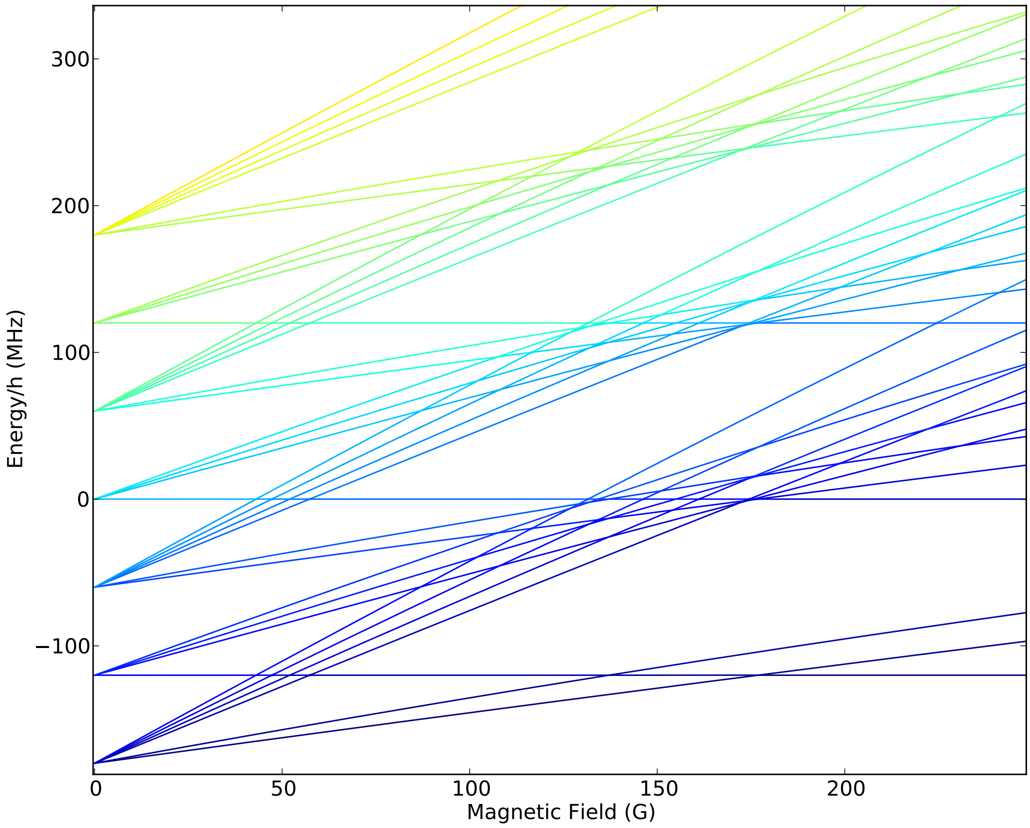

Figure 8.6: Asymptotic energy levels of ^{85}RbCs with a σ_x polarised applied rf field, propagating in the same direction as the static field, with $\omega_{\rm rf} = 60$ MHz and $B_{\rm osc} = 5$ G. A series of avoided crossings occur around 250 G.

the $(2,2) + (3,3)$ channel dressed with $n = 0$ photons; unlike the undressed channel it has avoided crossings with some of the states that cross it. These avoided crossings in the threshold can lead to changes in the background scattering length [266] and also mean that particular care has to be taken with calculations to guarantee that the correct threshold is being used. The asymptotic energy levels at zero field show the $(2n + 1)$ manifolds, of the hyperfine threshold with each possible n value, separated by 60 MHz. Only levels which correspond to $M_{\rm tot} = 5$ are allowed so for each n a different number of M_F states appear. These states have crossings and avoided crossings at higher field with manifolds corresponding to different n, the strength of which is controlled by $B_{\rm osc}$.

Using a σ_- polarised rf field with $B_{\rm osc} = 5$ G and varying $\omega_{\rm rf}$ between 120 and 140 MHz a resonance is found which, based on Fig. 8.5, is induced by coupling to the $M_F = 4$ state.

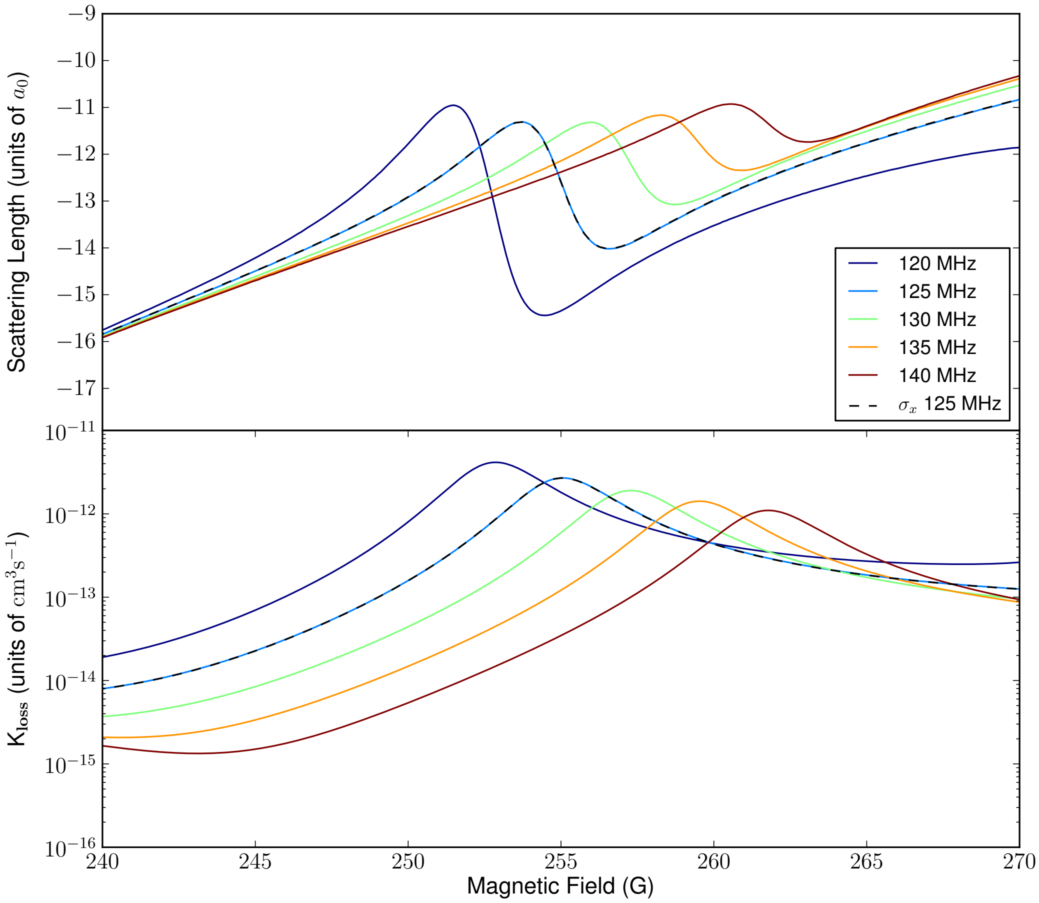

Figure 8.7: Resonance caused by σ_- polarised rf field in the s-wave $(f, m_f) = (2, +2) + (3, +3)$ channel of ^{85}RbCs. The rf field is propagating in the same direction as the static field and has a coupling strength $B_{\rm osc}$ =5 G. The frequency of the applied field is varied between $\omega_{\rm rf} = 120$ and 140 MHz (coloured); at $\omega_{\rm rf} = 125$ MHz the scattering length for a σ_x polarised rf field is also shown (black dotted).

In Fig. 8.7 the resonance moves to higher field with increasing $\omega_{\rm rf}$, as expected. The resonance is strongly decayed, as there are multiple lower-energy channels coupled to the incoming channel which give rise to inelastic losses. The value of $a_{\rm res}$ for the resonance decreases with increasing $\omega_{\rm rf}$. The resonance length $a_{\rm res}$ provides a means of controlling the scattering length which will change depending on the value of $\omega_{\rm rf}$. In this instance if $\omega_{\rm rf}$ becomes small enough (below $\sim$ 80 MHz) then the incoming channel becomes the lowest-energy channel allowed and the resonance is no longer decayed; in this case there will be no inelastic losses and so $K_{\rm loss} = 0$. A single case of σ_x polarisation is also shown in Fig. 8.7 for $\omega_{\rm rf} = 125$ MHz. As σ_x polarisation couples in more states it is possible that its $K_{\rm loss}$ could deviate from that of σ_- polarisation, but in this case there is no other

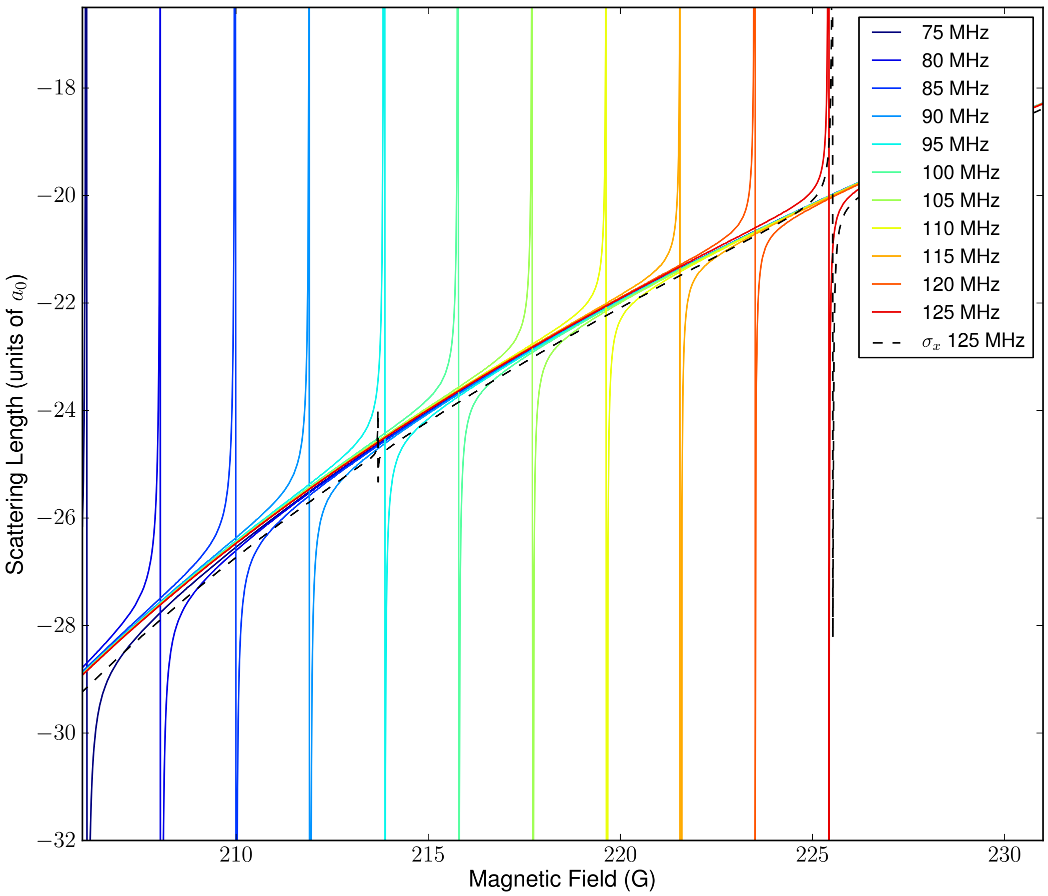

Figure 8.8: Resonance caused by σ_+ polarised rf field in the s-wave $(f, m_f) = (2, +2) + (3, +3)$ channel of ^{85}RbCs. The rf field is propagating in the same direction as the static field and has a coupling strength $B_{\rm osc} = 5$ G. The frequency of the applied field is varied between $\omega_{\rm rf} = 75$ and 125 MHz (coloured); at $\omega_{\rm rf} = 125$ MHz the scattering length for a σ_x polarised rf field is also shown (black dotted).

coupling near enough to cause a visible difference.

An additional resonance is found at slightly lower fields, shown in Fig. 8.8, using a σ_+ polarised rf field with $B_{\rm osc} = 5$ G and varying $\omega_{\rm rf}$ between 75 and 125 MHz. Based on Fig. 8.5 this resonance is caused by coupling to the $M_F = 6$ state. In this case the σ_+ polarisation does not couple to any lower-energy channels and so there are no inelastic losses involved. The bound state that causes the resonance is roughly linear in the region observed and so varying $\omega_{\rm rf}$ has little effect on anything other than the position of the resonance. The effect of σ_x polarisation is also shown for $B_{\rm osc} = 5$ G and $\omega_{\rm rf} = 125$ MHz; the σ_x polarisation does couple in lower energy channels and therefore the resonance in this case is a decaying resonance, there is also a resonance that appears due to higher-order coupling around 214 G.

The width of the resonance can be significantly varied by changing the value of the coupling strength $B_{\rm osc}$. In Fig. 8.9 four different values of coupling strength are compared. When $B_{\rm osc} = 0$ G then no coupling occurs and the resonance does not exist; as $B_{\rm osc}$ increases so does the width of the resonance. As the resonance is caused by a single transition to a bound state we expect the strength Γ and therefore the width Δ of the resonance to scale as $B_{\rm osc}^2$, and this relationship can indeed be seen in Fig. 8.9. The resonance position B_0 also shifts with increasing $B_{\rm osc}$ as the increased coupling between the bound states perturbs the levels which shifts the crossing between the bound state and threshold.

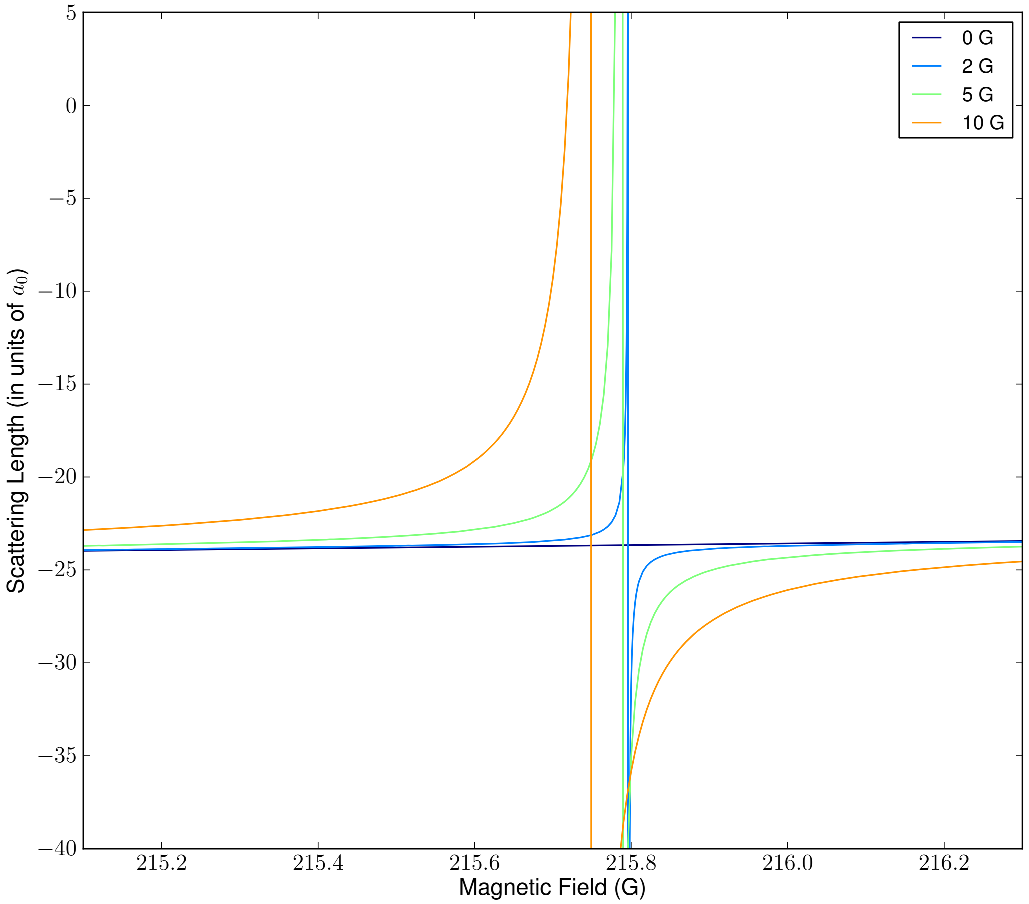

Figure 8.9: Resonance caused by σ_+ polarised rf field in the s-wave $(f, m_f) = (2, +2) + (3, +3)$ channel of ^{85}RbCs. The rf field is propagating in the same direction as the static field and has a frequency $\omega_{\rm rf} = 100$ MHz. The coupling strength of the applied field is varied between $B_{\rm osc} = 0$ and 10 G.

We have shown that Feshbach resonances can be induced using an rf field in conjunction with a static magnetic field in the case of ^{85}RbCs and that these resonances have properties such as $a_{\rm res}$, $K_{\rm loss}$, and Δ, as defined in Chapter 2, which can be controlled by changing the coupling strength and frequency of the applied rf field. These type of resonances have previously been calculated for homonuclear systems in Refs. [266, 267, 278], and demonstrated experimentally in Ref. [279]. In heteronuclear systems there can be an additional effect from an rf-electric-field component, which interacts with the instantaneous dipole moment of the molecule, which we have not considered here [265] but may be important in developing a complete picture of behaviour at each resonance. As research in this field progresses, many different combinations of external fields, both magnetic and electric, will be used to manipulate and control the atoms and molecules that are trapped. A discussion of the future development of this work, towards the control of molecular collisions using external fields, is presented in the following Chapter.

Chapter 9

Conclusions

In this Thesis scattering and bound-state calculations on alkali-metal mixtures of rubidium, potassium and cesium have been presented. The Feshbach resonances detailed in these calculations can be used to create samples of ultracold molecules, via magnetoassociation. In the case of heteronuclear mixturesm ultracold polar molecules can be created which are of great interest as they provide numerous new and exciting avenues of research. Ultracold polar molecules have permanent electric dipole moments which give rise to anisotropic, long-range dipole-dipole interactions. These dipole-dipole interactions can operate over a larger range then optical lattice spacings and could be used in quantum processing applications and to create novel quantum phases.

Homonuclear Scattering

In Chapter 4 we presented the results of scattering calculations on various states of ^{85}Rb. Coupled-channels scattering calculations were used to predict Feshbach resonances in both the $(f, m_f) = (2, -2) + (2, -2)$ channel (designated ee), and $(f, m_f) = (2, +2) + (2, +2)$ channel (designated aa). In the ee channel 18 resonances were found. As inelastic scattering can occur in this channel, some of the resonances are strongly decayed. Of the 18 resonances found 11 were pole-like and their positions and widths were calculated. Nine of the resonances were confirmed experimentally in Ref. [72]. Two of the resonances found are broad resonances which could be used to tune the scattering length to values which are acceptable for evaporative cooling, thus providing regions where BECs can be created. The lower-field resonance at 155 G has previously been used for this purpose [125,148] but we have found that there is a higher-field resonance at 532 G which could also be used. In the aa channel 12 resonances are predicted and their positions and widths were calculated. Seven of these resonance were confirmed experimentally in Ref. [72]. One of the resonances found in the aa channel is a broad resonance which may be used to tune the scattering length to modest positive values, improving the evaporation efficiency and offering the prospect of BEC formation directly in the absolute ground state. The mixed-state scattering lengths of the $(f_{\rm Rb}, f_{\rm Rb}) = (2, 3)$ hyperfine manifold were calculated to find more wide tunable resonances. A resonance in the mixed spin channel $(f, m_f) = (2, +2)+(3, +3)$ was also confirmed experimentally in Ref. [72]. In addition we presented an example of a mixed-state scattering length for the $(2, +2) + (3, +2)$ channel, which has the requisite properties to be used in the proposal of Billam *et al.* [74] to create mesoscopic entangled states from soliton collisions.

The scattering properties of ^{87}Rb and Cs are also presented as it is important to have a full understanding of the intraspecies behaviour of the components used in a heteronuclear mixture in order to optimise molecule formation. Once the properties of homonuclear mixtures had been determined we moved on to calculating the scattering properties of heteronuclear mixtures.

Heteronuclear Scattering

The motivation for the creation of ultracold polar molecules was discussed in Chapter 1. In Chapter 5 we present the results of scattering calculations on mixtures of Rb and Cs, and K and Cs. The scattering results show that all isotopologues of RbCs and KCs have a rich Feshbach structure in an experimentally accessible magnetic-field range between 0 and 1000 G. Furthermore we have analysed the bound states responsible for the resonances and detailed their behaviour below the collision threshold.

In ^{85}RbCs we predict 32 resonances in the s-wave scattering length, for the ground state, between 0 and 1000 G. 14 of the resonances were confirmed experimentally in Ref. [75]. Of these resonances several have widths suitable for use in magnetoassociation. We have calculated the energies of the bound states just below threshold with varying magnetic field, which can be used to find which molecular bound states the Feshbach molecules can be created in. The calculations show that the interspecies background scattering length is close to zero over a large range of magnetic fields. This reduces losses due to interspecies 3-body collisions and means that good overlap of the atomic clouds should be possible. The difficulty with this system is in simultaneously creating ultracold high phase-space-density mixtures of ^{85}Rb and ^{133}Cs as BECs of each can only be created in very specific, and non-overlapping magnetic field ranges. Magnetoassociation could still be performed using ultracold mixtures rather than BECs if a high enough density of ultracold ^{85}Rb can be achieved, for example via the routes discussed in Section 4.1.

In ^{87}RbCs there are 31 resonances in the scattering length of the s-wave $(f, m_f) = (1, +1) + (3, +3)$ channel between 0 and 1000 G. 18 were confirmed experimentally in Ref. [118] and 7 were confirmed experimentally in Ref. [76]. Of these resonances several have widths suitable for use in magnetoassociation. Magnetoassociation has been performed successfully on the 197 G resonance as detailed in Refs. [76, 118]. Following magnetoassociation the Feshbach molecules can be transferred to various weakly bound molecular states by further tuning the magnetic field. We have shown the near-threshold bound states which can be reached, and calculated the magnetic moment of the relevant states around the 197 G resonance. Ro-vibrational ground-state molecules have been successfully produced via STIRAP from Feshbach molecules in the $|-6(2, 4)d(2, 4)\rangle$ state in Refs. [70, 71]. The number of molecules produced is limited by the poor overlap of the ultracold atomic clouds due to the high interspecies scattering length.

In ^{39}KCs we predict 35 resonances in the scattering length of the s-wave $(f, m_f) = (1, +1) + (3, +3)$ channel between 0 and 1000 G. Of these resonances several have widths suitable for use in magnetoassociation. We have calculated the energies of the bound states just below threshold with varying magnetic field, these calculations show which molecular bound states the Feshbach molecules can be created in. In ^{40}KCs we predict 84 resonances in the scattering length of the s-wave $(f, m_f) = (9/2, -9/2) + (3, +3)$ channel between 0 and 1000 G. Most of these resonance are too narrow for magnetoassociation, but there are some resonances caused by $L = 0$ bound states which have widths as high as 0.1 G. We have calculated the energies of the bound states just below threshold with varying magnetic field. In ^{41}KCs we predict 42 resonances in the scattering length of the s-wave $(f, m_f) = (1, +1) + (3, +3)$ channel between 0 and 1000 G. Of these resonances 27 occur below 130 G and several have widths suitable for use in magnetoassociation both in the low field and high field regions. Again we have also calculated the energies of the bound states just below threshold with varying magnetic field.

For each isotopolog we have compared the intraspecies scattering lengths of the components of the mixture and the interspecies scattering length of the mixture. For RbCs we see that there are no magnetic-field regions which are suitable for both species to be cooled to degeneracy simultaneously. In ^{87}RbCs there are regions where the condensates would be stable and miscible but these regions do not coincide with regions where Cs condensates can be formed. However, for KCs in all three of the isotopes there are regions where both species can be cooled simultaneously. In ^{39}KCs there is a small region where the condensates would be stable and miscible and in ^{41}KCs the condensates would be stable and miscible for most of the region between 0 and 1000 G. In particular there is a small region just above 885 G where both species can be cooled simultaneously and the condensates are miscible. Our scattering calculations for KCs show that it is a very promising system for the formation of high phase-space density ultracold samples of polar molecules. The calculations are based on reference potentials which have not yet been fitted to Feshbach resonance positions, and therefore are accurate only to within ~ 5 G. Once experimental measurements on the location of the Feshbach resonances in one of the isotopologues have been made then higher-accuracy potentials can be fitted and more accurate scattering calculations can be performed.

Energy dependence of the scattering length

Studies of cold atom collisions and few-body interactions often require the energy dependence of the scattering phase shift, which is usually expressed in terms of an effective-range expansion. In Chapter 7 we used accurate coupled-channel calculations on ^{6}Li, ^{39}K and ^{133}Cs to explore the behaviour of the effective range in the vicinity of both broad and narrow Feshbach resonances. We found that away from resonance the effective-range expansion is reasonably good at describing the energy dependence around broad resonances and away from zero-crossings in the scattering length. However, around narrow resonances the effective-range expansion can fail badly, even when the full field-dependence of the effective range is taken from coupled-channel calculations. We have presented an alternative parametrisation of the effective-range formula that is accurate through both resonance poles and zero-crossings but the expansion can still fail at low collision energies. To remedy the deficiencies of the effective-range expansion around narrow resonances, we advocate the use of an MQDT approach that fully describes the effect of a resonance as a function of both field and energy, as discussed in Chapter 7. The MQDT approach is only appropriate for cases for individual isolated resonances that have a reasonably constant background scattering term across their entire width. The MQDT approach for the near-threshold energy-dependent scattering length could be important in numerous areas of cold-atom research. For example, corrections to the zero-energy scattering length are important for studies of optical lattice structures, where the finite zero-point or band energy can lead to significant corrections to the energy of confinement-induced resonances [225] and accounting for it requires the scattering length at finite energy [250, 251]. Accurate finite-energy corrections to the phase shift could also be significant for the equation of state of cold fermions [252] and for understanding few-body phenomena [220, 222].

Future work

In Chapter 8 we briefly touched on the effects of a radio-frequency field being applied to the alkali-alkali scattering Hamiltonian in addition to an external static magnetic field. In future work we hope to expand this to perform scattering calculations under a variety of external electric and magnetic fields. As the field progresses, future experiments will use external fields to manipulate and control ultracold molecular samples to study their interaction properties, and so calculations that can account for these effects will be necessary. External fields have been shown to affect the collision properties of ultracold molecules and can be used to adjust the ratio of inelastic losses and to control reaction properties [280]. Electric fields are already being used to manipulate arrays of ultracold KRb molecules in optical lattices with very interesting results [281]. The complex structure of molecules means that additional fields such as microwave and infrared radiation fields can also be used to interact with the rotational and vibrational spectra of molecules. All of these methods offer 'control knobs' that can be used to aid in the study of our fundamental understanding of reaction processes, chemical reactivity and control over many-body phenomena. Before these results can be fully understood a framework for understanding the interactions of these molecules in arbitrary combinations of external fields, at arbitrary angles, will have to be developed.

Additionally, one of the long-term goals using ultracold polar molecules requires placing them into optical lattices where there long-range anisotropic interactions can be studied under the influence of an external magnetic field. Placing the molecules in an optical lattice restricts their movement in one or more dimensions, which can dramatically alter the scattering properties of the system. Collisions in confined dimensions, such as pancake traps induced by optical lattices, experience quasi-2D confinement at collision energies $\ll \hbar\omega_0$, where ω_0 is the trapping frequency. Under this confinement only the ground state of the axial harmonic oscillator is occupied. At collisions energies $\ll \hbar\omega_0$ there is a confinement-dominated 3D scattering regime [282]. The confinement effects of atoms in optical lattices have been studied but a full theory for atom-molecule and molecule-molecule behaviour does not exist. As we move forward with the creation of ultracold polar molecules and their use in quantum processing applications and to create novel quantum phases becomes a reality then these additional effects will need to be understood.

Ultracold molecules can also be used to study ultracold chemistry. In the same way as magnetoassociation has been used to create ultracold alkali-metal dimers it could also be used to create more complex molecules by associating one alkali-metal dimer molecule with another alkali-metal atom to form polyatomic species, or by associating two molecules, or various other perturbations. To fully understand these forms of ultracold chemistry will require the development of interaction potentials for the more complex systems.

In this Thesis we have presented scattering and bound-state calculations which have aided in the formation of ultracold polar molecules. Whilst the creation of these ultracold molecules is a huge scientific step forward they are only a small step towards the fundamental control and understanding that ultracold physics has to offer.

Appendix A

Angular Momentum coupling and matrix elements

A.1 Notes on angular momentum coupling

The notes in this Section serve to give a brief summary of the more commonly used expressions in angular-momentum algebra and to aid in the understanding of the derivation of the matrix elements presented in this Thesis. A more complete treatment of angular momentum theory can be found in Refs. [203, 283, 284]. We begin by summarising some of the more commonly used matrix elements of angular momentum operators,

$$\begin{aligned}\langle jm|\,\hat{\mathbf{j}}^2\,|j'm'\rangle &= j(j+1)\delta_{j,j'}\delta_{m,m'},\\ \langle jm|\,\hat{j}_z\,|j'm'\rangle &= m'\delta_{j,j'}\delta_{m,m'},\end{aligned}$$

and

$$\langle jm|\,\hat{j}_\pm\,|j'm'\rangle = \sqrt{j(j+1)-m'(m'\pm 1)}\delta_{j,j'}\delta_{m,m'\pm 1}.$$

A system which is made up of two components of angular momenta j_1 and j_2, with a total angular momentum j which is the sum of components of j_1 and j_2, can be expressed in terms of both a decoupled representation $|j_1m_1j_2m_2\rangle$ and a coupled representation $|j_1j_2jm\rangle$. The two descriptions are equivalent as both sets of angular momentum operators contain the same number of observables. The two representations are connected by a unitary transformation

$$|j_1j_2jm\rangle = \sum_{m_1,m_2} |j_1m_1j_2m_2\rangle\,\langle j_1m_1j_2m_2|j_1j_2jm\rangle\,,$$

and by the inverse transformation

$$|j_1 m_1 j_2 m_2\rangle = \sum_{j,m} |j_1 j_2 j m\rangle \langle j_1 j_2 j m | j_1 m_1 j_2 m_2\rangle \,.$$

The vector-addition coefficients $\langle j_1 m_1 j_2 m_2 | j_1 j_2 j m\rangle = \langle j_1 j_2 j m | j_1 m_1 j_2 m_2\rangle$ are referred to as Clebsch-Gordan coefficients and can also be expressed in terms of Wigner 3-j symbols,

$$\begin{aligned}\langle j_1 m_1 j_2 m_2 | j_1 j_2 j m\rangle = \langle j_1 j_2 j m | j_1 m_1 j_2 m_2\rangle &= C(j_1 j_2 j; m_1 m_2 m) \\ &= (-1)^{j_1 - j_2 + m} \sqrt{2j+1} \begin{pmatrix} j_1 & j_2 & j \\ m_1 & m_2 & -m \end{pmatrix} .\end{aligned}$$

For a given j_1 and j_2 the values of j are restricted by the ‘triangle’ condition of Dirac which states that

$$j_1 + j_2 \geq J \geq |j_1 - j_2|,$$

and the projection quantum number m is given by

$$m = m_1 + m_2.$$

The orthonormality of $|j_1 j_2 j m\rangle$ and $|j_1 m_1 j_2 m_2\rangle$ leads to the orthogonality relations

$$\sum_{m_1, m_2} \langle j_1 j_2 j m | j_1 m_1 j_2 m_2\rangle \langle j_1 m_1 j_2 m_2 | j_1 j_2 j m\rangle = \delta_{j,j'} \delta_{m,m'},$$

and

$$\sum_{m_1, m_2} \langle j_1 m_1 j_2 m_2 | j_1 j_2 j m\rangle \langle j_1 j_2 j m | j_1 m_1 j_2 m_2\rangle = \delta_{m_1, m_1'} \delta_{m_2, m_2'} .$$

6-j and 9-j symbols

The coupling of more than two angular momenta can be described by 6-j and 9-j symbols, where 6-j symbols arise from the coupling of three angular momenta and 9-j symbols from the coupling of four angular momenta. A decoupled representation of three angular momenta $|j_1 m_1 j_2 m_2 j_3 m_3\rangle$ may be coupled in different ways. Firstly, j_1 and j_2 can be coupled to form the resultant vector j_{12} which in turn can be coupled to j_3 to form j; the eigenfunctions of which are,

$$|(j_1, j_2) j_{12} j_3 j m\rangle = \sum_{m_{12}, m_3} \langle j_{12} m_{12}, j_3 m_3 | j_{12} j_3 j m\rangle \, |j_{12} m_{12}, j_3 m_3\rangle \,.$$

Alternatively j_2 and j_3 can be coupled to form the resultant vector j_{23} which in turn can be coupled to j_1 to form j; the eigenfunctions of which are,

$$|j_1 m_1, (j_2, j_3) j_{23}\rangle = \sum_{m_1, m_{23}} \langle j_1 m_1, j_{23} m_{23} | j_1 j_{2,3} j m\rangle \, |j_1 m_1, j_{23} m_{23}\rangle \, .$$

The two representations are physically equivalent, as in the case above, and are related by the unitary transformation,

$$|j_1 j_{23} j m\rangle = \sum_{j_{12}} \langle j_{12} j_3 j m | j_1 j_{23} j m\rangle \, |j_{12} j_3 j m\rangle \, \delta_{j,j'} \delta_{m,m'} .$$

The scalar product $\langle j_{12} j_3 j m | j_1 j_{23} j m\rangle$ can be expanded as

$$\begin{aligned} \langle j_{12} j_3 j m | j_1 j_{23} j m\rangle = \sum_{m_1, m_{12}} & \langle j_1 m_1, j_2 m_{12} - m_1 | j_{12} m_{12}\rangle \, \langle j_1 m_1, j_{23} m - m_1 | j m\rangle \\ & \langle j_2 m_{12} - m_1, j_3 m_3 | j_{23} m - m_1\rangle \, \langle j_{12} m_{12}, j_3 m - m_{12} | j m\rangle \, , \end{aligned}$$

where the recoupling coefficient $\langle j_{12} j_3 j m | j_1 j_{23} j m\rangle$ has been re-written as a sum over four 3-j symbols. This sum can be rewritten as either a Racah (W) coefficient or a 6-j symbol, where

$$\begin{aligned} \langle j_{12} j_3 j m | j_1 j_{23} j m\rangle &= (-1)^{-j_1 - j_2 - j_3 - j} \sqrt{(2 j_{12} + 1)(2 j_{23} + 1)} \begin{Bmatrix} j_1 & j_2 & j_{12} \\ j_3 & j & j_{23} \end{Bmatrix} \\ &= (-1)^{-j_1 - j_2 - j_3 - j} W(j_1 j_2 j j_3; j_{12} j_{23}). \end{aligned}$$

The 6-j symbol is invariant to the interchange of any two columns, or the interchange of the upper and lower arguments in each of any two columns. For example,

$$\begin{Bmatrix} j_1 & j_2 & j_3 \\ j_4 & j_5 & j_6 \end{Bmatrix} = \begin{Bmatrix} j_2 & j_1 & j_3 \\ j_5 & j_4 & j_6 \end{Bmatrix} = \begin{Bmatrix} j_1 & j_5 & j_6 \\ j_4 & j_2 & j_3 \end{Bmatrix} .$$

The recoupling of four angular momenta can be described by a 9-j symbol. Two possible coupling schemes are $|(j_1 j_4) j_{14} (j_2 j_3) j_{23} j m\rangle$ and $|(j_1 j_2) j_{12} (j_3 j_4) j_{34} j m\rangle$. As in the two previous cases, the two cases are related by a unitary transformation,

$$\begin{aligned} |(j_1 j_4) j_{14} (j_2 j_3) j_{23} j m\rangle = & \sum_{j_{12}} \sum_{j_{34}} \langle (j_1 j_2) j_{12} (j_3 j_4) j_{34} j m | (j_1 j_4) j_{14} (j_2 j_3) j_{23} j m\rangle \\ & \times |(j_1 j_2) j_{12} (j_3 j_4) j_{34} j m\rangle \, . \end{aligned}$$

The recoupling coefficient $\langle (j_1j_2)j_{12}(j_3j_4)j_{34}jm|(j_1j_4)j_{14}(j_2j_3)j_{23}jm\rangle$ can be written in terms of a 9-j symbol,

$$\langle (j_1j_2)j_{12}(j_3j_4)j_{34}jm|(j_1j_4)j_{14}(j_2j_3)j_{23}jm\rangle = \sqrt{(2j_{12}+1)(2j_{34}+1)(2j_{14}+1)(2j_{23}+1)} \times \begin{Bmatrix} j_1 & j_2 & j_{12} \\ j_3 & j_4 & j_{34} \\ j_{14} & j_{23} & j \end{Bmatrix}.$$

Any 9-j symbol can also be expressed as a sum over three 6-j symbols or a sum over six 3-j symbols.

The Wigner-Eckart Theorem

A spherical 'irreducible' tensor, $T_{k,q}$, is defined as being a spherical tensor of rank k such that any transformation under rotation must be equivalent to the transformation under rotation of the spherical harmonic of equal rank k [285]. By definition, irreducible tensors give the commutation relations [284, 286]

$$[\hat{J}_{\pm 1}, T_{k,q}] = \sqrt{k(k+1) - q(q\pm 1)}T_{k,q\pm 1},$$

and

$$[\hat{J}_z, T_{k,q}] = qT_{k,q}.$$

The Wigner-Eckart Theorem states that, for an irreducible tensor operator, the dependence of the matrix element $\langle jm|T_{k,q}|j'm'\rangle$ on the projection quantum numbers m and m' can be described by a Clebsch-Gordan coefficient, such that the matrix element can be re-written in terms of a 3-j symbol and a 'reduced' matrix element,

$$\langle jm|T_{k,q}|j'm'\rangle = (-1)^{j-m}\sqrt{2j+1} \begin{pmatrix} j & k & j' \\ -m & q & m' \end{pmatrix} \langle j||T_k||j\rangle. \tag{A.1.7}$$

The reduced matrix element $\langle j||T_k||j\rangle$ contains the physical information relevant to the system and the 3-j symbol contains the geometric information.

Some common equations for the reduced matrix elements of composite systems are

$$\begin{aligned}
\langle j_1,j_2,j||T_k(\hat{A}_1)||j_1',j_2',j'\rangle =&\delta_{j_2,j_2'}(-1)^{j'+j_1'+k+j_2}\sqrt{(2j+1)(2j'+1)(2j_1+1)}\\
&\times\begin{Bmatrix} j_1' & j' & j_2\\ j & j_1 & k\end{Bmatrix}\langle j_1||T_k(\hat{A}_1)||j_1'\rangle\,,\\
\langle j_1,j_2,j||T_k(\hat{A}_2)||j_1',j_2',j'\rangle =&\delta_{j_1,j_1'}(-1)^{j+j_1+k+j_2'}\sqrt{(2j+1)(2j'+1)(2j_2+1)}\\
&\times\begin{Bmatrix} j_2' & j' & j_1\\ j & j_2 & k\end{Bmatrix}\langle j_2||T_k(\hat{A}_2)||j_2'\rangle\,,
\end{aligned}$$

and

$$\begin{aligned}
\langle j_1,j_2,j||T_k(\hat{A}_1)\cdot T_k(\hat{A}_2)||j_1',j_2',j'\rangle =&\delta_{j,j'}(-1)^{j+j_1'+j_2}\sqrt{(2j+1)(2j_1+1)(2j_2+1)}\\
&\times\begin{Bmatrix} j_1' & j_2' & j\\ j_2 & j_1 & k\end{Bmatrix}\langle j_1||T_k(\hat{A}_1)||j_1'\rangle\,\langle j_2||T_k(\hat{A}_2)||j_2'\rangle\,.
\end{aligned}$$

The reduced matrix element of a tensor of rank 1 is given simply by $\langle j||T_1(\hat{j})||j'\rangle = \delta_{j,j'}\sqrt{j(j+1)}$ and the generalised reduced matrix element of a tensor of rank k is given by $\langle j||T_k(\hat{j})||j'\rangle = \delta_{j,j'}\sqrt{(2j+k+1)!/(2^k(2k)!(2j-k)!)}$.

A.2 Matrix elements in the $|(s_a,i_a)f_a\rangle\,|(s_b,i_b)f_b\rangle\,|F,M_F\rangle\,|L,M_L\rangle$ basis set

The matrix elements of the Hamiltonian given by Eq. (3.1.1) for the $|(s_a,i_a)f_a\rangle\,|(s_b,i_b)f_b\rangle\,|F,M_F\rangle\,|L,M_L\rangle$ basis set are presented in the following Section.

The matrix elements of the $\hat{V}^{\mathrm{c}}(R)$ isotropic potential operator are

$$\begin{aligned}
&\langle (s_a,i_a)f_a(s_b,i_b)f_bFM_FLM_L|\,\hat{V}^{\mathrm{c}}(R)\,|(s_a,i_a)f'_a(s_b,i_b)f'_bF'M'_FL'M'_L\rangle = \\
&\delta_{L,L'}\delta_{M_L,M'_L}\delta_{F,F'}\delta_{M_F,M'_F}\sum_{SM_SM'_S} V_S(R)(-1)^{f_a-f_b+f'_a-f'_b+2i_a+2i_b+M_S+M'_S} \\
&\times (2S+1)\sqrt{(2F+1)(2F'+1)(2f_a+1)(2f_b+1)(2f'_a+1)(2f'_b+1)} \\
&\times \begin{pmatrix} f_a & f_b & F \\ m_{f,a} & m_{f,b} & -M_F \end{pmatrix}\begin{pmatrix} f'_a & f'_b & F' \\ m'_{f,a} & m'_{f,b} & -M'_F \end{pmatrix}\begin{pmatrix} s_a & i_a & f_a \\ m_{s,a} & m_{i,a} & -m_{f,a} \end{pmatrix} \\
&\times \begin{pmatrix} s_b & i_b & f_b \\ m_{s,b} & m_{i,b} & -m_{f,b} \end{pmatrix}\begin{pmatrix} s_a & i_a & f'_a \\ m'_{s,a} & m'_{i,a} & -m'_{f,a} \end{pmatrix}\begin{pmatrix} s_b & i_b & f'_b \\ m'_{s,b} & m'_{i,b} & -m'_{f,b} \end{pmatrix} \\
&\times \begin{pmatrix} s_a & s_b & S \\ m_{s,a} & m_{s,b} & -m_{s,a}-m_{s,b} \end{pmatrix}\begin{pmatrix} s_a & s_b & S \\ m'_{s,a} & m'_{s,b} & -m'_{s,a}-m'_{s,b} \end{pmatrix}.
\end{aligned} \tag{A.2.1}$$

The matrix elements of the $\hat{V}^{\mathrm{d}}(R)$ dipolar spin-spin operator are

$$\begin{aligned}
&\langle (s_a,i_a)f_a(s_b,i_b)f_bFM_FLM_L|\,\hat{V}^{\mathrm{d}}(R)\,|(s_a,i_a)f'_a(s_b,i_b)f'_bF'M'_FL'M'_L\rangle = \\
&-\lambda(R)\sqrt{30}\sum_{q=-2}^{2}(-1)^q(-1)^{F-M_F+L-M_L}\sqrt{(2F+1)(2F'+1)(2L+1)(2L'+1)} \\
&\times \begin{pmatrix} F & 2 & F' \\ -M_F & q & M'_F \end{pmatrix}\begin{pmatrix} L & 2 & L' \\ 0 & 0 & 0 \end{pmatrix}\begin{pmatrix} L & 2 & L' \\ -M_L & q & M'_L \end{pmatrix}\begin{Bmatrix} F & F' & 2 \\ f_a & f'_a & 1 \\ f_b & f'_b & 1 \end{Bmatrix} \\
&\times \left[(-1)^{s_a+i_a+f'_a+1}\sqrt{(2f_a+1)(2f'_a+1)(2s_a+1)s_a(s_a+1)}\begin{Bmatrix} s_a & f'_a & i_a \\ f_a & s_a & 1 \end{Bmatrix}\right. \\
&\left.\times (-1)^{s_b+i_b+f'_b+1}\sqrt{(2f_b+1)(2f'_b+1)(2s_b+1)s_b(s_b+1)}\begin{Bmatrix} s_b & f'_b & i_b \\ f_b & s_b & 1 \end{Bmatrix}\right].
\end{aligned} \tag{A.2.2}$$

The matrix elements of $\hat{L}^2$ are

$$\begin{aligned}
&\langle (s_a,i_a)f_a(s_b,i_b)f_bFM_FLM_L|\,\hat{L}^2\,|(s_a,i_a)f'_a(s_b,i_b)f'_bF'M'_FL'M'_L\rangle = \\
&\delta_{L,L'}\delta_{M_L,M'_L}\delta_{F,F'}\delta_{M_F,M'_F}L(L+1).
\end{aligned} \tag{A.2.3}$$

The matrix elements of the hyperfine interaction in the monomer Hamiltonians are

$$\begin{aligned}
&\langle (s_a,i_a)f_a(s_b,i_b)f_bFM_FLM_L|\,\zeta^a_{\mathrm{hfs}}\hat{i_a}\cdot\hat{s_a}+\zeta^b_{\mathrm{hfs}}\hat{i_b}\cdot\hat{s_b}\,|(s_a,i_a)f'_a(s_b,i_b)f'_bF'M'_FL'M'_L\rangle = \\
&\delta_{L,L'}\delta_{M_L,M'_L}\delta_{F,F'}\delta_{M_F,M'_F}\delta_{f_a,f'_a}\delta_{f_b,f'_b}\frac{(-1)^{2F}}{2}\left[\zeta^a_{\mathrm{hfs}}\left(f_a(f_a+1)-s_a(s_a+1)-i_a(i_a+1)\right)\right. \\
&\left.+\zeta^b_{\mathrm{hfs}}\left(f_b(f_b+1)-s_b(s_b+1)-i_b(i_b+1)\right)\right].
\end{aligned} \tag{A.2.4}$$

The matrix elements of the Zeeman operator in the monomer Hamiltonians are

$$
\begin{aligned}
&\langle (s_a,i_a)f_a(s_b,i_b)f_bFM_FLM_L|\mu_\mathrm{B}B\left(g_{\mathrm{e},a}\hat{s}_{z,a}+g_{\mathrm{n},a}\hat{i}_{z,a}\right.\\
&\qquad\qquad\left.+g_{\mathrm{e},b}\hat{s}_{z,b}+g_{\mathrm{n},b}\hat{i}_{z,b}\right)|(s_a,i_a)f'_a(s_b,i_b)f'_bF'M'_FL'M'_L\rangle =\\
&\qquad\frac{\mu_\mathrm{B}B}{2}(-1)^{F-M_F}\sqrt{(2F+1)(2F'+1)}\begin{pmatrix} F & 1 & F' \\ -M_F & 0 & M'_F \end{pmatrix}\\
&\times\Bigg[\delta_{f_b,f'_b}(-1)^{F'+f_b+f_a}\sqrt{(2f_a+1)(2f'_a+1)}\begin{Bmatrix} f'_a & F' & f_b \\ F & f_a & 1 \end{Bmatrix}\\
&\qquad\times\Bigg[g_{\mathrm{e},a}(-1)^{f'_a+s_a+i_a}\sqrt{(2s_a+1)s_a(s_a+1)}\begin{Bmatrix} s_a & f'_a & i_a \\ f_a & s_a & 1 \end{Bmatrix}\\
&\qquad+g_{\mathrm{n},a}(-1)^{f_a+s_a+i_a}\sqrt{(2i_a+1)i_a(i_a+1)}\begin{Bmatrix} i_a & f'_a & s_a \\ f_a & i_a & 1 \end{Bmatrix}\Bigg]\Bigg]\\
&\times\delta_{f_a,f'_a}(-1)^{F+f'_b+f_a}\sqrt{(2f_b+1)(2f'_b+1)}\begin{Bmatrix} f'_b & F' & f_a \\ F & f_b & 1 \end{Bmatrix}\\
&\qquad\Bigg[g_{\mathrm{e},b}(-1)^{f'_b+s_b+i_b}\sqrt{(2s_b+1)s_b(s_b+1)}\begin{Bmatrix} s_b & f'_b & i_b \\ f_b & s_b & 1 \end{Bmatrix}\\
&\qquad+g_{\mathrm{n},b}(-1)^{f_b+s_b+i_b}\sqrt{(2i_b+1)i_b(i_b+1)}\begin{Bmatrix} i_b & f'_b & s_b \\ f_b & i_b & 1 \end{Bmatrix}\Bigg]\Bigg].
\end{aligned}
\tag{A.2.5}
$$

Appendix B

Complete list of p-wave resonances in ^{85}RbCs

The lowest-energy hyperfine state of ^{85}RbCs is the $(f, m_f) = (2, 2) + (3, 3)$ state. Scattering calculations on this state were performed for the p-wave incoming channel at 1 μK, including $L = 1$ and 3 functions (a p,f-basis), at collision energies of $E_{\text{coll}} = 1$ μK. Bound-state calculations were also performed immediately below the zero-energy threshold given by the energy of the separated atoms in their respective ground states. The magnetic-field positions of the bound states in this calculation give the location of resonances in the scattering length. The projection of L has three possible values for $L = 1$: $M_L = -1$, 0 and 1. Calculations were therefore performed for total angular momentum $M_{\text{tot}} = 4, 5$ and 6. The resonance positions for each M_{tot} are listed in Tables B.1−B.3 along with the L quantum number of the bound state causing the resonance.

B_0 (G)	L	B_0 (G)	L	B_0 (G)	L	B_0 (G)	L
16.18	3	70.54	1	427.06	1	570.36	3
19.66	3	154.98	1	442.56	3	601.34	3
23.18	3	163.57	1	444.19	3	609.71	3
32.07	3	299.02	3	460.67	1	614.81	1
37.74	1	323.66	3	475.12	3	628.95	3
46.76	3	345.57	3	509.95	3	642.13	3
48.35	3	373.18	3	526.42	1	967.88	3
51.57	3	401.05	1	550.51	3		
52.76	3	405.22	3	561.54	1		

Table B.1: Complete list of Feshbach resonances due to p,f-wave bound states in the scattering volume of the incoming $L = 1, M_L = +1$, $(f, m_f) = (2, +2) + (3, +3)$ channel of ^{85}RbCs in the field range from 0 to 1000 G.

B_0 (G)	L	B_0 (G)	L	B_0 (G)	L	B_0 (G)	L
1.64	1	54.68	3	459.43	1	605.33	3
10.36	3	70.15	1	474.96	3	609.18	3
12.13	3	155.55	1	486.71	3	613.27	1
13.9	3	163.51	1	497.05	1	628.02	3
16.28	3	165.68	1	499.42	3	640.9	3
17.05	3	191.28	1	509.59	3	663.16	1
19.58	3	217.15	1	528.15	1	704.73	1
23.09	3	299.05	3	549.14	3	725.72	3
32.11	3	324.17	3	550.3	3	781.03	3
37.52	3	345.78	3	560.07	1	820.19	3
46.8	3	373.1	3	569.2	3	865.5	3
48.32	3	405.06	3	570.39	3	967.47	3
51.3	1	428.8	1	573.33	3		
51.77	3	442.53	3	600.22	3		
53	3	444.4	3	600.8	1		

Table B.2: Complete list of Feshbach resonances due to p,f-wave bound states in the scattering volume of the incoming $L = 1, M_L = 0$, $(f, m_f) = (2, +2) + (3, +3)$ channel of ^{85}RbCs in the field range from 0 to 1000 G.

B_0 (G)	L	B_0 (G)	L	B_0 (G)	L	B_0 (G)	L
1.15	1	53.11	3	445	3	614.93	1
1.71	1	54.9	3	452.09	3	627.43	3
7.5	3	56.71	3	458.77	3	640.19	3
8.53	3	70.51	1	460.56	1	644.8	1
9.64	3	105.46	1	475.13	3	659.09	3
10.47	3	120.69	1	487.13	3	661.59	1
10.6	3	126.05	1	496.74	1	699.1	1
12.09	3	163.53	1	499.24	3	703.12	1
13.58	3	165.13	1	509.5	3	725.32	3
13.85	3	185.58	1	538.99	3	731.74	1
16.34	3	192.25	1	541.7	1	743.94	3
17.04	3	216.58	1	548.71	3	750.16	1
19.53	3	300.11	3	549.9	3	780.41	3
23.04	3	324.77	3	561.55	1	791.09	3
32.13	3	346.47	3	568.44	3	819.6	3
37.45	3	360.99	3	570.33	3	833.34	3
38.85	1	373.25	3	573.72	3	865.07	3
46.91	3	399.62	3	599.02	1	880.13	3
48.37	3	405.04	3	600.21	3	967.76	3
51.24	1	431.74	3	605.05	3		
51.82	3	442.63	3	609.02	3		

Table B.3: Complete list of Feshbach resonances due to p,f-wave bound states in the scattering volume of the incoming $L = 1, M_L = -1$, $(f, m_f) = (2, +2) + (3, +3)$ channel of ^{85}RbCs in the field range from 0 to 1000 G.

Appendix C

Complete list of Feshbach resonances in KCs

Scattering calculations were performed on mixtures of Cs and the isotopologues of K: ^{39}K, ^{40}K and ^{41}K. Calculations were performed on the s-wave incoming channel corresponding to each atomic species in the hyperfine ground state using an s,d-basis. Resonance positions were located by performing bound-state calculations at the zero-energy given by the energy of the separated atoms. Both resonance widths Δ and the background scattering length a_{bg} were calculated for each resonance by fitting, of the scattering length around the resonance pole, to Eq. (2.3.4). L and M_F quantum numbers were assigned to each resonance by performing calculations with an appropriately restricted basis set for each quantum number. The resonance positions, widths, background scattering length and quantum number assignments for resonances occuring between 0 and 1000 G are given in Table C.1 for ^{39}KCs, Table C.2 for ^{40}KCs, and Table C.3 for ^{41}KCs.

with spin-orbit coupling					without spin-orbit coupling				
B_0 (G)	Δ (G)	a_{bg} (bohr)	L	M_F	B_0 (G)	Δ (G)	a_{bg} (bohr)	L	M_F
3.00	1.00×10^{-5}	69.4	2	2	3.01	5.00×10^{-6}	69.4	2	2
5.48	7.00×10^{-5}	69.6	2	3	5.50	4.00×10^{-5}	69.6	2	3
10.78	4.00×10^{-7}	70.1	2	2	10.80	1.00×10^{-6}	70.1	2	2
16.31	6.00×10^{-6}	70.6	2	2	16.28	1.00×10^{-5}	70.6	2	2
18.15	5.00×10^{-6}	70.8	2	3	18.21	2.00×10^{-6}	70.8	2	3
49.57	0.001	73.2	2	4	51.22	9.00×10^{-4}	73.3	2	4
202.90	3.00×10^{-6}	80.0	2	2	202.80	4.00×10^{-7}	79.9	2	2
240.22	6.00×10^{-5}	81.5	2	3	240.24	3.00×10^{-5}	81.5	2	3
255.73	3.00×10^{-6}	82.4	2	2	255.78	5.00×10^{-6}	82.4	2	2
298.58	1.00×10^{-5}	87.2	2	3	298.47	1.00×10^{-5}	87.2	2	3
318.14	8.00×10^{-5}	94.5	2	5	317.91	9.00×10^{-6}	94.3	2	5
323.90	6.00×10^{-7}	99.6	2	2	324.18	1.00×10^{-7}	100	2	2
326.94	3.00×10^{-5}	103.8	2	4	327.57	0.001	104.9	2	4
341.90	4.8	78.8	0	4	341.89	4.8	78.8	0	4
373.85	2.00×10^{-6}	68.3	2	3	373.55	9.00×10^{-7}	68.3	2	3
375.35	0.006	68.5	2	4	377.04	0.003	68.5	2	4
412.43	1.00×10^{-6}	77.2	2	2	413.07	$< 10^{-9}$	77.5	2	2
421.36	0.4	74.7	0	4	421.37	0.4	74.7	0	4
697.02	0.03	80.0	2	6	695.40	9.00×10^{-4}	80	2	6
714.61	5.00×10^{-4}	79.8	2	5	715.32	1.00×10^{-5}	79.8	2	5
734.71	5.00×10^{-6}	80.0	2	4	736.16	3.00×10^{-7}	80	2	4
757.46	$< 10^{-9}$	80.4	2	3	758.18	$< 10^{-9}$	80.4	2	3
760.13	0.004	80.3	2	5	760.68	1.00×10^{-4}	80.3	2	5
778.98	1.00×10^{-4}	79.9	2	4	780.02	1.00×10^{-7}	80.5	2	4
798.34	2.00×10^{-7}	80.7	2	3	798.91	2.00×10^{-9}	80.7	2	3
813.14	3.00×10^{-4}	81.0	0	4	813.07	3.00×10^{-4}	81	0	4
819.98	1.00×10^{-7}	81.1	2	2	818.98	3.00×10^{-7}	81.1	2	2
848.78	2.00×10^{-4}	82.0	2	4	850.31	4.00×10^{-4}	82	2	4
849.80	4.00×10^{-4}	82.0	2	3	850.44	6.00×10^{-5}	82	2	3
860.52	0.05	82.0	0	4	860.45	0.05	82	0	4
869.41	9.00×10^{-6}	81.9	2	2	868.59	2.00×10^{-6}	81.9	2	2
907.54	0.02	92.7	2	3	908.07	0.004	92.7	2	3
915.56	1.2	80.1	0	4	915.48	1.2	80.1	0	4
926.77	1.00×10^{-4}	71.4	2	2	925.97	3.00×10^{-5}	71.4	2	2
983.40	4.00×10^{-6}	79.1	2	2	982.47	2.00×10^{-7}	79.1	2	2

Table C.1: Complete list of Feshbach resonances due to s-wave and d-wave states in ^{39}KCs $|1,1\rangle$ + ^{133}Cs $|3,+3\rangle$ in the field range from 0 to 1000 G. Resonances are colour-coded according to their L and M_F quantum numbers as in Fig. 5.12

B_0 (G)	Δ (G)	$a_{\rm bg}$ (bohr)	L	M_F
27.11	$< 10^{-9}$	−40.3	2	1/2
29.04	$< 10^{-9}$	−40.3	2	−1/2
31.29	$< 10^{-9}$	−40.3	2	−3/2
31.61	$< 10^{-9}$	−40.3	2	1/2
33.93	$< 10^{-9}$	−40.3	2	−5/2
34.39	$< 10^{-9}$	−40.3	2	−1/2
37.03	$< 10^{-9}$	−40.3	2	−7/2
37.70	$< 10^{-9}$	−40.3	2	−3/2
38.15	$< 10^{-9}$	−40.3	2	1/2
41.67	$< 10^{-9}$	−40.3	2	−5/2
42.37	$< 10^{-9}$	−40.3	2	−1/2
46.43	$< 10^{-9}$	−40.3	2	−7/2
47.55	$< 10^{-9}$	−40.3	2	−3/2
48.41	$< 10^{-9}$	−40.3	2	1/2
54.03	$< 10^{-9}$	−40.3	2	−5/2
55.44	$< 10^{-9}$	−40.3	2	−1/2
57.59	$< 10^{-9}$	−40.3	0	−3/2
62.30	$< 10^{-9}$	−40.3	2	−7/2
64.61	$< 10^{-9}$	−40.3	2	−3/2
66.58	$< 10^{-9}$	−40.3	2	1/2
69.85	$< 10^{-9}$	−40.3	0	−3/2
76.91	$< 10^{-9}$	−40.3	2	−5/2
80.52	$< 10^{-9}$	−40.3	2	−1/2
89.01	$< 10^{-9}$	−40.3	0	−3/2
93.91	$< 10^{-9}$	−40.3	2	−7/2
100.74	-7.00×10^{-9}	−40.3	2	−3/2
107.66	$< 10^{-9}$	−40.3	2	1/2
122.77	$< 10^{-9}$	−40.3	0	−3/2
131.53	-7.00×10^{-8}	−40.3	2	−5/2
146.13	$< 10^{-9}$	−40.2	2	−7/2
148.04	-7.00×10^{-7}	40.2	2	−1/2
149.18	$< 10^{-9}$	−40.2	2	−7/2
152.63	$< 10^{-9}$	−40.2	2	−7/2
156.29	-2.00×10^{-9}	−40.2	2	−7/2
157.12	$< 10^{-9}$	−40.2	2	−5/2
160.07	$< 10^{-9}$	−40.2	2	−5/2
163.64	$< 10^{-9}$	−40.2	2	−5/2
167.93	-5.00×10^{-9}	−40.2	2	−5/2
170.86	$< 10^{-9}$	−40.2	2	−3/2
172.61	-2.00×10^{-7}	−40.2	2	−5/2
173.42	$< 10^{-9}$	−40.2	2	−3/2
176.82	$< 10^{-9}$	−40.2	2	−3/2
180.76	-3.00×10^{-7}	−40.2	2	−7/2
181.08	-1.00×10^{-8}	−40.2	2	−3/2
185.94	-2.00×10^{-6}	−40.2	2	−3/2
188.71	$< 10^{-9}$	−40.2	2	−1/2
190.26	$< 10^{-9}$	−40.2	2	−1/2
192.18	−0.001	−40.2	2	−3/2
192.99	$< 10^{-9}$	−40.2	2	−1/2
196.71	-3.00×10^{-7}	−40.2	0	−3/2
196.98	-7.00×10^{-9}	−40.2	2	−1/2
202.19	-1.00×10^{-7}	−40.2	2	−1/2
208.40	-2.00×10^{-5}	−40.1	2	−1/2
211.94	$< 10^{-9}$	−40.2	2	1/2
213.62	$< 10^{-9}$	−40.0	2	1/2
214.74	$< 10^{-9}$	−40.01	2	1/2
215.96	−0.01	−40.2	2	−1/2
216.62	$< 10^{-9}$	−40.1	2	1/2
221.34	$< 10^{-9}$	−40.3	2	1/2
224.77	-8.00×10^{-6}	−40.2	2	−3/2
227.53	-1.00×10^{-9}	−40.2	2	1/2
230.24	$< 10^{-9}$	−40.2	0	−3/2
234.15	$< 10^{-9}$	−40.1	0	−3/2
235.27	-3.00×10^{-7}	−40.1	2	1/2
239.55	$< 10^{-9}$	−40.1	0	−3/2
246.44	-4.00×10^{-7}	−40.0	0	−3/2
254.52	-1.00×10^{-4}	−39.8	0	−3/2
264.34	−0.1	−40.3	0	−3/2
318.65	-3.00×10^{-7}	−40.3	2	1/2
379.66	−0.002	−40.3	2	−5/2
466.46	$< 10^{-9}$	−40.1	2	1/2
470.25	−0.01	−40.2	0	−3/2
531.47	$< 10^{-9}$	−40.3	2	−1/2
588.83	$< 10^{-9}$	−40.3	2	−3/2
627.82	$< 10^{-9}$	−40.3	2	1/2
642.01	$< 10^{-9}$	−40.3	2	−5/2
677.44	$< 10^{-9}$	−40.2	0	−3/2
692.46	$< 10^{-9}$	−40.2	2	−7/2
706.12	$< 10^{-9}$	−40.2	2	−1/2
779.66	$< 10^{-9}$	−40.2	2	−3/2
850.61	$< 10^{-9}$	−40.2	2	−5/2
892.62	$< 10^{-9}$	−40.2	2	1/2
902.84	$< 10^{-9}$	−40.2	0	−3/2
920.11	$< 10^{-9}$	−40.2	2	−7/2

Table C.2: Complete list of Feshbach resonances due to s-wave and d-wave states in ^{40}KCs $|9/2,-9/2\rangle$ + ^{133}Cs $|3,+3\rangle$ in the field range from 0 to 1000 G. Resonances are colour-coded according to their L and M_F quantum numbers as in Fig. 5.13.

B_0 (G)	Δ (G)	a_{bg} (bohr)	L	M_F
23.89	0.02	193.0	2	6
25.68	0.03	189.3	2	5
28.41	0.007	188.7	2	4
32.10	8.00×10^{-4}	190.4	2	3
36.63	3.00×10^{-5}	192.0	2	2
39.24	3.00×10^{-7}	192.7	2	5
42.86	1.00×10^{-5}	193.5	2	4
47.27	1.00×10^{-5}	194.5	2	3
50.85	2.00×10^{-6}	195.2	2	2
53.03	5.00×10^{-4}	195.6	2	4
55.54	6.00×10^{-5}	196.0	2	3
56.61	1.00×10^{-7}	196.2	2	2
64.87	2.00×10^{-5}	197.6	2	3
68.54	5.00×10^{-8}	198.3	2	2
87.38	0.003	201.6	2	4
90.10	0.008	201.1	2	5
90.44	2.00×10^{-4}	205.7	2	3
91.56	3.00×10^{-4}	200.3	2	2
94.28	0.001	201.5	2	3
98.50	8.00×10^{-4}	202.5	2	2
98.54	3.00×10^{-4}	202.3	2	4
108.84	7.00×10^{-7}	204.7	2	3
109.86	0.002	204.5	2	2
111.04	4.00×10^{-4}	204.3	0	4
113.93	3.00×10^{-4}	205.3	0	4
120.89	0.02	206.0	0	4
126.59	1.00×10^{-4}	206.4	2	2
168.19	0.6	262.9	0	4
171.20	1.2	151.0	0	4
629.69	1.00×10^{-4}	212.6	2	2
737.86	5.00×10^{-5}	216.3	2	2
746.95	1.00×10^{-4}	216.8	2	3
755.11	7.00×10^{-6}	217.3	2	2
806.40	7.00×10^{-5}	222.2	2	4
818.33	3.00×10^{-6}	224.3	2	3
830.92	3.00×10^{-9}	227.5	2	2
861.03	0.03	247.7	2	5
877.70	7.00×10^{-4}	330.8	2	4
884.92	4.1	212.7	0	4
894.13	4.00×10^{-8}	119.1	2	3
910.60	< 1 nG	178.4	2	2
966.89	0.1	201.5	0	4

Table C.3: Complete list of Feshbach resonances due to s-wave and d-wave states in ^{41}KCs $\|1, 1\rangle$ + ^{133}Cs $\|3, +3\rangle$ in the field range from 0 to 1000 G. Resonances are colour-coded according to their L and M_F quantum numbers as in Fig. 5.15.

Appendix D

Consideration of the intra- and inter-species scattering-length combinations in mixtures ^{85}RbCs

The scattering lengths from the s-wave $(f, m_f) = (2, +2) + (2, +2)$ and $(2, -2) + (2, -2)$ channels of ^{85}Rb are considered along with the scattering length of the s-wave $(f, m_f) = (2, +3) + (2, +3)$ channel of Cs and the scattering length of the s-wave $(f, m_f) = (2, -2) + (3, +3)$ and $(2, -2) + (3, -3)$ channels of ^{85}RbCs, to find regions conducive to molecule formation using degenerate condensates. Two excited-state scattering lengths of ^{85}RbCs are shown in Figures D.1 and D.2, respectively. The scattering lengths are compared using the criteria detailed in Sec. 5.3 in order to find magnetic-field regions where the species can be simultaneously cooled (marked in red and blue) and where the condensates would be stable and miscible (marked in green). There is no combination of scattering lengths which results in a magnetic-field region where both species can be cooled. There is a small region for both interspecies scattering lengths, in the comparison with the $(2, -2) + (2, -2)$ channel of ^{85}Rb, where the condensates would be stable and miscible. This occurs around the wide resonance at 155 G in the $(2, -2) + (2, -2)$ channel of ^{85}Rb.

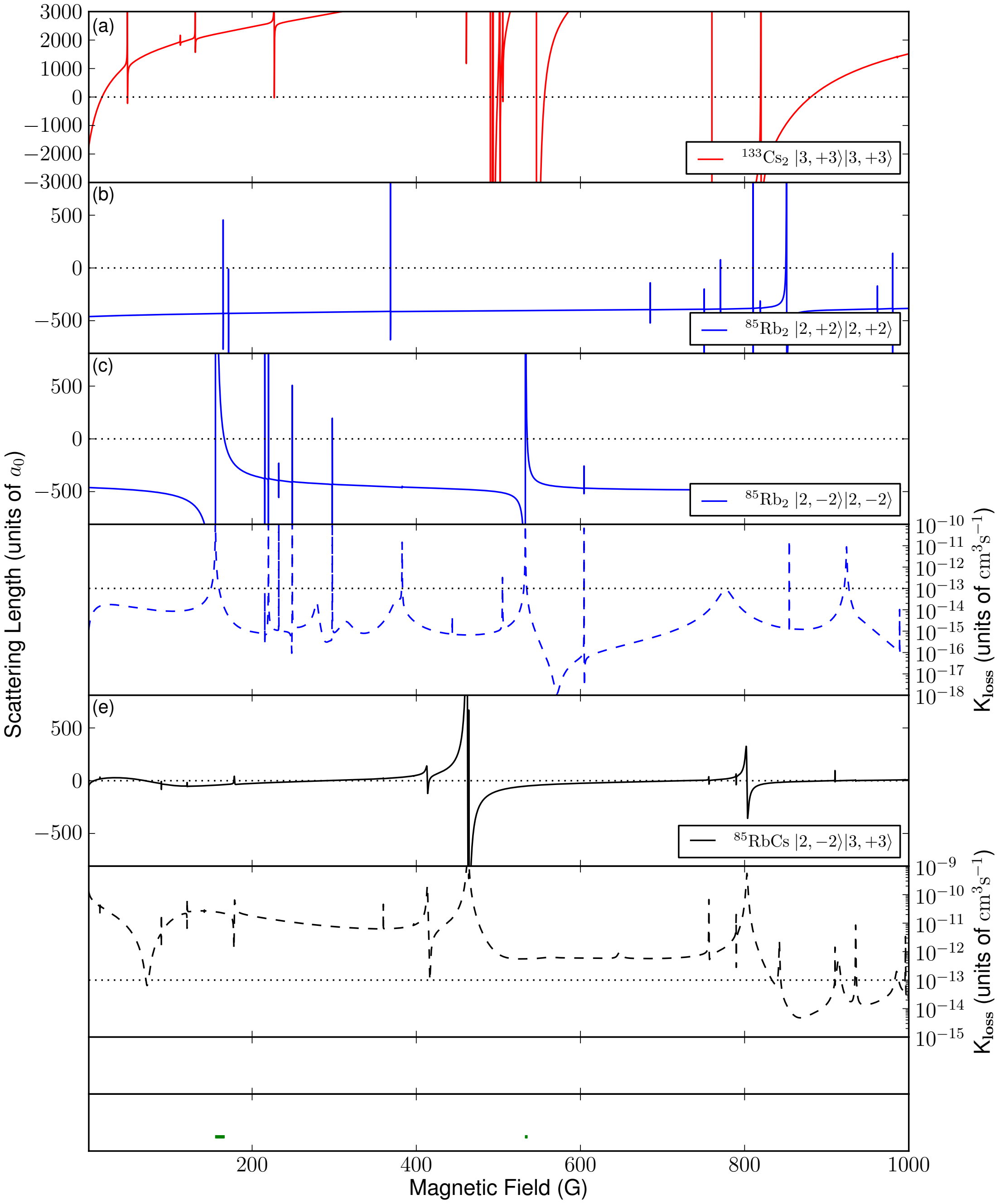

Figure D.1: ^{85}RbCs: (a) The s-wave scattering length in the $(f, m_f) = (3, 3) + (3, 3)$ channel of ^{133}Cs using an s,d,g-basis; (b) The s-wave scattering length in the $(f, m_f) = (2, 2) + (2, 2)$ channel of ^{85}Rb using an s,d-basis; (c) The real part of the s-wave scattering length in the $(f, m_f) = (2, -2) + (2, -2)$ channel of ^{85}Rb using an s,d-basis and below K_{loss} for this channel; (d) The real part of the s-wave scattering length in the $(f, m_f) = (2, -2) + (3, 3)$ channel of ^{85}RbCs using an s, d-basis and below K_{loss} for this channel. The coloured bars beneath the ^{85}RbCs scattering length indicate the fields at which both species can be cooled evaporatively (red, top), the fields at which one species can be cooled evaporatively and the other sympathetically (blue, center), and the fields at which the condensates are miscible (green, bottom): the top bar corresponds to comparison with the (2,+2) state of ^{85}Rb and the lower bar to the (2,-2) state.

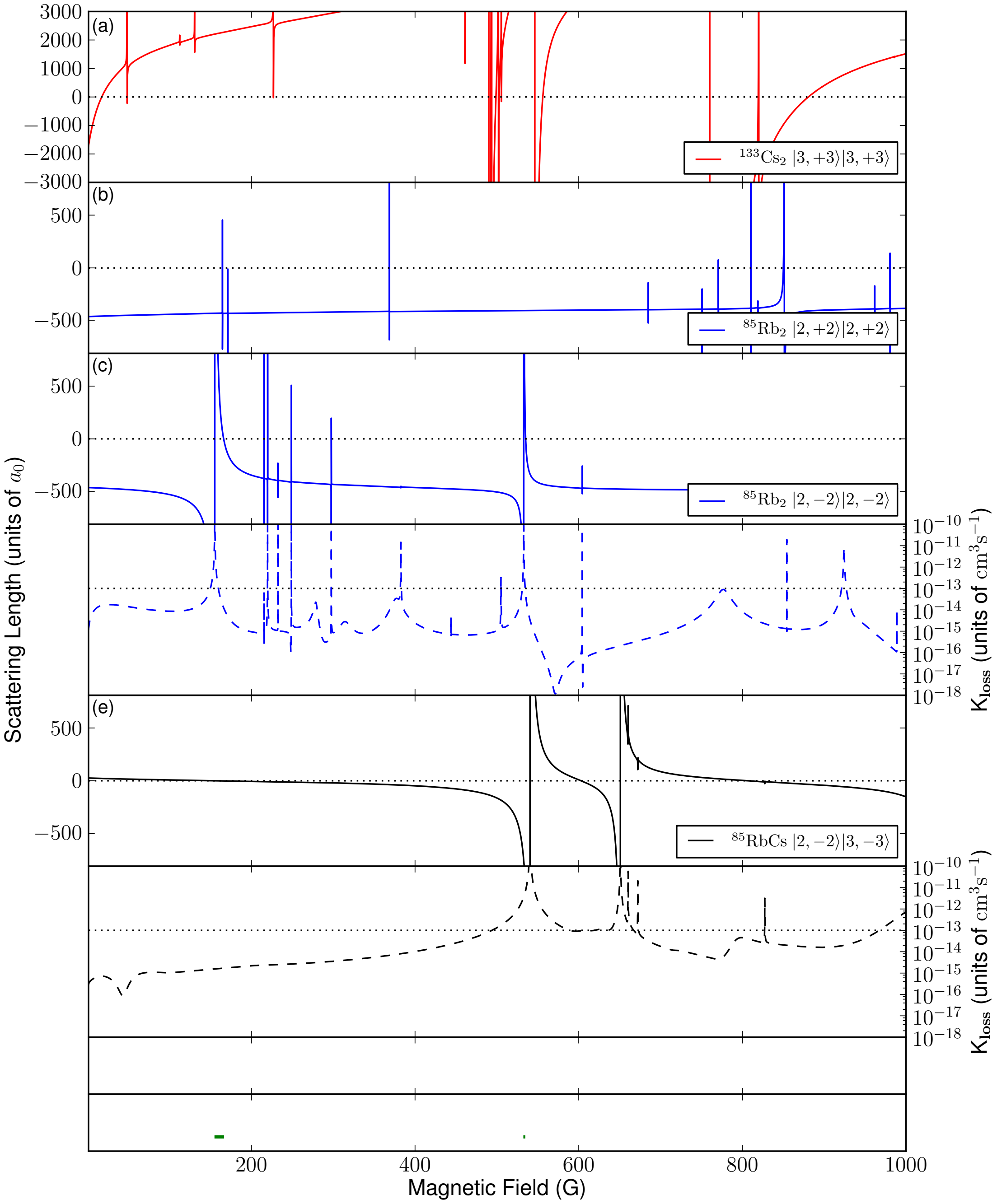

Figure D.2: ^{85}RbCs: (a) The s-wave scattering length in the $(f, m_f) = (3,3)+(3,3)$ channel of ^{133}Cs using an s,d,g-basis; (b) The s-wave scattering length in the $(f, m_f) = (2,2)+(2,2)$ channel of ^{85}Rb using an s,d-basis; (c) The real part of the s-wave scattering length in the $(f, m_f) = (2,-2)+(2,-2)$ channel of ^{85}Rb using an s,d-basis and below K_{loss} for this channel; (d) The real part of the s-wave scattering length in the $(f, m_f) = (2,-2)+(3,-3)$ channel of ^{85}RbCs using an s,d-basis and below K_{loss} for this channel. The coloured bars beneath the ^{85}RbCs scattering length indicate the fields at which both species can be cooled evaporatively (red, top), the fields at which one species can be cooled evaporatively and the other sympathetically (blue, center), and the fields at which the condensates are miscible (green, bottom): the top bar corresponds to comparison with the (2,+2) state of ^{85}Rb and the lower bar to the (2,-2) state.

Appendix E

Mixed-state scattering lengths in ^{85}Rb

Other scattering lengths for the series of mixed spin channels from the $(f_a, f_b) = (2, 3)$ hyperfine manifold were calculated as well as the scattering length discussed in Section 4.1.3. Of the possible combinations, a wide tunable resonance was found in the s-wave scattering lengths of the $(f, m_f) = (2, +2) + (3, +2)$, $(2, +2) + (3, +1)$ and $(2, +2) + (3, 0)$ incoming channels. Wide resonances can be used to tune the scattering length of the system; when the scattering length is tuned from positive to negative (or vice-versa) using a Feshbach resonance then the overall behaviour of the condensate switches between repulsive and attractive. The scattering length of the $(2, +2) + (3, 0)$ channel is shown in Fig. E.1; the wide resonance is located at 872.2 G and has a width of 27 G. The scattering length of the $(2, +2) + (3, +1)$ channel is shown in Fig. E.2; the wide resonance is located at 133 G and has a width of 4 G. The scattering length of the $(2, +2) + (3, +2)$ channel is shown in Fig. E.3; the wide resonance is located at 309.4 G and has a width of 14 G

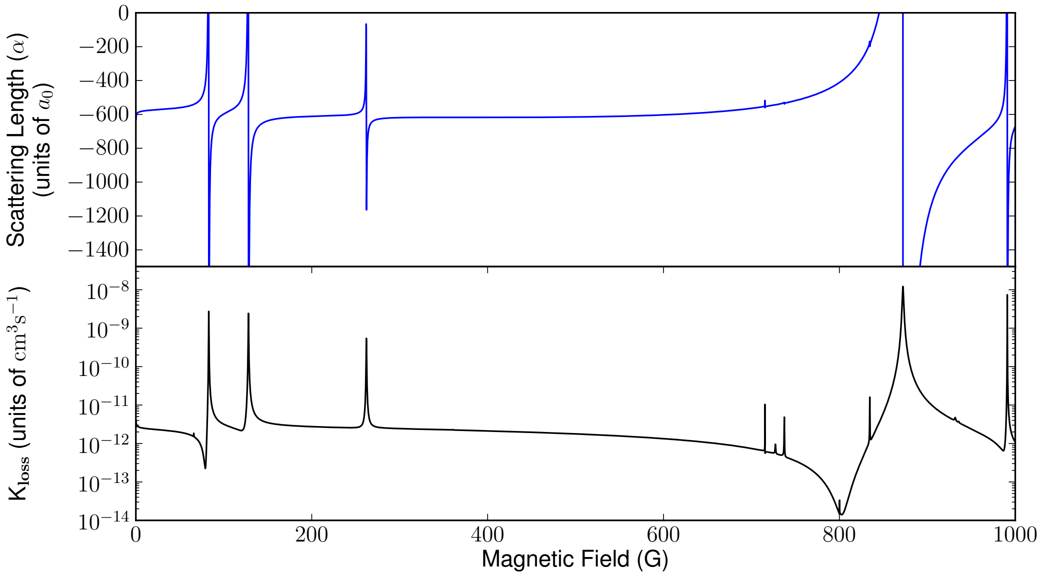

Figure E.1: Scattering length of the $(f, m_f) = (2, +2) + (3, +0)$ channel of ^{85}Rb. Top: Real part of the scattering length. Bottom: The co-efficient of the two-body loss rate.

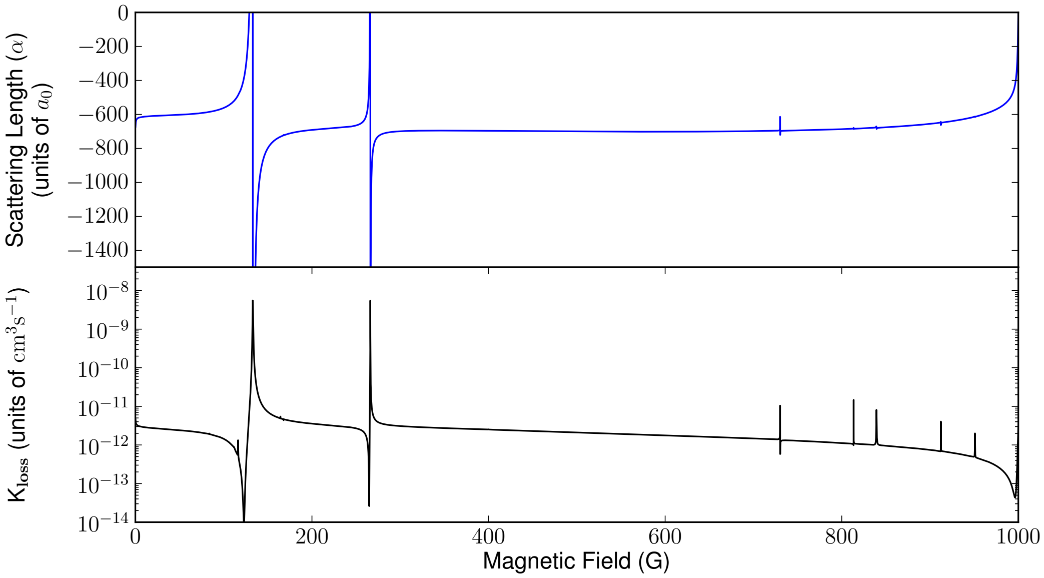

Figure E.2: Scattering length of the $(f, m_f) = (2, +2) + (3, +1)$ channel of ^{85}Rb. Top: Real part of the scattering length. Bottom: The co-efficient of the two-body loss rate.

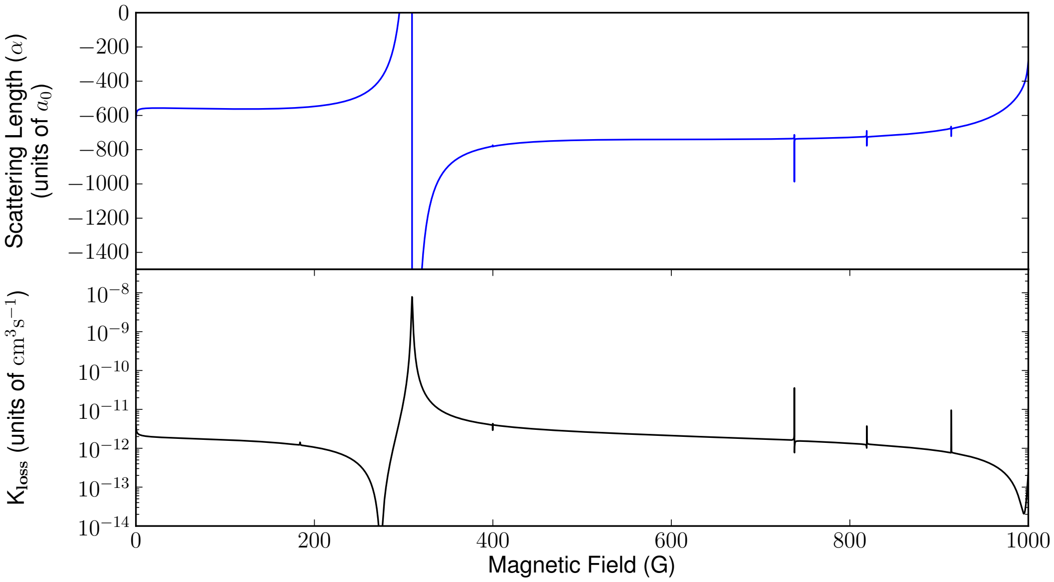

Figure E.3: Scattering length of the $(f, m_f) = (2, +2) + (3, +2)$ channel of ^{85}Rb. Top: Real part of the scattering length. Bottom: The co-efficient of the two body loss rate.

Appendix F

Triplet fraction in products of field-dressed eigenfunctions of ^{85}RbCs

In Section 6.2 the transformation from the products of the field-dressed atomic eigenfunctions to the $|SM_S m_{i,a} m_{i,b}\rangle$ basis is given. This transformation can be used to calculate the singlet and triplet fraction of each field-dressed atomic eigenfunction. In Figures F.1−F.3 the triplet fractions of ^{85}RbCs are shown. The field-dressed atomic eigenfunctions are labelled according to their low-field $(m_{f_{\rm Rb}}, m_{f_{\rm Cs}})$ quantum numbers. The states which correspond to the $(f_{\rm Rb}, f_{\rm Cs}) = (3, 3)$ hyperfine manifold at zero field are shown in Fig. F.1; the states which correspond to the $(2, 4)$ hyperfine manifold at zero field are shown in Fig. F.2; and the states which correspond to the $(3, 4)$ hyperfine manifold at zero field are shown in Fig. F.3. The spin-stretched state $(f_{\rm Rb}, m_{f_{\rm Rb}}, f_{\rm Cs}, m_{f_{\rm Cs}}) = (3, 3, 4, 4)$ has completely triplet character as expected.

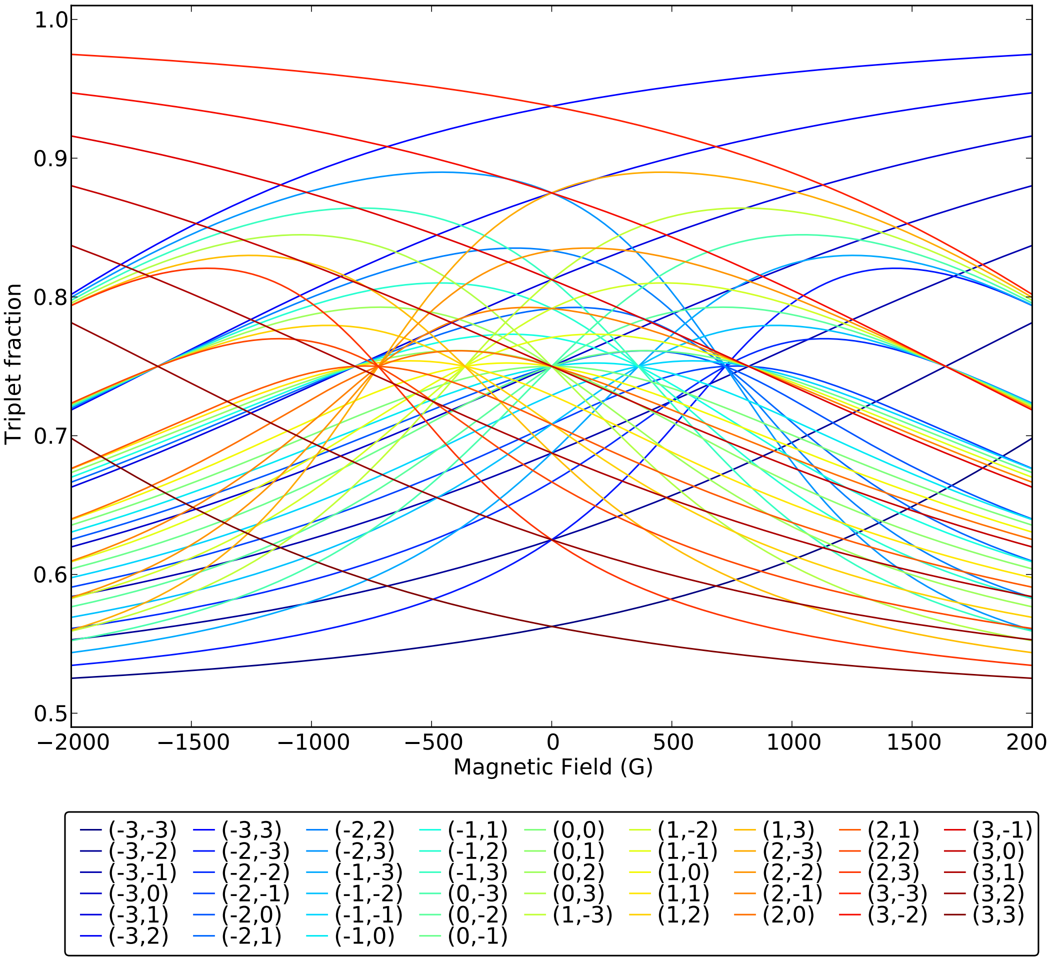

Figure F.1: Triplet fraction of the products of the field-dressed atomic eigenfunctions of ^{85}RbCs. Each state is labelled by its $(m_{f_{\rm Rb}}, m_{f_{\rm Cs}})$ quantum number and correlates with $(f_{\rm Rb}, f_{\rm Cs}) = (3, 3)$ at zero field although the different f levels will be mixed at higher fields.

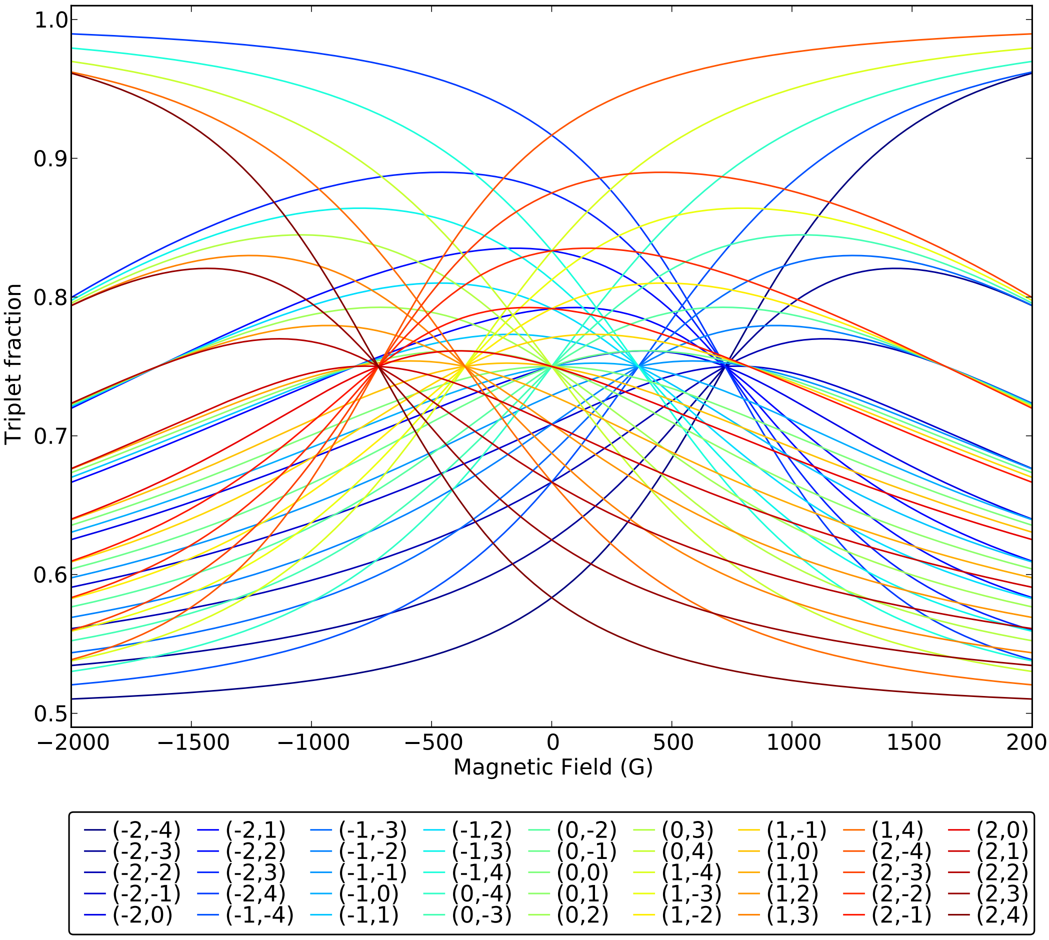

Figure F.2: Triplet fraction of the products of the field-dressed atomic eigenfunctions of ^{85}RbCs. Each state is labelled by its $(m_{f_{\rm Rb}}, m_{f_{\rm Cs}})$ quantum number and correlates with $(f_{\rm Rb}, f_{\rm Cs}) = (2,4)$ at zero field although the different f levels will be mixed at higher fields.

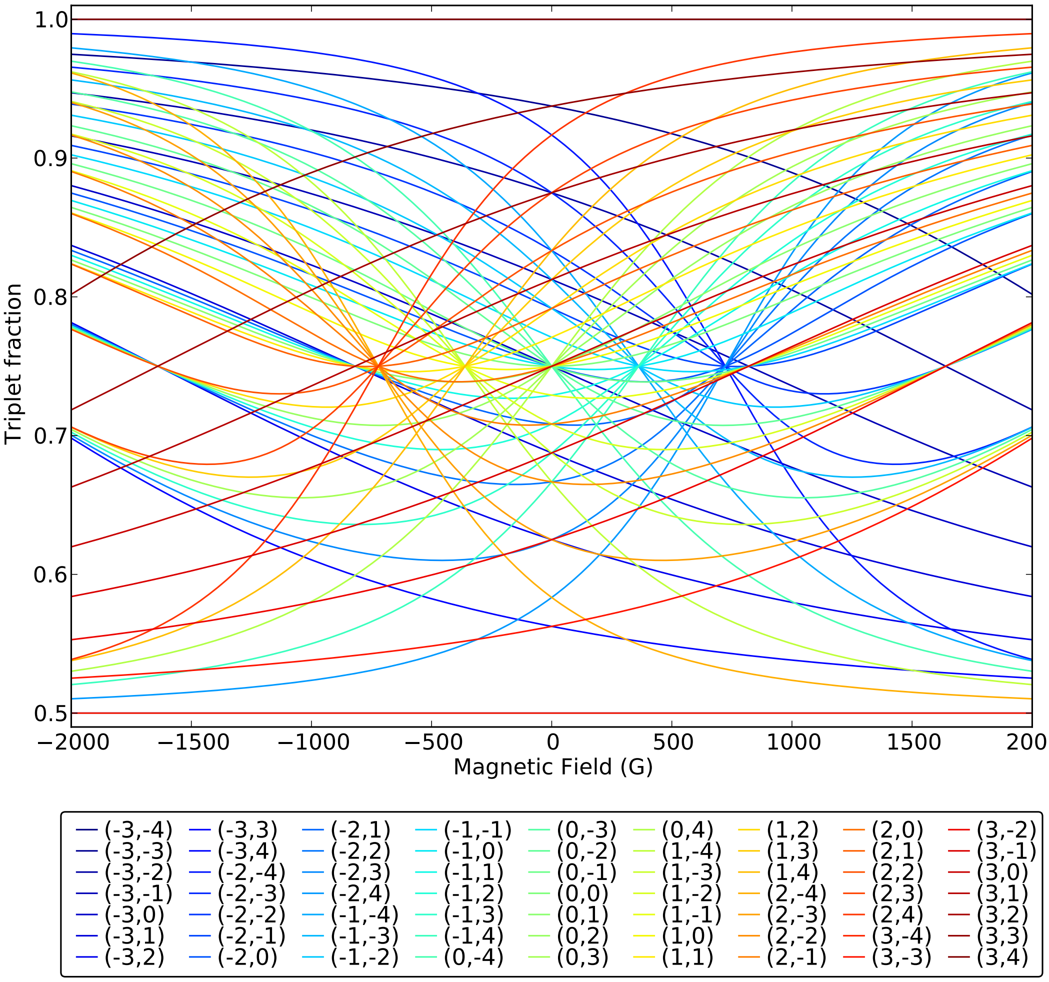

Figure F.3: Triplet fraction of the products of the field-dressed atomic eigenfunctions of ^{85}RbCs. Each state is labelled by its $(m_{f_{\rm Rb}}, m_{f_{\rm Cs}})$ quantum number and correlates with $(f_{\rm Rb}, f_{\rm Cs}) = (3, 4)$ at zero field although the different f levels will be mixed at higher fields.

Bibliography

[1] Amontons, G. *Histoire de l'Académie Royale des Sciences avec les Mémoires de Mathématique et de Physique* , 50 (1703).

[2] Thomson, W. *Proceedings of the Cambridge Philosophical Society* , 66 (1848).

[3] Thilorier, A. *Comptes Rendus* **1**, 194–196 (1835).

[4] Dewar, J. *Annales de Chimie et de Physique* **18**, 145–150 (1899).

[5] Onnes, H. In *Nobel Lectures in Physics (1901-1921),* Lundqvist, S., editor, 303–336. (1998).

[6] Kapitza, P. *Nature* **141**(74) (1938).

[7] Allen, J. and Misener, A. *Nature* **141**(75) (1938).

[8] Chu, S. *Rev. Mod. Phys.* **70**, 685–706 (1998).

[9] Cohen-Tannoudji, C. N. *Rev. Mod. Phys.* **70**, 707–719 (1998).

[10] Phillips, W. D. *Rev. Mod. Phys.* **70**(3), 721–741 (1998).

[11] Bose, S. N. *Z. Phys.* **26**, 178 (1924).

[12] Einstein, A. *Sitzber. Kgl. Preuss. Akad. Wiss.* , 261 (1924).

[13] Cornell, E. A. and Wieman, C. E. *Rev. Mod. Phys.* **74**(3), 875–893 (2002).

[14] Ketterle, W. *Rev. Mod. Phys.* **74**(4), 1131–1151 (2002).

[15] DeMarco, B. and Jin, D. S. *Science* **285**(5434), 1703–1706 (1999).

[16] Anderson, M. H., Ensher, J. R., Matthews, M. R., Wieman, C. E., and Cornell, E. A. *Science* **269**(5221), 198–201 (1995).

[17] Davis, K. B., Mewes, M.-O., Andrews, M. R., van Druten, N. J., Durfee, D. S., Kurn, D. M., and Ketterle, W. *Phys. Rev. Lett.* **75**(22), 3969–3973 (1995).

[18] Bradley, C. C., Sackett, C. A., Tollett, J. J., and Hulet, R. G. *Phys. Rev. Lett.* **75**(9), 1687–1690 (1995).

[19] Fried, D. G., Killian, T. C., Willmann, L., Landhuis, D., Moss, S. C., Kleppner, D., and Greytak, T. J. *Phys. Rev. Lett.* **81**(18), 3811–3814 (1998).

[20] Weber, T., Herbig, J., Mark, M., Nägerl, H. C., and Grimm, R. *Science* **299**(5604), 232–235 (2003).

[21] Takasu, Y., Maki, K., Komori, K., Takano, T., Honda, K., Kumakura, M., Yabuzaki, T., and Takahashi, Y. *Phys. Rev. Lett.* **91**(4), 040404 (2003).

[22] Aikawa, K., Akamatsu, D., Hayashi, M., Oasa, K., Kobayashi, J., Naidon, P., Kishimoto, T., Ueda, M., and Inouye, S. *Phys. Rev. Lett.* **105**, 203001 (2010).

[23] Carr, L. D., DeMille, D., Krems, R. V., and Ye, J. *New J. Phys.* **11**, 055049 (2009).

[24] Krems, R. V. *Int. Rev. Phys. Chem.* **24**(1), 99–118 (2005).

[25] Friedrich, B. and Doyle, J. M. *ChemPhysChem* **10**(4), 604–623 (2009).

[26] Chin, C., Flambaum, V. V., and Kozlov, M. G. *New J. Phys.* **11**(5), 055048 (2009).

[27] Hinds, E. A. *Phys. Scr.* **1997**, 34 (1997).

[28] Hudson, J. J., Sauer, B. E., Tarbutt, M. R., and Hinds, E. A. *Phys. Rev. Lett.* **89**(2), 023003 (2002).

[29] Krems, R. V. *Phys. Chem. Chem. Phys.* **10**(28), 4079–4092 (2008).

[30] Hutson, J. M. and Soldán, P. *Int. Rev. Phys. Chem.* **25**(4), 497–526 (2006).

[31] Weck, P. F. and Balakrishnan, N. *Int. Rev. Phys. Chem.* **25**(3), 283–311 (2006).

[32] Shuman, E. S., Barry, J. F., and DeMille, D. *Nature* **467**, 820–823 (2010).

[33] Weinstein, J. D., deCarvalho, R., Guillet, T., Friedrich, B., and Doyle, J. M. *Nature* **395**(6698), 148–150 (1998).

[34] Köhler, T., Góral, K., and Julienne, P. S. *Rev. Mod. Phys.* **78**, 1311–1361 (2006).

[35] Chin, C., Grimm, R., Tiesinga, E., and Julienne, P. S. *Rev. Mod. Phys.* **82**, 1225–1286 (2010).

[36] Doyle, J. M., Fredrich, B., Kim, J., and Patterson, D. *Phys. Rev. A* **52**(4), R2515–R2518 (1995).

[37] deCarvalho, R., Doyle, J. M., Friedrich, B., Guillet, T., Kim, J., Patterson, D., and Weinstein, J. D. *Eur. Phys. J. D* **7**(3), 289–309 (1999).

[38] Campbell, W. C. and Doyle, J. M. In *Cold Molecules: Theory, Experiment, Applications,* Krems, R. V., Friedrich, B., and Stwalley, W. C., editors, 473–508. Taylor & Francis (2009).

[39] Roth, B. and Schiller, S. In *Cold Molecules: Theory, Experiment, Applications,* Krems, R. V., Friedrich, B., and Stwalley, W. C., editors, 651–704. Taylor & Francis (2009).

[40] Mølhave, K. and Drewsen, M. *Phys. Rev. A* **62**, 011401 (2000).

[41] Djeu, N. and Whitney, W. T. *Phys. Rev. Lett.* **46**, 236–239 (1981).

[42] Bahns, J. T., Stwalley, W. C., and Gould, P. L. *J. Chem. Phys.* **104**(24), 9689–9697 (1996).

[43] Zhelyazkova, V., Cournol, A., Wall, T. E., Matsushima, A., Hudson, J. J., Hinds, E. A., Tarbutt, M. R., and Sauer, B. E. *Phys. Rev. A* **89**, 053416 (2014).

[44] Hummon, M. T., Yeo, M., Stuhl, B. K., Collopy, A. L., Xia, Y., and Ye, J. *Phys. Rev. Lett.* **110**, 143001 (2013).

[45] Barry, J. F., McCarron, D. J., Norrgard, E. B., Steinecker, M. H., and DeMille, D. *Nature* **512**, 286–289 (2014).

[46] Bethlem, H. L., Berden, G., and Meijer, G. *Phys. Rev. Lett.* **83**(8), 1558–1561 (1999).

[47] Bochinski, J. R., Hudson, E. R., Lewandowski, H. J., and Ye, J. *Phys. Rev. A* **70**, 043410 (2004).

[48] Crompvoets, F. M. H., Jongma, R. T., Bethlem, H. L., van Roij, A. J. A., and Meijer, G. *Phys. Rev. Lett.* **89**(9), 093004 (2002).

[49] Heiner, C. E., Bethlem, H. L., and Meijer, G. *Phys. Chem. Chem. Phys.* **8**(23), 2666–2676 (2006).

[50] Tarbutt, M. R., Bethlem, H. L., Hudson, J. J., Ryabov, V. L., Ryzhov, V. A., Sauer, B. E., Meijer, G., and Hinds, E. A. *Phys. Rev. Lett.* **92**(17), 173002 (2004).

[51] Vanhaecke, N., Meier, U., Andrist, M., Meier, B. H., and Merkt, F. *Phys. Rev. A* **75**, 031402(R) (2007).

[52] Hogan, S. D., Sprecher, D., Andrist, M., Vanhaecke, N., and Merkt, F. *Phys. Rev. A* **76**, 023412 (2007).

[53] Narevicius, E., Libson, A., Parthey, C. G., Chavez, I., Narevicius, J., Even, U., and Raizen, M. G. *Phys. Rev. A* **77**, 051401 (2008).

[54] Yamakita, Y., Procter, S. R., Goodgame, A. L., Softley, T. P., and Merkt, F. *J. Chem. Phys.* **121**(3), 1419–1431 (2004).

[55] Vliegen, E., Wörner, H. J., Softley, T. P., and Merkt, F. *Phys. Rev. Lett.* **92**, 033005 (2004).

[56] Barker, P. F. and Shneider, M. N. *Phys. Rev. A* **66**, 065402 (2002).

[57] Thorsheim, H. R., Weiner, J., and Julienne, P. S. *Phys. Rev. Lett.* **58**(23), 2420–2423 (1987).

[58] Nikolov, A. N., Ensher, J. R., Eyler, E. E., Wang, H., Stwalley, W. C., and Gould, P. L. *Phys. Rev. Lett.* **84**(2), 246–249 (2000).

[59] Fioretti, A., Comparat, D., Crubellier, A., Dulieu, O., Masnou-Seeuws, F., and Pillet, P. *Phys. Rev. Lett.* **80**(20), 4402–4405 (1998).

[60] Deiglmayr, J., Grochola, A., Repp, M., Mörtlbauer, K., Glück, C., Lange, J., Dulieu, O., Wester, R., and Weidemüller, M. *Phys. Rev. Lett.* **101**, 133004 (2008).

[61] Banerjee, J., Rahmlow, D., Carollo, R., Bellos, M., Eyler, E. E., Gould, P. L., and Stwalley, W. C. *Phys. Rev. A* **86**, 053428 (2012).

[62] Bruzewicz, C. D., Gustavsson, M., Shimasaki, T., and DeMille, D. *New J. Phys.* **16**(2), 023018 (2014).

[63] Timmermans, E., Tommasini, P., Hussein, M., and Kerman, A. *Phys. Rep.* **315**(1-3), 199–230 (1999).

[64] van Abeelen, F. A. and Verhaar, B. J. *Phys. Rev. Lett.* **83**(8), 1550–1553 (1999).

[65] Mies, F. H., Tiesinga, E., and Julienne, P. S. *Phys. Rev. A* **61**(2), 022721 (2000).

[66] Gaubatz, U., Rudecki, P., Schiemann, S., and Bergmann, K. *J. Chem. Phys.* **92**(9), 5363–5376 (1990).

[67] Ni, K.-K., Ospelkaus, S., de Miranda, M. H. G., Pe'er, A., Neyenhuis, B., Zirbel, J. J., Kotochigova, S., Julienne, P. S., Jin, D. S., and Ye, J. *Science* **322**, 231 (2008).

[68] Danzl, J. G., Mark, M. J., Haller, E., Gustavsson, M., Hart, R., Aldegunde, J., Hutson, J. M., and Nägerl, H.-C. *Nature Phys.* **6**, 265–270 (2010).

[69] Lang, F., Winkler, K., Strauss, C., Grimm, R., and Hecker Denschlag, J. *Phys. Rev. Lett.* **101**, 133005 (2008).

[70] Takekoshi, T., Reichsöllner, L., Schindewolf, A., Hutson, J. M., Le Sueur, C. R., Dulieu, O., Ferlaino, F., Grimm, R., and Nägerl, H.-C. *Phys. Rev. Lett.* **113**, 205301 (2014).

[71] Molony, P. K., Gregory, P. D., Ji, Z., Lu, B., Köppinger, M. P., Le Sueur, C. R., Blackley, C. L., Hutson, J. M., and Cornish, S. L. *Phys. Rev. Lett.* **113**, 255301 (2014).

[72] Blackley, C. L., Le Sueur, C. R., Hutson, J. M., McCarron, D. J., Köppinger, M. P., Cho, H.-W., Jenkin, D. L., and Cornish, S. L. *Phys. Rev. A* **87**, 033611 (2013).

[73] Gertjerenken, B., Billam, T. P., Khaykovich, L., and Weiss, C. *Phys. Rev. A* **86**, 033608 (2012).

[74] Billam, T. P., Blackley, C. L., Gertjerenken, B., Cornish, S. L., and Weiss, C. *J. Phys. Conf. Ser.* **497**(1), 012033 (2014).

[75] Cho, H.-W., McCarron, D. J., Köppinger, M. P., Jenkin, D. L., Butler, K. L., Julienne, P. S., Blackley, C. L., Le Sueur, C. R., Hutson, J. M., and Cornish, S. L. *Phys. Rev. A* **87**, 010703(R) (2013).

[76] Köppinger, M. P., McCarron, D. J., Jenkin, D. L., Molony, P. K., Cho, H.-W., Cornish, S. L., Le Sueur, C. R., Blackley, C. L., and Hutson, J. M. *Phys. Rev. A* **89**, 033604 (2014).

[77] Patel, H. J., Blackley, C. L., Cornish, S. L., and Hutson, J. M. *Phys. Rev. A* **90**, 032716 (2014).

[78] Blackley, C. L., Julienne, P. S., and Hutson, J. M. *Phys. Rev. A* **89**, 042701 (2014).

[79] Mott, N. F. and Massey, H. S. W. *The Theory of Atomic Collisions.* Clarendon Press, Oxford, 3rd edition, (1965).

[80] Child, M. S. *Molecular Collision Theory.* Academic Press, London, (1974).

[81] Taylor, J. R. *Scattering Theory: The Quantum Theory of Nonrelativistic Collisions.* Wiley, New York, (1972).

[82] Hutson, J. M. *Comput. Phys. Commun.* **84**, 1–18 (1994).

[83] Abramowitz, M. and Stegun, I. A. *Handbook of Mathematical Functions.* Dover, New York, 9th dover printing edition, (1964).

[84] Wigner, E. P. *Phys. Rev.* **73**(9), 1002–1009 (1948).

[85] Hutson, J. M. In *Cold Molecules: Theory, Experiment, Applications,* Krems, R. V., Stwalley, W. C., and Friedrich, B., editors, 3–37. Taylor & Francis, London (2009).

[86] Gribakin, G. F. and Flambaum, V. V. *Phys. Rev. A* **48**, 546 (1993).

[87] Julienne, P. S. and Mies, F. H. *J. Opt. Soc. Am. B* **6**(11), 2257–2269 (1989).

[88] Gao, B. *Phys. Rev. A* **62**(5), 050702 (2000).

[89] Hutson, J. M. *New J. Phys.* **9**, 152 (2007).

[90] Moerdijk, A. J., Verhaar, B. J., and Axelsson, A. *Phys. Rev. A* **51**(6), 4852–4861 (1995).

[91] Bohn, J. L. and Julienne, P. S. *Phys. Rev. A* **56**(2), 1486–1491 (1997).

[92] Hutson, J. M., Beyene, M., and González-Martínez, M. L. *Phys. Rev. Lett.* **103**, 163201 (2009).

[93] Fano, U. *Phys. Rev.* **124**, 1866 (1961).

[94] Feshbach, H. *Ann. Phys.* **5**(4), 357–390 (1958).

[95] Feshbach, H. *Ann. Phys.* **19**, 287–313 (1962).

[96] Bryant, H. C., Dieterle, B. D., Donahue, J., Sharifian, H., Tootoonchi, H., Wolfe, D. M., Gram, P. A. M., and Yates-Williams, M. A. *Phys. Rev. Lett.* **38**, 228–230 (1977).

[97] Rice, O. K. *J. Chem. Phys.* **1**, 375–389 (1933).

[98] Stwalley, W. C. *Phys. Rev. Lett.* **37**, 1628–1631 (1976).

[99] Tiesinga, E., Verhaar, B. J., and Stoof, H. T. C. *Phys. Rev. A* **47**, 4114–4122 (1993).

[100] Inouye, S., Andrews, M. R., Stenger, J., Miesner, H. J., Stamper-Kurn, D. M., and Ketterle, W. *Nature* **392**(6672), 151–154 (1998).

[101] Courteille, P., Freeland, R. S., Heinzen, D. J., van Abeelen, F. A., and Verhaar, B. J. *Phys. Rev. Lett.* **81**(1), 69–72 (1998).

[102] F. Ferlaino, S. K. and Grimm, R. In *Cold Molecules: Theory, Experiment, Applications,* Krems, R. V., Stwalley, W. C., and Friedrich, B., editors, 319–354. Taylor & Francis, London (2009).

[103] Johnson, B. R. *J. Chem. Phys.* **69**(10), 4678–4688 (1978).

[104] Johnson, B. R. *J. Comput. Phys.* **13**(3), 445–449 (1973).

[105] Manolopoulos, D. E. *J. Chem. Phys.* **85**(11), 6425–6429 (1986).

[106] Mrugała, F. and Secrest, D. *J. Chem. Phys.* **78**(10), 5954–5961 (1983).

[107] Manolopoulos, D. E., Jamieson, M. J., and Pradhan, A. D. *J. Comp. Phys.* **105**(1), 169 – 172 (1993).

[108] Manolopoulos, D. E. *Close-coupled equations: the log derivative approach to inelastic scattering, bound state and photofragmentation problems.* PhD thesis, University of Cambridge, Cambridge, UK, (1988).

[109] Alexander, M. H. and Manolopoulos, D. E. *J. Chem. Phys.* **86**, 2044 (1987).

[110] Hutson, J. M. and Green, S. distributed by Collaborative Computational Project No. 6 of the UK Engineering and Physical Sciences Research Council, (1994). MOLSCAT computer program, version 14.

[111] Hutson, J. M. distributed by Collaborative Computational Project No. 6 of the UK Engineering and Physical Sciences Research Council, (1993). BOUND computer program, version 5.

[112] Hutson, J. M., (2011). FIELD computer program, version 1.

[113] Hutson, J. M., (2011). BOUND computer code.

[114] González-Martínez, M. L. and Hutson, J. M. *Phys. Rev. A* **75**, 022702 (2007).

[115] Breit, G. and Rabi, I. I. *Phys. Rev. A* **38**, 2082–2083 (1931).

[116] Stoof, H. T. C., Koelman, J. M. V. A., and Verhaar, B. J. *Phys. Rev. B* **38**, 4688–4697 (1988).

[117] Smirnov, B. M. and Chibisov, M. I. *Sov. Phys. JETP* **21**, 624 (1965).

[118] Takekoshi, T., Debatin, M., Rameshan, R., Ferlaino, F., Grimm, R., Nägerl, H.-C., Le Sueur, C. R., Hutson, J. M., Julienne, P. S., Kotochigova, S., and Tiemann, E. *Phys. Rev. A* **85**, 032506 (2012).

[119] Ferber, R., Nikolayeva, O., Tamanis, M., Knöckel, H., and Tiemann, E. *Phys. Rev. A* **88**, 012516 (2013).

[120] Mies, F. H., Williams, C. J., Julienne, P. S., and Krauss, M. *J. Res. Natl. Inst. Stand. Technol* **101**, 521 (1996).

[121] Leo, P. J., Tiesinga, E., Julienne, P. S., Walker, D. K., Kadlecek, S., and Walker, T. G. *Phys. Rev. Lett.* **81**, 1389–1392 (1998).

[122] Kotochigova, S., Tiesinga, E., and Julienne, P. S. *Phys. Rev. A* **63**, 012517 (2000).

[123] Hutson, J. M., Tiesinga, E., and Julienne, P. S. *Phys. Rev. A* **78**, 052703 (2008).

[124] Burke, J. P., Bohn, J. L., Esry, B. D., and Greene, C. H. *Phys. Rev. Lett.* **80**(10), 2097 (1998).

[125] Cornish, S. L., Claussen, N. R., Roberts, J. L., Cornell, E. A., and Wieman, C. E. *Phys. Rev. Lett.* **85**(9), 1795–1798 (2000).

[126] Vogels, J. M., Tsai, C. C., Freeland, R. S., Kokkelmans, S. J. J. M. F., Verhaar, B. J., and Heinzen, D. J. *Phys. Rev. A* **56**, R1067–R1070 (1997).

[127] Roberts, J. L., Claussen, N. R., Cornish, S. L., Donley, E. A., Cornell, E. A., and Wieman, C. E. *Phys. Rev. Lett.* **86**(19), 4211–4214 (2001).

[128] Donley, E. A., Claussen, N. R., Cornish, S. L., Roberts, J. L., Cornell, E. A., and Wieman, C. E. *Nature* **412**(6844), 295–299 (2001).

[129] Altin, P. A., Dennis, G. R., McDonald, G. D., Döring, D., Debs, J. E., Close, J. D., Savage, C. M., and Robins, N. P. *Phys. Rev. A* **84**, 033632 (2011).

[130] Cornish, S. L., Thompson, S. T., and Wieman, C. E. *Phys. Rev. Lett.* **96**, 170401 (2006).

[131] Wild, R. J., Makotyn, P., Pino, J. M., Cornell, E. A., and Jin, D. S. *Phys. Rev. Lett.* **108**, 145305 (2012).

[132] Tsai, C. C., Freeland, R. S., Vogels, J. M., Boesten, H. M. J. M., Verhaar, B. J., and Heinzen, D. J. *Phys. Rev. Lett.* **79**, 1245–1248 (1997).

[133] Roberts, J. L., Claussen, N. R., Cornish, S. L., and Wieman, C. E. *Phys. Rev. Lett.* **85**(4), 728–731 (2000).

[134] Roberts, J. L., Burke, J. P., Claussen, N. R., Cornish, S. L., Donley, E. A., and Wieman, C. E. *Phys. Rev. A* **64**(2), 024702 (2001).

[135] Claussen, N. R., Kokkelmans, S. J. J. M. F., Thompson, S. T., Donley, E. A., Hodby, E., and Wieman, C. E. *Phys. Rev. A* **67**(6), 060701 (2003).

[136] Donley, E. A., Claussen, N. R., Thompson, S. T., and Wieman, C. E. *Nature* **417**(6888), 529–533 (2002).

[137] Thompson, S. T., Hodby, E., and Wieman, C. E. *Phys. Rev. Lett.* **95**(19), 190404 (2005).

[138] Köhler, T., Tiesinga, E., and Julienne, P. S. *Phys. Rev. Lett.* **94**(2), 020402 (2005).

[139] Hodby, E., Thompson, S. T., Regal, C. A., Greiner, M., Wilson, A. C., Jin, D. S., Cornell, E. A., and Wieman, C. E. *Phys. Rev. Lett.* **94**(12), 120402 (2005).

[140] Brown, B. L., Dicks, A. J., and Walmsley, I. A. *Phys. Rev. Lett.* **96**(17), 173002 (2006).

[141] Stoll, M. and Köhler, T. *Phys. Rev. A* **72**(2), 022714 (2005).

[142] Alexander, M. H. *J. Chem. Phys.* **81**, 4510–4516 (1984).

[143] Strauss, C., Takekoshi, T., Lang, F., Winkler, K., Grimm, R., Hecker Denschlag, J., and Tiemann, E. *Phys. Rev. A* **82**, 052514 (2010).

[144] Seto, J. Y., Le Roy, R. J., Vergès, J., and Amiot, C. *J. Chem. Phys* **113**(8), 3067–3076 (2000).

[145] McCarron, D. J., Cho, H. W., Jenkin, D. L., Köppinger, M. P., and Cornish, S. L. *Phys. Rev. A* **84**, 011603 (2011).

[146] Cho, H. W., McCarron, D. J., Jenkin, D. L., Köppinger, M. P., and Cornish, S. L. *Eur. Phys. J. D* **65**, 125 (2011).

[147] Altin, P. A., Robins, N. P., Poldy, R., Debs, J. E., Döring, D., Figl, C., and Close, J. D. *Phys. Rev. A* **81**, 012713 (2010).

[148] Marchant, A. L., Händel, S., Hopkins, S. A., Wiles, T. P., and Cornish, S. L. *Phys. Rev. A* **85**, 053647 (2012).

[149] K. E. Strecker, G. B. Partridge, A. G. T. and Hulet, R. G. *Nature* **417**, 150–153 (2005).

[150] Gertjerenken, B., Billam, T. P., Blackley, C. L., Le Sueur, C. R., Khaykovich, L., Cornish, S. L., and Weiss, C. *Phys. Rev. Lett.* **111**, 100406 (2013).

[151] Martin, A. D. and Ruostekoski, J. *New Journal of Physics* **14**(4), 043040 (2012).

[152] Cuevas, J., Kevrekidis, P. G., Malomed, B. A., Dyke, P., and Hulet, R. G. *New Journal of Physics* **15**(6), 063006 (2013).

[153] Weiss, C. and Castin, Y. *Phys. Rev. Lett.* **102**, 010403 (2009).

[154] Pu, H. and Bigelow, N. P. *Phys. Rev. Lett.* **80**, 1130–1133 (1998).

[155] Timmermans, E. *Phys. Rev. Lett.* **81**, 5718–5721 (1998).

[156] Öhberg, P. and Santos, L. *Phys. Rev. Lett.* **86**, 2918–2921 (2001).

[157] Bergeman, T., Moore, M. G., and Olshanii, M. *Phys. Rev. Lett.* **91**(16), 163201 Oct (2003).

[158] Olshanii, M. *Phys. Rev. Lett.* **81**(5), 938–941 (1998).

[159] Haller, E., Mark, M. J., Hart, R., Danzl, J. G., Reichsöllner, L., Melezhik, V., Schmelcher, P., and Nägerl, H.-C. *Phys. Rev. Lett.* **104**, 153203 (2010).

[160] Strauss, C., Takekoshi, T., Lang, F., Winkler, K., Grimm, R., Hecker Denschlag, J., and Tiemann, E. *Phys. Rev. A* **82**, 052514 (2010).

[161] Julienne, P. S. and Hutson, J. M. *Phys. Rev. A* **89**, 052715 (2014).

[162] Le Roy, R. J., Dattani, N. S., Coxon, J. A., Ross, A. J., Crozet, P., and Linton, C. *J. Chem. Phys.* **131**, 204309 (2009).

[163] Dattani, N. S. and Le Roy, R. J. *J. Mol. Spectrosc.* **268**, 199–210 (2011).

[164] Dürr, S., Volz, T., Marte, A., and Rempe, G. *Phys. Rev. Lett.* **92**(2), 020406 (2004).

[165] Marte, A., Volz, T., Schuster, J., Dürr, S., Rempe, G., van Kempen, E. G. M., and Verhaar, B. J. *Phys. Rev. Lett.* **89**(28), 283202 (2002).

[166] Berninger, M., Zenesini, A., Huang, B., Harm, W., Nägerl, H.-C., Ferlaino, F., Grimm, R., Julienne, P. S., and Hutson, J. M. *Phys. Rev. A* **87**, 032517 (2013).

[167] Kishimoto, T., Kobayashi, J., Noda, K., Aikawa, K., Ueda, M., and Inouye, S. *Phys. Rev. A* **79**, 031602 (2009).

[168] Weber, T., Herbig, J., Mark, M., Nägerl, H.-C., and Grimm, R. *Science* **299**(5604), 232–235 (2003).

[169] Herbig, J., Kraemer, T., Mark, M., Weber, T., Chin, C., Nägerl, H. C., and Grimm, R. *Science* **301**(5639), 1510–1513 (2003).

[170] Köppinger, M. P., Gregory, P. D., Jenkin, D. L., McCarron, D. J., Marchant, A. L., and Cornish, S. L. *New J. Phys.* **16**(11), 115016 (2014).

[171] Danzl, J. G., Haller, E., Gustavsson, M., Mark, M. J., Hart, R., Bouloufa, N., Dulieu, O., Ritsch, H., and Nägerl, H.-C. *Science* **321**, 1062–1066 (2008).

[172] Efimov, V. *Phys. Lett. B* **33**, 563–564 (1970).

[173] Kraemer, T., Mark, M., Waldburger, P., Danzl, J. G., Chin, C., Engeser, B., Lange, A. D., Pilch, K., Jaakkola, A., Nägerl, H. C., and Grimm, R. *Nature* **440**(7082), 315–318 (2006).

[174] Berninger, M., Zenesini, A., Huang, B., Harm, W., Nägerl, H.-C., Ferlaino, F., Grimm, R., Julienne, P. S., and Hutson, J. M. *Phys. Rev. Lett.* **107**, 120401 (2011).

[175] Huang, B., Sidorenkov, L. A., Grimm, R., and Hutson, J. M. *Phys. Rev. Lett.* **112**, 190401 (2014).

[176] Baranov, M., Dobrek, Ł., Góral, K., Santos, L., and Lewenstein, M. *Phys. Scr.* **T102**, 74–81 (2002).

[177] Żuchowski, P. S. and Hutson, J. M. *Phys. Rev. A* **81**, 060703(R) (2010).

[178] Köppinger, M. P. *Creation of ultracold RbCs molecules.* PhD thesis, Durham University, Durham, (2014).

[179] Jachymski, K. and Julienne, P. S. *Phys. Rev. A* **88**, 052701 (2013).

[180] Jenkin, D. L. *Feshbach spectroscopy of an ultracold Rb-Cs mixture.* PhD thesis, Durham University, Durham, UK, (2012).

[181] Aymar, M. and Dulieu, O. *J. Chem. Phys.* **122**(20), 204302 (2005).

[182] Julienne, P. S., Mies, F. H., Tiesinga, E., and Williams, C. J. *Phys. Rev. Lett.* **78**, 1880–1883 (1997).

[183] Schuster, T., Scelle, R., Trautmann, A., Knoop, S., Oberthaler, M. K., Haverhals, M. M., Goosen, M. R., Kokkelmans, S. J. J. M. F., and Tiemann, E. *Phys. Rev. A* **85**, 042721 (2012).

[184] Kokkelmans, S. J. J. M. F., Boesten, H. M. J. M., and Verhaar, B. J. *Phys. Rev. A* **55**, R1589–R1592 (1997).

[185] Mark, M., Kraemer, T., Herbig, J., Chin, C., Nägerl, H. C., and Grimm, R. *Europhys. Lett.* **69**(5), 706–712 (2005).

[186] Mark, M., Ferlaino, F., Knoop, S., Danzl, J. G., Kraemer, T., Chin, C., Nägerl, H.-C., and Grimm, R. *Phys. Rev. A* **76**, 042514 (2007).

[187] Ketterle, W. and van Druten, N. *Adv. At. Mol. Opt. Phys.* **37**, 181 (1996).

[188] Weiner, J., Bagnato, V. S., Zilio, S., and Julienne, P. S. *Rev. Mod. Phys.* **71**, 1–85 (1999).

[189] Myatt, C. J., Burt, E. A., Ghrist, R. W., Cornell, E. A., and Wieman, C. E. *Phys. Rev. Lett.* **78**(4), 586–589 (1997).

[190] Modugno, G., Modugno, M., Riboli, F., Roati, G., and Inguscio, M. *Phys. Rev. Lett.* **89**, 190404 (2002).

[191] Hadzibabic, Z., Stan, C. A., Dieckmann, K., Gupta, S., Zwierlein, M. W., Görlitz, A., and Ketterle, W. *Phys. Rev. Lett.* **88**(16), 160401 (2002).

[192] Roati, G., Riboli, F., Modugno, G., and Inguscio, M. *Phys. Rev. Lett.* **89**, 150403 (2002).

[193] Silber, C., Günther, S., Marzok, C., Deh, B., Courteille, P. W., and Zimmermann, C. *Phys. Rev. Lett.* **95**, 170408 (2005).

[194] Papp, S. B., Pino, J. M., and Wieman, C. E. *Phys. Rev. Lett.* **101**, 040402 (2008).

[195] Esry, B. D., Greene, C. H., Burke, Jr., J. P., and Bohn, J. L. *Phys. Rev. Lett.* **78**, 3594–3597 (1997).

[196] Damski, B., Santos, L., Tiemann, E., Lewenstein, M., Kotochigova, S., Julienne, P., and Zoller, P. *Phys. Rev. Lett.* **90**(11), 110401 (2003).

[197] Hung, C.-L., Zhang, X., Gemelke, N., and Chin, C. *Phys. Rev. A* **78**, 011604 (2008).

[198] McCarron, D. J., Cho, H. W., Jenkin, D. L., Köppinger, M. P., and Cornish, S. L. *Phys. Rev. A* **84**, 011603 (2011).

[199] Cornish, S. private communication, (2015).

[200] Roati, G., Zaccanti, M., D'Errico, C., Catani, J., Modugno, M., Simoni, A., Inguscio, M., and Modugno, G. *Phys. Rev. Lett.* **99**, 010403 (2007).

[201] Landini, M., Roy, S., Roati, G., Simoni, A., Inguscio, M., Modugno, G., and Fattori, M. *Phys. Rev. A* **86**, 033421 (2012).

[202] Brown, J. M. and Carrington, A. *Rotational Spectroscopy of Diatomic Molecules*, 646. Cambridge University Press, Cambridge (2003).

[203] Brink, D. M. and Satchler, G. R. *Angular Momentum.* Oxford University Press, 2nd edition, (1975).

[204] Inouye, S., Andrews, M. R., Stenger, J., Miesner, H.-J., Stamper-Kurn, D. M., and Ketterle, W. *Nature* **392**, 151–154 (1998).

[205] Cornish, S. L., Claussen, N. R., Roberts, J. L., Cornell, E. A., and Wieman, C. E. *Phys. Rev. Lett.* **85**, 1795–1798 (2000).

[206] Cornell, E. A. and Wieman, C. E. *Rev. Mod. Phys.* **74**, 875–893 (2002).

[207] Ketterle, W. *Rev. Mod. Phys.* **74**, 1131–1151 (2002).

[208] Bourdel, T., Khaykovich, L., Cubizolles, J., Zhang, J., Chevy, F., Teichmann, M., Tarruell, L., Kokkelmans, S. J. J. M. F., and Salomon, C. *Phys. Rev. Lett.* **93**, 050401 (2004).

[209] Zwierlein, M. W., Stan, C. A., Schunck, C. H., Raupach, S. M. F., Kerman, A. J., and Ketterle, W. *Phys. Rev. Lett.* **92**, 120403 (2004).

[210] Inguscio, M., Ketterle, W., and Salomon, C., editors. *Ultracold Fermi Gases.* IOS Press, Amsterdam, (2008). Proceedings of the International School of Physics “Enrico Fermi”, Course CLXIV, Varenna, 20-30 June 2006.

[211] Jochim, S., Bartenstein, M., Altmeyer, A., Hendl, G., Chin, C., Hecker Denschlag, J., and Grimm, R. *Phys. Rev. Lett* **91**, 240402 (2003).

[212] Greiner, M. and Fölling, S. *Nature* **453**, 736–738 (2008).

[213] Bloch, I. *Nature Phys.* **1**, 23–30 (2005).

[214] Wang, Y. and Esry, B. D. *New J. Phys.* **13**(3), 035025 (2011).

[215] Roy, S., Landini, M., Trenkwalder, A., Semeghini, G., Spagnolli, G., Simoni, A., Fattori, M., Inguscio, M., and Modugno, G. *Phys. Rev. Lett.* **111**, 053202 (2013).

[216] Ferlaino, F., Zenesini, A., Berninger, M., Huang, B., Nägerl, H., and Grimm, R. *Few-Body Syst.* **51**(2-4), 113–133 (2011).

[217] Berninger, M., Zenesini, A., Huang, B., Harm, W., Nägerl, H.-C., Ferlaino, F., Grimm, R., Julienne, P. S., and Hutson, J. M. *Phys. Rev. Lett.* **107**, 120401 (2011).

[218] Bethe, H. A. *Phys. Rev.* **76**, 38–50 (1949).

[219] Hinckelmann, O. and Spruch, L. *Phys. Rev. A* **3**, 642 (1971).

[220] Braaten, E. and Hammer, H.-W. *Phys. Rep.* **428**, 259–390 (2006).

[221] Blume, D. *Rep. Prog. Phys.* **75**, 046401 (2012).

[222] Wang, Y., D'Incao, J. P., and Esry, B. D. *Adv. At., Mol., Opt. Phys.* **62**, 1–115 (2013).

[223] Wang, Y., D'Incao, J. P., and Greene, C. H. *Phys. Rev. Lett.* **107**, 233201 (2011).

[224] Dyke, P., Pollack, S. E., and Hulet, R. G. *Phys. Rev. A* **88**, 023625 (2013).

[225] Naidon, P., Tiesinga, E., Mitchell, W. F., and Julienne, P. S. *New J. Phys.* **9**, 19 (2007).

[226] Mies, F. H. and Julienne, P. S. *J. Chem. Phys.* **77**(12), 6162–6176 (1982).

[227] Zinner, N. T. and Thogersen, M. *Phys. Rev. A* **80**, 023607 (2009).

[228] Gao, B. *Phys. Rev. A* **58**(5), 4222–4225 (1998).

[229] Flambaum, V. V., Gribakin, G. F., and Harabati, C. *Phys. Rev. A* **59**, 1998 (1999).

[230] Gao, B. *Phys. Rev. A* **84**, 022706 (2011).

[231] Julienne, P. S. and Gao, B. *AIP Conference Proceedings* **869**, 261–268 (2006).

[232] Naidon, P. and Ueda, M. *C. R. Phys.* **12**(1), 13–26 (2011).

[233] Braaten, E., Hammer, H. W., Kang, D., and Platter, L. *Phys. Rev. A* **81**, 013605 (2010).

[234] Ottenstein, T. B., Lompe, T., Kohnen, M., Wenz, A. N., and Jochim, S. *Phys. Rev. Lett.* **101**, 203202 (2008).

[235] Huckans, J. H., Williams, J. R., Hazlett, E. L., Stites, R. W., and O'Hara, K. M. *Phys. Rev. Lett.* **102**, 165302 (2009).

[236] Zaccanti, M., Deissler, B., D'Errico, C., Fattori, M., Jona-Lasinio, M., Muller, S., Roati, G., Inguscio, M., and Modugno, G. *Nat. Phys.* **5**, 586 (2009).

[237] Zürn, G., Lompe, T., Wenz, A. N., Jochim, S., Julienne, P. S., and Hutson, J. M. *Phys. Rev. Lett.* **110**, 135301 (2013).

[238] Falke, S., Knöckel, H., Friebe, J., Riedmann, M., Tiemann, E., and Lisdat, C. *Phys. Rev. A* **78**, 012503 (2008).

[239] Petrov, D. S. *Phys. Rev. Lett.* **93**, 143201 (2004).

[240] Bruun, G. M., Jackson, A. D., and Kolomeitsev, E. E. *Phys. Rev. A* **71**, 052713 (2005).

[241] Werner, F. and Castin, Y. *Phys. Rev. A* **86**, 013626 (2012).

[242] Mies, F. H. *J. Chem. Phys.* **80**(6), 2514–2525 (1984).

[243] Mies, F. H. and Julienne, P. S. *J. Chem. Phys.* **80**(6), 2526–2536 (1984).

[244] Gao, B. *Phys. Rev. A* **64**(1), 010701 (2001).

[245] Gao, B. *J. Phys. B* **37**(21), 4273–4279 (2004).

[246] Gao, B. *Phys. Rev. A* **78**, 012702 (2008).

[247] Gao, B. *Phys. Rev. A* **58**(3), 1728–1734 (1998).

[248] Gao, B. *Phys. Rev. Lett.* **83**(21), 4225–4228 (1999).

[249] Gao, B. University of Toledo, Ohio, (2003).

[250] Blume, D. and Greene, C. H. *Phys. Rev. A* **65**(4), 043613 (2002).

[251] Bolda, E. L., Tiesinga, E., and Julienne, P. S. *Phys. Rev. A* **66**, 013403 (2002).

[252] Liu, X.-J. *Phys. Rep.* **524**(2), 37–83 (2013).

[253] Chin, C. and Julienne, P. *Phys. Rev. A* **71**(1) (2005).

[254] Ospelkaus, S., Ospelkaus, C., Humbert, L., Sengstock, K., and Bongs, K. *Phys. Rev. Lett.* **97**, 120403 (2006).

[255] Beaufils, Q., Crubellier, A., Zanon, T., Laburthe-Tolra, B., Marchal, ., Vernac, L., and Gorceix, O. *Eur. Phys. J. D.* **56**(1), 99–104 (2010).

[256] Klempt, C., Henninger, T., Topic, O., Scherer, M., Kattner, L., Tiemann, E., Ertmer, W., and Arlt, J. J. *Phys. Rev. A* **78**, 061602(R) (2008).

[257] Hofferberth, S., Fischer, B., Schumm, T., Schmiedmayer, J., and Lesanovsky, I. *Phys. Rev. A* **76**, 013401 (2007).

[258] Suominen, K.-A., Band, Y. B., Tuvi, I., Burnett, K., and Julienne, P. S. *Phys. Rev. A* **57**, 3724–3738 (1998).

[259] Moerdijk, A. J., Verhaar, B. J., and Nagtegaal, T. M. *Phys. Rev. A* **53**, 4343–4351 (1996).

[260] Lompe, T., Ottenstein, T. B., Serwane, F., Wenz, A. N., Zrn, G., and Jochim, S. *Science* **330**(6006), 940–944 (2010).

[261] Tscherbul, T. V. and Rittenhouse, S. T. *Phys. Rev. A* **84**, 062706 (2011).

[262] Shotter, M., Trypogeorgos, D., and Foot, C. *Phys. Rev. A* **78**, 051602 (2008).

[263] Tscherbul, T. V., Calarco, T., Lesanovsky, I., Krems, R. V., Dalgarno, A., and Schmiedmayer, J. *Phys. Rev. A* **81**(5), 050701(R) (2010).

[264] Kaufman, A. M., Anderson, R. P., Hanna, T. M., Tiesinga, E., Julienne, P. S., and Hall, D. S. *Phys. Rev. A* **80**, 050701 (2009).

[265] Xie, T., Wang, G.-R., Huang, Y., Zhang, W., and Cong, S.-L. *J. Phys. B* **45**(14), 145302 (2012).

[266] Hanna, T. M., Tiesinga, E., and Julienne, P. S. *New J. Phys.* **12**(8), 083031 (2010).

[267] Papoular, D. J., Shlyapnikov, G. V., and Dalibard, J. *Phys. Rev. A* **81**, 041603 (2010).

[268] Zhang, P., Naidon, P., and Ueda, M. *Phys. Rev. Lett.* **103**, 133202 (2009).

[269] DeMille, D., Sainis, S., Sage, J., Bergeman, T., Kotochigova, S., and Tiesinga, E. *Phys. Rev. Lett.* **100**, 043202 (2008).

[270] Avdeenkov, A. V. *New J. of Phys.* **11**(5), 055016 (2009).

[271] Avdeenkov, A. V. *Phys. Rev. A* **86**, 022707 (2012).

[272] Alyabyshev, S. V. and Krems, R. V. *Phys. Rev. A* **80**(3), 033419 (2009).

[273] Alyabyshev, S. V., Tscherbul, T. V., and Krems, R. V. *Phys. Rev. A* **79**, 060703(R) (2009).

[274] Agosta, C. C., Silvera, I. F., Stoof, H. T. C., and Verhaar, B. J. *Phys. Rev. Lett.* **62**, 2361 (1989).

[275] Cohen-Tannoudji, C., Dupont-Roc, J., Grynberg, G., and Thickstun, P. *Atom-photon interactions: basic processes and applications.* Wiley Online Library, (1992).

[276] Shirley, J. H. *Phys. Rev.* **138**, B979–B987 (1965).

[277] Dalibard, J. and Cohen-Tannoudji, C. *J. Phys. B* **18**(8), 1661 (1985).

[278] Tscherbul, T. V., Calarco, T., Lesanovsky, I., Krems, R. V., Dalgarno, A., and Schmiedmayer, J. *Phys. Rev. A* **81**, 050701 (2010).

[279] Kaufman, A. M., Anderson, R. P., Hanna, T. M., Tiesinga, E., Julienne, P. S., and Hall, D. S. *Phys. Rev. A* **80**(5) (2009).

[280] Tscherbul, T. V. and Krems, R. V. *J. Chem. Phys.* **125**, 194311 (2006).

[281] Chotia, A., Neyenhuis, B., Moses, S. A., Yan, B., Covey, J. P., Foss-Feig, M., Rey, A. M., Jin, D. S., and Ye, J. *Phys. Rev. Lett.* **108**, 080405 (2012).

[282] Petrov, D. S. and Shlyapnikov, G. V. *Phys. Rev. A* **64**(1), 012706 Jun (2001).

[283] Zare, R. N. *Angular Momentum.* John Wiley & Sons, (1987).

[284] Rose, M. E. *Elementary Theory of Angular Momentum.* John Wiley & Sons, (1963).

[285] Wigner, E. P. *Am. J. Math* **63** (1941).

[286] Racah, G. *Phys. Rev.* **61** (1942).